

Dynamical coupling of the stratosphere and troposphere in a changing climate

Roland Walz

Deutsches Zentrum für Luft- und Raumfahrt
Institut für Physik der Atmosphäre
Oberpfaffenhofen



DLR

Deutsches Zentrum
für Luft- und Raumfahrt

Forschungsbericht 2022-17

Dynamical coupling of the stratosphere and troposphere in a changing climate

Roland Walz

Deutsches Zentrum für Luft- und Raumfahrt
Institut für Physik der Atmosphäre
Oberpfaffenhofen

165 Seiten

61 Bilder

3 Tabellen

197 Literaturstellen



Deutsches Zentrum
DLR für Luft- und Raumfahrt



Herausgeber:

Deutsches Zentrum
für Luft- und Raumfahrt e. V.
Wissenschaftliche Information
Linder Höhe
D-51147 Köln

ISSN 1434-8454
ISRN DLR-FB-2022-17

DOI: <https://doi.org/10.57676/6dvm-wj32>

Erklärung des Herausgebers:

Als Manuskript gedruckt.
Abdruck oder sonstige Verwendung nur
nach Absprache mit dem DLR gestattet.

Stratosphäre-Troposphäre Kopplung, Polarwirbel, Jetstreams, Residualzirkulation, Rossby-Wellen, idealisiertes Klimamodell

Roland WALZ

DLR, Institut für Physik der Atmosphäre, Oberpfaffenhofen

Dynamische Kopplung der Stratosphäre und Troposphäre im Klimawandel

Ludwig-Maximilians-Universität München

Der stratosphärische Polarwirbel ist in der Lage, bodennahe Bedingungen in der erweiterten Wintersaison erheblich zu beeinflussen. Induziert durch meridionale Temperaturgradienten, die sich zum Herbst hin entwickeln, bildet der Polarwirbel einen Wellenleiter, über den sich planetare Rossby-Wellen von der Troposphäre bis in die obere Stratosphäre ausbreiten können. Dissipieren diese Wellen, wird die gemittelte stratosphärische Strömung abgebremst und eine meridionale Zirkulation angetrieben. Darüber hinaus können aufwärts propagierende Rossby-Wellen auch reflektiert und sogar in die Troposphäre zurückgeführt werden, was mit einer begrenzten Geometrie des Wellenleiters zusammenhängt.

Um die gekoppelte Reaktion von Stratosphäre und Troposphäre auf thermische Antriebe zu untersuchen, wird in dieser Arbeit ein idealisiertes Klimamodell verwendet. In einem ersten Experiment wird der Einfluss verschiedener Realisierungen des stratosphärischen Polarwirbels auf die Troposphäre untersucht und die Möglichkeit eines Regimewechsels von einem schwachen und variablen zu einem starken und stabilen Polarwirbel mit begrenzter Wellenleitergeometrie beschrieben. Ein zweites Experiment zeigt, dass ein ähnlicher Regimewechsel durch kritische Werte troposphärischer Erwärmung ausgelöst werden kann. Der entdeckte dynamische Mechanismus wird schließlich im Hinblick auf realistischere Klimamodelle diskutiert. Es zeigt sich, dass künftige Verstärkungen des südhemisphärischen Polarwirbels mit der Entwicklung einer begrenzteren Wellenleitergeometrie verbunden sind.

Stratosphere-troposphere coupling, polar vortex, jet streams, residual circulation, Rossby waves, idealized climate model
(Published in English)

Roland WALZ

DLR, Institut für Physik der Atmosphäre, Oberpfaffenhofen

Dynamical coupling of the stratosphere and troposphere in a changing climate

Ludwig-Maximilians-Universität München

The stratospheric polar vortex can significantly influence surface conditions during extended winter seasons. Induced by meridional temperature gradients developing towards autumn, the polar vortex provides a waveguide which allows planetary-scale Rossby waves originating in the troposphere to propagate to the upper stratosphere. Upon dissipation, these waves decelerate the stratospheric mean flow and drive a meridional circulation. Apart from that, upward propagating Rossby waves can also be reflected and even be guided back to the troposphere which is associated with a confined geometry of the waveguide.

In order to investigate the coupled stratosphere-troposphere response to thermal forcings, an idealized climate model is used in this thesis. In a first experiment, the influence of different realizations of the stratospheric polar vortex on the troposphere is assessed, and the possibility of a regime transition from a weak and variable to a strong and stable polar vortex developing a confined waveguide geometry is described. A second experiment shows that a similar regime transition can be triggered by critical levels of tropospheric warming. Finally, the discovered dynamical mechanism is discussed in light of more realistic climate models. It is found that the future strengthening of the southern-hemispheric polar vortex is associated with the development of a more confined waveguide geometry.

Dynamical coupling of the stratosphere and troposphere in a changing climate

Roland Walz



München 2022

Dynamical coupling of the stratosphere and troposphere in a changing climate

Roland Walz

Dissertation
an der Fakultät für Physik
der Ludwig–Maximilians–Universität
München

vorgelegt von
Roland Walz
aus Nürnberg

München, den 03. Februar 2022

Erstgutachterin:	Prof. Dr. Hella Garny
Zweitgutachter:	Prof. Dr. Thomas Birner
Tag der Abgabe:	03. Februar 2022
Tag der mündlichen Prüfung:	05. April 2022

Zusammenfassung

Die dynamische Kopplung von Stratosphäre und Troposphäre ist im Winter besonders ausgeprägt, da starke Westwinde polare Regionen umkreisen und den stratosphärischen Polarwirbel bilden. Induziert durch strahlungsbedingte meridionale Temperaturgradienten stellt der Polarwirbel einen Wellenleiter zur Verfügung, über den sich planetare Rossby-Wellen von der Troposphäre bis in die obere Stratosphäre ausbreiten können. Dissipieren diese Wellen, wird die gemittelte stratosphärische Strömung abgebremst, was bis hin zum vollständigen Zusammenbruch des Polarwirbels führen kann, mit entsprechenden Auswirkungen auf die Troposphäre wie Kälteeinbrüchen. Abgesehen davon können planetare Wellen auch an der oberen Stratosphäre reflektiert und unter bestimmten Bedingungen sogar in die Troposphäre zurückgeführt werden, was polwärtige Verschiebungen des troposphärischen Jetstreams auslösen kann und als Downward Wave Coupling Event bekannt ist. Daher sind künftige Trends des stratosphärischen Polarwirbels für robuste Prognosen von Zirkulationsänderungen als Reaktion auf erhöhte Treibhausgaskonzentrationen von entscheidender Bedeutung, weisen derzeit aber in Simulationen mit komplexen Klimamodellen große Unsicherheiten auf.

Um die Reaktion des gekoppelten Systems aus Stratosphäre und Troposphäre auf erhöhte Treibhausgaskonzentrationen besser zu verstehen, wird in dieser Arbeit ein trockenes, rein dynamisches Klimamodell verwendet, das thermodynamische Prozesse wie Strahlung und Konvektion durch einfache Relaxation der Temperaturen zu vorgeschriebenen Gleichgewichtswerten ersetzt und die reale Atmosphäre nachahmt. Auf diese Weise können Zirkulationsänderungen direkt auf Änderungen der Gleichgewichtstemperatur zurückgeführt und nicht durch andere Prozesse, die die Temperatur beeinflussen, verwischt werden. In einer ersten Reihe von Experimenten wird der troposphärische Einfluss verschiedener Realisierungen des stratosphärischen Polarwirbels analysiert. Es zeigt sich, dass der Polarwirbel die Troposphäre nur dann beeinflussen kann, wenn er sich weit genug in die untere Stratosphäre erstreckt. Durch eine kältere untere polare Stratosphäre kann der Polarwirbel einen Übergang von einem schwachen und variablen hin zu einem starken und stabilen Regime vollziehen, der mit einer polwärtigen Verschiebung des troposphärischen Jets einhergeht. Die begrenzte Geometrie des Wellenleiters für planetare Wellen und die erhöhte Anzahl von Events mit abwärts gerichtetem Wellenfluss sind Hinweise darauf, dass der Regimewechsel mit dem Auftreten von Downward Wave Coupling Events zusammenhängt.

In einer zweiten Reihe von Experimenten werden Zirkulationsänderungen als Reaktion auf eine Erwärmung der oberen tropischen Troposphäre untersucht, die eine erhöhte Treibhausgaskonzentration nachahmt. Es zeigt sich, dass es kritische Werte der troposphärischen Erwärmung gibt, die einen Regimewechsel auslösen, der dem bereits in den Experimenten zur Kühlung der unteren polaren Stratosphäre beobachteten ähnelt. Im Vergleich zu einem Setup ohne

Polarwirbel wird der Regimewechsel hin zu einem starken und stabilen stratosphärischen Polarwirbel von einer verstärkten polwärtigen Verschiebung des troposphärischen Jets begleitet. Eine kombinierte Analyse zeigt, dass sowohl Abkühlungen in der unteren polaren Stratosphäre als auch Erwärmungen in der oberen tropischen Troposphäre den meridionalen Gradienten der potenziellen Vortizität in der unteren Stratosphäre der mittleren Breiten während der Entwicklung eines begrenzten Wellenleiters mit reflektierender Schicht erhöhen, was auf das Auftreten von Downward Wave Coupling Events hinweist. Während die wichtige Rolle der unteren Stratosphäre für die Kopplung zwischen Stratosphäre und Troposphäre in früheren Studien auf subsaisonalen Zeitskalen aufgedeckt wurde, erweitert diese Arbeit ihre Rolle auf Klima-Zeitskalen und verfeinert das Verständnis für Form und Stärke des Wellenleiters.

Um abzuschätzen, ob die Ergebnisse aus idealisierten Modellexperimenten für komplexe Klimamodelle relevant sind, wird eine kurze Analyse eines Multi-Modell-Ensembles durchgeführt, das einen exponentiellen Anstieg von Kohlenstoffdioxidkonzentrationen simuliert. Es zeigt sich, dass die Verstärkung des südhemisphärischen Polarwirbels mit der Entwicklung eines für planetare Wellen begrenzten Wellenleiters zusammenhängt, was die extrem seltenen Zusammenbrüche des südhemisphärischen Polarwirbels in künftigen Klimazuständen erklären könnte. Die große Streuung der Trends des nordhemisphärischen Polarwirbels ist konsistent mit den unterschiedlichen Entwicklungen der entsprechenden Wellenleiter und erfordert weitere Untersuchungen. Nichtsdestotrotz könnte der in dieser Arbeit vorgeschlagene dynamische Mechanismus dazu beitragen, künftige Entwicklungen der atmosphärischen Zirkulation zu beschreiben und in Einklang mit den Prognosen zu bringen.

Abstract

The dynamical coupling of the stratosphere and troposphere is particularly pronounced during winter seasons, when strong westerly winds encircle polar regions, constituting the stratospheric polar vortex. Induced by radiatively driven meridional temperature gradients, the polar vortex provides a waveguide which allows planetary-scale Rossby waves originating in the troposphere to propagate to the upper stratosphere. Upon dissipation, these waves decelerate the stratospheric mean flow, which might even cause a complete breakdown of the polar vortex with imminent tropospheric impacts including cold spells. Apart from that, planetary-scale waves can also be reflected at the upper stratosphere and even be guided back to the troposphere under certain conditions which can induce poleward displacements of tropospheric jet streams, known as downward wave coupling events. Therefore, future stratospheric polar vortex trends are vital for robust projections of circulation changes in response to increased greenhouse-gas concentrations, but are currently found to exhibit large uncertainties in simulations with complex climate models.

Aiming for a better understanding of the coupled stratosphere-troposphere response to increased greenhouse-gas concentrations, this thesis employs a dry dynamical-core model which replaces thermodynamic processes such as radiation and convection by a simple relaxation of temperatures to prescribed equilibrium values, mimicking the real atmosphere. In this way, circulation changes can directly be attributed to changes in the equilibrium temperature and are not blurred by other processes affecting temperature. In a first set of experiments, the tropospheric influence of different realizations of the stratospheric polar vortex is analyzed. It is found that the polar vortex can only affect the troposphere if the polar vortex extends sufficiently into the lower stratosphere. Induced by a colder polar lower stratosphere, the polar vortex is able to undergo a transition from a weak and variable to a strong and stable regime, which is accompanied by a poleward shift of the tropospheric jet. The confined geometry of the waveguide for planetary-scale waves and the occurrence of an increased number of downward wave flux events provide evidence that the regime transition is associated with the emergence of downward wave coupling events.

In a second set of experiments, circulation changes in response to tropical upper-tropospheric warming, mimicking increased greenhouse-gas concentrations, are analyzed. It is found that critical tropospheric warming levels exist at which a transition to a strong polar vortex occurs that is similar to the one observed in stratospheric cooling experiments. Compared to a setup without polar vortex, the transition to a strong and stable stratospheric polar vortex is accompanied by an enhanced poleward shift of the tropospheric jet. A combined analysis reveals that both polar lower-stratospheric cooling and tropical upper-tropospheric warming act to increase the meridional gradient of potential vorticity in the midlatitude lower strato-

sphere during the development of a confined waveguide with reflecting surface in the upper stratosphere, providing evidence for the occurrence of downward wave coupling events. While the important role of the lower stratosphere for stratosphere-troposphere coupling has been discovered by previous studies to appear on subseasonal time scales, this thesis extends its role to time scales relevant for climate change, and refines the understanding of the shape and strength of the waveguide.

In order to estimate whether the results from idealized model experiments are relevant for complex climate models, a brief analysis of a multi-model ensemble that is forced by an exponential increase in carbon dioxide concentrations is conducted. It is found that the southern-hemispheric polar vortex strengthening is associated with the development of a more confined waveguide for planetary-scale waves, which might explain the extremely rare formation of polar vortex breakdowns in future climates. The large spread in northern-hemispheric polar vortex trends is consistent with various waveguide developments and requires additional investigations. Nevertheless, this thesis proposes a new dynamical mechanism which could contribute to describe and reconcile future atmospheric circulation changes.

List of publications

Parts of the results presented in this thesis have been published or are intended for publication according to the following articles:

- Garny, H., Walz, R., Nützel, M., and Birner, T. Extending the Modular Earth Submodel System (MESSy v2.54) model hierarchy: the ECHAM/MESSy IdeaLized (EMIL) model setup. *Geoscientific Model Development*, 13(11):5229–5257, 2020. <https://doi.org/10.5194/gmd-13-5229-2020>.
- Walz, R., Garny, H., and Birner, T. Stratospheric Modulation of Tropical Upper-Tropospheric Warming-Induced Circulation Changes in an Idealized General Circulation Model. *Journal of the Atmospheric Sciences*, in review.

Contents

Zusammenfassung	v
Abstract	vii
List of publications	ix
1 Introduction	1
1.1 State of the art	4
1.1.1 The general circulation in the stratosphere	4
1.1.2 Circulation response to global warming	15
1.1.3 Idealized climate models	19
1.2 Research questions and outline	20
2 Methodology	23
2.1 The idealized general circulation model EMIL	23
2.1.1 Rayleigh friction and Newtonian damping	24
2.1.2 Tropical upper-tropospheric warming	28
2.1.3 Generation of planetary-scale waves	28
2.2 Simulations	29
2.2.1 Polar stratospheric cooling	29
2.2.2 Tropical warming	30
2.3 Diagnostics	34
2.3.1 Latitude of a zonal-mean maximum	34
2.3.2 Eliassen–Palm flux components of a meridional subdomain	36
2.3.3 Strength of the residual circulation	37
2.3.4 Autocorrelation time scale	40
3 The role of the LS for stratosphere-troposphere coupling	41
3.1 Motivation: circulation sensitivity to the lower-stratospheric thermal structure	42
3.2 Comparison of different winter-climate setups	43
3.3 Nonlinear circulation response to polar stratospheric cooling	50
3.4 Discussion of the relevant dynamical mechanism	53
3.5 Conclusions	58

4	Stratospheric modulation of TUTW-induced circulation changes	61
4.1	Guiding hypotheses	62
4.2	Stratospheric influence of polar vortex regimes on the tropospheric jet	62
4.3	Weak polar vortex regime	68
4.4	Strong polar vortex regime	76
4.5	Robust criterion for the regime transition	81
4.6	Sensitivity to the tropical heating location	85
4.7	Discussion	92
4.8	Conclusions	96
5	Combined perspectives and implications beyond idealized models	99
5.1	Universal behavior of the waveguide in idealized models	100
5.2	Implications for the CMIP6 1pctCO2 experiment	109
5.3	Conclusions	120
6	Summary and outlook	125
	Acronyms	135
	List of figures	137
	List of tables	141
	Bibliography	143
	Used software, data, and computational resources	163
	Acknowledgments	165

Chapter 1

Introduction

The projection of future climates is a challenging endeavor. In order to most realistically reproduce the climate system, modern-day earth-system models couple physical, chemical, and biological processes from a variety of compartments including the atmosphere, ocean, land, and ice sheets (e.g., Jöckel et al., 2005; Collins et al., 2011; Hurrell et al., 2013; Swart et al., 2019a). These complex climate models prove the anthropogenic influence on increasing global surface temperatures since the preindustrial era, and are used to assess future climate change (IPCC, 2014, 2022). Inherent in climate projections are, however, certain degrees of uncertainty arising from three major sources: model uncertainty, scenario uncertainty, and internal variability (Hawkins and Sutton, 2009). Model uncertainty describes the fact that different climate models produce different results in response to identical boundary conditions (Tebaldi and Knutti, 2007). Missing information of these boundary conditions, e.g., the future development of greenhouse-gas concentrations or volcanic eruptions, represents scenario uncertainty. And even if boundary conditions are perfectly known, natural fluctuations of the climate system can cause deviations from predicted trends, denoting internal variability (Deser et al., 2012). Whereas scenario uncertainty dominates on longer terms, model uncertainty and internal variability are more important for short-term predictions and especially on regional scales (Hawkins and Sutton, 2009). In order to reduce uncertainties in future climate projections, ensembles of many models are consulted (Tebaldi and Knutti, 2007; Eyring et al., 2016) and a variety of possible scenarios is assessed (Tebaldi et al., 2021).

The degree of uncertainty underlying specific aspects of future climates also depends on the physical quantity analyzed from model output (Shepherd, 2014). Ice sheet extents, snow covers, and surface temperatures can be projected more robustly due to their thermodynamic foundation. In contrast to this, changes of regional precipitation patterns and circulation regimes exhibit drastically lower robustness due to their strong dependence on changes in atmospheric dynamics with its chaotic nature as visualized in Fig. 1.1. Large regions of Europe,

North Africa, America, Australia, and in the Middle East are exposed to uncertainties in the precipitation change by the end of the twenty-first century due to disagreeing models. In midlatitudes of both hemispheres, these uncertainties arise from diverse projections of future position and strength of tropospheric jet streams (Shepherd, 2014)—bands of westerly winds that encircle polar regions. Seasonal variations of their latitudinal position are connected to annular modes which can be defined via surface pressure differences between midlatitude and polar regions (e.g., Thompson and Wallace, 2000). For example, positive phases of the annular mode over the North Atlantic sector correspond to poleward displacements of the jet stream with increased storms and precipitation in Northern Europe, whereas negative phases are in general associated with enhanced Mediterranean precipitation (e.g., Hurrell, 1995). Climate change over Europe is in particular sensitive to the developments of many domains of the atmosphere and especially to stratospheric circulation changes, including contrasting future precipitation patterns (Zappa and Shepherd, 2017).

The stratosphere is able to exert significant influence on the troposphere. During winter seasons when sunlight ceases to reach polar regions, strong circumpolar westerly winds extend to the top of the stratosphere, constituting the stratospheric polar vortex which plays an essential role in the dynamical coupling of the stratosphere and troposphere (Gerber et al., 2012; Kidston et al., 2015; Zappa and Shepherd, 2017). In general, the strength of the polar vortex is correlated with the phase of tropospheric annular modes (Baldwin and Dunkerton, 2001; Thompson et al., 2005). A strong polar vortex involves a positive annular mode phase (Limpasuvan et al., 2005), whereas weak polar vortices are observed in combination with negative annular modes (Limpasuvan et al., 2004). In this way, the stratospheric polar vortex is coupled to tropospheric jet streams. Abrupt decelerations of the stratospheric polar vortex or breakdowns with wind reversals, known as sudden stratospheric warmings (SSWs), can lead to extreme tropospheric anomalies including cold-air outbreaks during northern-hemispheric winter seasons (Kolstad et al., 2010) and heat waves during southern-hemispheric spring seasons (Lim et al., 2019). Since extreme developments of the polar vortex can act as precursors of tropospheric conditions, improved understanding of relevant coupling processes offers the possibility of extended and robust predictions of severe surface impacts (Baldwin et al., 2003).

The crucial region for stratosphere-troposphere coupling has been identified to be the lower stratosphere (LS). Most significant annular mode anomalies associated with SSWs that propagate downward from the stratosphere are observed in the troposphere shortly after appearing in the lower stratosphere (Hitchcock and Simpson, 2014). The actual onset date of the SSW defined in the upper stratosphere is much earlier. Moreover, the lower stratosphere determines whether annular mode anomalies are able to propagate downward to the troposphere or not (Karpechko et al., 2017). This aspect of stratosphere-troposphere coupling applies also to the developing stage of SSWs. Only about one third of observed and modeled SSWs are generated

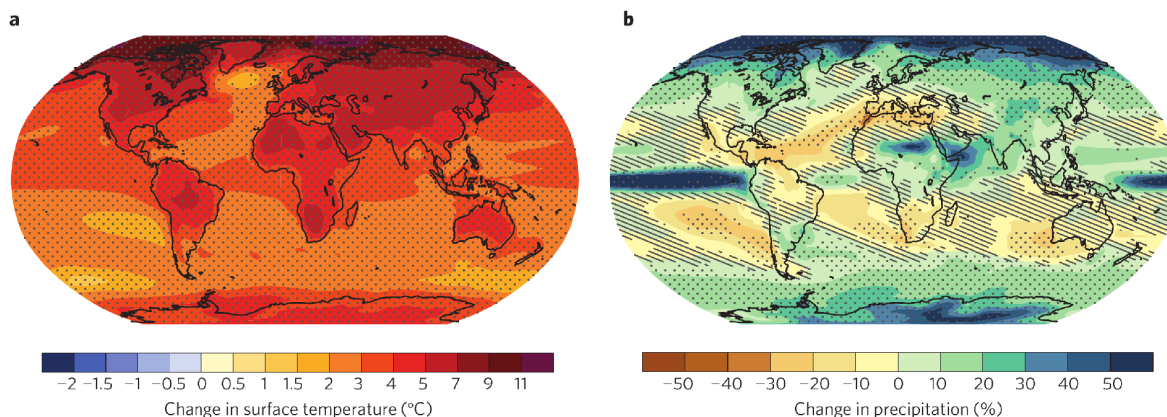


Figure 1.1: Changes in surface air temperature (a) and precipitation (b) between the end and the beginning of the twenty-first century for the Representative Concentration Pathway 8.5 scenario projected by the Coupled Model Intercomparison Project Phase 5 (CMIP5) multi-model ensemble. Robust (not significant) changes are indicated by stippling (hatching). The figure is taken from Shepherd (2014).

by extreme events in the troposphere, whereas the majority of SSWs are products of internal variability of the lower stratosphere (Birner and Albers, 2017; White et al., 2019).

To this end, a robust projection of future stratospheric circulation changes is vital. Up to now, however, a variety of possible polar vortex developments in the northern hemisphere (NH) in response to increased carbon dioxide (CO_2) concentrations is present in complex climate models (Manzini et al., 2014; Ayarzagüena et al., 2020). Paradoxically, their demand to represent Earth’s climate most realistically prevents the detection of reasons for this spread in complexity gaining Earth-system models (Wu et al., 2019). Circulation changes can not be uniquely attributed to arise from radiative or purely dynamical processes which both affect temperature. Better understanding of future circulation changes and differences in their projections therefore requires an opposite approach via hierarchies of models (Held, 2005). Starting from basic principles, only those dynamical equations, physical processes, and space-time scales are included which are absolutely necessary to investigate the question of interest (Maher et al., 2019).

Pursuing the strategy of idealized climate models, this thesis aims for a better understanding of the dynamical coupling of the stratosphere and troposphere on climatological time scales by simulating the dry-atmosphere response to different thermodynamic forcings mimicking, among other forcings, higher carbon dioxide concentrations (Wang et al., 2012). This can be achieved by prescribing an equilibrium temperature the atmosphere of the model is relaxed to (Held and Suarez, 1994; Polvani and Kushner, 2002). In this way, circulation changes for different equilibrium temperatures are known to arise from purely dynamical effects. Gained knowledge about dynamical mechanisms is in the end used to interpret the different circulation

changes of complex climate models in response to increased carbon dioxide concentrations. Accordingly, this thesis contributes to reducing model uncertainty in future climate projections.

1.1 State of the art

To set the stage for this thesis, well-established concepts necessary to comprehend the dynamical coupling of the stratosphere and troposphere are presented first. Derivations throughout this section are frequently based on standard literature (Andrews et al., 1987; Holton, 2004; Vallis, 2017). The formed foundation is then used to embed the aims of this thesis which are addressed in the subsequent Sec. 1.2.

1.1.1 The general circulation in the stratosphere

In contrast to the troposphere, temperatures tend to increase with height in the stratosphere due to the presence of ozone absorbing ultraviolet radiation from the sun in the summer hemisphere and equatorward parts of the winter hemisphere (e.g., Holton, 2004). Polar regions in the winter hemisphere which are not reached by sunlight exhibit, however, far colder temperatures. As a result, a strong meridional temperature gradient is radiatively developed towards every winter season in both hemispheres. These temperature differences are balanced by a meridional overturning circulation which is—in contrast to the overturning Hadley cell (HC) in the troposphere—not driven by locally maximized heating, but rather by waves propagating upward from the troposphere (Andrews et al., 1987). When these waves dissipate in the stratosphere, a zonal force is exerted on the mean flow causing air masses in the summer hemisphere to ascend and to move towards the winter hemisphere where they descend (Holton et al., 1995). Due to the Coriolis force, the resulting flow from summer to winter hemisphere is accelerated in westward direction in the summer hemisphere, and in eastward direction in the winter hemisphere, respectively. The wave-driven circulation tends to attenuate the radiatively generated meridional temperature gradient and balances the fast westerly zonal winds in the winter hemisphere, surrounding the polar vortex. Intruding air from the troposphere below has to pass through the cold point of the tropical tropopause layer which drastically reduces the content of water vapor in the stratosphere. Consequently, the stratosphere is extremely dry compared to the troposphere (Brewer, 1949; Dobson et al., 1926; Dobson and Massey, 1956). In the following, the mathematical framework is introduced which describes the stratospheric flow and its interactions with waves driving the meridional overturning circulation.

Primitive equations

Adapted to the stratospheric environment, the primitive equations for the case of a dry, hydrostatic, inviscid flow on a rotating sphere with radius a and angular rotation rate Ω can be developed from the Navier–Stokes equations. Expressed in a coordinate system employing

longitude λ and latitude ϕ in the horizontal plane as well as pressure p in the vertical direction, they read (Andrews et al., 1987; Vallis, 2017)

$$\frac{du}{dt} - v \left(f + \frac{u \tan \phi}{a} \right) = -\frac{\partial_\lambda \Phi}{a \cos \phi} + X, \quad (1.1)$$

$$\frac{dv}{dt} + u \left(f + \frac{u \tan \phi}{a} \right) = -\frac{\partial_\phi \Phi}{a} + Y, \quad (1.2)$$

$$\partial_p \Phi = -\frac{RT}{p}, \quad (1.3)$$

$$\frac{\partial_\lambda u}{a \cos \phi} + \frac{\partial_\phi (v \cos \phi)}{a \cos \phi} + \partial_p \omega = 0, \quad (1.4)$$

$$c_p \frac{dT}{dt} - \frac{RT}{p} \omega = J. \quad (1.5)$$

The flow is characterized by zonal, meridional, and vertical wind components $u \equiv a \cos \phi d\lambda/dt$, $v \equiv a d\phi/dt$, and $\omega \equiv dp/dt$, respectively, with total time derivative

$$\frac{d}{dt} = \left(\partial_t + \frac{u \partial_\lambda}{a \cos \phi} + \frac{v \partial_\phi}{a} + \omega \partial_p \right). \quad (1.6)$$

Partial derivatives with respect to the coordinate x are denoted by ∂_x . Additional variables include temperature T , geopotential Φ , diabatic heating rate J per unit mass, and nonconservative mechanical forcings X and Y . The specific gas constant for dry air is represented by R , the heat capacity at constant pressure by c_p , and $f = 2\Omega \sin \phi$ is the Coriolis parameter. This set of equations is solved in dynamical cores of atmospheric general circulation models (GCMs, e.g., Roeckner et al., 2003). Different models can share the same dynamical core, but vary in complexity by coupling various compartments of the atmospheric system as radiation and cloud effects to the dynamical core (Maher et al., 2019). Nevertheless, essential features of the general circulation can be simulated solidly without additional physical and chemical processes, as long as consistent idealized heating rates are provided that mimic the aforementioned processes (Held and Suarez, 1994; Polvani and Kushner, 2002).

The transformed Eulerian-mean framework

A convenient advancement of the primitive equations is achieved within the transformed Eulerian-mean (TEM) framework (Andrews et al., 1987) which allows to investigate the interaction of the zonal-mean flow with deviations from it—hereafter referred to as waves or eddies. To this end, every variable A occurring in the primitive equations (1.1)–(1.5) is decomposed into zonal mean \bar{A} and disturbance A' via

$$\bar{A}(t, p, \phi) = \frac{1}{2\pi} \int_0^{2\pi} A(t, p, \phi, \lambda) d\lambda \quad (1.7)$$

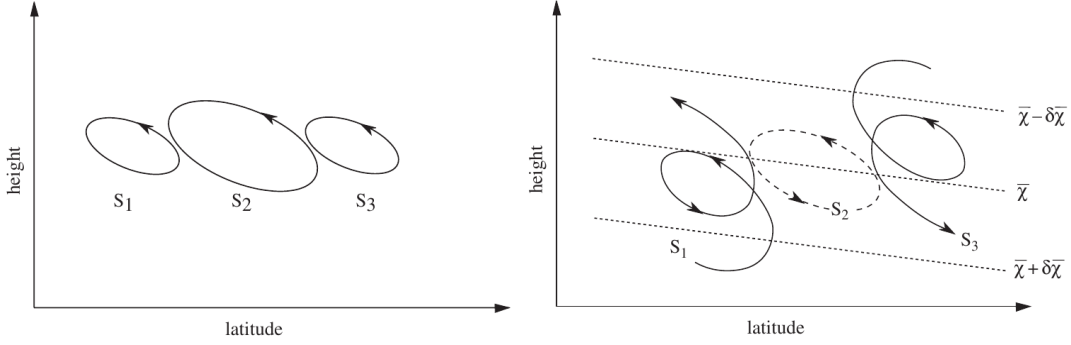


Figure 1.2: Meridional motion of air parcels in presence of planetary-scale waves. For adiabatic flow, no net transport emerges (left). When tropical regions are diabatically heated and polar regions are diabatically cooled, the circulation induces a net transport with upwelling in low latitudes and downwelling in high latitudes influencing the concentration $\bar{\chi}$ of an arbitrary tracer (right). Both figures are taken from Holton (2004).

and

$$A'(t, p, \phi, \lambda) \equiv A - \bar{A}. \quad (1.8)$$

After zonally averaging the primitive equations including the wave-mean flow decomposition (1.8), the conventional Eulerian-mean equations are obtained. Inherent in this Eulerian-mean framework, however, is the nontransport paradox for adiabatic flow in the stationary limit (Andrews et al., 1987; Holton, 2004). Under these circumstances, planetary-scale waves induce a nonzero zonal-mean meridional circulation $(\bar{v}, \bar{\omega})$ that reflects no net transport in the vertical direction since adiabatic flow prevents motion across isentropes. Hence, air parcels move in closed ellipses in the meridional plane as shown in the left panel of Fig. 1.2. Only in presence of diabatic processes, a net transport of the meridional circulation can be observed as shown in the right panel of Fig. 1.2.

The misleading nontransport of adiabatic motion can be circumvented by a transformation to the residual-mean meridional circulation $(\bar{v}^*, \bar{\omega}^*)$ given by (Andrews et al., 1983)

$$\bar{v}^* = \bar{v} - \partial_p \left(\frac{\overline{v'\theta'}}{\partial_p \bar{\theta}} \right), \quad (1.9)$$

$$\bar{\omega}^* = \bar{\omega} + \frac{1}{a \cos \phi} \partial_\phi \left(\cos \phi \frac{\overline{v'\theta'}}{\partial_p \bar{\theta}} \right), \quad (1.10)$$

introducing the potential temperature $\theta = T(p_r/p)^\kappa$ with reference pressure p_r usually taken to be 1000 hPa and with $\kappa \equiv R/c_p \approx 2/7$. The zonal momentum and thermodynamic equations

in the transformed Eulerian-mean framework then read¹

$$\partial_t \bar{u} = -\bar{v}^* \hat{f} - \bar{\omega}^* \partial_p \bar{u} + \frac{\nabla \cdot \mathbf{F}}{a \cos \phi} + \bar{X}, \quad (1.11)$$

$$\partial_t \bar{\theta} = -\frac{\bar{v}^*}{a} \partial_\phi \bar{\theta} - \bar{\omega}^* \partial_p \bar{\theta} - \partial_p \left(\frac{\overline{v' \theta'}}{a \partial_p \bar{\theta}} + \overline{\omega' \theta'} \right) + \bar{Q}, \quad (1.12)$$

respectively, with $\hat{f} = (a \cos \phi)^{-1} \partial_\phi (\bar{u} \cos \phi) - f$, the diabatic heating term $\bar{Q} = (\bar{J}/c_p)(p_r/p)^\kappa$, and the Eliassen–Palm flux divergence (EPFD)

$$\nabla \cdot \mathbf{F} = \frac{\partial_\phi (F^{(\phi)} \cos \phi)}{a \cos \phi} + \partial_p F^{(p)} \quad (1.13)$$

with meridional and vertical Eliassen–Palm (EP) flux components

$$F^{(\phi)} = a \cos \phi \left(-\overline{u' v'} + \frac{\overline{v' \theta'}}{\partial_p \bar{\theta}} \partial_p \bar{u} \right), \quad (1.14)$$

$$F^{(p)} = a \cos \phi \left(-\overline{u' \omega'} - \frac{\overline{v' \theta'}}{\partial_p \bar{\theta}} \hat{f} \right), \quad (1.15)$$

respectively.

In contrast to the zonal momentum equation in the conventional Eulerian-mean framework which only includes the eddy fluxes of momentum, both eddy fluxes of momentum and heat are comprised in the EP flux divergence $\nabla \cdot \mathbf{F}$ entering the TEM zonal momentum equation (1.11). Considering the identical case of steady and conservative waves on adiabatic flow that led to the nontransport paradox in the conventional Eulerian-mean framework, the EP flux divergence vanishes and the solution $\bar{v}^* = \bar{\omega}^* = 0$ exists in the TEM framework indicating no net transport as expected. Only if waves dissipate, generating diabatic conditions, a nonzero residual-mean meridional circulation (RC) is driven (Andrews et al., 1987).

Rossby-wave propagation

Atmospheric waves originate from various sources on Earth. Horizontal oscillations that are restored by the northward increasing Coriolis parameter are denoted by Rossby waves, and vertical oscillations that are restored by buoyancy in a stably stratified environment are denoted by gravity waves (Andrews et al., 1987). Rossby waves can be generated by different surface heating rates over oceans and continents, by the overflow of mountain ranges (Plumb, 1985), by nonlinear wave-wave interaction (Scinocca and Haynes, 1998; Domeisen and Plumb, 2012), and by baroclinic instabilities (Farrell, 1989). Gravity waves can be excited by displaced air

¹Expressions of the remaining primitive equations in the conventional as well as in the transformed Eulerian-mean framework can be found in Andrews et al. (1987).

masses following the orography (Smith et al., 2009) and by convection (Larsen et al., 1982).² This thesis focuses on planetary- and synoptic-scale Rossby waves, where waves with zonal wavenumbers (WNs) of 1, 2, and 3 are considered as planetary-scale and waves with WNs larger than 3 are considered as synoptic-scale waves.

Originating from the troposphere, Rossby waves are able to propagate in the meridional plane. In order to derive which regions of the meridional plane are accessible via Rossby-wave propagation, linearized versions of the Eulerian-mean momentum and thermodynamic equations are required. For adiabatic and frictionless motion upon a slowly varying, purely zonal, and geostrophically balanced zonal-mean flow \bar{u} with logarithmic pressure $z = -H \ln(p/p_r)$ as vertical coordinate, the thermodynamic and vorticity equations for small-amplitude zonal perturbations read (Matsumo, 1970)

$$\left(\partial_t + \frac{\bar{u} \partial_\lambda}{a \cos \phi} \right) \partial_z \Phi' - f v' \partial_z \bar{u} + N^2 w' = 0 \quad (1.16)$$

and

$$\left(\partial_t + \frac{\bar{u} \partial_\lambda}{a \cos \phi} \right) \zeta' + \frac{v'}{a} \partial_\phi \bar{\eta} - \frac{f}{p} \partial_z (p w') = 0, \quad (1.17)$$

respectively, neglecting contributions of the order of perturbations squared and with scale height H , buoyancy frequency N^2 , vertical wind perturbation w' , relative vorticity perturbation $\zeta' = (a \cos \phi)^{-1} [\partial_\lambda v' - \partial_\phi (u' \cos \phi)]$, and latitudinal gradient of zonal-mean absolute vorticity $\partial_\phi \bar{\eta} = 2\Omega \cos \phi - \partial_\phi [(a \cos \phi)^{-1} \partial_\phi (\bar{u} \cos \phi)]$. The quasi-geostrophic (QG) potential vorticity equation can then be derived by employing the thermodynamic equation (1.16) solved for w' in the vorticity equation (1.17) which leads to (Andrews et al., 1987)

$$\left(\partial_t + \frac{\bar{u} \partial_\lambda}{a \cos \phi} \right) q' + \frac{v'}{a} \partial_\phi \bar{q} = 0, \quad (1.18)$$

identifying the QG potential vorticity perturbation

$$q' = \zeta' + \frac{f}{p} \partial_z \left(\frac{p}{N^2} \partial_z \Phi' \right) \quad (1.19)$$

and the latitudinal gradient of the zonal-mean QG potential vorticity

$$\partial_\phi \bar{q} = \partial_\phi \bar{\eta} - \frac{f^2 a}{p} \partial_z \left(\frac{p}{N^2} \partial_z \bar{u} \right). \quad (1.20)$$

In order to arrive at the QG potential vorticity equation (1.18), geostrophic balance for the meridional wind perturbation v' is assumed. Following Harnik and Lindzen (2001), the QG

²Thorough reviews on gravity-wave dynamics are provided by Fritts and Alexander (2003) and Alexander et al. (2010).

potential vorticity equation (1.18) can be transformed into a wave propagation equation by redefining the perturbations of geostrophic winds according to $u' = -a^{-1}\partial_\phi\Upsilon'$ and $v' = (a\cos\phi)^{-1}\partial_\lambda\Upsilon'$ with $\Upsilon' = \Phi'/f$, in combination with the transformation

$$\Upsilon' = \psi \exp\left(\frac{z}{2H}\right) N \exp\left[ik\left(\lambda - \frac{c}{a\cos\phi}t\right)\right] \quad (1.21)$$

that incorporates wave-like solutions of zonal wavenumber k and zonal phase speed c . Neglecting all terms with explicit time dependence, the wave equation for the rescaled geopotential perturbation ψ reads

$$\frac{\partial_\phi(\cos\phi\partial_\phi\psi)}{\cos\phi} + \frac{f^2a^2}{N^2}\partial_z^2\psi + n_{c,k}^2\psi = 0 \quad (1.22)$$

including the refractive index squared

$$n_{c,k}^2 = \left[\frac{\partial_y\bar{q}}{\bar{u} - c} - \left(\frac{k}{a\cos\phi}\right)^2 + f^2F(N^2) \right] a^2 \quad (1.23)$$

with $\partial_y = a^{-1}\partial_\phi$ and $F(N^2) = -(2NH)^{-2}$ for constant N^2 (Simpson et al., 2009; Gerber, 2012). Transforming back to pressure p as vertical coordinate, meridional gradient of zonal-mean QG potential vorticity and buoyancy frequency are given by

$$\partial_y\bar{q} = \frac{2\Omega\cos\phi}{a} - \frac{1}{a^2}\partial_\phi\left(\frac{\partial_\phi(\bar{u}\cos\phi)}{\cos\phi}\right) + \frac{f^2}{R}\partial_p\left(\frac{p\bar{\theta}}{T}\frac{\partial_p\bar{u}}{\partial_p\bar{\theta}}\right), \quad (1.24)$$

$$N^2 = -\frac{gp}{H}\frac{\partial_p\bar{\theta}}{\bar{\theta}}, \quad (1.25)$$

respectively.

Wave-like solutions for ψ are obtained from Eq. (1.22) for a positive refractive index squared $n_{c,k}^2$. In regions of the meridional plane with $n_{c,k}^2 < 0$, wave amplitudes ψ are exponentially damped (Charney and Drazin, 1961). In general, waves are refracted towards regions with higher values of the refractive index squared (Karoly and Hoskins, 1982; Chen and Robinson, 1992). A positive refractive index squared requires its first term to be positive since both its second and third term are always negative. The first term of the refractive index squared is proportional to the meridional potential vorticity gradient $\partial_y\bar{q}$ divided by the difference of the zonal-mean zonal wind \bar{u} and the phase speed c of the propagating wave. Assuming only positive $\partial_y\bar{q}$, wave propagation is therefore only allowed if the zonal-mean flow exceeds the phase speed of the wave, i.e., $\bar{u} - c > 0$, but with the second condition that the difference $\bar{u} - c$ falls below a critical value which depends in general on the wavenumber k and on $\partial_y\bar{q}$, thus on the flow itself (Charney and Drazin, 1961; Andrews et al., 1987).

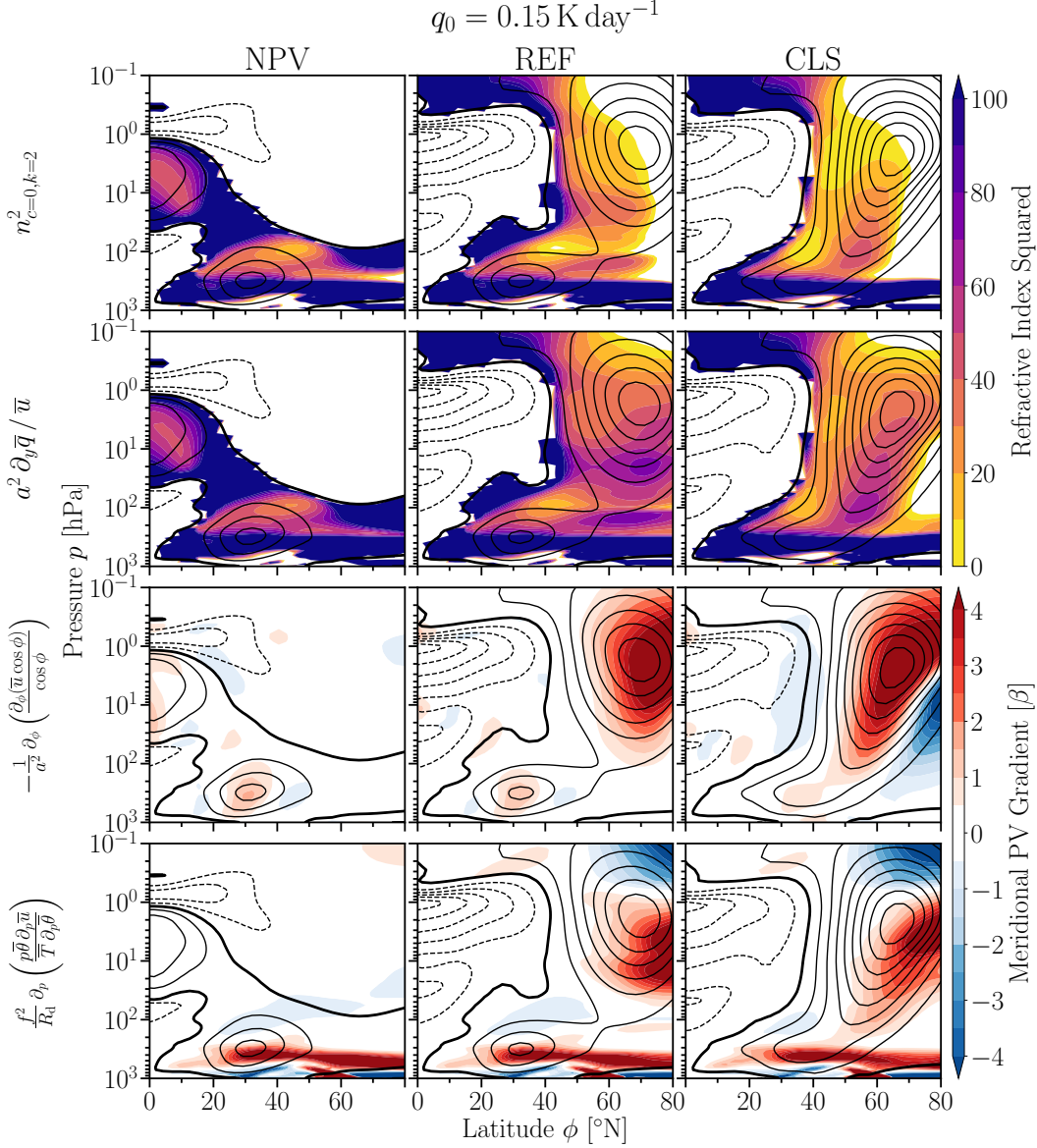


Figure 1.3: Refractive index squared $n_{c=0,k=2}^2$ for stationary waves of wavenumber 2 (first row), its first term $a^2 \partial_y \bar{q} / \bar{u}$ including the meridional potential vorticity gradient $\partial_y \bar{q}$ (second row), and contributions to $\partial_y \bar{q}$ from meridional and vertical curvature terms of the zonal-mean zonal wind \bar{u} (third and fourth row, respectively) as functions of latitude ϕ and pressure p for different representations of the wintertime stratosphere without polar vortex (NPV, left), with polar vortex (REF, middle), and with a stronger polar vortex (CLS, right). Details of the displayed quantities can be inferred from Eqs. (1.23)–(1.25). Contributions to $\partial_y \bar{q}$ are given in units of $\beta = 2\Omega a^{-1} \cos \phi$ as shown in the third and fourth row. The zonal-mean zonal wind \bar{u} (black contour lines with a contour interval of 10 m s^{-1} , negative contours dashed, thick zero-contour line) is added in each panel. The simulations used for this figure correspond to the tropical upper-tropospheric warming (TUTW) experiments with a heating amplitude of $q_0 = 0.15 \text{ K day}^{-1}$ and resolution T42L90 introduced in Sec. 2.2.2.

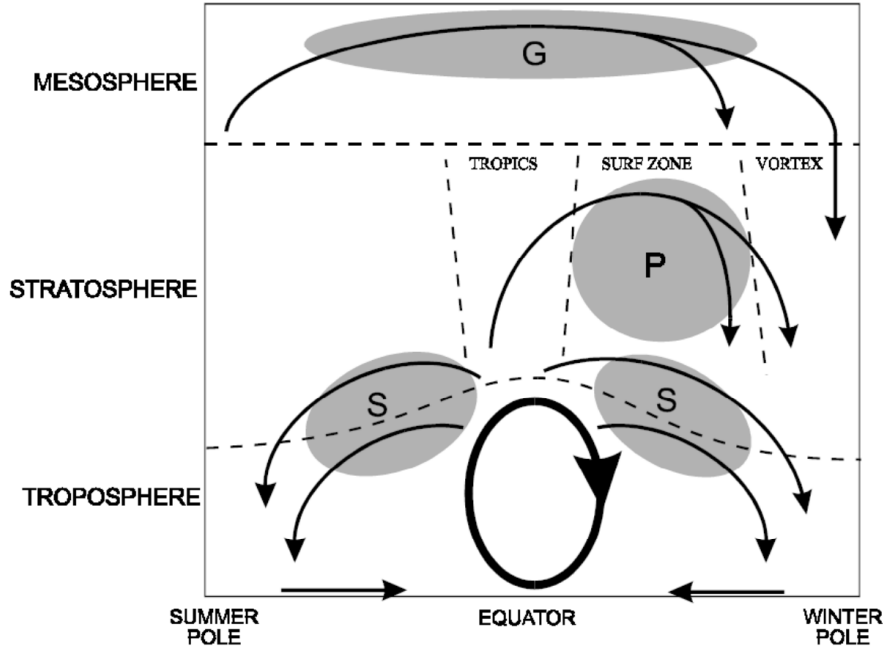


Figure 1.4: Wave-driven residual-mean meridional circulation (RC) in the stratosphere and mesosphere as well as the thermally-driven Hadley cell (HC) in the tropical troposphere. Shallow branches of the RC exist in the lower stratosphere of both hemispheres and are driven by the dissipation of upward propagating synoptic-scale waves (S). In the winter hemisphere, planetary-scale wave dissipation (P) can reach the upper stratosphere, driving the deep branch of the RC. Gravity-wave breaking (G) is relevant for atmospheric layers as high as the mesosphere. The figure is taken from Plumb (2002).

In order to get familiar with this concept, Fig. 1.3 visualizes the refractive index squared $n_{c=0,k=2}^2$ for stationary waves ($c = 0$) of wavenumber $k = 2$ together with its most important contributions for different stratospheric basic states. Wave propagation is in principle enabled for $\bar{u} > 0$ as indicated in the first row of Fig. 1.3. Hence, planetary-scale waves can only reach the upper stratosphere in presence of sufficiently upward extending positive zonal-mean zonal winds which are provided by the polar vortex during winter seasons (middle and right columns of Fig. 1.3). During summer seasons, wave propagation above the lower stratosphere is suppressed (left column of Fig. 1.3).³ Towards polar regions, the second term of the refractive index squared, i.e., $k^2 (\cos \phi)^{-2}$, eventually leads to negative values such that very high latitudes are excluded from wave propagation already for low wavenumbers $k \leq 3$ corresponding to planetary-scale waves (compare first and second rows of Fig. 1.3). As a result, Rossby waves are refracted equatorward in the stratosphere until encountering a critical line $\bar{u} = c$ where they dissipate their momentum and energy to the mean flow. Synoptic-scale Rossby waves with $k \geq 4$ are impeded to penetrate the polar vortex in high latitudes. Instead, synoptic-scale waves dissipate in the lower stratosphere poleward of subtropical regions (Randel and Held, 1991).

³The effect different stratospheric mean flows have on wave propagation and dissipation is also summarized in Fig. 8 of Gerber (2012).

The dissipation of Rossby waves implies a zonal acceleration $(a \cos \phi)^{-1} \nabla \cdot \mathbf{F}$ on air parcels of the mean flow \bar{u} as described by the TEM equation (1.11) and propels the residual circulation $(\bar{v}^*, \bar{\omega}^*)$ (Holton et al., 1995). Since planetary- and synoptic-scale Rossby waves obey different wave propagation criteria, their dissipation is associated with different branches of the residual circulation as displayed schematically in Fig. 1.4. Synoptic-scale waves are filtered by high latitudes and deposit their momentum in the subtropical lower stratosphere, driving the shallow branch of the residual circulation. Planetary-scale waves can reach the upper stratosphere to drive the deep branch of the circulation. Gravity waves can propagate up to the mesosphere and obey a different index of refraction which is not discussed in this thesis.

Important for the shape of the waveguide for Rossby waves, i.e., the connected region of positive refractive index squared, is the structure of the zonal-mean zonal wind \bar{u} . Meridional and vertical curvature of \bar{u} enter the meridional potential vorticity gradient $\partial_y \bar{q}$. As indicated in the third and fourth row of Fig. 1.3, regions around maxima of \bar{u} in latitudinal direction and regions below maxima of \bar{u} in vertical direction contribute positively to $\partial_y \bar{q}$, respectively. Regions around minima of \bar{u} in latitudinal direction and decreasing zonal-mean zonal winds with height contribute negatively to $\partial_y \bar{q}$, respectively, constraining the waveguide. The crucial region that determines the amount of planetary-scale wave activity that is able to penetrate the stratosphere resides in the lower stratosphere poleward of the tropospheric jet and below the polar vortex at around 100 hPa in idealized model setups. Small contributions from $\partial_y \bar{q}$ can result in small or even negative values of $n_{c=0, k=2}^2$ as visible in the middle column of Fig. 1.3. Larger values of the refractive index squared in the midlatitude lower stratosphere arising from a stronger curved zonal-mean flow as shown in the right column of Fig. 1.3 enhance upward wave propagation (Chen and Robinson, 1992; Gerber, 2012).

Wave reflection events

Apart from planetary-scale waves being absorbed in the stratosphere and driving the residual circulation, special geometries of the waveguide offer the possibility of wave reflections (Charney and Drazin, 1961) relevant in both hemispheres (Perlwitz and Graf, 2001; Shaw et al., 2010). Strong reflection events can even reverse the residual circulation with upwelling in extratropical regions (Shaw and Perlwitz, 2014). The separation of the general refractive index squared $n_{c,k}^2$ for propagation in the meridional plane into meridional and vertical contributions reveals horizontally aligned regions of wave evanescence for vertical propagation in the upper stratosphere. These reflecting surfaces at the top of the stratosphere form in both hemispheres (Shaw et al., 2010). In case of the general refractive index squared $n_{c,k}^2$, large regions at the top of the polar vortex with values below 10 as shown in the top right panel of Fig. 1.3 are assumed to contain such a region of wave evanescence for vertical propagation (Harnik and Lindzen, 2001). Analyses of the zonal background flow identify a strong vertical curvature of the mean flow as the source of the reflecting surface. Short pulses of upward propagating

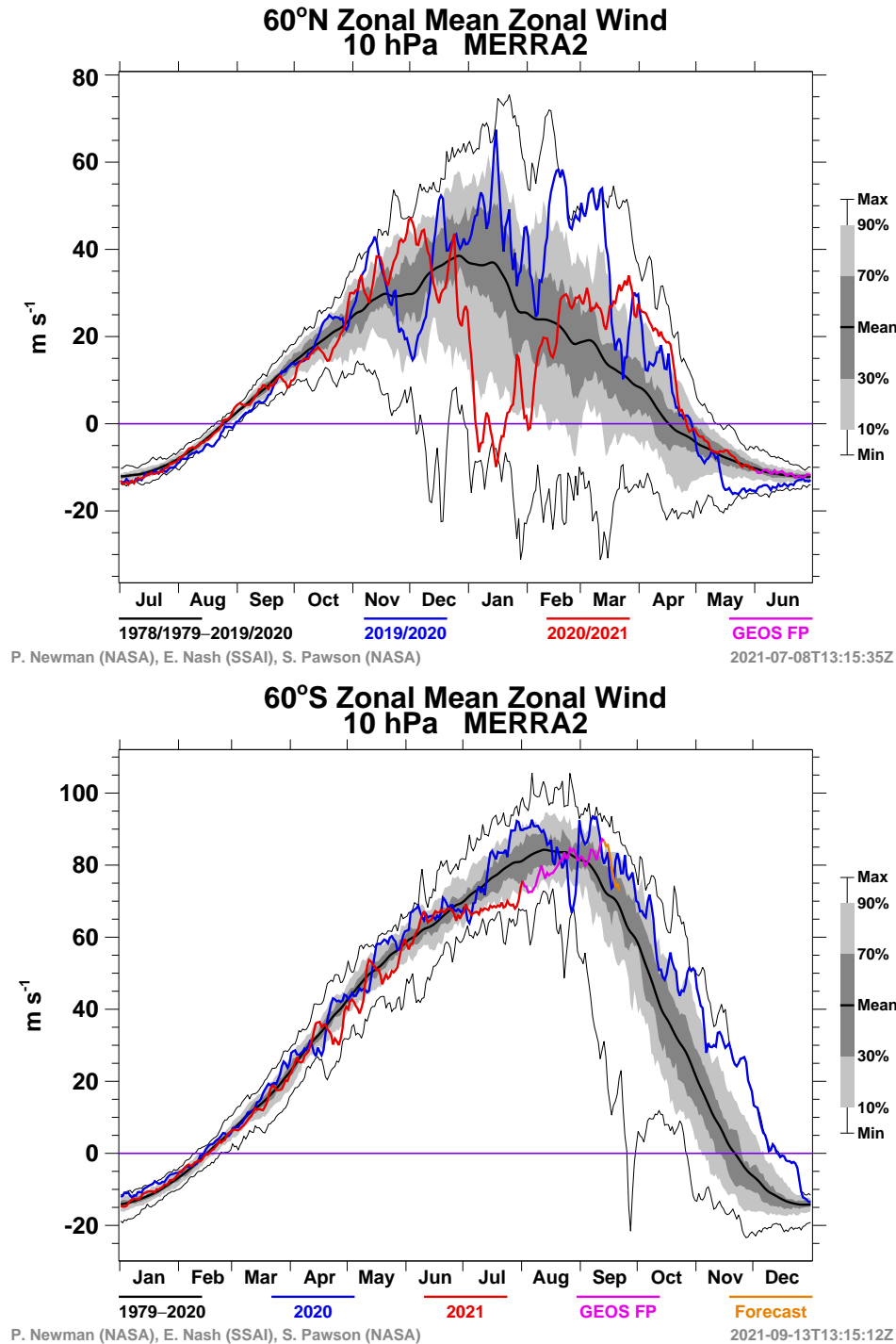


Figure 1.5: Annual statistics of the 10 hPa zonal-mean zonal wind at 60°N (top) and 60°S (bottom) including the mean (thick black line) as well as the 30th–70th percentile range (darker gray shading), the 10th–90th percentile range (lighter gray shading), and minima and maxima (thin black lines) from the Modern-Era Retrospective analysis for Research and Applications, Version 2 (MERRA-2). Blue and red lines indicate individual years, with data from the red lines not included in the statistics. Similar figures for various variables and pressure levels can be generated at https://acd-ext.gsfc.nasa.gov/Data_services/met/ann_data.html (Newman et al., 2021).

planetary-scale waves themselves can induce the required curvature. Longer pulses of wave activity, instead, tend to decelerate the polar vortex as a whole, causing sudden stratospheric warmings (Harnik, 2009).

Downward propagating reflected waves still have the possibility to dissipate within the stratosphere when critical lines in subtropical regions are encountered. Therefore, reflected waves can only reach the troposphere when the meridional waveguide is narrow enough to prevent the waves from meridional dispersion (Perlwitz and Harnik, 2003). When the meridional curvature of the zonal-mean flow is not strong enough, meridional dispersion of the wave is likely to occur and hence, no significant influence of the reflected wave on the troposphere is observed (Shaw et al., 2010). A bounded geometry of the waveguide with a reflecting surface in the upper stratosphere and a narrow meridional waveguide is developed between January and March in the northern hemisphere, and between September and December in the southern hemisphere (SH), respectively (Shaw et al., 2010). The general refractive index squared $n_{c,k}^2$ can also reveal the presence of a meridionally confined waveguide. In case of weak meridional curvature of the polar vortex as present in the climate state of the middle column of Fig. 1.3, high values of $n_{c,k}^2$ occur on the equatorward side of the polar vortex. In contrast to this, a polar vortex with strong meridional curvature as present in the climate state of the right column of Fig. 1.3 exhibits a vertically aligned region of minimum $n_{c,k}^2$ on its equatorward side. As a result, so-called downward wave coupling events where reflected planetary-scale waves exert a significant influence on the troposphere can only occur in the latter climate state due to the bounded geometry of the waveguide. The tropospheric influence during downward wave coupling events is characterized by a poleward shift of the tropospheric jet associated with a positive phase of annular modes (Shaw and Perlwitz, 2013; Shaw et al., 2014; Dunn-Sigouin and Shaw, 2015). This is consistent with the well-known correlation of the strength of the polar vortex and annular modes (Baldwin and Dunkerton, 2001; Limpasuvan et al., 2004, 2005).

In summary, the waveguide for planetary-scale waves offers two regimes for the dynamical coupling of the stratosphere and troposphere. Upward propagating planetary-scale waves from the troposphere can either be entirely absorbed by the mean flow in the stratosphere, decelerating the polar vortex and causing zonal-mean anomalies to propagate downward to the troposphere, or be reflected without zonal-mean anomalies propagating downward (Perlwitz and Harnik, 2004; Dunn-Sigouin and Shaw, 2015). Considering the annular statistics of the polar vortex strength in both hemispheres as shown in Fig. 1.5 reveals that northern and southern hemisphere polar vortices are fundamentally different. The northern hemispheric polar vortex is in general weaker than its southern hemispheric counterpart and exhibits far larger variability. Sudden stratospheric warmings occur, on average, six times per decade in the northern hemisphere (Charlton and Polvani, 2007; Butler et al., 2017), whereas only two sudden warmings have ever been observed in the southern hemisphere (Krüger et al.,

2005; Rao et al., 2020). Consistently, downward wave coupling events are the dominating feature of stratosphere-troposphere coupling in the southern hemisphere (Shaw et al., 2010), whereas planetary-scale wave reflection and absorption alternates in different winter seasons in the northern hemisphere (Perlwitz and Harnik, 2004). Changes in ozone concentrations, as observed in the southern hemisphere, can have an impact on the period and intensity of downward wave coupling events (Shaw et al., 2011; Harnik et al., 2011), but can be neglected compared to the changes induced by increased carbon dioxide concentrations towards the end of the twenty-first century (Jucker et al., 2021). In the following section, expected and uncertain atmospheric circulation changes in response to increased CO₂ concentrations are discussed.

1.1.2 Circulation response to global warming

Increased carbon dioxide concentrations in the atmosphere warm the troposphere and cool the stratosphere (Vallis et al., 2015) as shown in the top left panel of Fig. 1.6. In the troposphere, convection-dominated regions as the tropics exhibit higher warming rates in the upper troposphere since larger water vapor content leads to greater latent heat release of upwelling air masses when water vapor condensates (Held, 1993; Vallis et al., 2015). The associated increased meridional temperature gradient due to tropical upper-tropospheric warming (TUTW, Shepherd and McLandress, 2011; Vallis et al., 2015; Shaw, 2019) and stratospheric cooling leads to accelerated upper flanks of the subtropical jets (bottom left panel of Fig. 1.6) and a tropopause rise (Lorenz and DeWeaver, 2007). Additionally, tropospheric midlatitude eddy-driven jets robustly shift poleward in both hemispheres in response to increased greenhouse-gas concentrations towards the end of the twenty-first century (Wilcox et al., 2012; Barnes and Polvani, 2013), for which various dynamical mechanisms have been proposed so far (Lu et al., 2010; Shaw, 2019). Apart from the tropical upper troposphere (TUT), increased warming in the troposphere is observed in the Arctic arising from ice-albedo feedbacks of shrinking sea-ice, which is not particularly pronounced in the Antarctic (Held, 1993; Holland and Bitz, 2003). Hence, as long as sea-ice is present, but shrinking, opposing temperature differences in the lower troposphere complicate the eddy-driven jet response to global warming (Oudar et al., 2017; Zappa et al., 2018; Peings et al., 2019). In the southern hemisphere, however, polar lower-stratospheric warming due to current ozone recovery can act to attenuate greenhouse-gas induced temperature gradients in the upper troposphere–lower stratosphere (UTLS) region (Wilcox et al., 2012). As already mentioned, ozone effects might be small compared to carbon dioxide effects towards the end of the twenty-first century (Jucker et al., 2021).

The pronounced TUTW causing the upper flanks of subtropical jets to strengthen has consequences for the lower-stratospheric residual-mean meridional circulation as shown in the right panel of Fig. 1.6. Critical layers up to which Rossby-wave propagation is enabled, as described

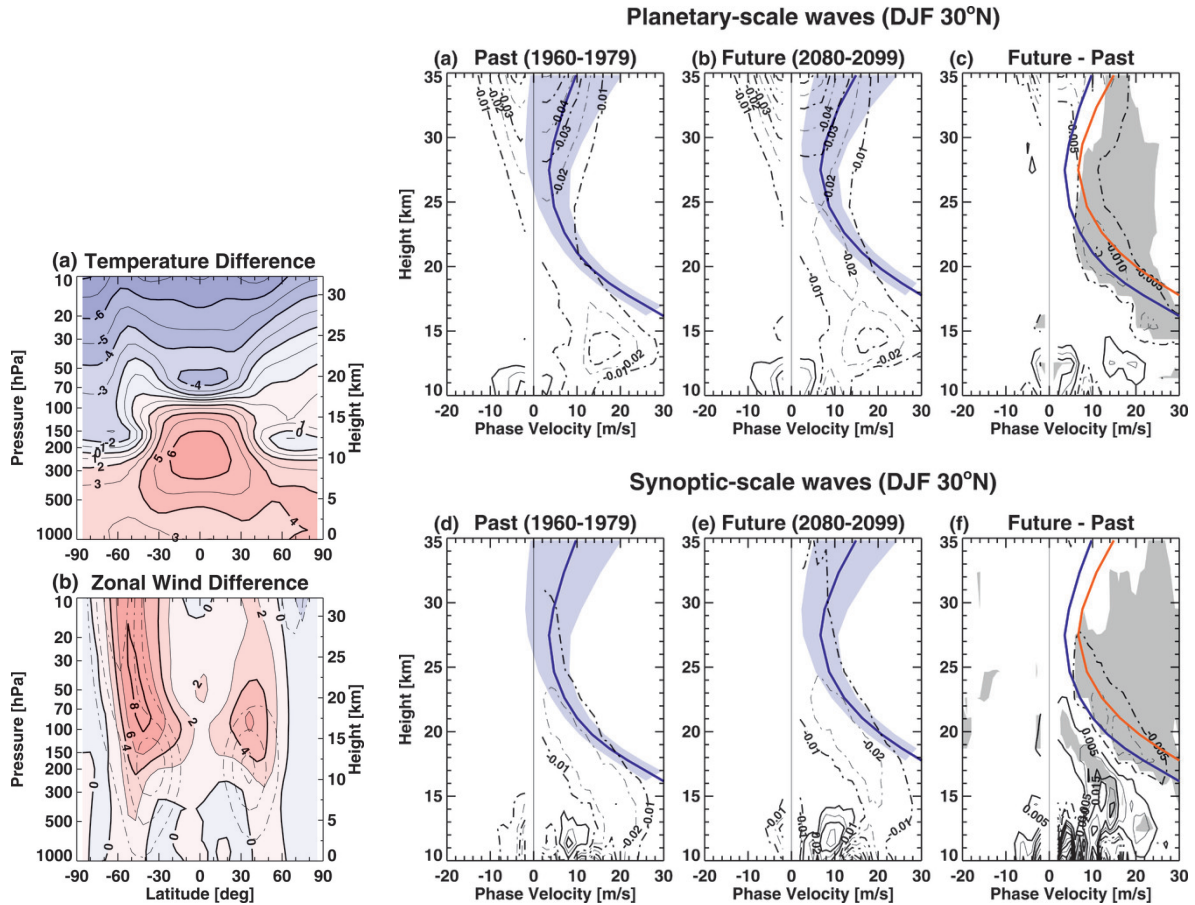


Figure 1.6: Annual-mean changes of zonal-mean temperature (top left, color shading, in K) and zonal wind (bottom left, color shading, in m s^{-1}) from past (1960–1979) to future (2080–2099) climates as functions of latitude and pressure simulated with a complex-model ensemble following a medium greenhouse-gas emission scenario (Nakicenovic et al., 2000; Eyring et al., 2007), as well as corresponding December-January-February (DJF) seasonal-mean planetary- (top right) and synoptic-scale (bottom right) Eliassen–Palm flux divergence (EPFD) spectra for past and future climates (black contours with a contour interval of $0.01 \text{ m s}^{-1} \text{ day}^{-1}$) and their differences (black contours with a contour interval of $0.005 \text{ m s}^{-1} \text{ day}^{-1}$) together with the zonal-mean zonal winds (solid blue and orange lines) as functions of height at 30°N . The figures correspond to Figs. 1 and 5 of Shepherd and McLandress (2011) where a more detailed description of each panel can be found.

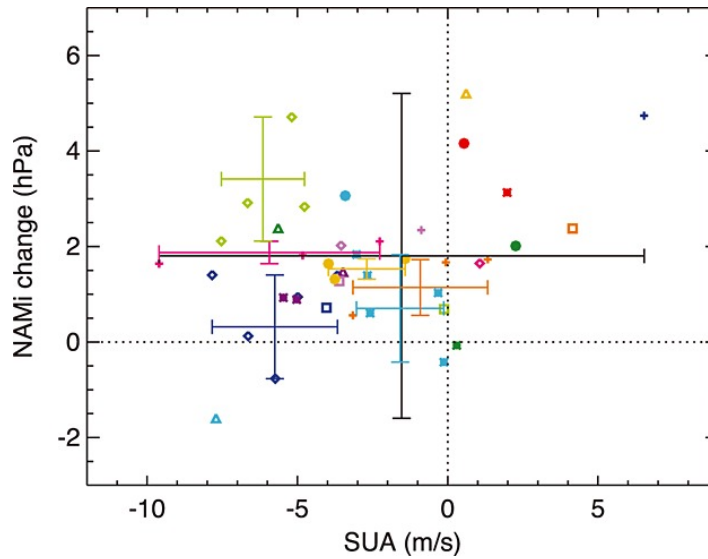


Figure 1.7: December-January-February (DJF) seasonal-mean change in the northern annular mode (NAM) as a function of the change in northern-hemispheric stratospheric polar vortex strength (SUA) from past (1961–2000) to future (2061–2100) climates simulated with the Coupled Model Intercomparison Project Phase 5 (CMIP5) multi-model ensemble following a high greenhouse-gas emission scenario (Taylor et al., 2012). The figure is taken from Manzini et al. (2014) where a more detailed description can be found.

in the preceding section, rise in the lower stratosphere of subtropical latitudes. Therefore, more wave activity of both planetary- and synoptic-scale waves penetrates into and dissipates within the lower stratosphere which induces a strengthened residual circulation (Shepherd and McLandress, 2011). This robust feature of climate change has been confirmed in model experiments of various complexity (Wang et al., 2012; Manzini et al., 2014; Hardiman et al., 2014; Sigmond and Shepherd, 2014; Abalos et al., 2021) and is consistent with decreasing time periods air parcels need to travel across the tropopause into the lower stratosphere (Ray et al., 2014). Since the troposphere expands vertically in response to increased carbon dioxide concentrations, the strengthened lower-stratospheric circulation can also be interpreted as a rising tropopause (Oberländer-Hayn et al., 2016).

The response of the stratospheric polar vortex to increased greenhouse-gas concentrations is by far less clear. About 70% of the models forced with the Representative Concentration Pathway 8.5 scenario contributing to the Coupled Model Intercomparison Project Phase 5 (CMIP5) protocol (Taylor et al., 2012) predict a weakening of the northern-hemispheric stratospheric polar vortex by the end of the twenty-first century, but there is substantial uncertainty even in the sign of this change as shown in Fig. 1.7 (Manzini et al., 2014; Kretschmer et al., 2020). This spread is still present in the more recent Coupled Model Intercomparison Project Phase 6 (CMIP6) multi-model ensemble (Eyring et al., 2016) when carbon dioxide (CO_2) concentrations are abruptly quadrupled (Ayarzagüena et al., 2020). Additional complexity to the transient atmospheric circulation response is added by the nonlinear behavior of the

stratospheric circulation for two consecutive periods of identical global warming. In a large ensemble of a fully-coupled general circulation model (GCM) forced by a 1% increase of the CO₂ concentration per year, a weakening of the northern-hemispheric stratospheric polar vortex during the first period of 2K global warming, but a strengthening during the second period is found (Manzini et al., 2018). A possible reason for the nonlinear polar vortex response is the abrupt decrease of Arctic amplification over marginal Arctic seas when they become ice-free. Shrinking sea ice, in particular associated with Barents–Kara seas, enhances upward propagating wave activity which weakens the stratospheric polar vortex (Kim et al., 2014; Kim and Kim, 2020; Kretschmer et al., 2020). As soon as Barents–Kara seas are ice-free, this additional source of tropospheric wave forcing is missing (Manzini et al., 2018; Kretschmer et al., 2020). The overall causal effect of sea-ice changes on nonlinear polar vortex responses in future climates is, however, small due to the large variability of the northern-hemispheric polar vortex and the unknown intraseasonal time scale at which sea ice changes couple upward to the stratosphere. Furthermore, it is unclear how important other climate effects that originate in the Arctic are for the polar vortex, and why the polar vortex strengthens after Barents–Kara seas are ice free (Kretschmer et al., 2020).

Apart from sea-ice changes, enhanced tropospheric wave activity associated with a polar vortex weakening has been related to the strengthening of subtropical jets (Karpechko and Manzini, 2017). Regarding the uncertainty of the polar vortex response to climate change as present in CMIP5 and CMIP6 multi-model ensembles, differences in the basic state of the preindustrial or present-day climate from which experiments are started in various models have been invoked to lead to different waveguides when subtropical jets are strengthened (Sigmond and Scinocca, 2010). Neither one of the former mechanisms was, however, confirmed. Instead, stationary wave activity is found to be responsible for contrasting circulation changes only to a limited extent (Wu et al., 2019). Due to the significant downward stratospheric influence on the tropospheric circulation during extended winter seasons, e.g., by the downward migration of extreme zonal-mean anomalies (Baldwin and Dunkerton, 2001), or by the reflection of upward propagating planetary-scale Rossby waves (Perlwitz and Graf, 2001), reliable projections of stratospheric climate change are vital. Otherwise, the full spectrum of possible stratospheric climate projections blurs the tropospheric evolution (Simpson et al., 2018), e.g., with potentially extreme precipitation changes in the Mediterranean region (Zappa and Shepherd, 2017).

In the southern hemisphere, polar vortex changes to increased greenhouse-gas concentrations are more robust (Wilcox and Charlton-Perez, 2013; Jucker et al., 2021). In a recent study, the southern-hemispheric polar vortex was shown to strengthen in response to quadrupled CO₂ concentrations in a coupled chemistry-climate model with ocean (Jucker et al., 2021). SSWs in this climate scenario are projected to occur only every 309 years compared to the estimated present-day return time of 22 years. The strengthening of the polar vortex is suggested to

be linked to stratospheric cooling which occurs when CO₂ concentrations rise (Jucker et al., 2021). Stronger meridional temperature gradients are, however, only induced in the UTLS region consistent with strengthened upper flanks of subtropical jets or the lowest part of the polar vortex. Further up in the stratosphere, latitudinal dependent cooling rates are absent (Thompson et al., 2012; Santer et al., 2013), challenging CO₂-induced stratospheric cooling as the cause for polar vortex strengthening.

1.1.3 Idealized climate models

In order to reconcile the different climate-change responses of the stratospheric polar vortex and the tropospheric jets, climate models of different complexity can help to expose the relevant processes (Held, 2005; Garny et al., 2020). The simplest approach of three-dimensional flow on a rotating planet which is governed by the dry primitive equations (1.1)–(1.5) is to replace all thermodynamic forcings with a simple Newtonian damping to a prescribed equilibrium temperature. In addition, Rayleigh friction is imposed at the top and bottom boundaries of the atmosphere to account for wind decelerations induced by breaking gravity waves and surface friction, respectively (Held and Suarez, 1994; Polvani and Kushner, 2002). The equilibrium temperature employed in these so-called dry dynamical-core models represents an equilibrium that includes all temperature effects of radiation and convection, i.e., the absorption and emission of long- and short-wave radiation, chemical reactions, and latent heat release. Originally, the method of driving an atmospheric general circulation model via a prescribed equilibrium temperature was intended to assess different dynamical cores (Held and Suarez, 1994; Wan et al., 2008), but idealized models have proven to be very useful for investigating dry atmospheric dynamics. Some examples are the positive correlation of the polar vortex strength and the latitudinal position of the tropospheric jets (Polvani and Kushner, 2002; Gerber and Polvani, 2009), a strengthened upper-stratospheric RC associated with an improved waveguide of stationary planetary-scale waves (Gerber, 2012), the importance of the extratropical lower stratosphere for the generation of SSWs (Lindgren et al., 2018; Martineau et al., 2018), as well as the circulation response to climate change-like TUTW without (Butler et al., 2010) and with stratospheric wind structures (Wang et al., 2012). The latter study revealed a regime transition of the polar vortex from a weak and variable to a strong and stable regime at a critical temperature increase of the TUT. Up to the critical warming amplitude, the RC accelerates and the polar vortex strength stays roughly constant. Beyond the critical warming amplitude, the RC decelerates and the polar vortex strengthens sharply in combination with an enormous poleward shift of the eddy-driven jet. Consistent with the TEM framework, the regime transition is accompanied by a reduction of upward propagating wave flux into the stratosphere and by increased equatorward propagation within the troposphere (Wang et al., 2012; Kushner and Polvani, 2004).

The fact that the polar vortex can occupy different regimes can be illustrated by even simpler, one-dimensional models of wave–mean flow interaction (Holton and Mass, 1976). A critical amplitude of the lower boundary forcing, representing the upward propagating wave activity from the troposphere, separates the SSW-state from the state close to radiative equilibrium.⁴ A closer analysis of the bifurcation diagram of this model reveals two stable solutions for specific tropospheric forcings consistent with observed polar vortex variability (Yoden, 1987). Remarkably, the periodic solution of the Holton–Mass model exists for constant lower boundary forcing. In an analogous study with a stratosphere-only GCM with a time-independent amplitude of stationary planetary-scale waves at the lower boundary, Scott and Polvani (2006) observe alternating phases of SSWs and polar vortex recoveries consistent with pulses of upward wave activity flux. The special role of the lower stratosphere has been confirmed by Martineau et al. (2018) who found that a colder lower stratosphere favors a broader spectrum of upward propagating wave activity, whereas wave propagation is much less sensitive to the thermal structure of the upper stratosphere. Chen and Robinson (1992) identify static stability and zonal-mean zonal winds in the UTLS region as the deciding factors for the transmission of wave activity. Accordingly, only about one third of observed and modeled SSWs are preceded by extreme planetary-scale wave events originating in the troposphere, whereas the majority of SSWs are products of internal stratospheric variability (Birner and Albers, 2017; White et al., 2019).

1.2 Research questions and outline

During extended winter seasons, the extratropical stratosphere characterized by the polar vortex is capable of significantly impacting surface conditions (Kidston et al., 2015). Therefore, large uncertainties in stratospheric circulation changes in future climate scenarios (Manzini et al., 2014; Ayarzagüena et al., 2020) add uncertainties to tropospheric circulation trends (Simpson et al., 2018). This issue gives rise to general research questions regarding the dynamical coupling of the stratosphere and troposphere that are targeted throughout this thesis:

- **G1:** How strongly do changes in the middle atmospheric circulation alter the circulation at the surface through dynamical downward coupling?
- **G2:** Is there a feedback of tropospheric warming via a strengthened stratospheric circulation on the troposphere?

In other words, how do different realizations of the stratospheric circulation impact the troposphere (**G1**) and can the troposphere itself cause stratospheric changes that in turn couple back downward during climate change (**G2**)?

⁴In the mostly stably stratified and very dry stratosphere, convective processes can be neglected (Vallis, 2017).

In this regard, aiming for a complete understanding of all relevant causal chains could help to reconcile the different responses of complex climate models to increased greenhouse-gas concentrations—a desirable, but ambitious endeavor. State-of-the-art climate models are too complex to robustly identify causal chains. Changes in temperatures that lead to changes in the general circulation can not uniquely be distinguished to arise from radiative processes, chemical reactions or dynamical effects, i.e., changes in upwelling or downwelling. Hence, instead of taking various coupling processes of modern Earth-system models into account, this thesis aims at a better mechanistic understanding of dry three-dimensional atmospheric flow and its evolution during global warming, neglecting effects of radiation, clouds, latent heat release, and chemistry. The framework of idealized general circulation models enables to detect causal chains of purely dynamical effects. Revealed mechanisms can then be used to interpret circulation changes in more complex models (Held, 2005).

In order to contribute to the general research questions **G1** and **G2**, more specific research questions with respect to the dynamical coupling of the stratosphere and troposphere are formulated in the following to structure this thesis. The winter-hemispheric extratropical lower stratosphere has been shown to be crucial in controlling the amount of wave flux that is able to enter the stratosphere from below (Chen and Robinson, 1992; Scott and Polvani, 2006; Birner and Albers, 2017; Martineau et al., 2018; White et al., 2019), which raises the question:

- **S1:** How does the extratropical lower stratosphere control the dynamical coupling of the stratosphere and troposphere?

In a changing climate, stratosphere-troposphere coupling can be subject to abrupt changes when temperature signatures associated with increased greenhouse-gas concentrations exceed a critical threshold as found by Wang et al. (2012). Attempting to reveal the dynamical mechanism that is responsible for this regime transition, the second specific research question is:

- **S2:** How does tropical upper-tropospheric warming (TUTW) trigger a nonlinear response of the coupled stratosphere-troposphere circulation?

The first two questions are addressed with different idealized-model experiments. In order to search for possible implications for complex models representing a more realistic atmosphere, the final question is:

- **S3:** Do indications of the dynamical mechanism revealed in idealized models exist in complex models?

The corresponding investigations of the third question could help to comprehend future polar vortex changes (Manzini et al., 2014; Jucker et al., 2021).

A major part of this thesis relies on idealized-model experiments. Therefore, Chap. 2 introduces the employed dry dynamical-core model and the performed simulations. Furthermore, frequently used diagnostics of the atmospheric circulation are derived. Chap. 3 is designed to address the specific research question **S1**. Different states of the stratospheric polar vortex are modeled, and corresponding circulations and tropospheric impacts are investigated. Chap. 4 answers the question **S2** by investigating the circulation responses to incremental tropospheric temperature rises. Different stratospheric basic states with and without polar vortex allow to quantify the tropospheric impact exerted by the nonlinear stratospheric circulation change. The purpose of Chap. 5 is twofold. First, building on the results of Chaps. 3 and 4, a universal criterion for the behavior of stratosphere-troposphere coupling is established that applies to both stratospheric cooling and tropical upper-tropospheric warming experiments. Second, the CMIP6 multi-model ensemble is consulted to investigate whether aspects of the findings from idealized models can be used to explain the stratospheric polar vortex response to increased carbon dioxide concentrations to answer question **S3**. Finally, Chap. 6 summarizes the conclusions of this thesis with respect to specific and general research questions proposed above and provides an outlook for future studies.

Chapter 2

Methodology

This thesis employs the ECHAM/MESSy IdeaLized model (EMIL, Garny et al., 2020) to study the dry atmospheric circulation response to polar stratospheric cooling in the winter hemisphere as well as to tropical upper-tropospheric warming. Sec. 2.1 introduces EMIL with all relevant parameters. Sec. 2.2 describes the performed simulations with key parameters that are varied. Frequently used diagnostics to determine the location of atmospheric jet streams, the distribution of wave activity, the strength of the residual circulation, as well as the vicinity to regime transitions are derived in Sec. 2.3.

2.1 The idealized general circulation model EMIL

Within the Modular Earth Submodel System (MESSy) framework, models of different physical or chemical processes can be combined with a base model (Jöckel et al., 2005, 2006, 2010, 2016). Base models include simple box models denoting “the smallest meaningful entity for a certain process” to analyze, e.g., chemical reactions in an isolated environment, as well as comprehensive general circulation models (GCMs) for the atmosphere (Jöckel et al., 2005). In terms of EMIL, which is an idealized-model setup within MESSy, the atmospheric dynamical core of the European Centre HAMburg general circulation model 5 (ECHAM5) is the base model (Roeckner et al., 2003, 2006)⁵, and the only processes which are connected to this base model are the relaxations of temperature and winds to prescribed values to drive a circulation (Garny et al., 2020). ECHAM5 is a spectral model, i.e., the primitive equations are solved by transforming the prognostic variables (vorticity, divergence, temperature, water mixing ratio, and the natural logarithm of surface pressure) to series of spherical harmonics

⁵In principle, dynamical cores of other GCMs, as the Community Earth System Model (Baumgaertner et al., 2016) could be used instead of ECHAM5.

in the horizontal.⁶ The wavenumber at which this series is truncated determines the effective resolution of the atmospheric circulation. For example, triangular truncation at wavenumber 42, denoted by T42, corresponds to 128 longitudes and 64 latitudes. In the vertical direction, ECHAM5 employs a hybrid sigma-pressure coordinate with model levels following the terrain in the lower atmosphere with a smooth transition to levels defined by the quotient of pressure and surface pressure in the upper atmosphere. An exemplary number of 90 vertical model levels is denoted by L90. Time integration is achieved via a semi-implicit scheme with a time filter to suppress spurious modes (Roeckner et al., 2003, 2006). Phenomena that are explicitly neglected in EMIL are radiation, convection, clouds, chemical reactions, gravity waves, as well as mass, momentum, and heat exchanges with soil, snow, ice, and liquid water at the surface. The atmosphere is completely dry, no ocean is present, and apart from an idealized orography employed in some experiments, the surface is completely flat (Garny et al., 2020; Roeckner et al., 2003). The atmospheric circulation in EMIL is driven by relaxing the temperature to a prescribed equilibrium temperature that mimics radiative and convective effects. Convection dominated regions as the tropics are thus obviously unrealistically represented in EMIL such that the Hadley cell (HC) is weaker than observed (Wang et al., 2012). In the following, relevant functions of EMIL are explained.

2.1.1 Rayleigh friction and Newtonian damping

EMIL is set up following previous idealized GCMs (Held and Suarez, 1994; Polvani and Kushner, 2002) employing Newtonian damping and Rayleigh friction. Rayleigh friction is used to attenuate horizontal winds $\mathbf{u} = (u, v)$ via

$$\frac{\delta \mathbf{u}}{\delta t} = -k \mathbf{u} \quad (2.1)$$

where the damping coefficient

$$k(p) = \begin{cases} k_{\text{drag}} c^{10-i_{\text{lev}}(p)} & \text{for } p \leq p_{\text{sp}} \\ 0 & \text{for } p_{\text{sp}} < p \leq p_{\text{b}} \\ k^{\text{HS}} \max\left(0, \frac{p-p_{\text{b}}}{p_{\text{surf}}-p_{\text{b}}}\right) & \text{for } p > p_{\text{b}} \end{cases} \quad (2.2)$$

mimics friction in the boundary layer for $p > p_{\text{b}} = 0.7 p_{\text{surf}}$ with surface pressure p_{surf} and $k^{\text{HS}} = 1.1574 \times 10^{-5} \text{ s}^{-1}$ (Held and Suarez, 1994) as well as gravity wave drag in the sponge layer at the model top for $p \leq p_{\text{sp}} = 0.5 \text{ hPa}$ with $k_{\text{drag}} = 5.02 \times 10^{-7} \text{ s}^{-1}$, $c = 1.5238$, and $i_{\text{lev}}(p)$ being the pressure level number starting at the model top for resolution L90. The sponge-layer damping for other vertical resolutions is computed by inter-

⁶In contrast to spectral models, finite-volume dynamical cores solve the primitive equations in real space as, for example, the ICOSahedral Nonhydrostatic (ICON) model (Zängl et al., 2015). An overview of the development of spectral and finite-volume dynamical cores is given by Williamson (2007).

polation from the L90-damping. As an alternative, the sponge-layer damping of the form $2.3148 \times 10^{-5} \text{ s}^{-1} (1 - p/p_{\text{sp}})^2$ can be chosen in EMIL (Polvani and Kushner, 2002), but the exponential form of Eq. (2.2) is used throughout the entire thesis as it represents the wind damping by dissipating gravity waves more closely (Garny et al., 2020). The top left panel of Fig. 2.1 shows the damping coefficient in the boundary layer as well as in the sponge layer for the two implemented alternatives.

Newtonian damping is used to relax simulated temperatures T towards a selected equilibrium temperature profile T_{equ} via

$$\frac{\delta T}{\delta t} = -\frac{T - T_{\text{equ}}}{\tau_r} + Q, \quad (2.3)$$

where τ_r is the relaxation time scale and Q incorporates additional temperature tendencies that are described in Sec. 2.1.2. The relaxation time scale is identical to Held and Suarez (1994) and reads

$$\tau_r(\phi, p) = \left[\frac{1}{\tau_a} + \left(\frac{1}{\tau_s} - \frac{1}{\tau_a} \right) \max \left(0, \frac{p - p_b}{p_{\text{surf}} - p_b} \right) \cos^4(\phi) \right]^{-1} \quad (2.4)$$

with $\tau_a = 40$ days and $\tau_s = 4$ days. As displayed in the bottom right panel of Fig. 2.1, the relaxation time scale is 40 days in the upper atmosphere and decreases to 4 days in the tropical lower troposphere to avoid an unrealistic inversion layer close to the tropical surface (Held and Suarez, 1994).

The equilibrium temperature implemented in EMIL is very similar to the one introduced by Polvani and Kushner (2002) and consists of zonally-symmetric temperature schemes in the troposphere and stratosphere separated by a newly developed, latitudinally dependent transition pressure $p_T(\phi)$ according to

$$T_{\text{equ}}(\phi, p) = \begin{cases} T_{\text{equ}}^{\text{trop}}(\phi, p) & \text{for } p \geq p_T(\phi) \\ T_{\text{equ}}^{\text{strat}}(\phi, p) & \text{for } p < p_T(\phi) \end{cases} \quad (2.5)$$

as shown generically in the top right panel of Fig. 2.1. In contrast to Polvani and Kushner (2002), the transition pressure p_T is not equal to 100 hPa everywhere, but varies smoothly between summer and winter hemisphere corresponding to

$$p_T(\phi) = (p_{T_w} - p_{T_s}) W(\phi) + p_{T_s} \quad (2.6)$$

with separate transition pressures p_{T_s} and p_{T_w} in the summer and winter hemispheres, respectively. In this way, it is possible to change the transition pressure only in the winter hemisphere to achieve more realistic, colder temperatures in the polar lower stratosphere (Garny et al.,

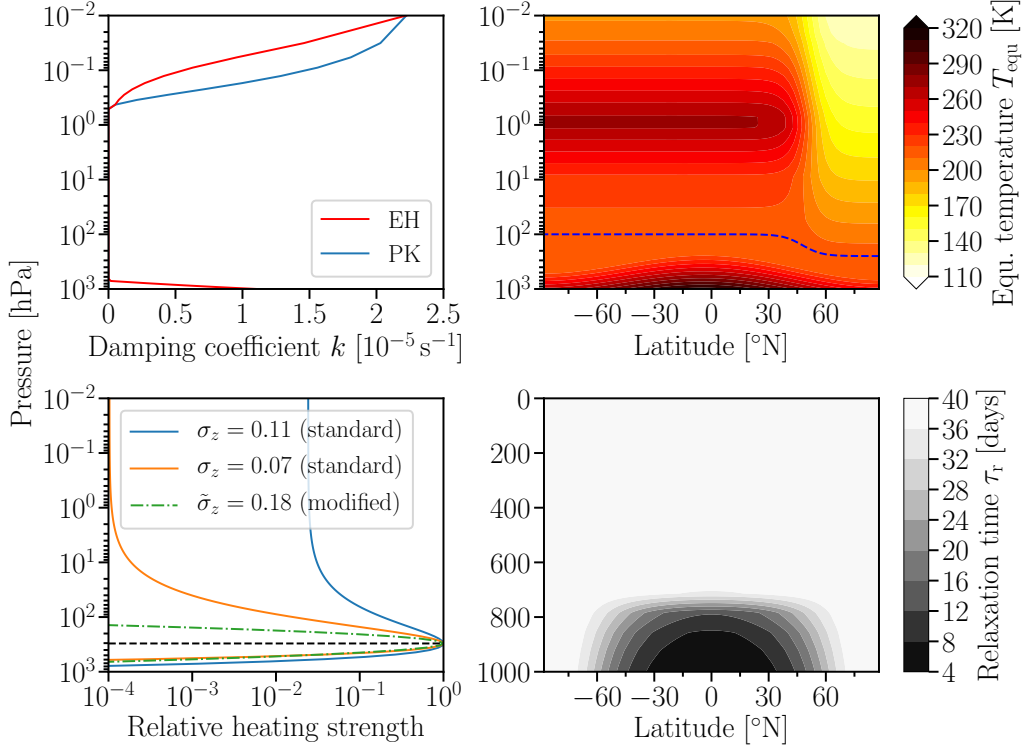


Figure 2.1: Visualization of important, zonally-symmetric parameters of EMIL, i.e., the damping coefficient k given in Eq. (2.2) (EH) together with the option for the sponge layer introduced by Polvani and Kushner (2002, PK) (top left), the equilibrium temperature T_{equ} given in Eq. (2.5) with latitudinally dependent transition pressure $p_{\text{T}}(\phi)$ (dashed blue line) defined in Eq. (2.6) for $p_{\text{Ts}} = 100$ hPa, $p_{\text{Tw}} = 250$ hPa, and $\gamma = 2$ K km $^{-1}$ (top right), the vertical profiles of the additional thermal forcings of standard and modified form given in Eqs. (2.10) and (2.11), respectively, that can be chosen to mimic tropical upper-tropospheric warming (TUTW, bottom left) as well as the relaxation time scale τ_{r} given in Eq. (2.4) (bottom right).

2020). In a different approach, Sheshadri et al. (2015) increased the transition pressure to $p_{\text{T}} \equiv 200$ hPa everywhere.

The weighting function $W(\phi)$ ensures a smooth transition of $p_{\text{T}}(\phi)$ between the hemispheres and reads

$$W(\phi) = \frac{1}{2} \left[1 + h_{\text{fac}} \tanh \left(\frac{\phi - \phi_0}{\delta\phi} \right) \right] \quad (2.7)$$

with $\phi_0 = h_{\text{fac}} \times 50^\circ\text{N}$ and $\delta\phi = 10^\circ$ where $h_{\text{fac}} = +1(-1)$ determines the northern (southern) hemisphere as the winter hemisphere. $W(\phi)$ has been consulted from the stratospheric equilibrium temperature (Polvani and Kushner, 2002)

$$T_{\text{equ}}^{\text{strat}}(\phi, p) = [1 - W(\phi)]T_{\text{US}}(p) + W(\phi)T_{\text{US}}(p_{\text{Ts}}) \left(\frac{p}{p_{\text{T}}(\phi)} \right)^{\frac{R\gamma}{g}} \quad (2.8)$$

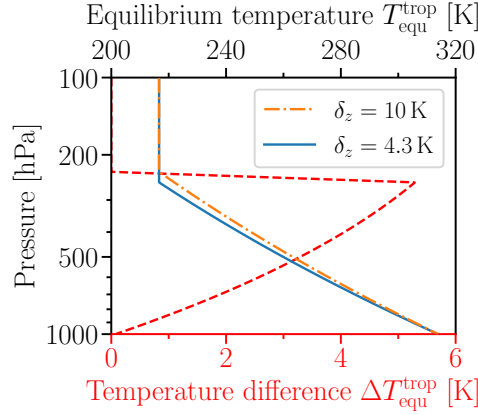


Figure 2.2: Tropospheric equilibrium temperature $T_{\text{equ}}^{\text{trop}}$ at the equator ($\phi = 0$) for $\delta_z = 10$ K (dash-dotted orange line), $\delta_z = 4.3$ K (solid blue line), and their difference $\Delta T_{\text{equ}}^{\text{trop}} = T_{\text{equ}, \delta_z = 10 \text{ K}}^{\text{trop}} - T_{\text{equ}, \delta_z = 4.3 \text{ K}}^{\text{trop}}$ (dashed red line).

where it connects the temperature increase with height in the summer hemisphere corresponding to the U.S. Standard Atmosphere T_{US} (U.S. Government Printing Office, 1976) with the temperature decrease with height corresponding to the polar vortex with lapse rate γ in the winter hemisphere. In the troposphere,

$$T_{\text{equ}}^{\text{trop}}(\phi, p) = \max \left\{ T_{\text{US}}(p_{\text{Ts}}), \left[T_0 - \delta_y \sin^2(\phi) - \epsilon \sin(\phi) - \delta_z \ln \left(\frac{p}{p_0} \right) \cos^2(\phi) \right] \left(\frac{p}{p_0} \right)^{\frac{R}{c_p}} \right\} \quad (2.9)$$

introduces equatorial surface temperatures of $T_0 = 315$ K that are reduced by $\delta_y = 60$ K at the poles. Tropospheric asymmetry between summer and winter hemispheres is established by $\epsilon = h_{\text{fac}} \times 10$ K. In addition to the original value of $\delta_z = 10$ K encoding the tropospheric stratification (Held and Suarez, 1994), some simulations are performed with $\delta_z = 4.3$ K.⁷ Differences between equilibrium temperatures due to different values of δ_z are most pronounced in the tropical upper troposphere (TUT), as shown in Fig. 2.2 (see also Fig. 2b of Garny et al., 2020). Throughout this thesis, time-independent profiles of the equilibrium temperature are used to ensure perpetual mid-winter conditions. Nevertheless, the introduction of a seasonal cycle is possible (Kushner and Polvani, 2006; Jucker et al., 2013; McGraw and Barnes, 2016).

⁷Instead of the natural logarithm, a logarithm with base 10 was implemented in the tropospheric equilibrium temperature of EMIL, scaling the magnitude of the original value of $\delta_z = 10$ K by a factor of $1/\ln(10) \approx 0.43$ (Garny et al., 2020).

2.1.2 Tropical upper-tropospheric warming

The relaxation (2.3) towards a prescribed equilibrium temperature can be extended by additional thermal forcings Q . In EMIL, two functions mimicking tropical upper-tropospheric warming are implemented. On the one hand, the standard thermal forcing introduced by Butler et al. (2010) and also used by Wang et al. (2012) can be chosen which is given by

$$Q(\phi, p) = q_0 \exp \left\{ -\frac{1}{2} \left[\frac{\phi}{0.4} \frac{\pi}{180^\circ} \right]^2 - \frac{1}{2} \left[\frac{p/p_{\text{surf}} - z_0}{\sigma_z} \right]^2 \right\}, \quad (2.10)$$

where q_0 is the heating amplitude, $z_0 = 0.3$ is the fraction of the surface pressure at which the thermal forcing is centered, and $\sigma_z = 0.11$ is its vertical standard deviation. Butler et al. (2010) used a fixed heating amplitude of $q_0 = 0.5 \text{ K day}^{-1}$, whereas Wang et al. (2012) varied q_0 from -0.1 to 0.5 K day^{-1} . As shown in the bottom left panel of Fig. 2.1, the standard thermal forcing asymptotically approaches a constant heating rate in the upper atmosphere even for a smaller vertical standard deviation of $\sigma_z = 0.07$.

The modified thermal forcing

$$\tilde{Q}(\phi, p) = q_0 \exp \left\{ -\frac{1}{2} \left[\frac{\phi}{0.4} \frac{\pi}{180^\circ} \right]^2 - \frac{1}{2} \left[\frac{\ln(p/p_{\text{surf}}) - \ln(\tilde{z}_0)}{\tilde{\sigma}_z} \right]^2 \right\}, \quad (2.11)$$

on the other hand, prevents the tropical lower stratosphere from heating by ensuring a more rapid decrease of the heating strength away from its vertical center at $\tilde{z}_0 = 0.3$. The value of $\tilde{\sigma}_z = 0.18$ for the modified thermal forcing was found by approximately matching the heating strengths of the standard thermal forcing of Eq. (2.10), but with $\sigma_z = 0.07$, and the modified thermal forcing of Eq. (2.11) below a common center of $z_0 = \tilde{z}_0 = 0.3$ as shown in the bottom left panel of Fig. 2.1.

2.1.3 Generation of planetary-scale waves

In order to induce a more realistic stratospheric circulation strength, two methods for the additional generation of planetary-scale waves are implemented in EMIL. On the one hand, the idealized wave-like topography that introduces zonal asymmetries in the surface geopotential according to

$$\Phi_0(\lambda, \phi) = \begin{cases} g h_0 \cos(m\lambda) \sin^2 \left(\pi \frac{\phi - \phi_1}{\phi_2 - \phi_1} \right) & \text{for } \phi_1 \leq \phi \leq \phi_2, \\ 0 & \text{otherwise} \end{cases} \quad (2.12)$$

with wavenumber $m = 2$ and an amplitude of $h_0 = 3 \text{ km}$ between $\phi_1 = 25^\circ \text{N}$ and $\phi_2 = 65^\circ \text{N}$ can be employed (WN2T). It was shown in Gerber and Polvani (2009) that this configuration resembles the stratospheric variability in the northern hemisphere very closely when $p_T \equiv$

100 hPa and $\gamma = 4 \text{ K km}^{-1}$ are employed, resulting in SSWs every 200–300 days. In the real atmosphere, SSWs are counted to form on average 0.62 times during extended winter seasons from November to March with 151 days (Charlton and Polvani, 2007) which validates the WN2T setup. Other combinations of m and h_0 generate either too weak, or too strong wave fluxes that prevent the stratospheric polar vortex from reaching realistic wind speeds with intermittent breakdowns (Gerber and Polvani, 2009).

On the other hand, planetary-scale waves can be generated by wave-like heating as suggested by Lindgren et al. (2018). In this case, the time-independent thermal forcing

$$Q_0(\lambda, \phi, p) = \begin{cases} q'_0 \sin(m\lambda) \exp\left[-\frac{1}{2} \left(\frac{\phi - \phi_0}{\sigma_\phi}\right)^2\right] \sin\left(\pi \frac{\log(p/p_{\text{bot}})}{\log(p_{\text{top}}/p_{\text{bot}})}\right) & \text{for } p_{\text{top}} \leq p \leq p_{\text{bot}}, \\ 0 & \text{otherwise} \end{cases} \quad (2.13)$$

with $q'_0 = 6 \text{ K day}^{-1}$, $m = 2$, $\phi_0 = 45^\circ\text{N}$, $\sigma_\phi = 0.175 \times 180^\circ/\pi$, $p_{\text{top}} = 200 \text{ hPa}$, and $p_{\text{bot}} = 800 \text{ hPa}$ is added to the Newtonian damping (2.3) (WN2H). The WN2H setup with $\epsilon = 0$, $p_{\text{T}} \equiv 200 \text{ hPa}$, and $\gamma = 4 \text{ K km}^{-1}$ produces more SSWs than the WN2T setup of Gerber and Polvani (2009) introduced above, and leads to displacement events in about one quarter of all SSWs, whereas almost only split events are observed in the WN2T setup (Lindgren et al., 2018).

Simulation setups that employ neither WN2T (2.12), nor WN2H (2.13) are denoted by WN0 in the stratospheric cooling experiments listed in Tab. 2.1.

2.2 Simulations

The idealized GCM EMIL introduced in the previous section is used to address the specific research questions **S1** and **S2** formulated in Sec. 1.2. In a first set of experiments, temperatures in the winter-hemispheric polar stratosphere are varied via transition pressure p_{T_w} and polar vortex lapse rate γ as described in Sec. 2.2.1. The second set of experiments is dedicated to tropical upper-tropospheric warming implemented by an increase of the tropical heating amplitude q_0 as described in Sec. 2.2.2. The corresponding circulation impacts of polar stratospheric cooling and tropical upper-tropospheric warming are then analyzed in Chaps. 3 and 4, respectively.

2.2.1 Polar stratospheric cooling

The downward impacts of different strengths and onset pressure levels of the polar vortex on the troposphere are studied for the topographical wave forcing (WN2T, Gerber and Polvani, 2009), the thermal wave forcing (WN2H, Lindgren et al., 2018), as well as for no additional

wave forcing (WN0, Polvani and Kushner, 2002). The key parameters that are modified are the transition pressure p_{Tw} in the polar winter hemisphere and the polar vortex lapse rate γ . Higher values of p_{Tw} lower the height at which the polar vortex lapse rate starts in the lower stratosphere, causing stronger meridional temperature gradients in a rather uniform way throughout the entire midlatitude stratosphere. In contrast to this, stronger lapse rates γ lead to meridional temperature gradients that increase with height.

First, the warm bias of the polar UTLS region in previous idealized-model setups (Sheshadri et al., 2015; Garny et al., 2020) is approached by incremental increases of p_{Tw} from 100 to 450 hPa for various γ with WN2T. In order to restrict the amount of data, simulations are integrated for 5 years with 300 days of spin-up being excluded. Since $p_{\text{Tw}} = 400$ hPa turned out to be necessary for simulated temperatures in the polar UTLS region to fall below observations, stratospheric circulation impacts are investigated for this transition pressure with WN2H as well. For comparison, different polar vortex strengths are tested for the original WN0 setup. Second, a limited set of simulations is extended to 30 years with 1000 days of spin-up being excluded to analyze the observed dynamical phenomena in more detail. As a sensitivity for the circulation changes induced by polar stratospheric cooling, the troposphere is prepared with two different stratifications of $\delta_z = 4.3$ K and $\delta_z = 10$ K. Tab. 2.1 contains the polar stratospheric cooling experiments with all relevant parameters. All simulations employ time steps of 540 s.

2.2.2 Tropical warming

Circulation changes in response to tropical upper-tropospheric warming are investigated for three different stratospheric basic states by increasing tropical heating amplitudes q_0 of the standard and modified thermal forcings introduced in Sec. 2.1.2. The stratospheric basic states are defined by p_{Tw} , γ , and whether or not $W(\phi)$ is set to zero in the stratospheric equilibrium temperature given in Eq. (2.8). All TUTW simulations employ a summer-hemispheric transition pressure of $p_{\text{Ts}} = 100$ hPa. The reference experiment (REF) employs $p_{\text{Tw}} = 100$ hPa and $\gamma = 4$ K km⁻¹ exhibiting realistic stratosphere-troposphere coupling (Gerber and Polvani, 2009). A sensitivity experiment with a colder lower stratosphere (CLS) in the polar winter hemisphere is performed by employing $p_{\text{Tw}} = 400$ hPa and $\gamma = 2$ K km⁻¹ to avoid the previously mentioned warm bias in the UTLS region of the polar winter hemisphere (Sheshadri et al., 2015; Garny et al., 2020). In contrast to the REF and CLS experiments, the third experiment does not include a polar vortex (NPV) which is achieved by setting $W(\phi) \equiv 0$ in Eq. (2.8) (Polvani and Kushner, 2002). Additionally, the NPV experiment employs $p_{\text{Tw}} = 100$ hPa.

For the primary set of TUTW simulations with $z_0 = 0.3$ of the NPV, REF, and CLS experiments in Secs. 4.2–4.4, the parameter δ_z which determines the stratification in the troposphere is set to $\delta_z = 4.3$ K. Some simulations are repeated with the original value of $\delta_z = 10$ K (Held and Suarez, 1994) in order to guarantee robust results. Temperature differences due to dif-

ferent values of δ_z are most pronounced in the TUT (Fig. 2b in Garny et al., 2020). Hence, circulation changes in the experiments with TUTW are very similar for different δ_z and only appear at different heating amplitudes which will be shown in Sec. 4.5. Circulation changes for tropical heatings that are located in the lower stratosphere ($z_0 = 0.1$) and in the middle troposphere ($z_0 = 0.5$) are investigated in Sec. 4.6. A list of all experiments with corresponding settings for important parameters is given in Table 2.2. All simulations are integrated for 30 years with time steps between 360 and 540 s and with 1000 days of spin-up being excluded.

Wave forcing	Transition pressures		Polar vortex lapse rate γ [K km ⁻¹]	Stratification δ_z [K]	Integration length [years]	
	p_{Ts} [hPa]	p_{Tw} [hPa]				
WN0	100	100	1, 2, 3, 4, 5, 6	4.3	10	
				10	30	
WN2T	100	100, 150, 200, 250, 300, 350, 450	1, 2, 3, 4	4.3	5	
					30	
				400	1, 1.5, 2, 2.5, 3, 4	4.3, 10
					1, 2, 3, 4, 5, 6	30
WN2H	100	400	1, 1.5, 2, 2.5, 3, 3.5, 4, 4.5	4.3	5	
				1, 2, 3, 4	10	30
				200	200	4

Table 2.1: List of polar stratospheric cooling experiments with a resolution of T42L90 analyzed in Chap. 3.

Name	Resolution	Heating amplitudes q_0 [K day ⁻¹]	Heating shape	Heating center z_0	Stratification δ_z [K]
NPV	T42L90	-0.1, -0.05, 0, 0.05, 0.1, 0.15, 0.2, 0.25, 0.3, 0.35, 0.4, 0.45, 0.5, 0.55, 0.6, 1			
NPV-L47	T42L47	-0.1, 0, 0.1, 0.2, 0.3, 0.4, 0.5, 0.6, 1			4.3
NPV-T85L90	T85L90	0	standard, Eq. (2.10)	0.3	
NPV-T85	T85L47	0, 0.15, 0.2, 0.25, 0.3, 0.35, 0.4, 0.45, 0.5, 0.6, 1			
NPV-d10		0, 0.05, 0.1, 0.15, 0.2, 0.25, 0.3, 0.35, 0.4, 0.5, 1			10
REF	T42L90	-0.1, -0.05, 0, 0.05, 0.1, 0.15, 0.2, 0.25, 0.3, 0.35, 0.4, 0.45, 0.5, 0.55, 0.6, 1			
REF-L47	T42L47	-0.1, 0, 0.1, 0.2, 0.3, 0.4, 0.5, 0.6, 1			4.3
REF-T85		0, 0.15, 0.2, 0.25, 0.3, 0.35, 0.4, 0.45, 0.5, 0.6, 1	standard, Eq. (2.10)	0.3	
REF-d10	T85L47	0, 0.05, 0.1, 0.15, 0.2, 0.25, 0.3, 0.35, 0.4, 0.5, 1			10
REF-mod		0.2, 0.4, 0.5, 0.6, 0.7, 0.8, 1, 1.2		0.3	
REF-mod-LS		0.2, 0.4, 0.6, 0.8, 1, 1.2, 1.6, 2	modified, Eq. (2.11)	0.1	4.3
REF-mod-MT		0.2, 0.4, 0.6, 0.8, 1, 1.2, 1.6, 2		0.5	
CLS	T42L90	-0.1, -0.05, 0, 0.05, 0.1, 0.15, 0.2, 0.25, 0.3, 0.35, 0.4, 0.45, 0.5, 0.55, 0.6, 1	standard, Eq. (2.10)	0.3	4.3
CLS-T85	T85L47	-0.1, -0.05, 0, 0.05, 0.1, 0.15, 0.2, 0.3, 0.5			

Table 2.2: List of tropical warming experiments analyzed in Chap. 4.

2.3 Diagnostics

The detailed analysis of climate states with respect to their stratosphere-troposphere dynamical coupling in this thesis relies on essential quantities. Strength \bar{u}_{\max} and latitude ϕ_{\max} of zonal-mean zonal wind maxima at different pressure levels contribute to the shape of the waveguide that influences the exchange of planetary-scale waves between stratosphere and troposphere (2.3.1). In order to quantify the amount of wave flux B_{top} that is exchanged between stratosphere and troposphere, relating to the polar vortex strength, as well as the wave flux B_{S} between tropics and extratropics in the upper troposphere, relating to the location of the tropospheric jet, the wave flux budget of a meridional subdomain is considered (2.3.2). Apart from the polar vortex, wave flux propagating into and dissipating within the stratosphere affects the strength and structure of the residual circulation (2.3.3) which, in turn, is consistent with the mean flow. When the dynamical coupling of the stratosphere and troposphere investigated by its crucial entities—mean flow, wave flux, and residual circulation—is subject to imminent fundamental changes, an increased memory of the system can be expected (Scheffer et al., 2009). This specific indication of regime transitions is measured by the autocorrelation time scale τ in this thesis (2.3.4). Due to the frequent use of these quantities throughout Chaps. 3 to 5, their computation is introduced in the following.

2.3.1 Latitude of a zonal-mean maximum

The calculation of the latitude ϕ_{\max} of a zonal-mean zonal wind maximum \bar{u}_{\max} at a given pressure level relies on five data points \bar{u}^{peak} of the zonal-mean zonal wind surrounding its maximum. Together with the corresponding latitudes ϕ^{peak} , continuous results for ϕ_{\max} can be obtained with the method introduced by Adam et al. (2018). To be precise, the following algorithm is used for the calculation of ϕ_{\max} :

1. Determine the absolute maximum zonal-mean zonal wind $\bar{u}_{\max} \equiv \bar{u}_{i_{\max}}$ at a given pressure level in one hemisphere.
2. Collect the two adjacent data points northward and southward of \bar{u}_{\max} , respectively, to obtain data sets \bar{u}^{peak} and ϕ^{peak} for the zonal-mean zonal wind and the latitude around the peak, respectively:

$$\begin{aligned}\bar{u}^{\text{peak}} &= [\bar{u}_{i_{\max}-2}, \bar{u}_{i_{\max}-1}, \bar{u}_{i_{\max}}, \bar{u}_{i_{\max}+1}, \bar{u}_{i_{\max}+2}], \\ \phi^{\text{peak}} &= [\phi_{i_{\max}-2}, \phi_{i_{\max}-1}, \phi_{i_{\max}}, \phi_{i_{\max}+1}, \phi_{i_{\max}+2}].\end{aligned}$$

3. Exclude elements \bar{u}_i^{peak} and ϕ_i^{peak} from the data sets created in step 2 for which the condition $0^\circ\text{N} \leq \phi_i^{\text{peak}} \leq 90^\circ\text{N}$ ($90^\circ\text{S} \leq \phi_i^{\text{peak}} \leq 0^\circ\text{S}$) is not fulfilled when the northern (southern) hemisphere is considered.

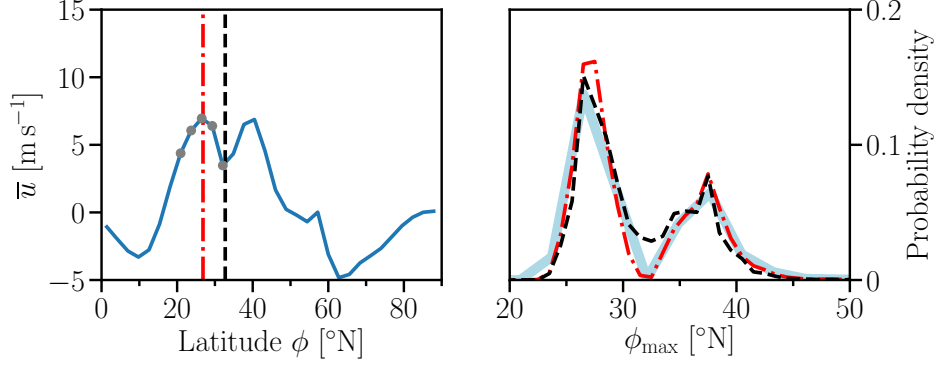


Figure 2.3: Zonal-mean zonal wind \bar{u} at 850 hPa as a function of latitude ϕ for an arbitrary time step with double-peak structure of the 30-year WN2T simulation with $p_{T_w} = 400$ hPa, $\gamma = 1 \text{ K km}^{-1}$, and $\delta_z = 10 \text{ K}$ (left) and the corresponding probability density function (PDF) of the latitude ϕ_{\max} of maximum \bar{u} at 850 hPa computed from all time steps for three different methods (right). Employing the latitude $\phi_{i_{\max}}$ of maximum \bar{u} on the model grid (central gray dot in the left panel) for every time step, only the discrete intervals around the model-grid latitudes can contribute to the probability density of ϕ_{\max} (thick solid light-blue line in the right panel). Smoother results are obtained with the algorithm provided by Adam et al. (2018). The exact value of ϕ_{\max} , however, can be missed significantly for double peaks when integrating over all available latitudes in the northern hemisphere in Eq. (2.14), leading to finite values of the PDF of ϕ_{\max} at latitudes where maximum winds are never found (dashed black lines). Restricting the integral in Eq. (2.14) to five latitudes ϕ^{peak} around the true maximum (gray dots in the left panel) solves this issue (dash-dotted red lines).

4. Transform \bar{u}^{peak} to an array S ranging from 0 to 1 via (Adam et al., 2018)

$$\tilde{S} = \bar{u}^{\text{peak}} - \min(\bar{u}^{\text{peak}}),$$

$$S = \frac{\tilde{S}}{\max(\tilde{S})}.$$

5. Compute ϕ_{\max} via Eq. (1) of Adam et al. (2018) using only data points of the peak:

$$\phi_{\max} = \frac{\int_{\phi^{\text{peak}}} S(\phi)^n \phi \, d\phi}{\int_{\phi^{\text{peak}}} S(\phi)^n \, d\phi} \quad (2.14)$$

with $n = 6$. Note that in general $\phi_{\max} \neq \phi_{i_{\max}}$.

When the integral in Eq. (2.14) is not restricted to contain only a small number of data points surrounding the true maximum, complicated double-peak structures of the zonal-mean zonal wind can cause inaccuracies as shown in Fig. 2.3. Therefore, the number of points in \bar{u}^{peak} and ϕ^{peak} must not exceed a certain threshold that depends on the horizontal resolution of the model. For example, seven data points still guarantee correct results for the horizontal resolution of T85, but not for T42 any more. To this end, data sets of the peak are chosen to contain five points to apply this method to all resolutions. When the data sets only contain

three points, the advantage of this method being to lead to smooth results disappears in favor of discontinuous probability density functions (PDFs) of ϕ_{\max} .

2.3.2 Eliassen–Palm flux components of a meridional subdomain

In order to analyze fractions of upward propagating wave activity across the extratropical middle troposphere that are refracted equatorward within the troposphere, or propagate further up into the stratosphere, or dissipate in the extratropical upper troposphere, EP fluxes associated with a meridional subdomain are defined. To this end, the isobaric EP flux divergence (EPFD, Andrews et al., 1983; Cohen et al., 2014)

$$\nabla \cdot \mathbf{F} = \frac{\partial_\phi (F^{(\phi)} \cos(\phi))}{a \cos(\phi)} + \partial_p F^{(p)} \quad (2.15)$$

is integrated over the area given by $\phi_S \leq \phi \leq \phi_N$ and $p_{\text{top}} \leq p \leq p_{\text{bot}}$ which yields

$$\begin{aligned} \underbrace{\frac{2\pi a^2}{g} \int_{p_{\text{top}}}^{p_{\text{bot}}} \int_{\phi_S}^{\phi_N} \cos(\phi) \nabla \cdot \mathbf{F} \, d\phi \, dp}_{B_{\text{net}}} &= \underbrace{\frac{2\pi a \cos(\phi)}{g} \int_{p_{\text{top}}}^{p_{\text{bot}}} F^{(\phi)} \, dp}_{B_N} \Big|_{\phi_N} \\ &- \underbrace{\frac{2\pi a \cos(\phi)}{g} \int_{p_{\text{top}}}^{p_{\text{bot}}} F^{(\phi)} \, dp}_{B_S} \Big|_{\phi_S} \\ &+ \underbrace{\frac{2\pi a^2}{g} \int_{\phi_S}^{\phi_N} \cos(\phi) F^{(p)} \, d\phi}_{B_{\text{bot}}} \Big|_{p_{\text{bot}}} \\ &- \underbrace{\frac{2\pi a^2}{g} \int_{\phi_S}^{\phi_N} \cos(\phi) F^{(p)} \, d\phi}_{B_{\text{top}}} \Big|_{p_{\text{top}}}, \quad (2.16) \end{aligned}$$

where $F^{(\phi)}$ and $F^{(p)}$ are latitudinal and vertical components of the EP flux vector \mathbf{F} , respectively, and a and g are Earth's radius and gravitational acceleration, respectively.

Climate regime transitions investigated with EMIL in this thesis involve sharp changes of the wave flux from the troposphere to the stratosphere as well as from the extratropical to the tropical troposphere. The corresponding dynamical differences can be detected with the choice $\phi_S = 38^\circ\text{N}$, $\phi_N = 90^\circ\text{N}$, $p_{\text{top}} = 100 \text{ hPa}$, and $p_{\text{bot}} = 590 \text{ hPa}$ as turned out during the analyses of Chap. 4. The meridional subdomain with associated EP fluxes B_S , B_N , B_{top} , B_{bot} , and its corresponding budget B_{net} is visualized in Fig. 2.4 together with the zonal-mean zonal wind of the control run of the REF experiment. Due to $\phi_N = 90^\circ\text{N}$, the EP flux component

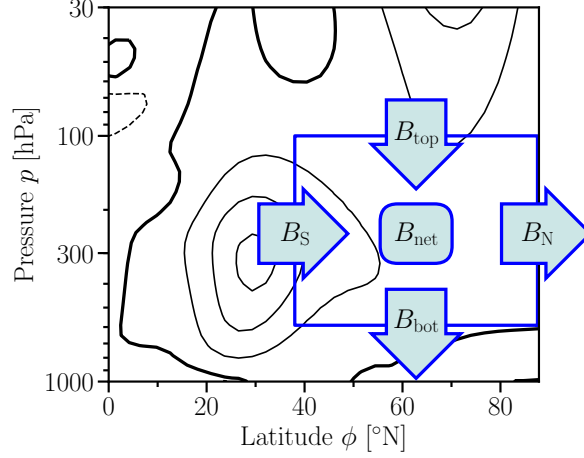


Figure 2.4: Eliassen–Palm (EP) fluxes associated with a meridional subdomain with boundaries at $\phi_S = 38^\circ\text{N}$, $\phi_N = 90^\circ\text{N}$, $p_{\text{top}} = 100$ hPa, and $p_{\text{bot}} = 590$ hPa. B_S and B_N are the northward (positive ϕ -direction) EP fluxes integrated from p_{top} to p_{bot} at ϕ_S and ϕ_N , respectively. Similarly, B_{top} and B_{bot} are the downward (positive p -direction) EP fluxes integrated from ϕ_S to ϕ_N at p_{top} and p_{bot} , respectively. According to Eq. (2.16) the net EP flux budget inside the box is $B_{\text{net}} = B_N - B_S + B_{\text{bot}} - B_{\text{top}}$. The zonal-mean zonal wind climatology (black contour lines with a contour interval of 10 m s^{-1} , negative contours dashed, thick zero-contour line) of the control run ($q_0 = 0$) of the REF experiment described in Sec. 2.2.2 is added to relate the location of the meridional subdomain.

B_N across the northern boundary can be neglected such that the EP flux budget B_{net} can be approximated according to

$$B_{\text{net}} \approx -B_S + B_{\text{bot}} - B_{\text{top}}. \quad (2.17)$$

Since pressure is used as a vertical coordinate, upward propagating waves correspond to negative values of the vertical EP fluxes B_{top} and B_{bot} .

2.3.3 Strength of the residual circulation

Strength and structure of the RC can be quantified via the downward-control streamfunction (Haynes et al., 1991)

$$\Psi_{\text{dc}}^* = \frac{2\pi a \cos(\phi)}{g} \int_0^p \frac{\overline{\mathcal{F}} + \overline{X}}{\hat{f}} dp' \quad (2.18)$$

in the stationary limit of $\partial_t \bar{u} = 0$. Here, $\overline{\mathcal{F}} = (a \cos(\phi))^{-1} \nabla \cdot \mathbf{F}$ is the zonal-mean zonal wind tendency induced by the EP flux divergence $\nabla \cdot \mathbf{F}$, \overline{X} is parameterized drag, and $\hat{f} = (a \cos(\phi))^{-1} \partial_\phi (\bar{u} \cos(\phi)) - f$ is proportional to the latitudinal derivative of angular momentum with Coriolis parameter $f = 2\Omega \sin(\phi)$ and Earth's rotation rate Ω . Strictly speaking, the pressure integral in Eq. (2.18) has to be evaluated along lines of constant angular momentum (Haynes et al., 1991). Due to the fact that contour lines of angular momentum are

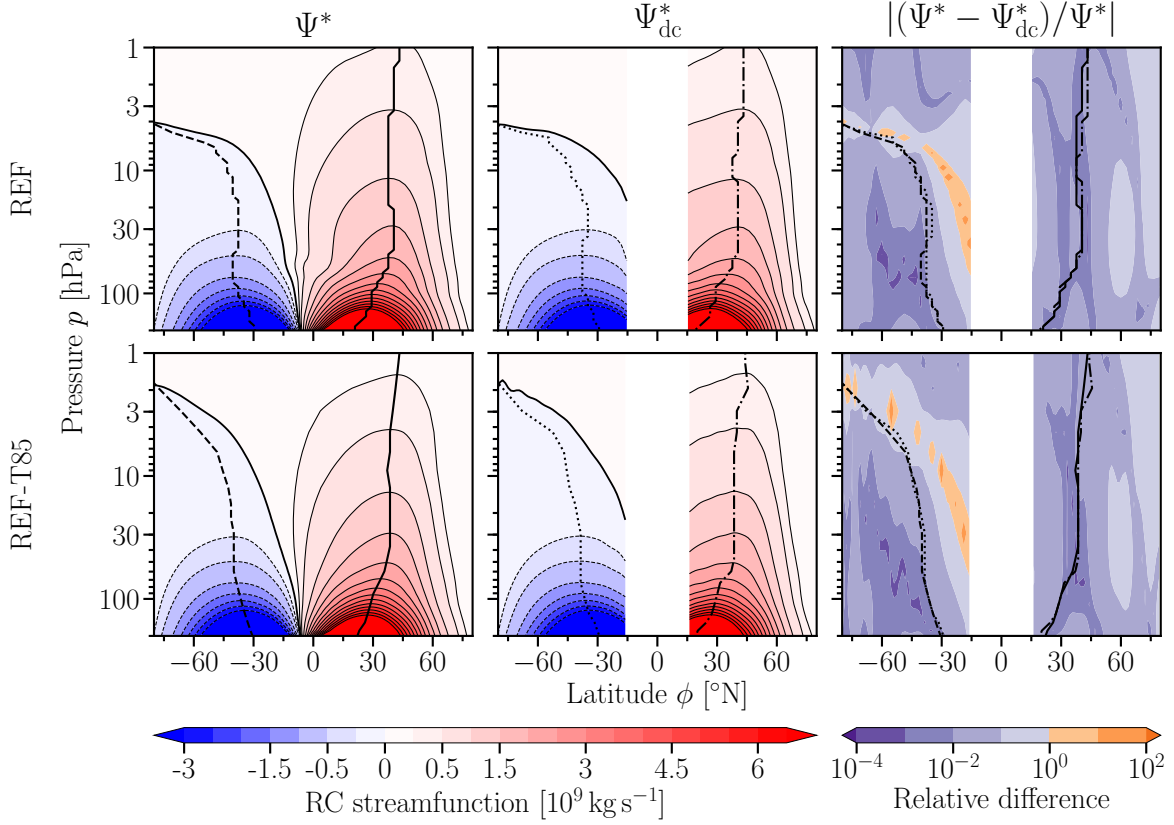


Figure 2.5: Standard residual-mean streamfunction Ψ^* (left), downward-control streamfunction Ψ_{dc}^* (middle), and their relative difference (right) as functions of latitude ϕ and pressure p for the control-run ($q_0 = 0$) climatologies of the TUTW reference experiments at resolutions T42L90 (top) and T85L47 (bottom). Turnaround latitudes are added representing maxima (solid and dash-dotted black lines) and minima (dashed and dotted black lines) of the residual-mean meridional circulation located in the northern and southern hemisphere, respectively. For a better distinction of the color shading representing Ψ^* and Ψ_{dc}^* , solid, thick solid, and dashed black lines are added for positive, zero, and negative contour lines, respectively.

almost parallel to the lines of constant latitude, and in order to simplify calculations, the integration proceeds at constant latitudes as in McLandress and Shepherd (2009, see their discussion of Eq. (3)). The middle panels of Fig. 2.5 show Ψ_{dc}^* for the control-run ($q_0 = 0$) climatologies of the reference experiments at resolutions T42L90 (top) and T85L47 (bottom). Increasing (decreasing) values of the streamfunction with increasing latitude indicate upwelling (downwelling), hence negative (positive) $\bar{\omega}^*$. The region of upwelling air masses is confined between the turnaround latitudes representing the maximum and minimum values of Ψ_{dc}^* at each pressure level located in the northern and southern hemisphere, respectively. Due to the denominator of the integrand in Eq. (2.18), Ψ_{dc}^* can not be computed for the deep tropics.

As a consistency check, the standard streamfunction of the residual-mean meridional circulation (Gerber and Manzini, 2016; Adam et al., 2018)

$$\Psi^* = \frac{2\pi a \cos(\phi)}{g} \int_0^p \bar{v}^* dp' \quad (2.19)$$

with a pressure integral along lines of constant latitude is shown in the left panels of Fig. 2.5. The turnaround latitudes of Ψ_{dc}^* and Ψ^* agree very well. Furthermore, relative differences between both streamfunctions are particularly small in the vicinity of turnaround latitudes and fall below 10^{-2} in the lower stratosphere of both hemispheres as shown in the right panels of Fig. 2.5.

The strength of the RC at a given pressure level is computed via $\max(\Psi_{\text{dc}}^*) + |\min(\Psi_{\text{dc}}^*)|$, i.e., by the sum of the absolute values of the downward-control streamfunction at its turnaround latitudes (Abalos et al., 2021; Rosenlof, 1995). Excluding the deep tropics and extreme polar regions which suffer from numerical inaccuracies, turnaround latitudes are searched for at latitudes ϕ fulfilling $15^\circ < |\phi| < 80^\circ$. For the total RC strength, $\bar{\mathcal{F}}$ is computed from all WNs, and \bar{X} is computed from Rayleigh friction of the climatological-mean zonal-mean zonal wind in the sponge layer of EMIL. Contributions to the RC strength from planetary- and synoptic-scale wave drag are computed from Ψ_{dc}^* where only the planetary- and synoptic-scale $\bar{\mathcal{F}}$ is used, and \bar{X} is set to zero, respectively.

Alternatively, the total RC strength can be inferred from the total upward mass flux (Wang et al., 2012)

$$\mathcal{M} = -\frac{2\pi a^2}{g} \int_{\phi_1}^{\phi_2} \cos(\phi) \bar{\omega}^* d\phi \quad (2.20)$$

between the turnaround latitudes ϕ_1 and ϕ_2 at the same pressure level. Figs. 3.12 and 4.11 confirm that the results of $\max(\Psi_{\text{dc}}^*) + |\min(\Psi_{\text{dc}}^*)|$ and \mathcal{M} lead to almost identical values for the total residual circulation strength.

2.3.4 Autocorrelation time scale

The persistence of atmospheric flow at a given pressure level p in a specific climate state can be quantified by the autocorrelation time scale τ . The calculation of τ is based on Gerber et al. (2008) and follows the subsequent algorithm:

1. Compute the zonal-mean zonal wind \bar{u}_p at pressure p weighted by $\sqrt{\cos \phi}$ for extratropical latitudes ϕ ranging from 30°N to 80°N , i.e., $\bar{u}_p^w(t, \phi) = \sqrt{\cos \phi} \bar{u}_p(t, \phi)$.
2. Determine the first principal component time series $\alpha(t)$ associated with the first empirical orthogonal function of $\bar{u}_p^w(t, \phi)$ (Dawson, 2016).
3. Calculate the autocorrelation $r(t)$ of the first principal component time series $\alpha(t)$.
4. Apply a least-square fit of $r(t)$ to $\exp(-t/\tau)$ for all $r(t) > \exp(-1)$ to estimate τ .⁸

Note that τ is only an approximation of the true autocorrelation time scale since the length of the principal component time series $\alpha(t)$ is finite (Gerber et al., 2008).

⁸Alternatively, the autocorrelation time scale τ can be estimated by the time when $r(t)$ falls below $\exp(-1)$ (Chan and Plumb, 2009). This can be beneficial when $r(t)$ does not behave like an exponential. In this thesis, τ is mainly used for identifying peaks in the autocorrelation time scale that indicate potential climate regime transitions. Since no significant differences in the location of those peaks were found between both methods, the exponential least-square fit of Gerber et al. (2008) is retained.

Chapter 3

The role of the LS for stratosphere-troposphere coupling

Parts of this chapter have contributed to the publication

Garny, H., Walz, R., Nützel, M., and Birner, T. Extending the Modular Earth Submodel System (MESSy v2.54) model hierarchy: the ECHAM/MESSy IdeaLized (EMIL) model setup. *Geoscientific Model Development*, 13(11):5229–5257, 2020. <https://doi.org/10.5194/gmd-13-5229-2020>.

Previous studies highlighted the importance of the winter-hemispheric lower stratosphere for the dynamical coupling of the stratosphere and troposphere (Chen and Robinson, 1992; Scott and Polvani, 2006; Karpechko et al., 2017; Birner and Albers, 2017; Martineau et al., 2018; White et al., 2019). In this chapter, the idealized general circulation model EMIL is operated with different stratospheric equilibrium temperatures that induce different states of the polar vortex. The range of possible tropospheric impacts is then used to address the specific research question **S1**. Since previous idealized-model setups incorporate unrealistically high temperatures in the polar UTLS region (Sheshadri et al., 2015; Garny et al., 2020), a new setup is prepared to better approximate observations. Regarding its importance for stratosphere-troposphere coupling, the winter-hemispheric circulation should be very sensitive to temperature changes in the lower stratosphere. In combination with traditional setups, the new setup is compared to midwinter conditions in the northern and southern hemisphere of the real atmosphere, revealing general deficiencies present in idealized GCMs which are, however, expected. It is by no means the aim of this chapter to develop an equilibrium temperature that induces most realistic circulations (Wu and Reichler, 2018). On the contrary, the first part of this chapter is dedicated to coarsely assess the relevant entities for stratosphere-troposphere coupling in idealized models, and to provide an overview of observations.

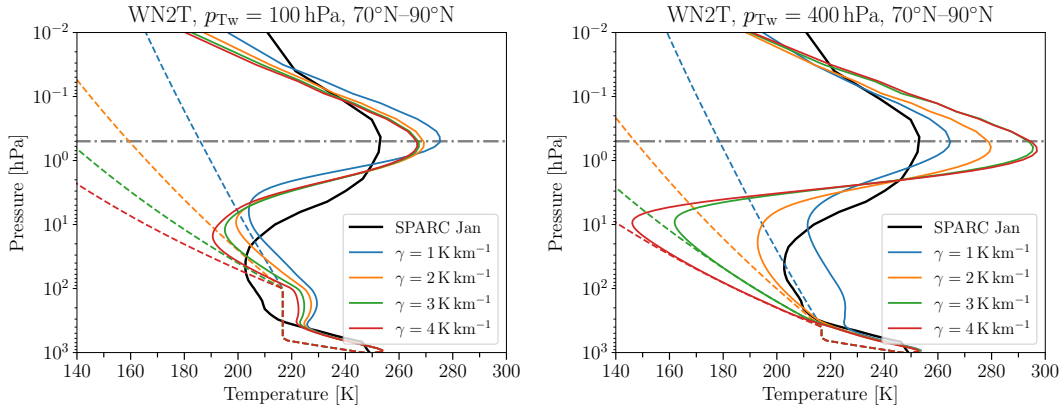


Figure 3.1: Profiles of zonal-mean temperatures of 30-year simulations with wavenumber-2 topography (WN2T) and $\delta_z = 10$ K averaged over 70°N – 90°N in the winter hemisphere for different polar vortex lapse rates γ and for equilibrium-temperature transition pressures of $p_{T_w} = 100$ hPa (left) and $p_{T_w} = 400$ hPa (right). Dashed colored lines show the profiles of the corresponding equilibrium temperatures. The January climatology of the SPARC data set is added for reference (SPARC, 2002; Randel et al., 2004; Swinbank and Ortland, 2003). The dash-dotted gray line represents the pressure level above which the spongy layer sets in. Both figures are taken from Garny et al. (2020).

3.1 Motivation: circulation sensitivity to the lower-stratospheric thermal structure

The equilibrium temperature T_{equ} introduced by Polvani and Kushner (2002) employs a constant pressure of $p_T \equiv 100$ hPa at which the tropospheric temperature scheme transitions to the stratospheric scheme. In the polar winter region, this implies an isotherm layer of large vertical extent separating tropospheric and stratospheric decreases of T_{equ} with height as shown in the left panel of Fig. 3.1. In the UTLS region, the equilibrium temperature even exceeds the observation-based January climatology of the Stratosphere-troposphere Processes And their Role in Climate (SPARC) data set (SPARC, 2002; Randel et al., 2004; Swinbank and Ortland, 2003). This poses the problem that simulated temperatures exceed the observations in the UTLS region even more since the general circulation warms the extratropical stratosphere (here shown for 30-year simulations with wavenumber-2 topography (WN2T) and $\delta_z = 10$ K, Gerber and Polvani, 2009). High values of the polar vortex lapse rate γ are not able to compensate for the warm bias of the polar lower stratosphere.

Colder temperatures in the polar-winter lower stratosphere can be achieved by reducing the height at which the polar vortex lapse rate γ sets in. To this end, the transition pressure p_T in EMIL is developed to be a function of latitude and allows for separate crossovers from tropospheric to stratospheric equilibrium temperatures in the summer and winter hemispheres via p_{T_s} and p_{T_w} , respectively. The first occurrence of equilibrium temperatures falling below observed temperatures in the polar winter UTLS region arises for $p_{T_w} = 400$ hPa as shown in the right panel of Fig. 3.1. Applying different values of the polar vortex lapse rate γ now

has a larger impact on the atmospheric circulation as opposed to $p_{\text{Tw}} = 100$ hPa, where polar temperature profiles show less sensitivity to γ . For $p_{\text{Tw}} = 400$ hPa and $\gamma = 2 \text{ K km}^{-1}$, the simulated temperature profile represents the best resemblance of the SPARC climatology for January in the UTLS region among the performed simulations.

In a similar study, where equilibrium temperatures were varied in the polar winter lower stratosphere, a colder lower stratosphere increased the variability of wave activity propagating upward (Martineau et al., 2018). To this end, the variability of the polar vortex strength for the simulation with $p_{\text{Tw}} = 400$ hPa and $\gamma = 2 \text{ K km}^{-1}$ is compared to other setups with planetary-scale wave generation by topography (Gerber and Polvani, 2009) and by heating (Lindgren et al., 2018) as well as to setups without additional wave generation (Polvani and Kushner, 2002) that have previously been used in literature. An analysis of the corresponding wave activity fluxes and waveguides for planetary-scale waves completes the following section.

3.2 Comparison of different winter-climate setups

Zonal-mean zonal wind and temperature climatologies for the Polvani and Kushner (2002)-setup with $p_{\text{Tw}} = 100$ hPa, $\gamma = 4 \text{ K km}^{-1}$ and with zonally symmetric surface conditions (WN0) are shown in the top left panel of Fig. 3.2. A strong stratospheric polar vortex with maximum wind speeds around 70 m s^{-1} at 10 hPa as well as a tropospheric jet located around 40°N are observed. The strong polar vortex is associated with large meridional temperature gradients adjacent to the polar stratosphere which leads to large deviations from temperatures of the observation-based SPARC data for January in that area (SPARC, 2002; Randel et al., 2004; Swinbank and Ortland, 2003) as shown in the top left panel of Fig. 3.3.

Retaining all parameters for the equilibrium temperature, the addition of a wavenumber-2 topography (WN2T) resulting in enhanced planetary-scale wave activity decelerates the stratospheric polar vortex and shifts the tropospheric jet equatorward to 30°N representing the Gerber and Polvani (2009)-setup (top right panel of Fig. 3.2). In balance with the thermal wind relation given in Eq. (4.1), meridional temperature gradients are reduced in the polar stratosphere compared to the Polvani and Kushner (2002)-setup leading to more realistic, but still considerably deviating temperatures in the polar upper stratosphere (top right panel of Fig. 3.3).

As discussed in Sec. 3.1, the polar lower stratosphere in both previously mentioned setups faces a warm bias compared to observations which can be attenuated when a higher transition pressure p_{Tw} in the winter hemisphere is employed (bottom left panel of Fig. 3.3). The reduced height at which the polar vortex lapse rate of $\gamma = 2 \text{ K km}^{-1}$ sets in for $p_{\text{Tw}} = 400$ hPa leads to an acceleration as well as to an equatorward shift of the lower polar vortex, but merely affects the location of the tropospheric jet when additionally $\delta_z = 4.3 \text{ K}$ is used (bottom left panel of Fig. 3.2).

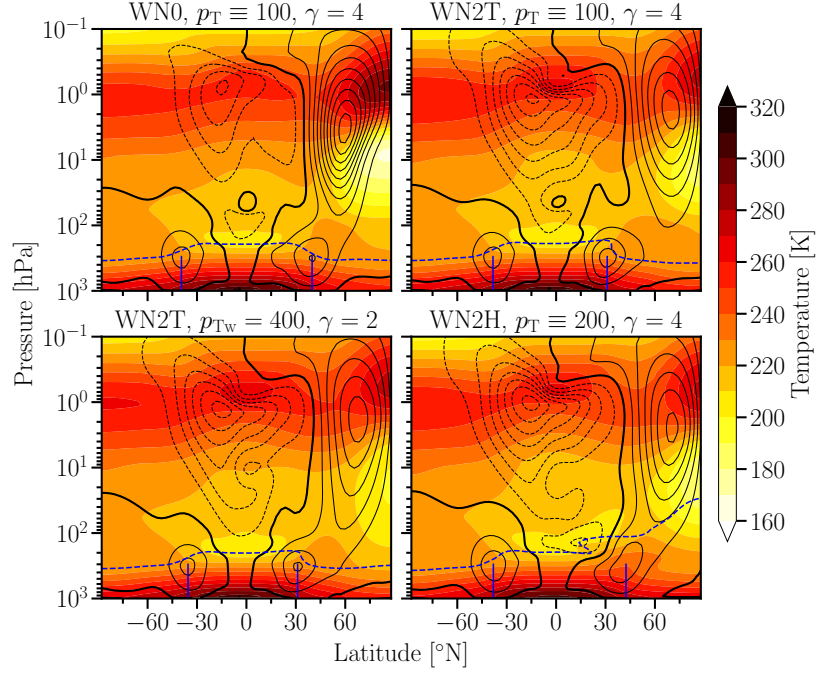


Figure 3.2: 30-year averages of zonal-mean zonal wind (black contour lines with a contour interval of 10 m s^{-1} , negative contours dashed, thick zero-contour line) and temperature (color shading with a contour interval of 10 K) as functions of latitude and pressure for the Polvani and Kushner (2002)-setup with both zonally symmetric surface conditions and equilibrium temperature (WN0), and with $\delta_z = 10 \text{ K}$ (top left), for the Gerber and Polvani (2009)-setup with wavenumber-2 topography (WN2T), and with $\delta_z = 10 \text{ K}$ (top right), as well as with additionally lower temperatures in the polar lower stratosphere by employing $p_{T_w} = 400 \text{ hPa}$ and $\gamma = 2 \text{ K km}^{-1}$, but with $\delta_z = 4.3 \text{ K}$ (bottom left), and for the Lindgren et al. (2018)-setup with zonally symmetric surface conditions, but with wavenumber-2 heating in the troposphere (WN2H), and with $\delta_z = 10 \text{ K}$ (bottom right). The dashed blue lines denote the lapse-rate tropopause which is defined by the first occurrence of $\Gamma = \frac{g}{R} \frac{\partial \ln T}{\partial \ln p} < 2 \text{ K km}^{-1}$ measured from the surface (WMO, 1957). The solid blue vertical lines show the latitudes of the zonal-mean zonal wind maxima in the troposphere.

In a different approach of planetary-scale wave generation, Lindgren et al. (2018) return to zonally symmetric surface conditions, but apply a wavenumber-2 heating (WN2H) together with $p_T \equiv 200 \text{ hPa}$ and $\gamma = 4 \text{ K km}^{-1}$. The resulting climatology exhibits a tropospheric jet located poleward of 40°N and a thermal tropopause that is noticeably different from the topographically forced simulations (bottom right panel of Fig. 3.2). Temperatures around the tropospheric jet are more than 10 K higher than in the three other setups. The comparison with observations suggests a stronger residual-mean meridional circulation in the extratropics (bottom right panel of Fig. 3.3).

Apart from the polar winter stratosphere, temperature deviations of the presented idealized-model setups from observations are most pronounced in the upper atmosphere of the summer hemisphere and in the tropical UTLS region. The former might be due to the latitudinally constant equilibrium temperature in the summer-hemispheric stratosphere. The latter region

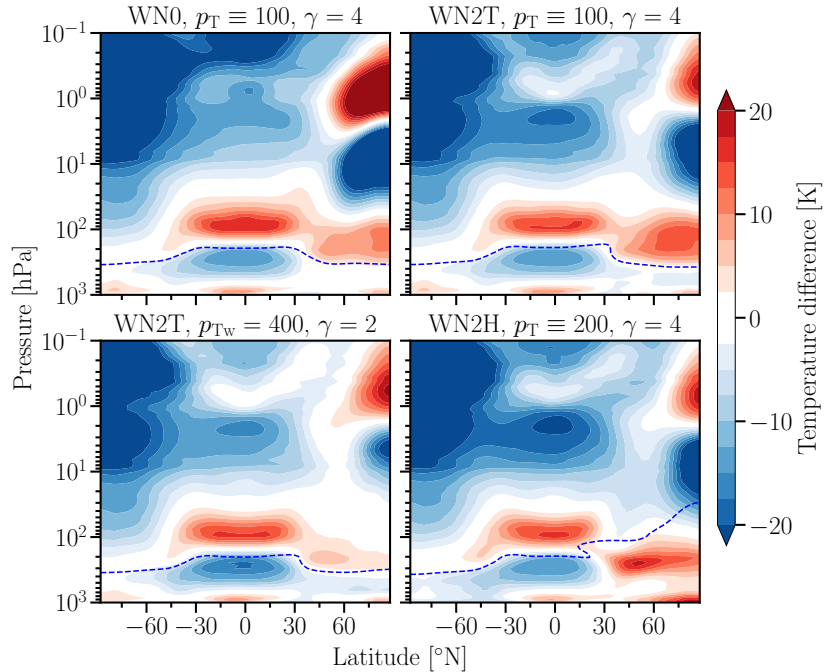


Figure 3.3: Differences of zonal-mean temperatures of the simulations presented in Fig. 3.2 and the SPARC climatology of January as functions of latitude and pressure. The dashed blue lines denote the lapse-rate tropopauses (WMO, 1957).

of enhanced temperature deviations represents a too low tropical tropopause layer ubiquitous in dry general circulation models. More realistic circulations can be achieved by adapting the equilibrium temperature to radiative observations (Jucker et al., 2013) or by including moist effects (Jucker and Gerber, 2017)

In combination with the mean state, the variability of the polar vortex characterizes a given climate state. Mean state and variability of the polar vortex strength measured by the maximum zonal-mean zonal wind \bar{u}_{\max} at 10 hPa are displayed in Fig. 3.4 for the four idealized-model setups introduced above as well as for the northern and southern hemisphere represented by the European Centre for Medium-Range Weather Forecasts (ECMWF) next-generation re-analysis ERA5 (ERA5) data (Hersbach et al., 2020) for December-January-February (DJF) and June-July-August (JJA), respectively. The southern-hemispheric polar vortex exhibits a much stronger climatological mean state in ERA5 than its northern-hemispheric counterpart and has not formed any SSWs during JJA so far.⁹ The variability of the northern-hemispheric polar vortex during DJF is noticeably amplified with an existing probability of SSWs where $\bar{u}_{\max} < 0$ at 10 hPa (compare with Fig. 1.5). In this regard, the Polvani and Kushner (2002)-setup with WN0 reflects both mean state and variability of the southern-hemispheric polar vortex. All other idealized-model setups with either WN2T or WN2H frequently form SSWs and thus rather correspond to the northern-hemispheric polar vortex, whose lower and upper

⁹Both observed southern hemisphere SSWs occurred in September (Krüger et al., 2005; Rao et al., 2020).

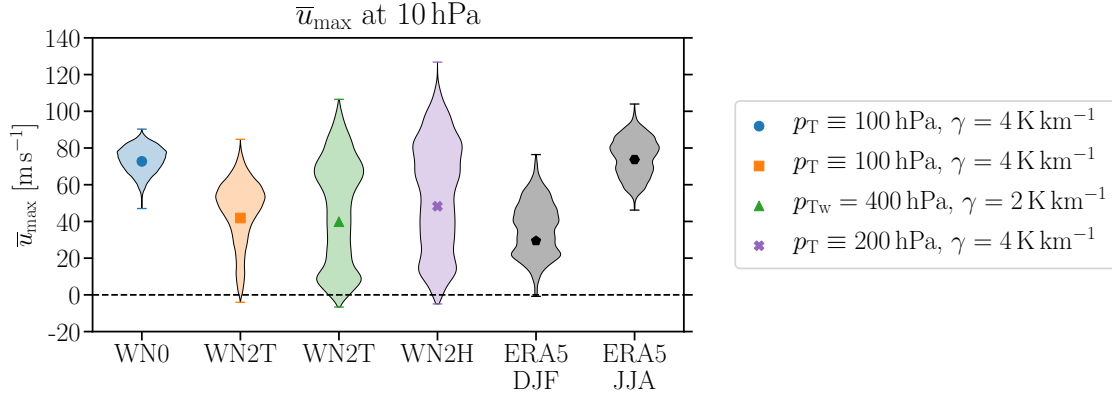


Figure 3.4: Strength \bar{u}_{\max} of the maximum zonal-mean zonal wind at 10 hPa for the simulations presented in Fig. 3.2 as well as for ERA5 data for DJF in the northern hemisphere and for JJA in the southern hemisphere (Hersbach et al., 2020). Markers display values of \bar{u}_{\max} that are computed from the climatological-mean zonal-mean zonal winds representing the mean polar vortex strength. For an impression of the polar vortex variability, shapes of the probability density functions (shadings) and extreme values (horizontal lines) are added for which \bar{u}_{\max} is computed for every time step first. Note that all probability densities are scaled in such a way that they have equal widths at their respective maxima and can therefore only serve for relative comparisons.

boundaries of \bar{u}_{\max} are closest approximated by the Gerber and Polvani (2009)-setup. The bimodality of the northern-hemispheric polar vortex strength is only represented in the WN2T setup with $p_{T_w} = 400$ hPa and $\gamma = 2$ K km $^{-1}$ as well as in the WN2H setup of Lindgren et al. (2018), of which both’s maximum strength, however, even exceeds the maximum strength of the polar vortex in the southern hemisphere. The enhanced variability in the WN2T setup with $p_{T_w} = 400$ hPa and $\gamma = 2$ K km $^{-1}$ compared to the WN2T setup with $p_{T_w} = 100$ hPa and $\gamma = 4$ K km $^{-1}$ is consistent with a colder lower stratosphere, permitting a broader spectrum of wave flux entering the stratosphere (Martineau et al., 2018).

Enhanced variability and reduced climatological-mean strength of the polar vortex in the WN2T and WN2H setups compared to the WN0 setup are associated with more Eliassen–Palm (EP) flux \mathbf{F} propagating into and dissipating within the stratosphere as shown in Fig. 3.5. In contrast to this, only weak upward propagation and dissipation of EP flux is present in the WN0 setup, enhanced negative EP flux divergence (EPFD) occurs in the upper stratosphere in the Gerber and Polvani (2009)-setup. In both setups with bimodal probability density functions of the polar vortex strength, the region of enhanced negative EPFD extends to the lower stratosphere. In addition, the polar vortex is located more equatorward which is consistent with decreased poleward and increased equatorward propagation of wave activity according to which more wave flux reaches the turnaround latitudes of the residual-mean meridional circulation. Correspondingly, stronger circulations can be expected in the WN2T setup with $p_{T_w} = 400$ hPa and $\gamma = 2$ K km $^{-1}$ as well as in the WN2H setup compared to the WN2T setup with $p_{T_w} = 100$ hPa and $\gamma = 4$ K km $^{-1}$.

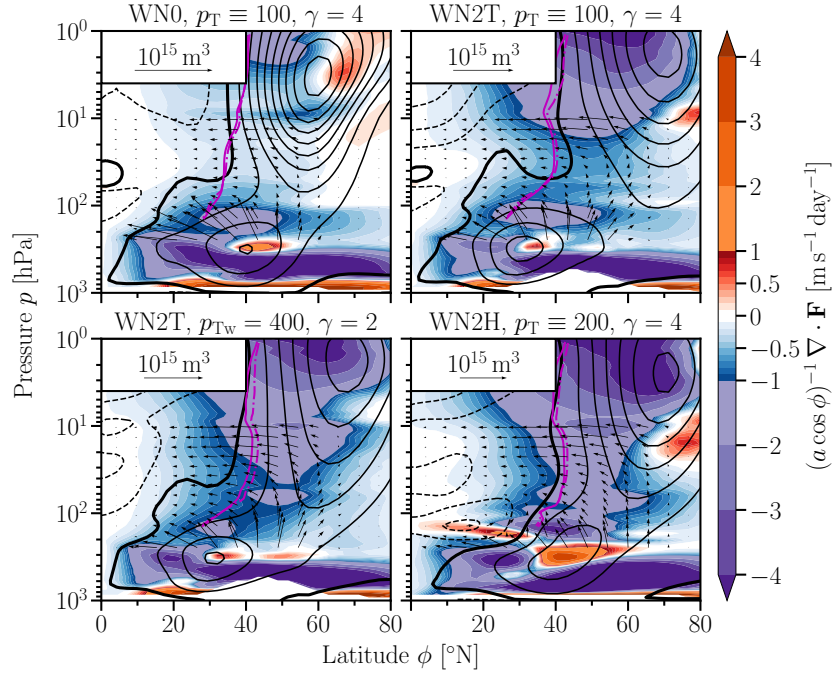


Figure 3.5: Tendencies of the zonal-mean zonal wind by the Eliassen–Palm (EP) flux divergence $(a \cos \phi)^{-1} \nabla \cdot \mathbf{F}$ (color shading), EP flux arrows $\hat{\mathbf{F}} = (\hat{F}(\phi), \hat{F}(p))$ (arrows) and zonal-mean zonal winds (black contour lines with a contour interval of 10 m s^{-1} , negative contours dashed, thick zero-contour line) as functions of latitude and pressure for the simulations presented in Fig. 3.2. EP flux arrows are defined as $(\hat{F}(\phi), \hat{F}(p)) = 2\pi a g^{-1} \cos \phi (F(\phi), aF(p)/(-80.4 \text{ kPa}))$ according to Edmon et al. (1980). The solid and dash-dotted magenta lines represent the turnaround latitudes of the residual-mean meridional circulation Ψ^* and the downward-control circulation Ψ_{dc}^* , respectively (Haynes et al., 1991; McLandress and Shepherd, 2009).

Apart from the troposphere close to the surface, the tropospheric jet core at 300 hPa is one of few regions with positive EPFD corresponding to wave generation. In the WN2H setup, this region of wave generation within the tropospheric jet core is particularly pronounced compared to the WN0 and WN2T setups. The wave-like heating centered at 45°N and 500 hPa in the WN2H setup represents an unrealistically strong source of planetary-scale waves in the upper troposphere causing the deformed shape and the fixed position of the tropospheric jet around 40°N . As will be shown in Sec. 3.4, the influence of the stratospheric polar vortex on the troposphere is inhibited in the WN2H setup.

Regions of the meridional plane that are accessible for propagating Rossby waves of phase speed c and wavenumber k can be inferred from the refractive index squared $n_{c,k}^2$. In general, wave-like solutions of the QG potential vorticity equation exist for $n_{c,k}^2 > 0$, whereas regions of wave evanescence are determined by $n_{c,k}^2 < 0$. Due to the employed wavenumber-2 forcings of topography or heating, wavenumber 2 dominates the planetary-scale wave spectrum in the WN2T and WN2H setups. As planetary-scale waves can be approximated to be stationary in most cases (see Dickinson, 1968, and references therein), $n_{c=0,k=2}^2$ is shown in Fig. 3.6

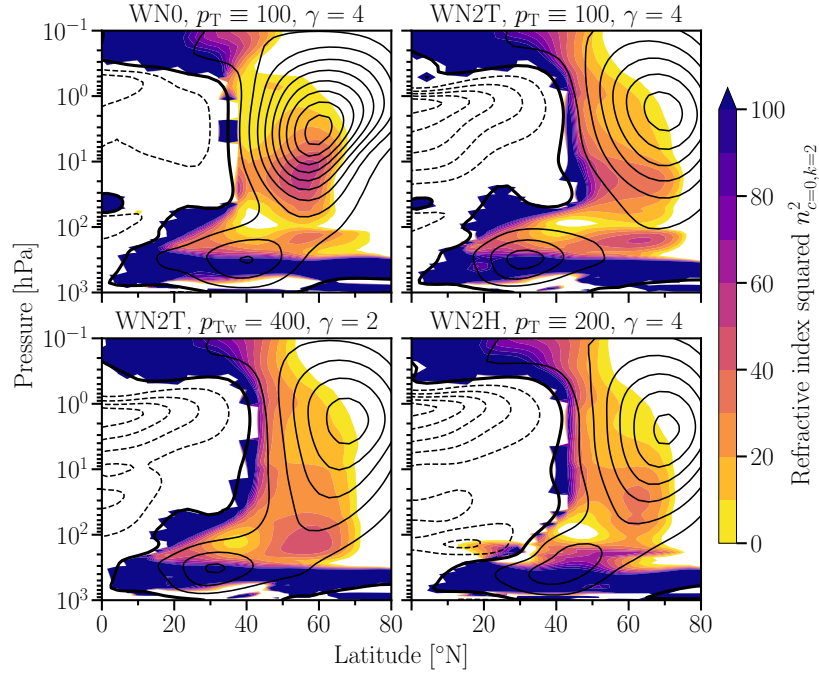


Figure 3.6: Refractive index squared $n_{c=0,k=2}^2$ for stationary waves of wavenumber 2 (color shading with a contour interval of 10) and zonal-mean zonal wind (black contour lines with a contour interval of 10 m s^{-1} , negative contours dashed, thick zero-contour line) as functions of latitude and pressure for the simulations presented in Fig. 3.2.

for the four idealized model setups. The WN0 setup is characterized by a narrow region of weakly positive $n_{c=0,k=2}^2$ at 100 hPa between 50°N and 60°N which is consistent with the weak generation of planetary-scale waves. The WN2T setup with $p_{\text{TW}} = 100 \text{ hPa}$ and $\gamma = 4 \text{ K km}^{-1}$ retains the shallow layer of weakly positive $n_{c=0,k=2}^2$ at 100 hPa, but increases its width toward 70°N corresponding to stronger upward wavenumber-2 fluxes. When the winter-hemispheric transition pressure is increased to $p_{\text{TW}} = 400 \text{ hPa}$, the structure of the circulation in the mid- to high-latitude UTLS region promotes higher values of $n_{c=0,k=2}^2$ consistent with even stronger upward wavenumber-2 fluxes in the topographically forced WN2T setup.

The thermally forced WN2H setup exhibits a positive mid- to high-latitude refractive index squared at 100 hPa with latitudinal extent. The region of negative $n_{c,k}^2$ above the tropospheric jet should, in principle, impede the propagation of wave fluxes. The concept of $n_{c,k}^2$ is, however, based on linear and adiabatic approximations and thus contains limitations which are certainly violated by the thermal generation of planetary-scale waves in the upper troposphere. Furthermore, a small region in the subtropical upper troposphere shows a positive refractive index squared despite a negative zonal-mean zonal wind, implying a negative meridional QG potential vorticity gradient in that region which is subject to strong wave generation. Therefore, the WN2H setup is not recommended to investigate the dynamical coupling of the stratosphere and troposphere in idealized models.

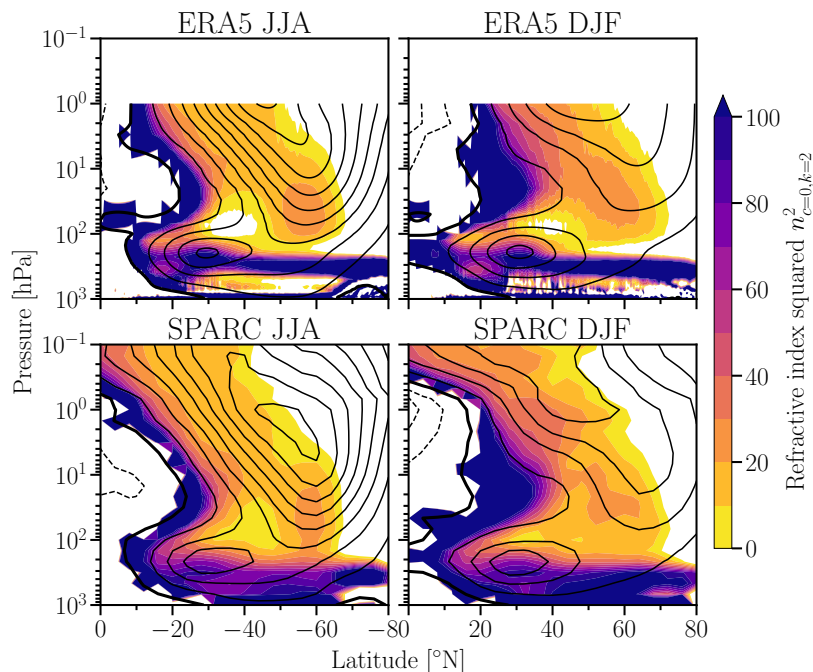


Figure 3.7: Refractive index squared $n_{c=0,k=2}^2$ for stationary waves of wavenumber 2 (color shading with a contour interval of 10) and zonal-mean zonal wind (black contour lines with a contour interval of 10 m s^{-1} , negative contours dashed, thick zero-contour line) as functions of latitude and pressure for the ERA5 (top) and SPARC (bottom) climatology for JJA (left) and DJF (right).

In contrast to idealized-model setups, both the southern-hemispheric JJA and the northern-hemispheric DJF stratospheric polar vortex of ERA5 and SPARC data sets are equatorward tilted with height as shown in Fig. 3.7, which might be due to the presence of gravity waves (Scaife et al., 2002), ozone or other processes. The equatorward tilt of the mean flow might be associated with stronger equatorward refraction of wave activity in the meridional plane compared to idealized model setups which exhibit a more vertically aligned mean flow. It is therefore difficult to determine which setup is more realistic in terms of theoretical wave propagation.

In summary, the WN0 setup is a good representation of the southern-hemispheric polar vortex regarding both mean strength and variability. Both the WN2T and WN2H setups with increased variability and reduced mean strength can approximate the polar vortex of the northern hemisphere. The dynamical coupling in the atmosphere is, however, certainly constricted in the WN2H setup. Nevertheless, all idealized-model setups lack a realistic geometry of the waveguide for planetary-scale waves. The fact that these simple-model setups are not able to precisely reproduce Earth’s general circulation is firstly not surprising due to the highly idealized physics at work and secondly not important for the aims of this thesis. On purpose, processes affecting temperature and wind have been replaced by Newtonian cooling and Rayleigh friction, respectively, to be left with the dry, atmospheric flow on Earth. Highlighting an opposing approach to understanding climate change than complex climate-model

activities (Taylor et al., 2012; Eyring et al., 2016), idealized models offer the possibility to reveal dynamical mechanisms which is usually refused in complex models. In the following section, the circulation response to various winter-hemispheric transition pressures and polar vortex lapse rates is investigated for the WN2T setup.

3.3 Nonlinear circulation response to polar stratospheric cooling

The parameter space of the topographically forced WN2T setup is explored by a large set of simulations with the winter-hemispheric transition pressure p_{Tw} ranging from 100 to 450 hPa in steps of 50 hPa and with polar vortex lapse rates γ of 1, 2, 3, and 4 K km⁻¹. Additional simulations with $\gamma = 1.5$ K km⁻¹ and $\gamma = 2.5$ K km⁻¹ were performed for the case of $p_{\text{Tw}} = 400$ hPa. In order to reduce the amount of data, simulations were integrated for 5 years only. Furthermore, a reduced value of $\delta_z = 4.3$ K is employed in this section. As displayed in Fig. 3.8, the simulations introduced above reveal the possibility of nonlinear circulation changes in response to increases of p_{Tw} and γ . First of all, latitudinal position of the tropospheric jet and polar vortex strength in the WN2T setup confirm the well-known correlation (left and middle top panels of Fig. 3.8, respectively). In the climatological mean, a strong stratospheric polar vortex is accompanied by a poleward shifted tropospheric jet (e.g., Baldwin and Dunkerton, 1999; Kidston et al., 2015). For either fixed low transition pressures of $p_{\text{Tw}} \leq 150$ hPa or fixed small polar vortex lapse rates of $\gamma \leq 1.5$ K km⁻¹, however, the tropospheric jet remains unaffected around 30°N despite small changes of the polar vortex strength for increasing γ . A parameter-dependent threshold of the polar vortex strength is necessary to shift the tropospheric jet poleward, indicated by the low- p_{Tw} and small- γ boundaries of the region surrounded by a dashed line. This nonlinear-response domain is chosen to mark the region of RC weakening in the lower stratosphere and the presence of a localized maximum of the RC strength in the upper stratosphere (bottom and top right panels of Fig. 3.8, respectively).

In the bottom and left areas outside the nonlinear-response domain, an increase in p_{Tw} leads to an acceleration of the lower stratospheric RC due to enhanced wave driving consistent with an improved waveguide in the lower stratosphere as previously shown in Figs 3.5 and 3.6. The improvement of the waveguide is caused by a reduction of negative $n_{c=0,k=2}^2$ within the midlatitude lower stratosphere (bottom left panel of Fig. 3.8). Likewise, an increase in γ leads to an acceleration of the mid-stratospheric RC. The process of positive $n_{c=0,k=2}^2$ filling the midlatitude lower stratosphere is visualized in Fig. 3.9. Starting from $p_{\text{Tw}} = 100$ hPa and $\gamma = 1$ K km⁻¹, both increases in p_{Tw} and γ represent a strengthening of the meridional equilibrium-temperature gradient which is, in principle, associated with higher zonal-wind speeds of the polar vortex. In the bottom and left areas outside the nonlinear-dynamics domain, however, the corresponding strengthening of the RC attenuates the imposed meridional temperature

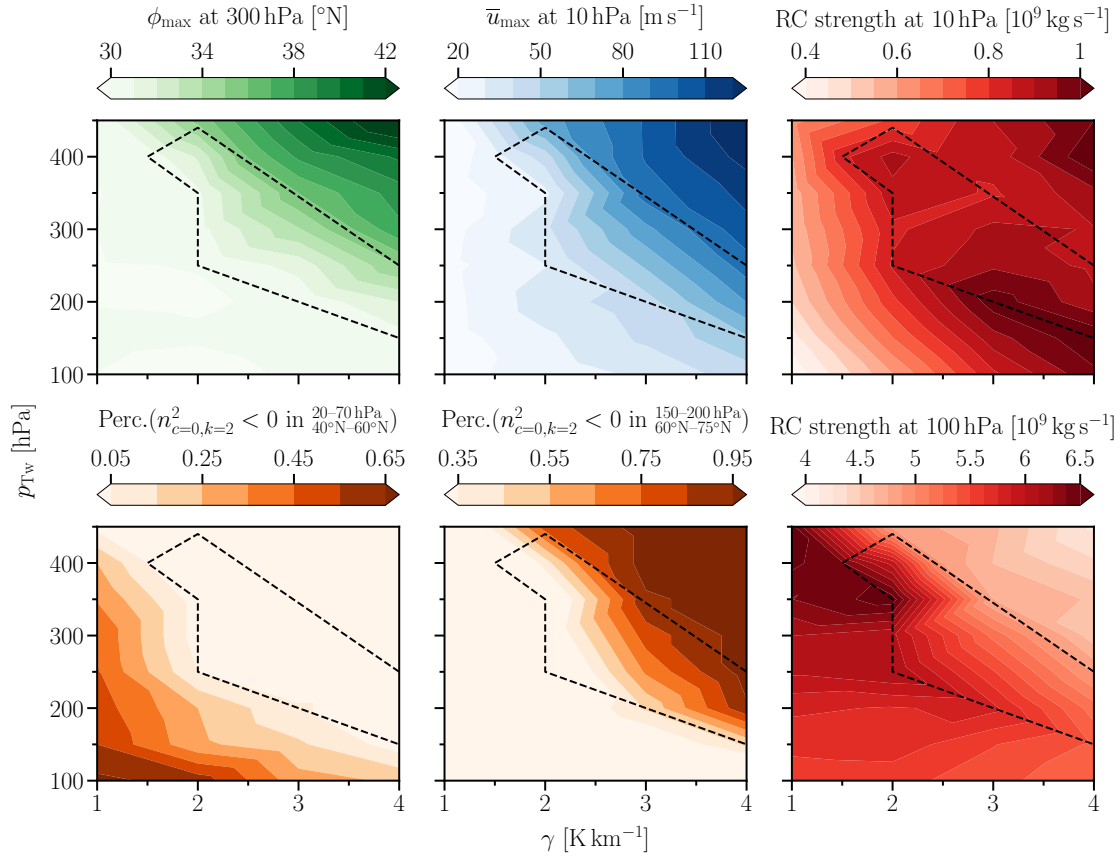


Figure 3.8: Latitude ϕ_{\max} of the maximum zonal-mean zonal wind at 300 hPa (top left), strength \bar{u}_{\max} of the maximum zonal-mean zonal wind at 10 hPa (top center), residual circulation strength at 10 hPa (top right) and at 100 hPa (bottom right), as well as the percentages of grid points with negative refractive index squared for stationary waves of wavenumber 2 in the regions of 40°N–60°N and 20–70 hPa (bottom left) as well as 60°N–75°N and 150–200 hPa (bottom center) as functions of the polar vortex lapse rate γ and the equilibrium-temperature transition pressure p_{Tw} in the polar winter hemisphere for WN2T simulations with $\delta_z = 4.3$ K integrated for 5 years. The dashed black contour line approximately encloses the domain of nonlinear dynamics.

gradient and prevents the polar vortex strength from a considerable increase (Garny et al., 2020).

Entering nonlinear circulation changes for $p_{Tw} > 150$ hPa and $\gamma > 1.5$ K km⁻¹, the lower-stratospheric RC weakens which is consistent with faster increases of the polar vortex strength and a poleward shift of the tropospheric jet. The mid-stratospheric RC keeps strengthening until the high-latitude lower stratosphere is occupied by a sufficient percentage of negative refractive index squared (bottom middle panel of Fig. 3.8), developing a confined waveguide for wavenumber-2 waves similar to the WN0 setup of Polvani and Kushner (2002) with reduced stratospheric wave driving (Figs 3.5 and 3.6). Simultaneously employing high values of p_{Tw} and γ is necessary to develop the polar lower-stratospheric region of wave evanescence as shown in the bottom middle panel of Fig. 3.8 and visualized in Fig. 3.9. For extremely high

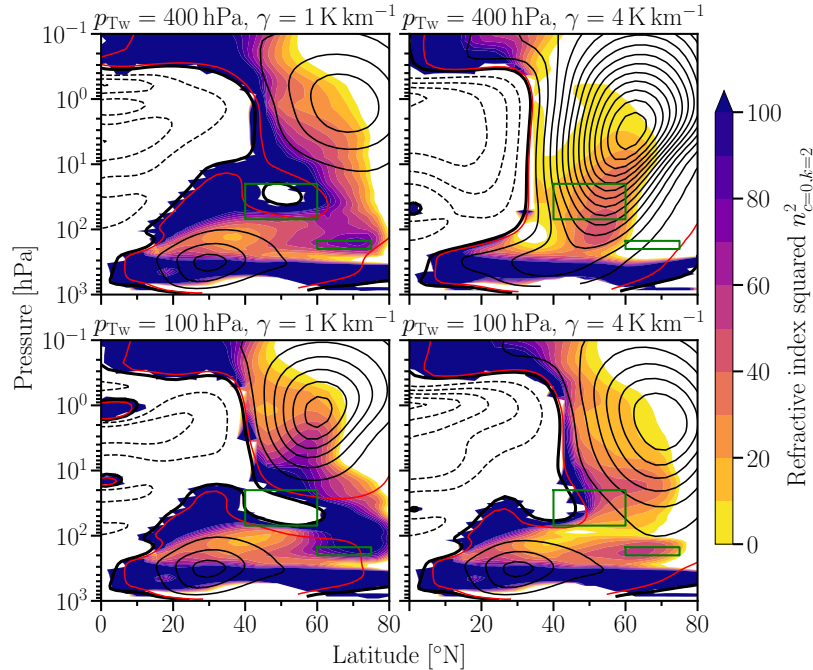


Figure 3.9: Refractive index squared $n_{c=0,k=2}^2$ for stationary waves of wavenumber 2 (color shading with a contour interval of 10) and zonal-mean zonal wind (black contour lines with a contour interval of 10 m s^{-1} , negative contours dashed, thick zero-contour line) as functions of latitude and pressure for 5-year integrated WN2T simulations employing $\delta_z = 4.3 \text{ K}$ with $p_{\text{Tw}} = 400 \text{ hPa}$ and $\gamma = 1 \text{ K km}^{-1}$ (top left), $p_{\text{Tw}} = 400 \text{ hPa}$ and $\gamma = 4 \text{ K km}^{-1}$ (top right), $p_{\text{Tw}} = 100 \text{ hPa}$ and $\gamma = 1 \text{ K km}^{-1}$ (bottom left), and $p_{\text{Tw}} = 100 \text{ hPa}$ and $\gamma = 4 \text{ K km}^{-1}$ (bottom right) representing the boundaries of the investigated parameter space. The regions in the midlatitude lower stratosphere and in the polar lower stratosphere for which percentages of $n_{c=0,k=2}^2 < 0$ are shown in Fig. 3.8 are added as green boxes. The red contour line indicates a zonal-mean zonal wind of 2 m s^{-1} .

p_{Tw} and γ , the mid-stratospheric RC strengthens again, and the polar vortex strengthening and the poleward movement of the tropospheric jet proceed jointly.

Due to the large number of parameter combinations consulted in this section, every simulation has been integrated for 5 years only.¹⁰ In order to provide robust insights into the dynamical mechanism responsible for the nonlinear circulation response to polar stratospheric cooling, selected simulations are extended to cover 30 years in the following section. The longer integration enables the reliable computation of autocorrelation time scales which will provide evidence for the existence of two distinct dynamical regimes (Scheffer et al., 2009; Chan and Plumb, 2009; Wang et al., 2012).

¹⁰The fact that simulation lengths of the idealized model EMIL are specified in years does not imply that different seasons are present. The equilibrium temperatures employed in this thesis are always time-independent and represent perpetual-mid winter conditions.

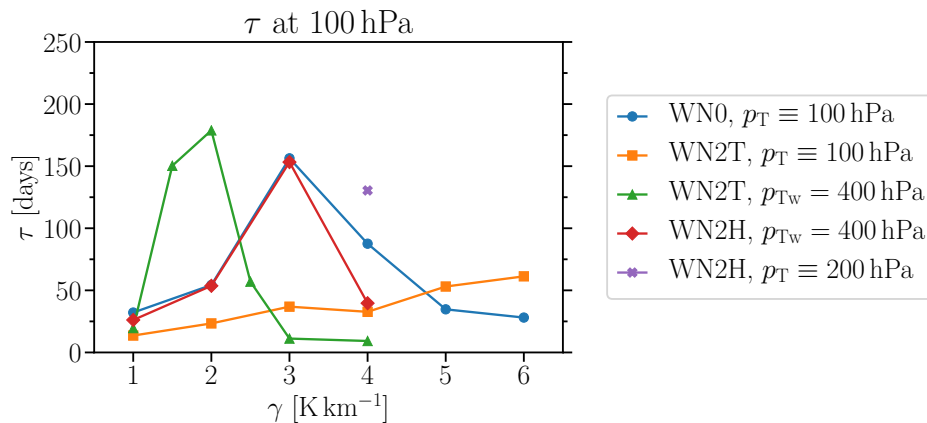


Figure 3.10: Autocorrelation time scale τ at 100 hPa as function of the polar vortex lapse rate γ for 30-year simulations with zonally symmetric surface conditions (WN0), with wavenumber-2 topography (WN2T), and with wavenumber-2 heating (WN2H) employing $\delta_z = 10$ K.

3.4 Discussion of the relevant dynamical mechanism

In the previous section, the transition of climate states from a weak to a strong polar vortex accompanied by a weakening of the residual circulation has been observed in response to polar-stratospheric cooling. One indication of a dynamical system undergoing a regime transition is a peaked autocorrelation time scale τ (Scheffer et al., 2009; Wang et al., 2012). An investigation of τ should therefore expose possible dynamical regime transitions. To this end, τ is displayed in Fig. 3.10 as a function of γ for the WN2T setups with $p_{Tw} = 100$ hPa and $p_{Tw} = 400$ hPa. In the former setup, no nonlinear dynamics has been observed in the previous section, whereas it has in the latter setup. The Polvani and Kushner (2002)-setup with WN0 as well as WN2H setups with $p_{Tw} = 400$ hPa and with $p_T \equiv 200$ hPa representing the Lindgren et al. (2018) setup have been added to Fig. 3.10. Indeed, the WN2T Gerber and Polvani (2009)-setup with $p_{Tw} = 100$ hPa is not subject to a regime transition. In this case, τ increases almost linearly up to 70 days for $\gamma = 6$ K km⁻¹. Higher values of the polar vortex lapse rate γ could in principle trigger a regime transition. The consequentially extreme meridional gradients of the equilibrium temperature in the polar stratosphere would, however, pose numerical instabilities. All other setups exhibit clear peaks in the autocorrelation time scale hinting at regime transitions. In spite of only one available data point for the Lindgren et al. (2018)-setup, enhanced autocorrelation is observed. Time scales of the northern and southern annular modes at 100 hPa reach values of up to 30 and 60 days during winter seasons, respectively (Baldwin et al., 2003).

The polar vortex strength in the WN0 Polvani and Kushner (2002)-setup increases linearly with γ and the shape of the probability density function of \bar{u}_{\max} at 10 hPa is conserved except for $\gamma = 1$ K km⁻¹ as shown in Fig. 3.11. Only the minimum polar vortex strength experiences a pronounced increase from $\gamma = 3$ K km⁻¹ to $\gamma = 4$ K km⁻¹ which is accompanied by an

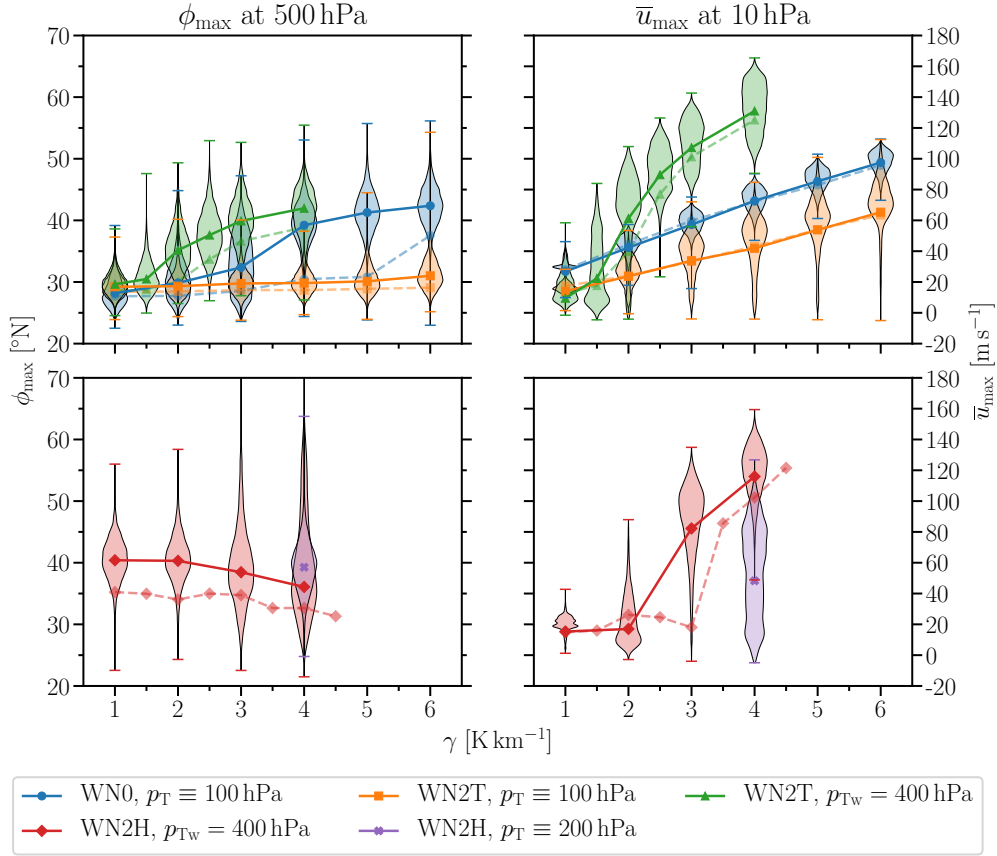


Figure 3.11: Latitude ϕ_{\max} of the maximum zonal-mean zonal wind at 500 hPa (left) and strength \bar{u}_{\max} of the maximum zonal-mean zonal wind at 10 hPa (right) as functions of γ for WN0 (top), WN2T (top), and WN2H (bottom) simulations. Similar to Fig. 3.4, colored markers display values of ϕ_{\max} and \bar{u}_{\max} that are computed from the climatological-mean zonal-mean zonal winds, whereas the shapes of probability density functions (PDFs, colored shadings) are based on values of ϕ_{\max} and \bar{u}_{\max} that are computed for every time step first. PDFs and nontransparent markers connected by nontransparent solid lines represent the 30-year simulations employing $\delta_z = 10$ K shown in Fig. 3.10, whereas transparent markers connected by transparent dashed lines represent simulations employing $\delta_z = 4.3$ K.

enhanced poleward shift of the tropospheric jet at 500 hPa from 30°N to 40°N . Employing the wavenumber-2 topography for otherwise identical parameters reduces the climatological-mean polar vortex strength and leads to larger variability as well as to the formation of SSWs that are present up to $\gamma = 6 \text{ K km}^{-1}$. In contrast to the WN0 setup, the tropospheric jet remains at a constant latitude around 30°N . When p_{Tw} is raised to 400 hPa, the WN2T setup exhibits a regime transition from a weak polar vortex at $\gamma = 1.5 \text{ K km}^{-1}$ with frequent SSWs to a strong polar vortex at $\gamma = 2.5 \text{ K km}^{-1}$ where SSWs are absent. The corresponding poleward shift of the tropospheric jet proceeds fastest around the strongest polar vortex increases. A similar polar vortex regime transition is observed in the WN2H setup with $p_{\text{Tw}} = 400$ hPa. The accompanied poleward shift of the tropospheric jet, however, never happens. On the contrary, the maximum zonal-mean zonal wind at 500 hPa moves equatorward. Reducing the tropical

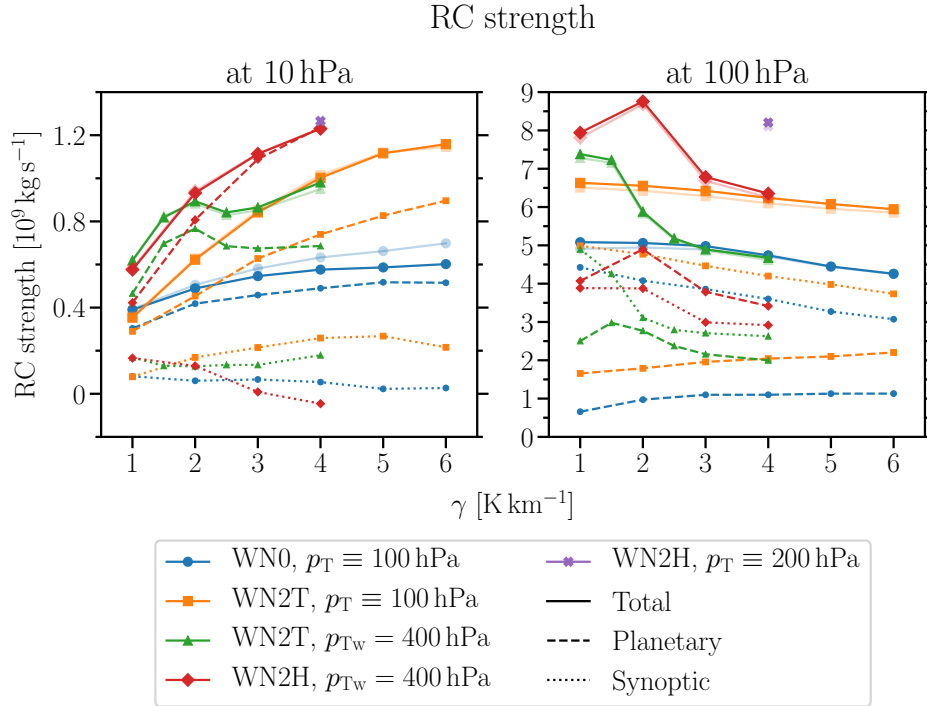


Figure 3.12: Residual circulation (RC) strength at 10 hPa (left) and 100 hPa (right) as function of the polar vortex lapse rate γ for the simulations presented in Fig. 3.10. The strength of the RC is based on the downward control streamfunction Ψ_{dc}^* given in Eq. (2.18) and computed via $\max(\Psi_{dc}^*) + |\min(\Psi_{dc}^*)|$ which allows to determine contributions from planetary- (dashed) and synoptic-scale (dotted) EPFD. Transparent markers connected by transparent solid lines representing the total upward mass flux \mathcal{M} between the turnaround latitudes given in Eq. (2.20) are added for comparison.

stratification δ_z from 10 K to 4.3 K (see Fig. 2.2) leads to an equatorward contraction of the tropospheric jets in all setups. In case of the setups with $p_{T_w} = 400$ hPa, the equatorward shifted tropospheric jets delay the polar vortex regime transitions compared to the setups with $\delta_z = 10$ K. In case of the WN0 and WN2T setup with $p_{T_w} = 100$ hPa, the reduction of δ_z has no effect on the polar vortex hinting at a weaker stratosphere-troposphere coupling.

The linear increase of the polar vortex strength with γ in the setups with $p_{T_w} = 100$ hPa improves the waveguide for planetary-scale waves. Hence, planetary-scale wave flux increases in the entire stratosphere which is consistent with growing planetary-scale contributions to the RC strength at 10 and 100 hPa as shown in Fig. 3.12. In the upper stratosphere where planetary-scale wave flux prevails, this is transferred to a strengthening of the total RC. In contrast to this, the total lower-stratospheric RC weakens, possibly due to a stronger mean flow that inhibits synoptic-scale contributions to the lower-stratospheric RC. Only in case of the WN2H setup, planetary-scale contributions to the RC strength exceed synoptic-scale contributions also in the lower stratosphere which might be due to the pronounced planetary-scale wave generation in the upper troposphere. Both setups with $p_{T_w} = 400$ hPa exhibit a nonlinear behavior of the lower-stratospheric RC strength with a sharp decrease at the

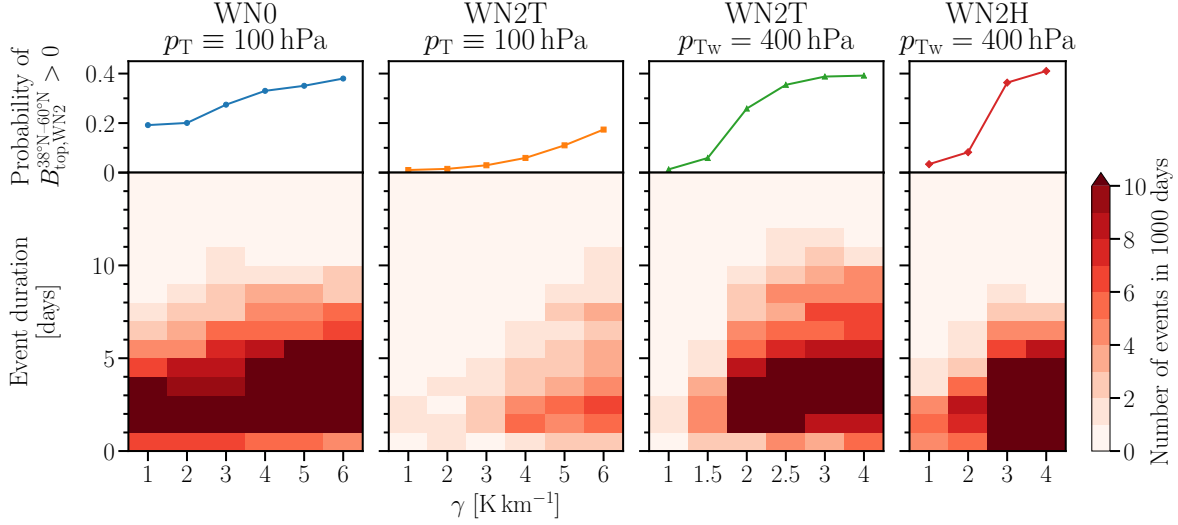


Figure 3.13: Probability of positive $B_{\text{top,WN2}}^{38^{\circ}\text{N}-60^{\circ}\text{N}}$, i.e. downward wavenumber-2 (WN2) Eliassen–Palm (EP) flux at 100 hPa integrated from 38°N to 60°N (top panels), as well as the number of events of downward $B_{\text{top,WN2}}^{38^{\circ}\text{N}-60^{\circ}\text{N}}$ as a function of the polar vortex lapse rate γ and the event duration (bottom panels) for 30-year simulations of the polar stratospheric cooling experiments with WN0 and $p_T \equiv 100$ hPa, with WN2T and $p_T \equiv 100$ hPa, with WN2T and $p_{T_w} = 400$ hPa, and with WN2H and $p_{T_w} = 400$ hPa (from left to right) employing $\delta_z = 10$ K. An event of the duration of l days is defined to require $B_{\text{top,WN2}}^{38^{\circ}\text{N}-60^{\circ}\text{N}} > 0$ for l consecutive days. Note that with pressure as vertical coordinate, positive wave flux points downward.

transition from a weak to a strong polar vortex. The nonlinearity of the RC strength extends to the upper stratosphere in case of the WN2T setup, but disappears in the WN2H setup. The poleward shift of the tropospheric jet in the WN2T setup is consistent with wave activity that is refracted away from the stratosphere. The lack of the poleward shift of the tropospheric jet in the WN2H setup instead supports a uniform strengthening of the upper-stratospheric RC.

The reorganization of planetary-scale wave flux characterizing the polar vortex regime transition in the setups with $p_{T_w} = 400$ hPa can be explained by investigating the statistics of downward wavenumber-2 wave flux events presented in Fig. 3.13. Accordingly, the sharp strengthening of the polar vortex and the simultaneous weakening of the lower-stratospheric RC are associated with a leap in the frequency of downward wavenumber-2 flux in the mid- to high-latitude lower stratosphere (top panels) caused by more and longer downward flux events (bottom panels). In the WN0 setup, the probability of downward wavenumber-2 fluxes for small polar vortex lapse rates of $\gamma \leq 2 \text{ K km}^{-1}$ is already one fifth and almost reaches two fifth at $\gamma = 6 \text{ K km}^{-1}$. In contrast to the setups with $p_{T_w} = 400$ hPa, even at small γ a large number of downward flux events with a duration of up to 5 days occurs in the WN0 setup. In the WN2T setup with $p_{T_w} = 100$ hPa no sharp, but a continuous increase of the probability for downward wavenumber-2 flux is observed, consistent with the absence of a

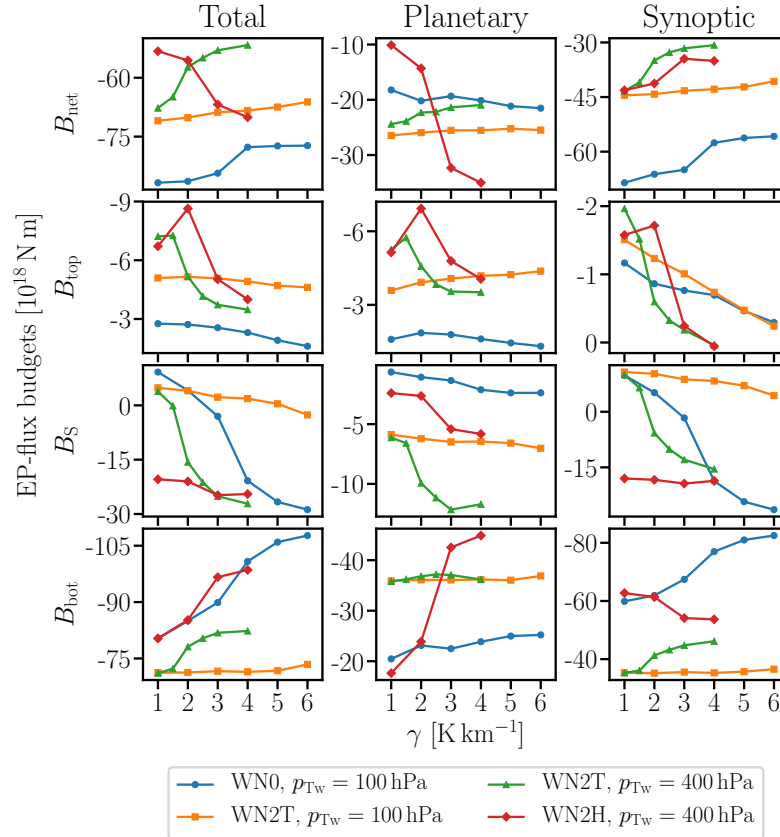


Figure 3.14: Total (left column), planetary- (middle column) and synoptic-scale (right column) net Eliassen–Palm (EP) flux budgets B_{net} (first row) as well as the EP flux components B_{top} (second row), B_{S} (third row), and B_{bot} (fourth row) associated with the extratropical upper-tropospheric area defined between Eqs. (2.16) and (2.17) as functions of the polar vortex lapse rate γ for 30-year simulations of the polar stratospheric cooling experiments with WN0 and $p_{\text{TW}} \equiv 100$ hPa, with WN2T and $p_{\text{T}} \equiv 100$ hPa, with WN2T and $p_{\text{TW}} = 400$ hPa, and with WN2H and $p_{\text{TW}} = 400$ hPa employing $\delta_z = 10$ K. Negative B_{top} and B_{bot} denote upward EP flux components, negative B_{S} denotes southward EP flux component and negative B_{net} denotes EP flux budget that is lost inside the area.

regime transition. The maximum duration of downward flux events exhibits a linear rise with γ , but the frequency of which remains at low levels.

Investigating the refractive index squared for stationary wavenumber-2 waves reveals that the waveguide changes its geometry in the setups with $p_{\text{TW}} = 400$ hPa during the regime transition (not shown). In the weak polar vortex regime, a latitudinally broad waveguide with access to the upper stratosphere favors upward propagation of planetary-scale waves. In the strong polar vortex regime, however, a waveguide with geometry similar to the top left panel in Fig. 3.6 is developed. The marked horizontal zero-line of the refractive index squared in the upper stratosphere likely represents a reflecting surface (Harnik and Lindzen, 2001). In the WN0 setup, the reflecting surface at the top of the stratosphere is omnipresent and already formed at $\gamma = 1 \text{ K km}^{-1}$. In addition, the waveguide is meridionally confined by negative

refractive index squared on both the pole- and equatorward side of the polar vortex (Shaw et al., 2010). Under these circumstances, so-called downward wave coupling events arise. Upward propagating planetary-scale waves are reflected at the top of the polar vortex and are guided back to the troposphere without the possibility to dissipate within the stratosphere. In the troposphere, the reflected wave activity is refracted equatorward which is consistent with a poleward shift of the tropospheric jet (Perlwitz and Graf, 2001; Shaw and Perlwitz, 2013).

The evolution of corresponding wave activity fluxes is presented in Fig. 3.14 by analyzing the budget of EP fluxes that are associated with a closed area in the extratropical UTLS region extending from 100 hPa to 590 hPa and from 38°N to 90°N as introduced in Sec. 2.3.2. The increase in total B_{net} observed in the WN0 setup as well as in the WN2T setup with $p_{\text{Tw}} = 400$ hPa represents a decrease of wave dissipation inside the closed area which is consistent with the poleward shift of their corresponding tropospheric jets gradually penetrating the closed area from the equatorward boundary. Analogously, the decrease in total B_{net} observed in the WN2H setup is consistent with the tropospheric jet shifting equatorward. In both setups with $p_{\text{Tw}} = 400$ hPa, planetary-scale wave flux decreases to propagate upward at 100 hPa and simultaneously increases to propagate equatorward at 38°N when the number of downward wave flux events sharply rises consistent with a weakening of the lower-stratospheric RC, a strengthening of the polar vortex, and a poleward shift of the tropospheric jet—hinting at downward wave coupling. In the WN0 setup, upward propagating planetary-scale wave fluxes at 100 hPa are approximately half as strong as in the setups with $p_{\text{Tw}} = 400$ hPa and, on top of that, do not show any sharp changes during the enhanced poleward shift of the tropospheric jet. Instead, the enhanced tropospheric jet shift in the WN0 setup is only reflected in a reorganization of synoptic-scale B_{S} which changes from pole- to equatorward. The strongly equatorward and constant synoptic-scale wave flux in the WN2H setup can be associated with the far poleward located tropospheric jet and suppresses planetary-scale contributions that could be associated with any additional tropospheric jet shift. For the increasing amount of planetary-scale wave flux from the bottom that is prevented from dissipating in the upper stratosphere consistent with the increased number of downward wave flux events, only the dissipation inside the closed area remains possible due to the frozen position of the tropospheric jet.

3.5 Conclusions

Idealized models with Polvani and Kushner (2002)-type equilibrium temperatures are able to reproduce relevant features of winter-climate states of the northern and southern hemisphere. Setups without additional zonal asymmetries can be used to study the stronger and stable stratospheric polar vortex in the southern hemisphere (Polvani and Kushner, 2002). Setups with topographically or thermally forced planetary-scale waves can incorporate SSWs asso-

ciated with the weaker polar vortex of the northern hemisphere (Gerber and Polvani, 2009; Lindgren et al., 2018). Nevertheless, the idealized physics at work leads to deficiencies in the thermal structure, especially in the convection-dominated tropical troposphere. Also the polar vortex in the dry stratosphere deviates from reality. More realistic circulations can be induced by equilibrium temperatures that are based on observations (Jucker et al., 2013) or by employing realistic topography and zonally varying equilibrium temperatures (Wu and Reichler, 2018). For the purposes of this thesis, the equilibrium temperature of Polvani and Kushner (2002) available in EMIL—augmented by a latitudinally varying pressure for the transition from tropospheric to stratospheric schemes—is sufficient.

Lowering the height at which a temperature decrease marks the onset of the polar vortex in the winter-hemispheric stratosphere, i.e., increasing p_{Tw} , leads to more realistic temperatures in the extratropical UTLS region, but contains the possibility of a regime transition from a weak and variable to a strong and stable polar vortex for $p_{\text{Tw}} > 150$ hPa. Consistently, the RC weakens during the regime transition. In the topographically forced setups the regime transition is accompanied by an enhanced poleward shift of the tropospheric jet. In the thermally forced setup, the tropospheric jet is more stable regarding its latitudinal position and even moves slightly equatorward. The reason for this unusual stratosphere-troposphere coupling might be the strong generation of wave flux in the mid-latitude upper troposphere, keeping the tropospheric jet in a fixed latitudinal position.

The waveguide that is developed during the transition to the strong polar vortex regime exhibits a horizontally aligned reflecting surface at the top of the stratosphere as well as a narrow meridional extent. Such a configuration has been identified to lead to downward wave coupling events where upward propagating planetary-scale waves are reflected at the top of the stratosphere (Perlwitz and Harnik, 2003; Shaw et al., 2010). The meridionally narrow waveguide prevents reflected waves from dissipating within the stratosphere and leads them back to the troposphere where they are refracted equatorward. These downward wave coupling events are consistent with a strong polar vortex and a poleward shifted tropospheric jet. Therefore, the results of this chapter provide strong evidence that downward wave coupling dominates the strong polar vortex regime during the performed idealized polar-stratospheric cooling experiments. For winter-hemispheric transition pressures of $p_{\text{Tw}} \leq 150$ hPa, the polar vortex does not undergo a regime transition even for very high polar vortex lapse rates. Figs. 3.8 and 3.9 suggest that the polar vortex does not shift sufficiently equatorward to establish the confined geometry of the waveguide. Sec. 5.1 provides an explanation why this is the case.

Regarding the specific research question **S1**, the extratropical lower stratosphere controls the dynamical coupling of the stratosphere and troposphere via the characteristics of the waveguide for planetary scale waves in this region (Chen and Robinson, 1992). As long as the waveguide is interrupted by regions of negative refractive index squared, upward propagating planetary-

scale waves are subject to dissipate in the lower stratosphere, driving the residual circulation. Moderate increases in the meridional temperature gradient improve the waveguide, but the increasing wave flux drives a stronger residual circulation which prevents the polar vortex from considerable amplifications. Accordingly, the tropospheric circulation does not change significantly. Only if the waveguide enables downward wave coupling events associated with the strong polar vortex regime described above, a poleward shift of the tropospheric jet and a weakened residual circulation are observed.

This chapter revealed the significant influence of the stratosphere on the troposphere described by the waveguide for planetary-scale waves. In the following chapter, the question is covered whether these stratospheric circulation changes that led to the observed tropospheric impacts can be induced by forcings within troposphere, in particular by climate change-like temperature increases. In other words, can tropospheric circulation changes induce a confined geometry of the waveguide for planetary-scale waves?

Chapter 4

Stratospheric modulation of TUTW-induced circulation changes

Large parts of this chapter have been submitted for publication in

Walz, R., Garny, H., and Birner, T. Stratospheric Modulation of Tropical Upper-Tropospheric Warming-Induced Circulation Changes in an Idealized General Circulation Model. *Journal of the Atmospheric Sciences*, in review,

and therefore contain literal excerpts.

The nonlinear circulation response to polar stratospheric cooling found in the previous chapter includes a sharp strengthening of the stratospheric polar vortex accompanied by a weakening of the residual circulation and a poleward shift of the tropospheric jet. Similar circulation changes have also been observed in idealized-model simulations that exceed a critical threshold of climate change-like tropical upper-tropospheric warming (TUTW, Wang et al., 2012). This chapter is dedicated to understand how tropospheric warming is able to trigger this nonlinear circulation response, answering the specific research question **S2**. To this end, the set of tropical upper-tropospheric warming experiments described in Sec. 2.2.2 is analyzed. Employing different stratospheric basic states including a setup without polar vortex, i.e., with passive stratosphere, the stratospheric influence on the troposphere can be quantified. At the beginning of this chapter, guiding hypotheses are formulated that help to structure the reasoning. Afterwards, the different stratospheric basic states and their respective responses to tropical upper-tropospheric warming are introduced. The rest of this chapter discusses the dynamics below the critical threshold of tropical heating and beyond, as well as the robustness of the proposed mechanism responsible for the regime transition. During the course of this chapter, the guiding hypotheses are evaluated.

4.1 Guiding hypotheses

In order to reveal the dynamical mechanism responsible for the polar vortex regime transition (PVRT) in idealized-model simulations in response to sufficiently strong TUTW as reported in Wang et al. (2012), the hypotheses laid out in the schematic displayed in Fig. 4.1 will be tested. Assuming the tropospheric response to TUTW consists of a poleward shift of the tropospheric jets with accelerated upper flanks (highlighted in red in Fig. 4.1), the following hypotheses are put forward:

1. TUTW leads to a strengthened shallow branch of the RC consistent with the critical-layer control mechanism (CLCM) in the experiments with and without polar vortex (gray boxes in Fig. 4.1, Shepherd and McLandress, 2011).
2. In presence of a polar vortex, the strengthened shallow branch of the RC influences the thermal structure of the LS resulting in an equatorward shift of the LS polar vortex (green box in Fig. 4.1, Butchart et al., 2010; Scaife et al., 2012).
3. Given the importance of the LS for stratosphere-troposphere coupling (Martineau et al., 2018), the changing thermal structure of the LS leads to a reorganization of EP fluxes at a critical TUTW level inducing a sharp strengthening of the polar vortex (blue box in Fig. 4.1, Wang et al., 2012).
4. Beyond the critical TUTW level, the increased strength of the stratospheric polar vortex leads to an enhanced poleward shift of the tropospheric jet (Polvani and Kushner, 2002; Dunn-Sigouin and Shaw, 2015; Kidston et al., 2015).

In Secs. 4.2, 4.3, and 4.4, the circulation response due to TUTW is diagnosed, and the hypotheses stated above are tested. Along the way, details of the mechanism of the PVRT are added to the green and blue boxes of the schematic in Fig. 4.1, representing the stratospheric responses during the weak and strong polar vortex regimes, respectively.

4.2 Stratospheric influence of polar vortex regimes on the tropospheric jet

The zonal-mean zonal wind control-run climatologies of the NPV, REF and CLS experiments without additional tropical upper-tropospheric heating ($q_0 = 0$) are shown in Fig. 4.2. In the winter hemisphere, tropospheric jet maxima are located at 30°N in the NPV and REF experiments as well as at 32°N in the CLS experiment, respectively. The polar vortex of the CLS experiment is weaker in the upper stratosphere, but stronger and equatorward shifted in the LS compared to the REF experiment due to the colder polar LS of the CLS experiment. By construction, there is no stratospheric polar vortex in the NPV experiment, but an additional jet appears in the tropical upper stratosphere when 90 vertical model levels are employed. In

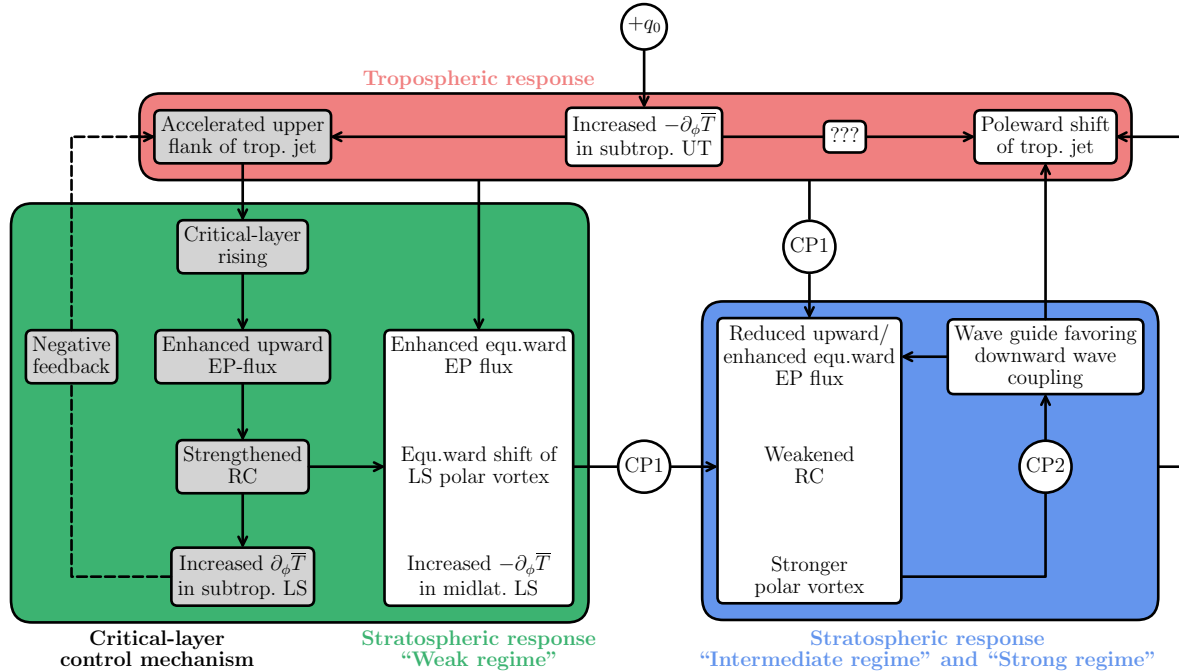


Figure 4.1: Schematic of the dynamical mechanism responsible for the regime transition from a weak to a strong polar vortex via critical points (CP1 and CP2) and the corresponding feedback on the troposphere in the idealized-model experiments with polar vortex (REF and CLS) forced by tropical upper-tropospheric heating of amplitude q_0 .

model simulations with only 47 vertical levels, no additional tropical upper-stratospheric jet is present as shown in Fig. 4.3. The existence of an additional jet in the tropical stratosphere in these idealized simulations with 90 levels might be attributed to an enhanced generation of tropical wave flux that tries to induce a quasi-biennial oscillation (Baldwin et al., 2001). Nevertheless, an influence of this additional jet on the essential parts of the discovered mechanism can be excluded when all experiments are repeated with 47 vertical levels as presented in Sec. 4.5. Therefore, differences in the circulation response to TUTW between the experiments with and without stratospheric polar vortex are interpreted to arise solely from the different conditions in the winter-hemispheric extratropical stratosphere.

In order to quantitatively capture the winter-hemispheric circulation response to thermal forcings in the TUT, latitude ϕ_{\max} and strength \bar{u}_{\max} of the maximum zonal-mean zonal wind are analyzed at pressure levels of 10, 100, 300, and 850 hPa as shown in Figs. 4.4 and 4.5 (see Sec. 2.3.1 for computational details). This reveals a close resemblance of the control-run ($q_0 = 0$) tropospheric jet positions and strengths at 300 hPa in the NPV and REF experiments. The control-run troposphere of the CLS experiment differs from the NPV and REF experiments with the tropospheric jet core at 300 hPa being weaker in the climatological mean and exhibiting a larger probability of poleward fluctuations.

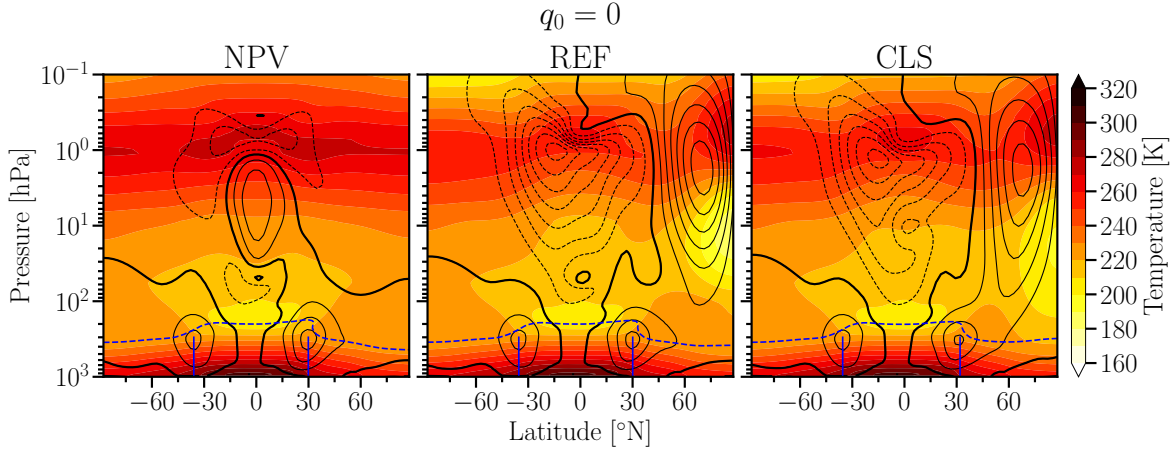


Figure 4.2: Control-run climatologies of zonal-mean zonal wind (black contour lines with a contour interval of 10 m s^{-1} , negative contours dashed, thick zero-contour line) and temperature (color shading with a contour interval of 10 K) at vanishing tropical upper-tropospheric heating ($q_0 = 0$) as functions of latitude and pressure for the experiment without polar vortex (NPV, left), the reference setup (REF, middle), and a colder polar lower stratosphere (CLS, right). The dashed blue lines denote the lapse-rate tropopause (WMO, 1957). The solid blue vertical lines show the latitudes of the zonal-mean zonal wind maxima in the troposphere.

In the stratosphere, both experiments with stratospheric polar vortex (REF and CLS) have a similar control-run climatological-mean polar vortex strength of approximately 40 m s^{-1} measured by \bar{u}_{\max} at 10 hPa , but a completely different variability. In the REF experiment, the control-run polar vortex has a zonal-mean zonal wind speed between 40 and 60 m s^{-1} most of the time with a finite, but small probability of very low wind speeds indicating SSWs. The probability density function (PDF) of \bar{u}_{\max} at 10 hPa in the CLS control run, however, is bimodal with two pronounced maxima around 10 and 70 m s^{-1} , respectively. This suggests that the polar vortex in the CLS control run exists in either a weak or a strong regime and rarely possesses its climatological mean strength of 40 m s^{-1} . In the LS, the polar vortex of the CLS experiment is located 10° more equatorward than in the REF experiment and exhibits larger mean strength and variability.

In response to increasing TUTW the tropospheric jet cores at 300 hPa move poleward in all three experiments. The major difference between the two experiments with polar vortex and the one without is the pronounced poleward shift of the tropospheric jet core occurring at the same heating amplitude as the sharp strengthening of their respective polar vortices. In the REF experiment, poleward fluctuations of the tropospheric jet start to strengthen at $q_0 = 0.3 \text{ K day}^{-1}$ compared to the NPV experiment. Simultaneously, a first increase in the polar vortex strength is visible in the REF experiment. At $q_0 = 0.35 \text{ K day}^{-1}$, poleward fluctuations of ϕ_{\max} at 300 hPa further increase, but the equatorward part of the PDF of ϕ_{\max} still overlaps to a large extent with the one from NPV. The climatological-mean polar vortex strength at $q_0 = 0.35 \text{ K day}^{-1}$ stays at the same level as at $q_0 = 0.3 \text{ K day}^{-1}$, but the

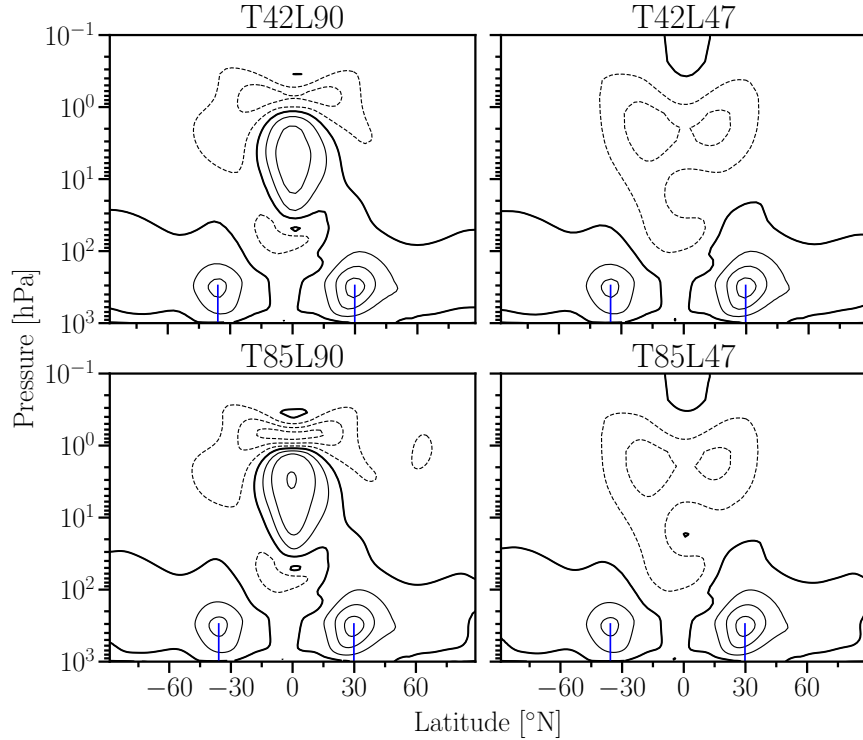


Figure 4.3: Control-run climatologies of zonal-mean zonal wind (black contour lines with a contour interval of 10 ms^{-1} , negative contours dashed, thick zero-contour line) at vanishing tropical upper-tropospheric heating ($q_0 = 0$) as functions of latitude and pressure for the experiments without polar vortex for horizontal resolutions T42 (top) and T85 (bottom), and vertical resolutions L90 (left) and L47 (right). The solid blue vertical lines show the latitudes of the zonal-mean zonal wind maxima in the troposphere.

likelihood of SSWs increases and reaches a local maximum in this climate state. The shape of the PDF of \bar{u}_{\max} at 10 hPa at $q_0 = 0.35 \text{ K day}^{-1}$ in the REF experiment is reminiscent of the CLS control run with oscillations between a weak and a strong polar vortex regime although the bimodality is by far not as pronounced as in the CLS control run. Eventually, at $q_0 = 0.4 \text{ K day}^{-1}$ the tropospheric jet core in the REF experiment has detached from the NPV experiment and experiences its strongest poleward shift for consecutive heating amplitudes. This is accompanied by a large increase of the climatological-mean polar vortex strength with highest probability for wind speeds larger than 60 ms^{-1} and a significant reduction of the likelihood of SSWs.

In the CLS experiment, the circulation response to TUTW is similar to the REF experiment, but the enhanced poleward movement of the tropospheric jet core and the accompanied PVRT happen already at smaller tropospheric heating amplitudes, from $q_0 = 0.05 \text{ K day}^{-1}$ to $q_0 = 0.1 \text{ K day}^{-1}$. This is due to the fact that the control-run climatology of the CLS experiment is already very close to the regime transition (Garny et al., 2020). The disappearance of

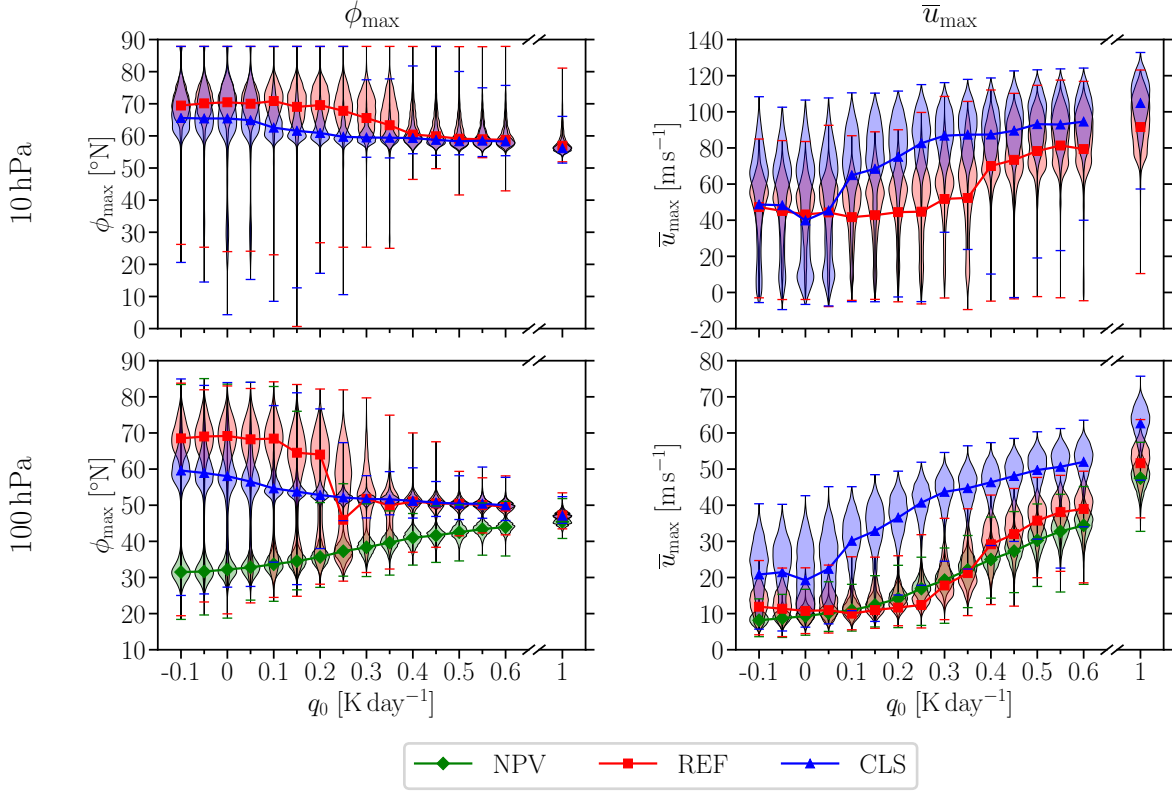


Figure 4.4: Latitude ϕ_{\max} (left) and strength \bar{u}_{\max} (right) of the maximum zonal-mean zonal wind at 10 hPa (top) and 100 hPa (bottom) as functions of the tropical upper-tropospheric heating amplitude q_0 for the experiment without polar vortex (NPV), the reference setup (REF), and a colder polar lower stratosphere (CLS). Markers display values of ϕ_{\max} and \bar{u}_{\max} that are computed from the climatological-mean zonal-mean zonal winds. Additionally, the shapes of the probability density functions (PDFs, shadings) and extreme values (horizontal lines) are provided for which ϕ_{\max} and \bar{u}_{\max} are computed for every time step first. Note that all PDFs are scaled in such a way that they have equal widths at their respective maxima and can therefore only serve for relative comparisons.

probabilities of a weak polar vortex in the CLS experiment, however, happens not as rapidly as in the REF experiment.

NPV, REF and CLS experiments performed with EMIL confirm the sharp poleward shift of the 850 hPa-jet by about 10° found in Wang et al. (2012). For weak heating amplitudes, bimodal PDFs of ϕ_{\max} at 850 hPa can be observed where the low-latitude peak is preferred in the climatological mean. Interestingly, the jump to the high-latitude peak of the PDF in the REF experiment occurs at a heating amplitude ($q_0 = 0.15 \text{ K day}^{-1}$) that is much weaker than the critical heating amplitude at which the PVRT is completed ($q_0 = 0.4 \text{ K day}^{-1}$). In contrast to this, Wang et al. (2012) found that lower-tropospheric and stratospheric regime transitions happen at similar heating amplitudes.

Apart from bimodal PDFs, further indications of a dynamical system undergoing a regime transition are, e.g., peaks in the autocorrelation time scale τ (Wang et al., 2012; Gerber and

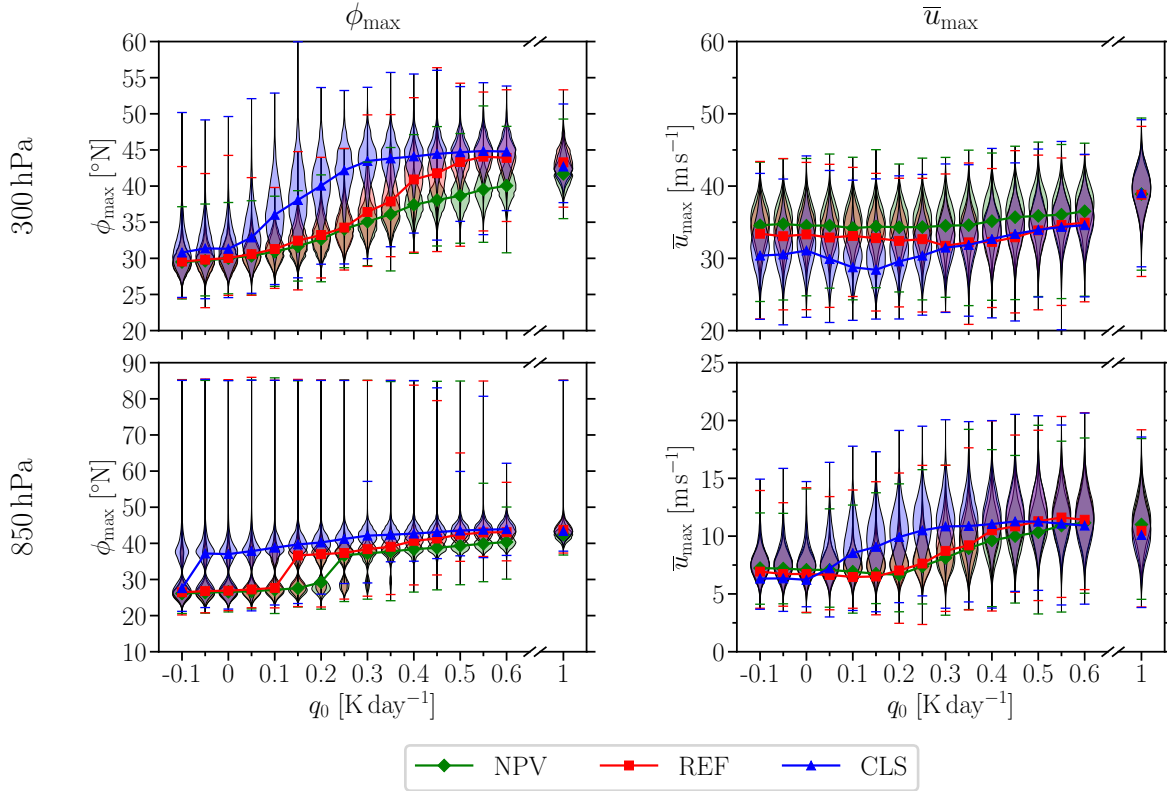


Figure 4.5: Same as Fig. 4.4, but for ϕ_{\max} (left) and \bar{u}_{\max} (right) evaluated at 300 hPa (top) and 850 hPa (bottom).

Polvani, 2009; Scheffer et al., 2009). They are found in both experiments with polar vortex as displayed in Fig. 4.6 where τ is shown as a function of the heating amplitude q_0 at 100 and 500 hPa. The calculation of τ follows Gerber et al. (2008) with the exception of using the zonal-mean zonal wind instead of the surface pressure field and restricting to extratropical latitudes ranging from 30°N to 80°N to compute the principal component time series.

In the REF experiment, a distinct maximum of τ at 100 hPa is observed at $q_0 = 0.35 \text{ K day}^{-1}$ just before the sharp strengthening of the polar vortex at $q_0 = 0.4 \text{ K day}^{-1}$, which corresponds to oscillations between phases of weak and strong polar vortices. The polar vortex remains in one of the phases for a relatively long time before switching to the other phase leading to enhanced autocorrelation (not shown, see Wang et al., 2012, and references therein). In the CLS experiment, τ at 100 hPa exhibits a broader peak between $q_0 = 0$ and $q_0 = 0.15 \text{ K day}^{-1}$ which is consistent with nonvanishing probabilities of a weak polar vortex even after the sharp increase of the climatological-mean polar vortex strength at $q_0 = 0.1 \text{ K day}^{-1}$. In general, tropospheric autocorrelation time scales seem to follow stratospheric autocorrelation time scales. Away from regime transitions, τ reaches values of up to 25 days in the troposphere which lie in the observable range of the real atmosphere (Baldwin et al., 2003; Wang et al., 2012).

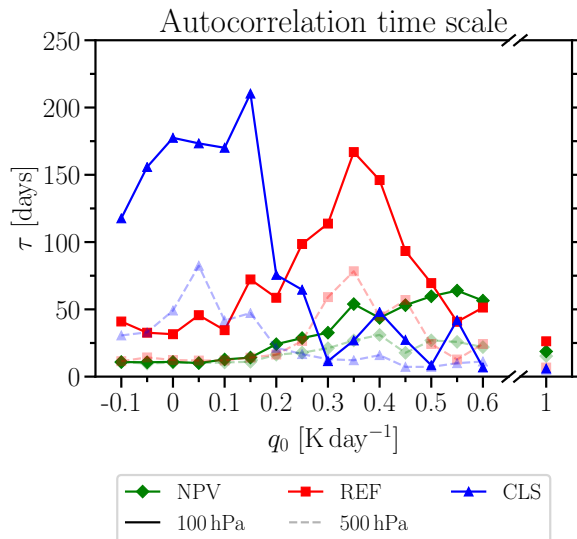


Figure 4.6: Autocorrelation time scale τ at 100 hPa (solid line) and 500 hPa (transparent dashed line) as function of the tropical upper-tropospheric heating amplitude q_0 for the experiment without polar vortex (NPV), the reference setup (REF), and a colder polar lower stratosphere (CLS). Details of the computation of τ are based on Gerber et al. (2008) and provided in Sec. 2.3.4.

The peaked autocorrelation in the REF and CLS experiments divide both experiments into two distinct dynamical regimes: a weak polar vortex regime with high variability and frequent SSWs for moderate heating amplitudes, and a strong polar vortex regime with low variability and rare SSWs for heating amplitudes beyond a critical threshold depending on the basic state of the stratosphere. Sec. 4.3 will focus on the dynamics of the weak polar vortex regime (green box in Fig. 4.1) restricted to the NPV and REF experiments in order to simplify the discussion. The transition to the strong polar vortex regime (blue box in Fig. 4.1) is then analyzed in Sec. 4.4, where important steps of the dynamical mechanism are recapitulated for the CLS experiment.

4.3 Weak polar vortex regime

Associated with the regime transition described above is a restructuring of Eliassen–Palm (EP) fluxes. As previously noted by Wang et al. (2012), less EP flux penetrates the stratosphere when the polar vortex enters the strong regime and more EP flux is refracted equatorward in the troposphere corresponding to the poleward shift of the tropospheric jet. The reorganization of wave fluxes can be quantified by considering a meridional subdomain in the extratropical upper troposphere as described in Sec. 2.3.2.

The relevant EP flux components B_{top} , B_{S} , and B_{bot} as well as the net EP flux budget B_{net} are shown in Fig. 4.7 together with their planetary- and synoptic-scale contributions. Taking the transformed Eulerian-mean zonal momentum equation (Eq. (1.11), Andrews et al., 1983)

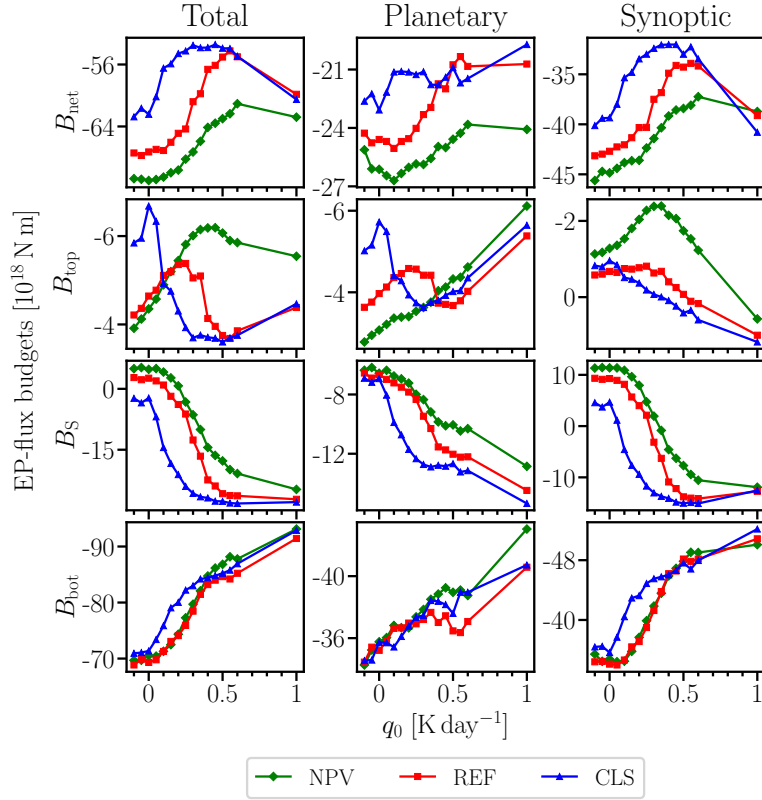


Figure 4.7: Total (left column), planetary- (middle column), and synoptic-scale (right column) net Eliassen–Palm (EP) flux budgets B_{net} (first row) as well as the EP flux components B_{top} (second row), B_{S} (third row), and B_{bot} (fourth row) associated with the extratropical upper-tropospheric area defined between Eqs. (2.16) and (2.17) as functions of the heating amplitude q_0 for the NPV, REF, and CLS experiments. Negative B_{top} and B_{bot} denote upward EP fluxes, negative B_{S} denotes southward EP flux, and negative B_{net} denotes EP flux that dissipates inside the area.

into account, a smaller amount of EP flux dissipated in a certain region can be associated with a smaller deceleration of the zonal-mean zonal wind in that region. Hence, the smaller negative B_{net} of the REF and CLS experiments is consistent with larger poleward fluctuations of their tropospheric jet cores at 300 hPa compared to the NPV experiment. Furthermore, the northward shift of the tropospheric jet increasingly occupying the extratropical upper-tropospheric area shown in Fig. 2.4 is consistent with more EP flux that is refracted to the South (decreasing B_{S}). In addition, the southern, bottom, and top boundaries of the area are provided with a better waveguide increasing wave activity entering the area from the bottom (decreasing B_{bot}) and leaving the area at the top (decreasing B_{top}) for weak heating amplitudes. In the NPV experiment, this process decays at $q_0 = 0.3 \text{ K day}^{-1}$ when synoptic-scale upward EP flux at 100 hPa decreases in favor for equatorward refraction at 38°N . The sharp reduction of upward wave flux into the stratosphere in the REF and CLS experiments is dominated by planetary-scale waves accompanying the corresponding PVRT from the weak to the strong regime.

The decrease of B_{top} for $q_0 \leq 0.25 \text{ K day}^{-1}$ in the NPV and REF experiments representing an increase of EP flux entering the stratosphere at 100 hPa is consistent with the CLCM described in Shepherd and McLandress (2011). This mechanism dominates the dynamics in the weak polar vortex regime as demonstrated in the following. According to Shepherd and McLandress (2011), an increased negative meridional temperature gradient from tropical to extratropical regions, associated with TUTW, strengthens the upper flanks of the tropospheric jets. Therefore, the critical layer at which wave propagation is prohibited rises in the vicinity of the tropospheric jet (Charney and Drazin, 1961).¹¹

In the NPV experiment which is not subject to a regime transition, the critical layer $\bar{u} = 0$ continuously rises for all values of the heating amplitude q_0 , consistent with the continuous increase of upward planetary-scale B_{top} . The increase of upward synoptic-scale B_{top} stops at a maximum at $q_0 = 0.3 \text{ K day}^{-1}$ when the synoptic-scale meridional flux B_S at 38°N changes from poleward to equatorward. The tropospheric jet has moved sufficiently poleward with a zonal-mean zonal wind above 30 m s^{-1} at 40°N to refract synoptic-scale wave flux equatorward. This hints at the existence of a critical position of the tropospheric jet that reduces the efficiency of the CLCM.

In the REF experiment, the critical layer $\bar{u} = 0$ rises up to $q_0 = 0.25 \text{ K day}^{-1}$ consistent with the increasing upward EP fluxes of all wavenumbers at 100 hPa. For larger values of q_0 the refractive index at 40°N is influenced by the stratospheric polar vortex, the critical layer disappears and a further increase in total upward wave fluxes at 100 hPa could be expected. Due to the changing dynamics, however, a sharp decrease in upward planetary-scale B_{top} is observed which will be discussed in Sec. 4.4. The maximum synoptic-scale upward B_{top} in the REF experiment is reached slightly earlier at $q_0 = 0.25 \text{ K day}^{-1}$ compared to the NPV experiment, but similarly when the synoptic-scale meridional flux B_S at 38°N is about to change from pole- to equatorward.

The critical-layer rise also influences the region at which EP flux dissipates and how the RC is driven. In the control run of the NPV experiment, a large region of strongly negative EPFD above the tropospheric jet extends over the entire hemisphere with maximum values poleward of 20°N (top row of Fig. 4.8). Planetary-scale wave fluxes contribute strongest between 40°N and 70°N , whereas synoptic-scale wave fluxes contribute strongest between 25°N and 45°N . In response to TUTW, the regions of wave dissipation of both planetary- and synoptic-scale waves move upward according to the CLCM (top row of Fig. 4.9). The dissipation of synoptic-scale waves happens at the LS turnaround latitudes, such that an upward shift of the region of dissipation is directly transferred to an acceleration of the RC at 100 hPa up to $q_0 = 0.2 \text{ K day}^{-1}$ (Fig. 4.11). For larger heating amplitudes shifting the tropospheric jet sufficiently

¹¹The critical-layer rise can be seen in Fig. 4.13 where zonal-mean zonal winds together with the refractive index squared $n_{c,k}^2$ (Matsuno, 1970; Simpson et al., 2009; Gerber, 2012) for zonally stationary ($c = 0$) waves of WN $k = 2$ are shown for three different heating amplitudes.

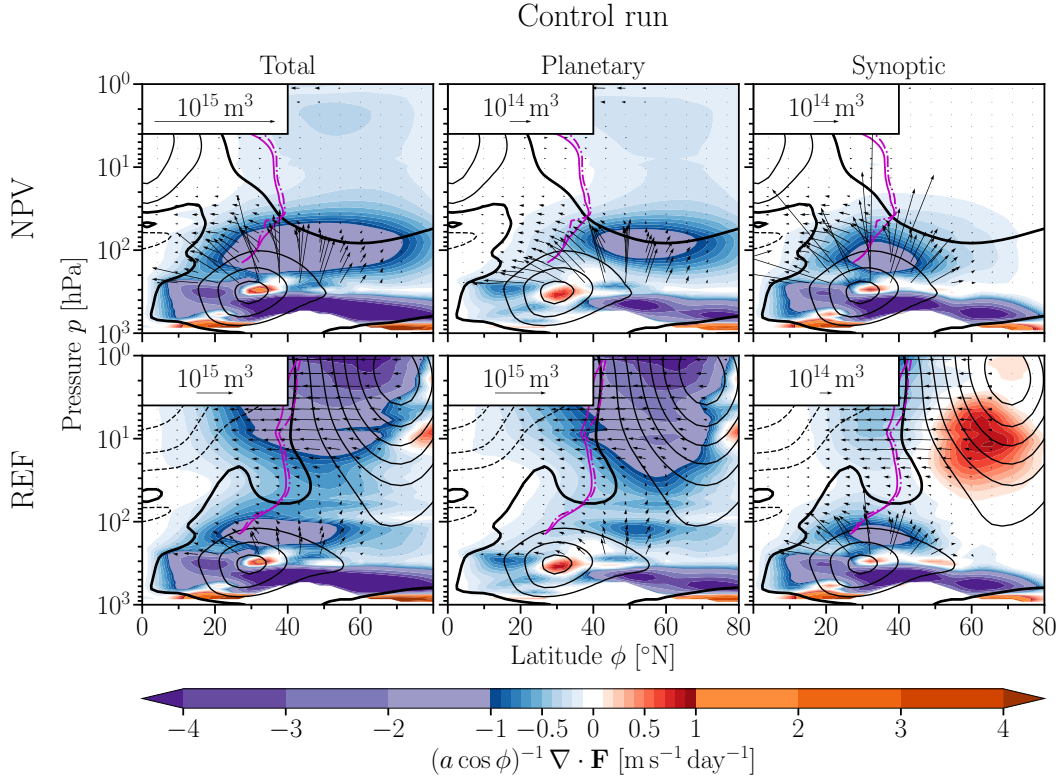


Figure 4.8: Control-run ($q_0 = 0$) tendencies of the zonal-mean zonal wind by the Eliassen–Palm (EP) flux divergence $\bar{\mathcal{F}} = (a \cos \phi)^{-1} \nabla \cdot \mathbf{F}$ (color shading), EP flux arrows $\hat{\mathbf{F}} = (\hat{F}^{(\phi)}, \hat{F}^{(p)})$ (arrows), and zonal-mean zonal winds (black contour lines with a contour interval of 10 m s^{-1} , negative contours dashed, thick zero-contour line) as functions of latitude and pressure for the NPV (top) and REF (bottom) experiments. EP flux diagnostics are presented in total (left) as well as only for planetary- (middle) and only for synoptic-scale wave contributions (right). EP flux arrows are defined as $(\hat{F}^{(\phi)}, \hat{F}^{(p)}) = 2\pi a g^{-1} \cos \phi (F^{(\phi)}, aF^{(p)}) / (-80.4 \text{ kPa})$ according to Edmon et al. (1980). The solid and dash-dotted magenta lines represent the turnaround latitudes of the residual-mean meridional circulation Ψ^* and the downward-control circulation Ψ_{dc}^* , respectively (McLandress and Shepherd, 2009; Haynes et al., 1991).

poleward, the CLCM for synoptic-scale waves loses efficiency, since less synoptic-scale wave flux reaches its critical layer and is instead refracted equatorward (top row of Fig. 4.10). Consequentially, the RC in the LS starts to be less driven by synoptic-scale waves for $q_0 > 0.2 \text{ K day}^{-1}$. In contrast, the region of strongest planetary-scale wave dissipation in the control run ($q_0 = 0$) is located poleward of the turnaround latitudes. Indeed, the CLCM leads to a continuous increase of upward planetary-scale wave flux, but up to $q_0 = 0.2 \text{ K day}^{-1}$, planetary-scale wave dissipation still happens mainly poleward of the turnaround latitudes leading only to a moderate increase in the driving of the LS RC. At $q_0 = 0.25 \text{ K day}^{-1}$, the tropospheric jet has reached a sufficiently poleward position in combination with a sufficient vertical extent, such that planetary-scale wave flux is refracted sufficiently equatorward to dissipate close to the turnaround latitudes. Thus, the contribution of planetary-scale waves to the LS RC strength is sharply enhanced for $q_0 \geq 0.25 \text{ K day}^{-1}$. Simultaneously, the mid-

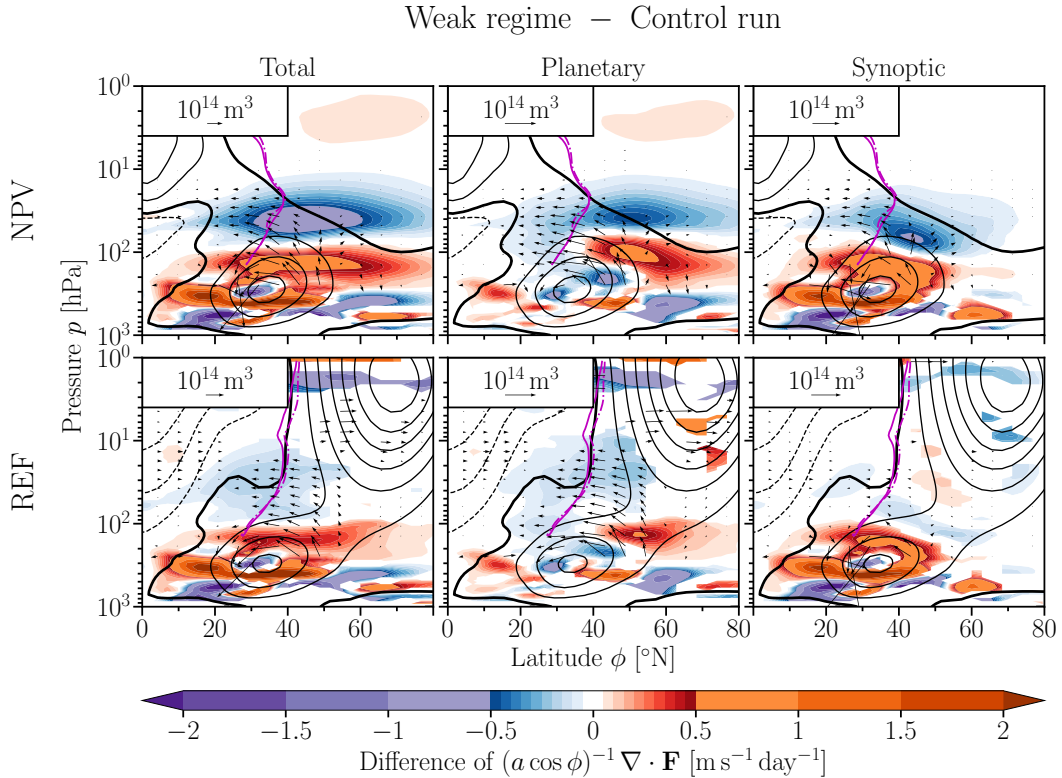


Figure 4.9: Same as Fig. 4.8, but for differences of $\bar{\mathcal{F}}$ and $\hat{\mathbf{F}}$ between climate states at $q_0 = 0.25 \text{ K day}^{-1}$ and $q_0 = 0$. Only differences that are statistically significant on a 95%-confidence level are shown. Zonal-mean zonal winds and turnaround latitudes are presented for climate states at $q_0 = 0.25 \text{ K day}^{-1}$.

stratospheric RC at 30 hPa exhibits a significant strengthening when planetary-scale waves are finally able to reach subtropical turnaround latitudes in the middle stratosphere.

In the control run of the REF experiment, the region of strongest negative EPFD above the tropospheric jet is confined to latitudes between 20°N and 60°N since planetary-scale EP fluxes northward of 60°N are able to propagate further up into the stratosphere due to the waveguide provided by the polar vortex (bottom row of Fig. 4.8). Hence, planetary-scale waves are much better able to drive the mid-stratospheric RC at 30 hPa compared to the NPV experiment (Fig. 4.11). The RC strength at 100 hPa increases slightly slower than in the NPV experiment up to $q_0 = 0.25 \text{ K day}^{-1}$ due to a smaller increase in synoptic-scale wave driving of the LS close to the turnaround latitudes (bottom row of Fig. 4.9). The CLCM in the weak polar vortex regime of the REF experiment is less efficient than in the NPV experiment since less synoptic-scale wave flux propagates poleward at 38°N which is then unable to propagate upward (Fig. 4.7). The mid-stratospheric RC in the REF experiment strengthens up to $q_0 = 0.2 \text{ K day}^{-1}$ and stays at this level up to $q_0 = 0.35 \text{ K day}^{-1}$ after which the regime transition to the strong polar vortex regime changes the dynamics completely

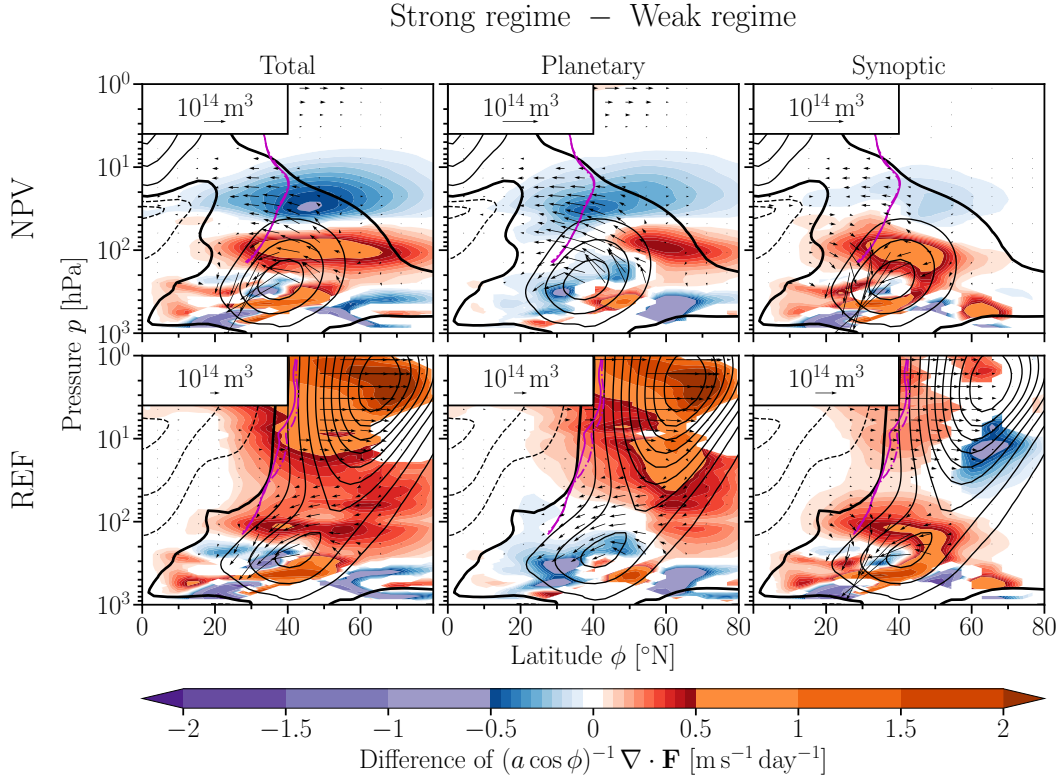


Figure 4.10: Same as Fig. 4.8, but for differences of $\bar{\mathcal{F}}$ and $\hat{\mathbf{F}}$ between climate states at $q_0 = 0.4 \text{ K day}^{-1}$ and $q_0 = 0.25 \text{ K day}^{-1}$. Only differences that are statistically significant on a 95%-confidence level are shown. Zonal-mean zonal winds and turnaround latitudes are presented for climate states at $q_0 = 0.4 \text{ K day}^{-1}$.

(Sec. 4.4). Overall, the presence of a polar vortex reduces the increase of total EPFD close to the LS turnaround latitudes in the weak polar vortex regime.

The results above confirm hypothesis 1. In both experiments with and without polar vortex (REF and NPV), the CLCM (gray boxes in Fig. 4.1) is responsible for a strengthened shallow branch of the RC. Due to the nonvanishing phase speeds of synoptic-scale waves, further investigations need to determine the location of their critical layers (Randel and Held, 1991; Shepherd and McLandress, 2011).

Crucial points to understand the PVRT are the structure of the RC and its effect on stratospheric temperatures. Upwelling air masses in the tropics are adiabatically cooled and downwelling air masses in the extratropics are adiabatically heated, respectively, resulting in a positive meridional temperature gradient in the subtropical UTLS region compared to the negative gradient below (not shown). Consistent with thermal wind balance, zonal-mean zonal winds in the subtropics are weakened with increasing height in the UTLS region. In case of the NPV experiment, the far poleward reaching dissipation of wave flux in the LS (Fig. 4.8) is associated with a region of downwelling poleward of 30°N of rather uniform strength (not

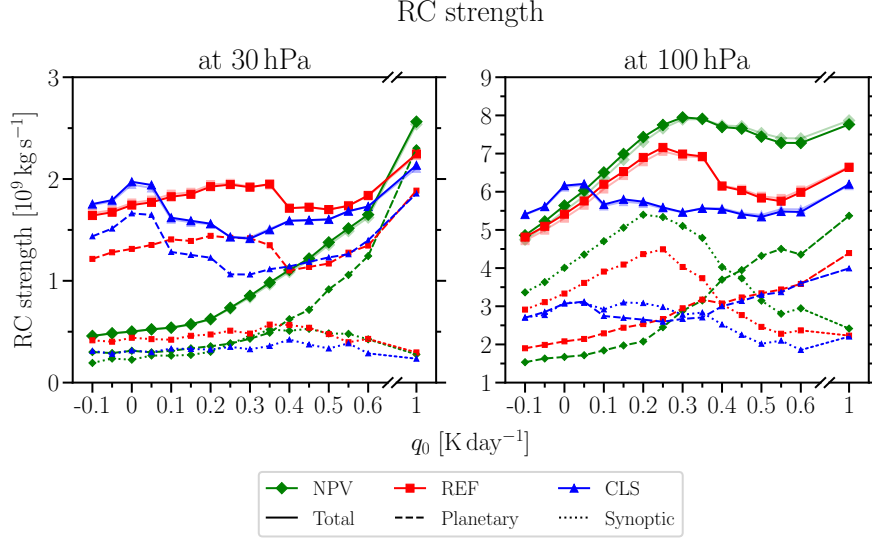


Figure 4.11: Residual circulation (RC) strength at 30 hPa (left) and 100 hPa (right) as a function of the heating amplitude q_0 for the NPV, REF, and CLS experiments. The strength of the RC is based on the downward control streamfunction Ψ_{dc}^* given in Eq. (2.18) and computed via $\max(\Psi_{dc}^*) + |\min(\Psi_{dc}^*)|$ which allows to determine contributions from planetary- and synoptic-scale EPFD. For comparison, the total upward mass flux \mathcal{M} between the turnaround latitudes is added as a transparent line.

shown). In case of the REF experiment, however, the presence of a polar vortex leads to a localized region of maximum downwelling at the equatorward edge of the polar vortex (not shown).

Structural differences of the residual circulation between the experiments with and without polar vortex are also reflected in different temperature signatures $\Delta\bar{T}_{q_0}$ that occur when the circulation is strengthened in response to TUTW. In order to translate these temperature signatures to a zonal wind that is in balance with $\Delta\bar{T}_{q_0}$, the solution of the thermal wind equation in spherical coordinates

$$\bar{u}_{th}(\Delta\bar{T}_{q_0}) = -\Omega a \cos(\phi) + \sqrt{\left[\bar{u}_{bot} + \Omega a \cos(\phi)\right]^2 + \frac{R}{\tan(\phi)} \int_{p_{bot}}^p \frac{\partial_\phi \Delta\bar{T}_{q_0}}{p'} dp'} \quad (4.1)$$

is consulted, where $\bar{u}_{bot} \equiv 0$ is the zonal-mean zonal wind at the surface $p_{bot} = 1000$ hPa. Stratospheric temperature and corresponding zonal-wind signatures can be highlighted by

$$\Delta\bar{u}_{th} = \bar{u}_{th}(\Delta\bar{T}_{q_0}) - \widetilde{\bar{u}_{th}(\Delta\bar{T}_{q_0})}, \quad (4.2)$$

where modified temperature differences

$$\widetilde{\Delta\bar{T}_{q_0}} = \begin{cases} 0 & \text{for } p < 150 \text{ hPa} \\ \Delta\bar{T}_{q_0} & \text{for } p \geq 150 \text{ hPa} \end{cases} \quad (4.3)$$

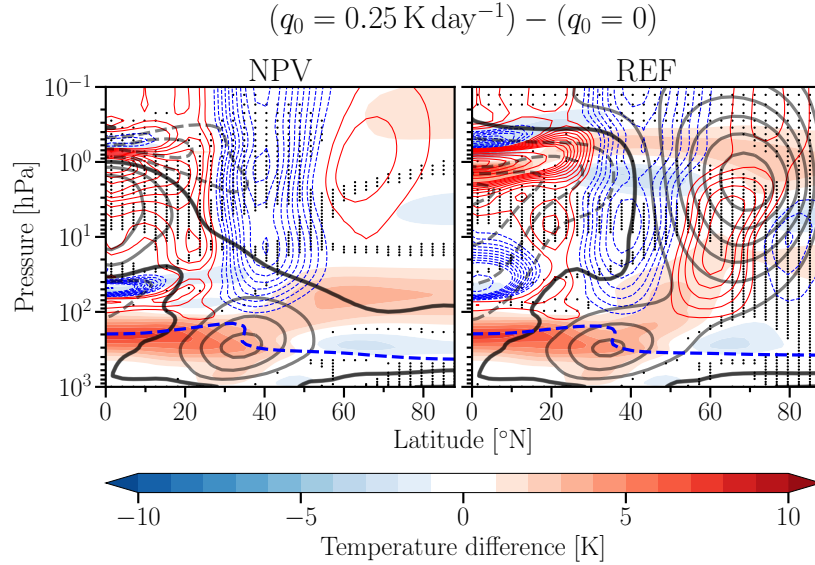


Figure 4.12: Zonal-mean temperature differences $\Delta \bar{T}_{q_0}$ of climatologies at $q_0 = 0.25 \text{ K day}^{-1}$ and control-run climatologies at $q_0 = 0$ (color shading) and zonal-mean zonal wind at $q_0 = 0.25 \text{ K day}^{-1}$ (gray contour lines with a contour interval of 10 m s^{-1} , negative contours dashed, black zero-contour line) as functions of latitude and pressure for the NPV (left) and REF (right) experiments. Dotted regions show temperature differences that are not significant on a 95%-confidence level. Furthermore, the positive (negative) thermal-wind effect $\Delta \bar{u}_{\text{th}}$ of temperature differences above 150 hPa is shown by thin solid red (thin dashed blue) contour lines starting at 1 m s^{-1} (-1 m s^{-1}) with a contour interval of 1 m s^{-1} below a magnitude of 10 m s^{-1} and with a contour interval of 5 m s^{-1} above a magnitude of 10 m s^{-1} . Details of the computation of $\Delta \bar{u}_{\text{th}}$ are provided in the body text around Eqs. (4.1)–(4.3). The thick dashed blue lines denote the lapse-rate tropopause of climate states at $q_0 = 0.25 \text{ K day}^{-1}$ (WMO, 1957).

are used in the subtrahend on the right hand side of Eq. (4.2). As a result, $\Delta \bar{u}_{\text{th}}$ only contains the thermal-wind effect of stratospheric temperature differences above 150 hPa as shown in Fig. 4.12.

In the tropical tropopause region, both experiments exhibit approximately the same warming when forced with a heating amplitude of $q_0 = 0.25 \text{ K day}^{-1}$. In the stratosphere, $\Delta \bar{T}_{q_0}$ differs due to different structures of the RC. In the NPV experiment, the entire extratropical LS is subject to heating associated with the widespread region of downwelling. In response to critical-layer rise, the region of strongly negative EPFD is lifted causing stronger downwelling, hence heating in the middle stratosphere and weaker downwelling, hence cooling in the LS as shown in the left panel of Fig. 4.12. Zonal-mean zonal winds are attenuated with increasing height in the region above the tropospheric jet due to the positive meridional temperature gradient in that region. The ongoing CLCM due to TUTW in the NPV experiment leads to an expansion of the tropospheric jet in upward and poleward direction, but the structure of the RC always exerts negative feedback on the upward expansion by a negative thermal-wind effect.

In the REF experiment, the localized downward mass flux maximum at the equatorward edge of the polar vortex in the LS causes a localized temperature increase in response to a strengthened RC in the same region (right panel of Fig. 4.12). The localized warming of the LS in the REF experiment is associated with a slightly weaker attenuation of zonal-mean zonal winds above the tropospheric jet than in the NPV experiment. Additionally, zonal-mean zonal winds are strengthened on the poleward side of the localized heating, which represents the equatorward side of the lower polar vortex. This feature of a strengthened RC in the weak regime—namely accelerating the equatorward side of the lower polar vortex and thereby shifting the lower vortex equatorward—is the crucial point that leads to the change in polar vortex geometry that eventually induces the transition to the strong regime. The continuous convergence of the poleward migrating tropospheric jet and the equatorward shifting LS polar vortex also explains the lower efficiency of the CLCM of synoptic-scale wave flux and hence contributes to the slower strengthening of the LS RC in the REF experiment. Whenever the critical layer around 40°N rises, the region of wave dissipation between the tropospheric jet and the LS polar vortex shrinks. This will eventually terminate the CLCM for synoptic-scale waves at $q_0 = 0.3 \text{ K day}^{-1}$ representing the first critical point (CP1) in the schematic of Fig. 4.1.

The results above provide evidence for hypothesis 2. Due to the localized region of maximum downwelling at the equatorward edge of the polar vortex in the REF experiment, the strengthened shallow branch of the RC is consistent with an equatorward shift of the LS polar vortex. In light of the NPV experiment, which shows that planetary-scale wave flux requires a sufficiently pole- and upward expansion of the tropospheric jet to reach subtropical latitudes, the equatorward shift of the LS polar vortex can also be explained directly by the equatorward shift of wave drag in the UTLS region. This is also consistent with the nonlinear equatorward migration of the zonal-mean jet at 100 hPa for $q_0 \geq 0.15 \text{ K day}^{-1}$ in the REF experiment. In contrast to this, the continuous increase of the LS RC strength rather suggests a linear equatorward migration.

4.4 Strong polar vortex regime

The first step towards the transition to the strong polar vortex regime in the REF experiment happens at $q_0 = 0.3 \text{ K day}^{-1}$ when tropospheric jet and LS polar vortex have reached a critical minimum distance, shrinking the region of possible synoptic-scale wave dissipation to the point that the CLCM terminates (CP1). The increase of upward synoptic-scale wave flux at 100 hPa stops, weakening the LS RC, and the meridional EP flux component B_S at 38°N changes from pole- to equatorward. This is consistent with an enhanced poleward shift of the tropospheric jet compared to the NPV experiment. Simultaneously, the polar vortex strengthens consistent with reduced high-latitude downwelling (not shown).

The climate state at $q_0 = 0.35 \text{ K day}^{-1}$ of the REF experiment exhibits only a weak poleward shift of the tropospheric jet compared to the climate state before. The contribution of synoptic-scale wave flux to the LS RC strength further decreases, which further strengthens the LS polar vortex. In contrast to this, planetary-scale contributions to the LS RC strength still increase maintaining the weak polar vortex regime. The maximum autocorrelation time scale is reached announcing the upcoming regime transition.

The transition to the strong polar vortex regime in the REF experiment is completed at the second critical point (CP2) at $q_0 = 0.4 \text{ K day}^{-1}$, consistent with the strongly reduced dissipation of planetary-scale EP flux in the entire stratosphere (bottom row of Fig. 4.10). Large amounts of previously upward propagating wave activity are instead refracted equatorward in the troposphere, increasing B_{net} (Fig. 4.7) which is consistent with the largest poleward shift of the tropospheric jet compared to the NPV experiment. The RC weakens significantly at all heights (Fig. 4.11) with a large decrease of downwelling in the polar UTLS region (not shown). The previously negative feedback of the RC on the polar vortex strength disappears. Consequently, a stronger negative meridional temperature gradient is consistent with a stronger polar vortex at all heights. Additionally, the polar vortex changes from a vertically aligned geometry in the weak regime to being poleward tilted with increasing height in the strong regime (Fig. 4.13).

Analyzing the refractive index squared for stationary waves of wavenumber 2 as displayed in Fig. 4.13, the evolution of planetary-scale EP fluxes can be explained. In the control run of the REF experiment, a thin layer of low refractive index below a value of 10 is found below the polar vortex. The continuing convergence of poleward moving tropospheric jet and equatorward moving lower stratospheric polar vortex due to TUTW improves the waveguide in the UTLS region, which increases upward wave flux in addition to the critical-layer rise in the subtropics. This process is stopped at $q_0 = 0.3 \text{ K day}^{-1}$ when the waveguide starts to change drastically, exhibiting a more reflective characteristic as will be explained in more detail in the following. Hence, upward EP flux suddenly decreases and is instead refracted equatorward in the troposphere (Fig. 4.7) which is consistent with the increased poleward movement of the tropospheric jet. As stated above, the wave-driven RC weakens consistent with a stronger polar vortex whose lower part is located more equatorward. This narrows the waveguide on the poleward side of the polar vortex, i.e., the region of negative refractive index squared prohibiting wave propagation expands southward. At $q_0 = 0.4 \text{ K day}^{-1}$, tropospheric and stratospheric wind structures have sufficiently merged to develop a narrow enough waveguide with the following properties. On the one hand, the waveguide with positive refractive index squared in the LS is limited to 30°N – 60°N with high values of the refractive index squared larger than 10 being even more confined within 45°N – 60°N . On the other hand, the upper part of the polar vortex is occupied by a thick layer of low refractive index below a value of 10 that even falls below 0 above 1 hPa. As revealed by Perlwitz and Harnik (2003) and Shaw

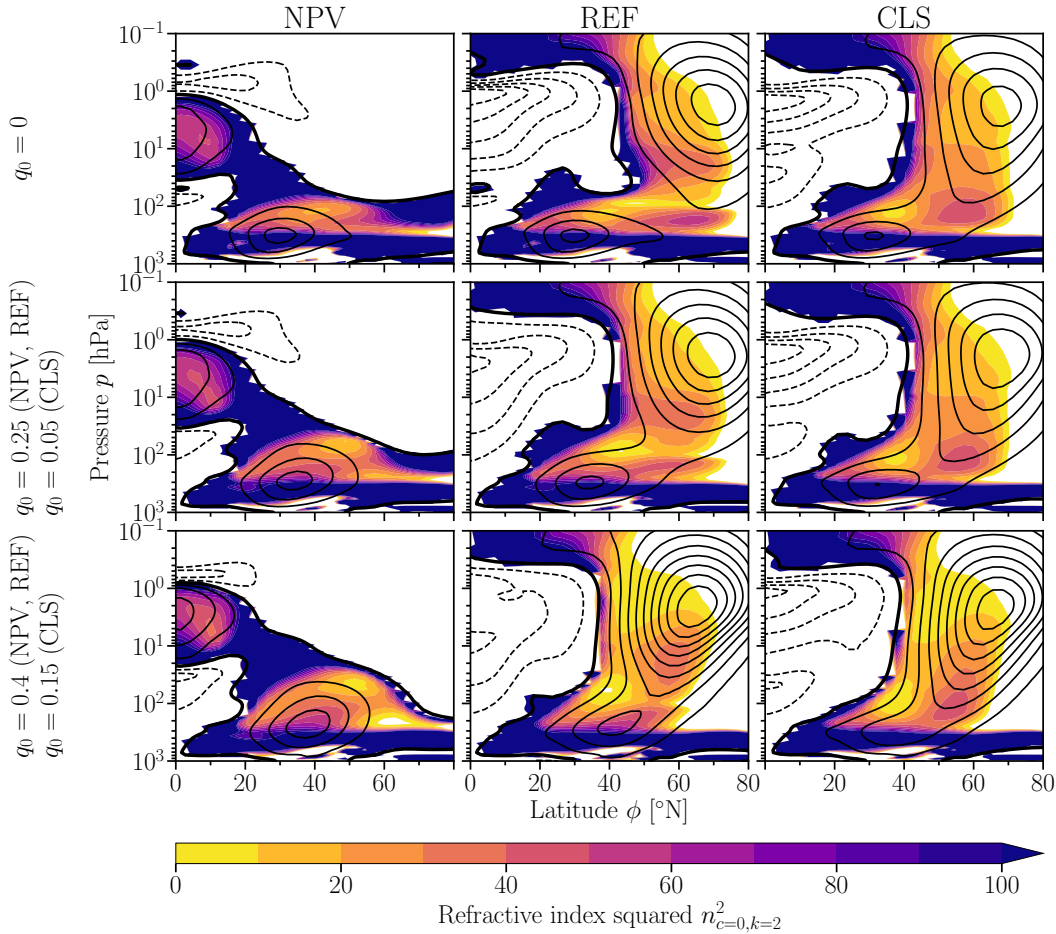


Figure 4.13: Refractive index squared $n_{c=0,k=2}^2$ for stationary waves of wavenumber 2 (color shading with a contour interval of 10) and zonal-mean zonal wind (black contour lines with a contour interval of 10 m s^{-1} , negative contours dashed, thick zero-contour line) for zero tropical upper-tropospheric heating (top row) and for heating amplitudes q_0 associated with climate states that are at the end of the weak (middle row) as well as already in the strong polar vortex regime (bottom row) as a function of latitude ϕ and pressure p for the NPV, REF, and CLS experiments.

et al. (2010), these two features of the waveguide—a meridionally narrow region of positive refractive index squared in combination with negative refractive index squared at the top of the stratosphere—lead to downward wave coupling, i.e., wave reflection with significant impact of the reflected waves on the troposphere.¹²

¹²It is emphasized here that the refractive index squared $n_{c,k}^2$ used in this thesis is only suitable to assess the general ability of wave propagation in the meridional plane. In order to classify the waveguide of the strong polar vortex regime as a waveguide that causes downward wave coupling events, the computation of separate refractive indices for meridional and vertical wave propagation is necessary as demonstrated by Harnik and Lindzen (2001).

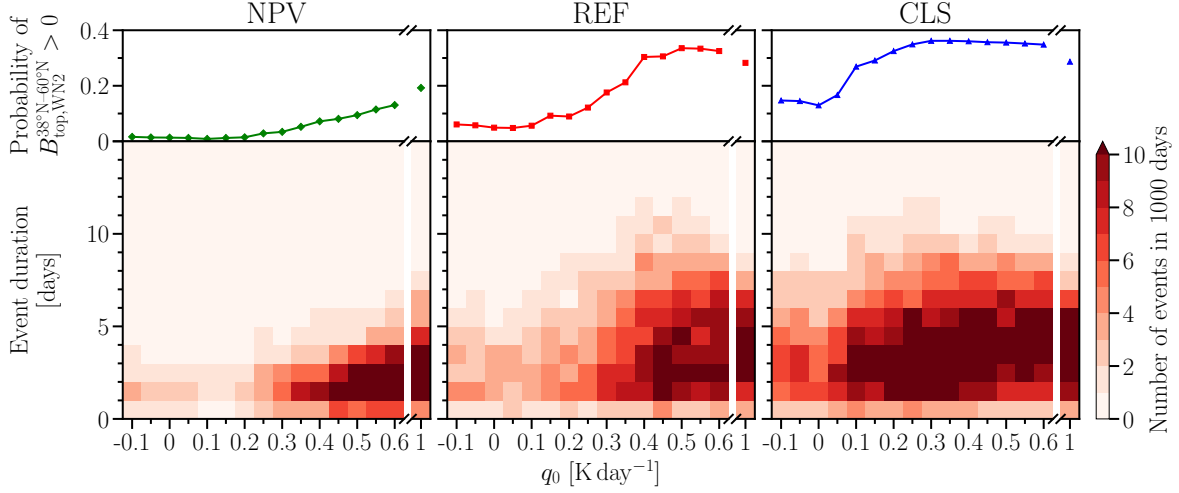


Figure 4.14: Probability of positive $B_{\text{top,WN2}}^{38^{\circ}\text{N}-60^{\circ}\text{N}}$, i.e. downward wavenumber-2 (WN2) Eliassen–Palm (EP) flux at 100 hPa integrated from 38°N to 60°N (top panels), as well as the number of events of downward $B_{\text{top,WN2}}^{38^{\circ}\text{N}-60^{\circ}\text{N}}$ as a function of the heating amplitude q_0 and the event duration (bottom panels) for the NPV, REF, and CLS experiments. An event of the duration of l days is defined to require $B_{\text{top,WN2}}^{38^{\circ}\text{N}-60^{\circ}\text{N}} > 0$ for l consecutive days. Note that with pressure as vertical coordinate, positive wave flux points downward. A large increase in both number and duration of downward flux events after the regime transition associated with wave reflection events is observed (for $q_0 \geq 0.35 \text{ K day}^{-1}$ in the REF and for $q_0 \geq 0.1 \text{ K day}^{-1}$ in the CLS experiment).

In order to show that the regime transition is accompanied by an increase in downward wave flux events,

$$B_{\text{top,WN2}}^{38^{\circ}\text{N}-60^{\circ}\text{N}} = \frac{2\pi a^2}{g} \int_{\frac{38^{\circ}}{180^{\circ}}\pi}^{\frac{60^{\circ}}{180^{\circ}}\pi} \cos(\phi) F_{\text{WN2}}^{(p)} d\phi \Big|_{p_{\text{top}}=100 \text{ hPa}} \quad (4.4)$$

is analyzed, representing the flux of WN2 waves between 38°N and 60°N crossing the 100 hPa-level. In contrast to the original definition of B_{top} , a narrower latitude band is chosen for the integration of the EP flux in Eq. (4.4) to reflect only the region of positive refractive index with upward climatological-mean flux for $q_0 \geq 0.4 \text{ K day}^{-1}$ (not shown). The probability of downward WN2 flux in the UTLS region of the midlatitudes is shown in the top panels of Fig. 4.14. It can be seen that the probability increases from below 10% in the weak regime to approximately 35% in the strong regime in the REF experiment. A better view can be obtained by counting the number as well as the duration of events with consecutive downward WN2 flux which is shown in the bottom panels of Fig. 4.14. The maximum duration of downward WN2 EP flux events in the REF experiment increases linearly from 5 days at $q_0 = 0$ to 9 days at $q_0 = 0.2 \text{ K day}^{-1}$ where it stays until $q_0 = 0.3 \text{ K day}^{-1}$. The accompanied increase in $P(B_{\text{top,WN2}}^{38^{\circ}\text{N}-60^{\circ}\text{N}} > 0)$ from $q_0 = 0.2 \text{ K day}^{-1}$ to $q_0 = 0.3 \text{ K day}^{-1}$ is caused by an increase in the number of downward wave flux events and not by longer-lasting events. The transition to the

strong polar vortex regime at $q_0 = 0.4 \text{ K day}^{-1}$ is marked by a sharp increase in the maximum duration of downward WN2 EP flux events to 12 days.

In case of the NPV experiment, downward WN2 EP flux events at 100 hPa are very rare up to $q_0 = 0.2 \text{ K day}^{-1}$ since the critical line for wave propagation has not risen sufficiently. For $q_0 \geq 0.25 \text{ K day}^{-1}$, a linear increase in $P(B_{\text{top,WN2}}^{38^\circ\text{N}-60^\circ\text{N}} > 0)$ with q_0 is observed and the number of downward WN2 EP flux events exhibiting a duration shorter than 7 days increases due to the large upward expansion of the tropospheric jet.

In reanalysis data, reflected downward propagating planetary-scale waves have been observed to couple the mid-stratosphere to the mid-troposphere on timescales of about one week (Perlwitz and Harnik, 2003, 2004). In this regard, the occurrence of proper wave-reflection events coupling the stratosphere to the troposphere is attributed to the strong polar vortex regime only, whereas the increase in downward flux events in the NPV experiment is considered as enhanced variability of alternating up- and downward fluxes.¹³

The probability for the reflected waves in the weak polar vortex regime to exert a considerable influence on the troposphere via downward wave coupling is small due to the lack of a confined meridional waveguide owing to the weak meridional curvature of the zonal-mean flow. Instead, wave dissipation close to critical surfaces in the subtropics is assumed to be much more relevant (Shaw et al., 2010) as is indeed observed for the weak polar vortex regime according to Figs. 4.8 and 4.9. Only the strong polar vortex regime with its strong meridional curvature of the mean flow is able to exert a considerable influence on the troposphere according to the enhanced poleward shift of the tropospheric jet compared to the weak polar vortex regime. Whether or not this stratospheric influence is related to downward wave coupling events remains an open question.

The influence of reflected wave activity on the troposphere is detected by the diagnostics of EP fluxes associated with the area in the extratropical upper troposphere. Similar to Perlwitz and Graf (2001) and Shaw and Perlwitz (2013) who found that wave activity which is reflected back into the troposphere propagates equatorward, the sharp increase of B_{top} associated with enhanced downward wave flux events during the regime transition in the experiments with polar vortex is accompanied by a sharp decrease of B_S representing enhanced equatorward propagation of wave activity compared to the NPV experiment (Fig. 4.7). The latter is consistent with the enhanced poleward shift of the tropospheric jet in the REF and CLS experiments as compared to the NPV experiment. Thus, the transition of the waveguide from a nonreflective configuration in the weak to a reflective configuration in the strong polar vortex regime appears crucial for the enhanced poleward shift of the tropospheric jet.

The results above confirm hypothesis 3. The circulation changes induced by TUTW—the poleward moving tropospheric jet and the equatorward moving LS polar vortex—support

¹³The evolution of wave-reflection events in the CLS experiment is discussed below.

enhanced upward propagation of planetary-scale waves in the weak polar vortex regime by generating a better waveguide in the UTLS region of the midlatitudes. When tropospheric and lower stratospheric jets have sufficiently converged, the waveguide for planetary-scale waves changes its characteristic to introduce more wave reflection events. This represents the second critical point (CP2) where the transition to the strong polar vortex regime is completed.

Hypothesis 4 is also confirmed. In the strong polar vortex regime beyond CP2, the tropospheric jet experiences an enhanced poleward shift compared to the tropospheric jet of the NPV experiment. Together with the confined meridional waveguide and the large number of downward wave flux events, the significant impact on the troposphere provides strong evidence for downward wave coupling in the strong polar vortex regime.

In the control run ($q_0 = 0$) of the CLS experiment, the polar vortex is in a state close to the regime transition (Garny et al., 2020). The colder polar LS compared to the REF experiment is implemented in a way which supports an already further equatorward located and stronger LS polar vortex (Fig. 4.4) providing a much better waveguide for planetary-scale waves in the UTLS region (Fig. 4.13). Thus, almost 50% more WN2 EP flux is able to propagate across the extratropical 100 hPa-level into the upper stratosphere compared to the REF experiment (Fig. 4.7) explaining the pronounced probability of SSWs in the CLS basic state (Fig. 4.4) and the stronger RC (Fig. 4.11). On the other hand, large numbers of downward wave flux events lasting up to 8 days are observed (Fig. 4.14) which are consistent with the second pronounced peak of the PDF of \bar{u}_{\max} at 10 hPa at 70 m s^{-1} representing a strong polar vortex after reflection events (Shaw and Perlwitz, 2013). As a consequence, a weak tropical upper-tropospheric heating amplitude of $q_0 = 0.1 \text{ K day}^{-1}$ is sufficient to shift the LS polar vortex equatorward in the position suitable to form the reflective waveguide with a sharp increase in downward wave flux events (Fig. 4.14). Starting from $q_0 = -0.1 \text{ K day}^{-1}$, the strengthened shallow branch of the RC (Fig. 4.11) is consistent with the equatorward shift of the LS polar vortex (Fig. 4.4) similar to the REF experiment.

4.5 Robust criterion for the regime transition

In this section, the robustness of the proposed dynamical mechanism responsible for the PVRT is tested. To this end, TUTW experiments of the previous sections are repeated with different resolutions (labeled, “-T85” and “-L47”), different tropical stratification (labeled “-d10”), and a different heating shape (labeled “-mod”, refer to Table 2.2 and Sec. 2.2.2 for details). In order to unify the circulation responses due to different realizations of TUTW, the average tropical upper-tropospheric temperature $\bar{T}_{\text{TUT}} := \langle \bar{T} \rangle_{25^\circ\text{S}-25^\circ\text{N}}^{150-280 \text{ hPa}}$ is used. The top left panel of Fig. 4.15 confirms the mainly linear relation between \bar{T}_{TUT} and the heating amplitude q_0 (Wang et al., 2012). Three groups of data points exist independently of stratospheric conditions: one group for the large number of experiments with $\delta_z = 4.3 \text{ K}$ employing the standard heating, one group

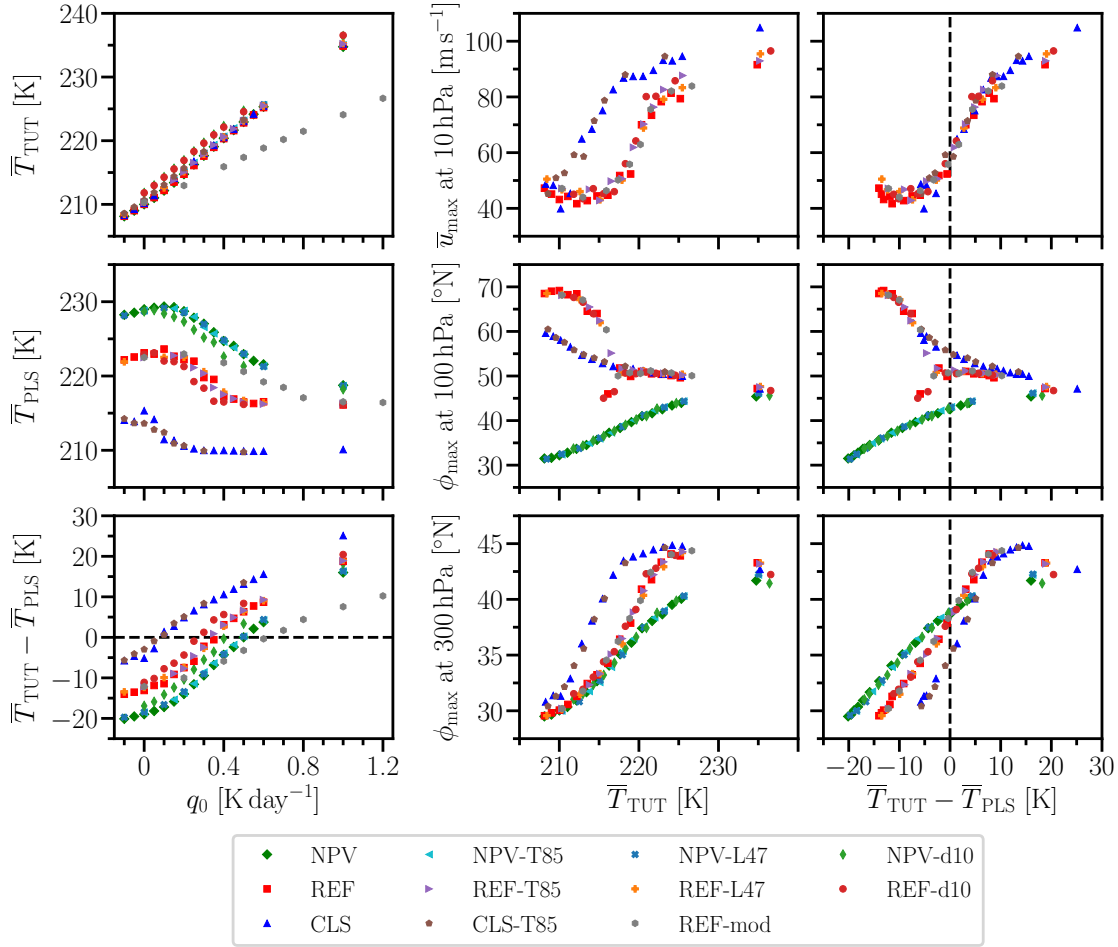


Figure 4.15: Average tropical upper-tropospheric temperature $\bar{T}_{\text{TUT}} := \langle \bar{T} \rangle_{25^\circ\text{S}-25^\circ\text{N}}^{150-280\text{ hPa}}$ (top), average polar lower-stratospheric temperature $\bar{T}_{\text{PLS}} := \langle \bar{T} \rangle_{65^\circ\text{N}-90^\circ\text{N}}^{180-280\text{ hPa}}$ (middle), and their difference $\bar{T}_{\text{TUT}} - \bar{T}_{\text{PLS}}$ (bottom) as functions of the heating amplitude q_0 (left column) as well as the maximum zonal-mean zonal wind \bar{u}_{max} at 10 hPa (top) and the latitude ϕ_{max} of the maximum zonal-mean winds at 100 (middle) and 300 hPa (bottom) as functions of \bar{T}_{TUT} (middle column) and $\bar{T}_{\text{TUT}} - \bar{T}_{\text{PLS}}$ (right column) for all available NPV, REF, and CLS experiments.

for the NPV-d10 and REF-d10 experiments with $\delta_z = 10\text{ K}$ employing the standard heating, and one group for the REF-mod experiment with $\delta_z = 4.3\text{ K}$ employing the modified heating. Both groups employing the standard heating share the same gradient of \bar{T}_{TUT} with respect to q_0 although the experiments with $\delta_z = 10\text{ K}$ are slightly offset to higher temperatures. The experiment with modified heating exhibits a less strong gradient of $\bar{T}_{\text{TUT}}(q_0)$, consistent with the smaller region that is heated (bottom left panel of Fig. 2.1).

Expressing the polar vortex strength (\bar{u}_{max} at 10 hPa), the latitude of the lower polar vortex (ϕ_{max} at 100 hPa), and the latitude of the tropospheric jet (ϕ_{max} at 300 hPa) as functions of \bar{T}_{TUT} , all experiments are clustered according to their stratospheric setup, regardless of the precise realization of TUTW (middle column of Fig. 4.15). The REF (CLS) experiments

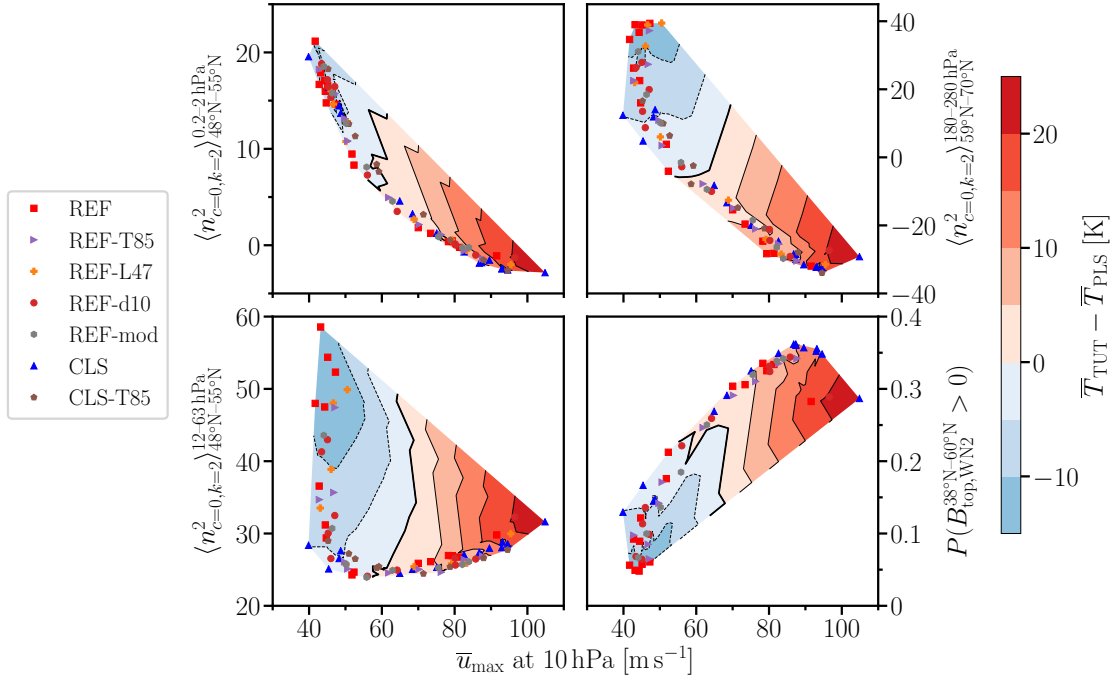


Figure 4.16: Climatological-mean values of the refractive index squared $n_{c=0, k=2}^2$ for stationary waves of wavenumber 2 (WN2) averaged over three different regions, namely at 0.2–2 hPa and 48°N–55°N (top left), at 12–63 hPa and 48°N–55°N (bottom left), and at 180–280 hPa and 59°N–70°N (top right), as well as the probability that the WN2 EP flux at 100 hPa integrated from 38°N to 60°N is downward, $P(B_{\text{top}, \text{WN2}}^{38^\circ\text{N}-60^\circ\text{N}} > 0)$ (bottom right), as functions of the polar vortex strength (\bar{u}_{\max} at 10 hPa) for all available experiments with polar vortex. The color shading represents the temperature difference between the tropical upper troposphere (TUT) and the polar lower stratosphere (PLS) with a contour interval of 5 K and a black zero-contour line.

exhibit a sharp strengthening of the polar vortex at $\bar{T}_{\text{TUT}} \gtrsim 217 \text{ K}$ ($\bar{T}_{\text{TUT}} \gtrsim 210 \text{ K}$) which is accompanied by an enhanced poleward shift of the tropospheric jet compared to the tropospheric jet of the NPV experiments.

In the study of Wang et al. (2012), the regime transition of the stratospheric polar vortex happens at temperature increases of the TUT of around 10 K, with uncertainty arising from resolution dependencies. In the REF experiment performed with EMIL (Garny et al., 2020), similar critical warming levels of the TUT are found, but hardly any resolution dependency. Resolution might have an impact on the sharpness of the regime transition in these simulations for a fixed set of heating amplitudes, but the strength of the polar vortex perfectly aligns when displayed as a function of \bar{T}_{TUT} .

The offset in the critical value of \bar{T}_{TUT} between the REF and CLS experiments can be attributed to temperature differences in the polar lower stratosphere (PLS). This is due to the fact that REF and CLS experiments are forced with different stratospheric equilibrium temperatures whose difference is most pronounced in the PLS. The center left panel of Fig. 4.15

shows a nonlinear relation of the average PLS temperature $\bar{T}_{\text{PLS}} := \langle \bar{T} \rangle_{65^{\circ}\text{N}-90^{\circ}\text{N}}^{180-280\text{hPa}}$ as a function of q_0 for all experiments consistent with their respective RC strengths (see Figs. 7 and 9 of Wang et al., 2012). \bar{T}_{PLS} stays approximately constant or slightly increases with respect to q_0 during the weak regime in all REF experiments consistent with the strengthened RC. At the transition to the strong polar vortex regime, a sudden cooling of the PLS is observed due to the sharp weakening of the RC. Once the strong polar vortex regime is reached, \bar{T}_{PLS} stays constant again. The behavior of \bar{T}_{PLS} in the CLS experiments is similar, but exhibits an offset by about 10 K towards lower temperatures.

Remarkably, the different stratospheric conditions of REF and CLS experiments can be reconciled when the polar vortex strength is displayed as a function of $\bar{T}_{\text{TUT}} - \bar{T}_{\text{PLS}}$ (top right panel of Fig. 4.15). Furthermore, the sharp strengthening of the polar vortex during the transition from the weak to the strong regime seems to occur near $\bar{T}_{\text{TUT}} = \bar{T}_{\text{PLS}}$. While \bar{T}_{PLS} is strongly coupled to the polar vortex strength, it is emphasized here that thermal forcings differ between the REF and CLS experiments in the PLS.

Testing the proposed mechanism of the previous section regarding the changes of the waveguide accompanying the PVRT, the refractive index for stationary waves of WN2 $n_{c=0,k=2}^2$ averaged for three different regions as well as the probability $P(B_{\text{top},\text{WN2}}^{38^{\circ}\text{N}-60^{\circ}\text{N}} > 0)$ that the WN2 EP flux at 100 hPa integrated from 38°N to 60°N is downward are shown in Fig. 4.16 as functions of the polar vortex strength (\bar{u}_{max} at 10 hPa). The regions for which $n_{c=0,k=2}^2$ is averaged are located at the top of the polar vortex at 0.2–2 hPa and 48°N – 55°N (top left panel), at the equatorward part of the polar vortex at 12–63 hPa and 48°N – 55°N (bottom left panel), and in high latitudes below the polar vortex at 180–280 hPa and 59°N – 70°N (top right panel).

At a first glance, the conformity of the entire set of experiments with polar vortex is visible and confirms that a unique behavior of the waveguide as a function of the polar vortex strength is observed in this study regardless of tropospheric or stratospheric realizations. The probability of downward WN2 EP flux in midlatitudes increases from 5 to 15% in the weak polar vortex regime without any significant strengthening of the polar vortex. The strong polar vortex regime with $\bar{u}_{\text{max}} > 60\text{ m s}^{-1}$ and $P(B_{\text{top},\text{WN2}}^{38^{\circ}\text{N}-60^{\circ}\text{N}} > 0) > 25\%$ is reached in some experiments via an intermediate step. The roughly linear decrease of the refractive index at the top of the polar vortex with increasing polar vortex strength suggests that the probability of the formation of a reflecting surface in the upper stratosphere rather gradually increases from the weak to the strong regime (Harnik and Lindzen, 2001). Thus, enhanced occurrence of reflecting surfaces in the upper stratosphere is not able to explain the sharp strengthening of the polar vortex during the regime transition since planetary-scale waves are still able to spread meridionally and dissipate close to critical surfaces in the subtropical stratosphere. Instead, the PVRT is only observed after a minimum of the refractive index on the equatorward side as well as a sufficiently wide region of negative refractive index on the poleward side of the polar vortex are simultaneously reached, consistent with Perlwitz and Harnik (2003) and Shaw et al.

(2010), such that wave dissipation close to critical surfaces in the subtropical stratosphere is prohibited allowing the polar vortex to strengthen. Although the presumed regions of wave evanescence have to be confirmed (see footnote 12), the consistent formation of a confined waveguide in all experiments when the polar vortex sharply strengthens together with the enhanced poleward shift of the tropospheric jet compared to the experiments without polar vortex supports downward wave coupling as the relevant process for the regime transition.

4.6 Sensitivity to the tropical heating location

In the previous section, the robustness of the dynamical mechanism underlying the PVRT in response to TUTW was established by varying the model resolution, the tropospheric stratification, and the shape of the thermal forcing in the tropical upper troposphere. In this section, the sensitivity of circulation changes to the vertical location of the thermal forcing in the tropics is investigated. To this end, the REF-mod experiment with resolution T85L47 and with the shallow modified thermal forcing of Eq. (2.11) centered at $z_0 = 0.3$ is supported by experiments with modified thermal forcings centered in the lower stratosphere at $z_0 = 0.1$ (REF-mod-LS) and in the middle troposphere at $z_0 = 0.5$ (REF-mod-MT). At first, latitude and strength of zonal-wind maxima in the REF-mod-LS and REF-mod-MT experiments are compared to the REF-mod experiment at four different pressure levels in the troposphere and stratosphere.

When the tropical heating is located in the lower stratosphere, similar circulation changes as in the REF-mod experiment are observed in the stratosphere which are, however, not as sharp, as shown in Fig. 4.17. The polar vortex at 10 hPa weakens for heating amplitudes up to $q_0 = 0.6 \text{ K day}^{-1}$, and strengthens for heating amplitudes beyond, and exhibits a moderate equatorward shift at larger heating. At the extreme heating amplitude of $q_0 = 2 \text{ K day}^{-1}$, the polar vortex strength of the REF-mod-LS experiment is comparable to the strong polar vortex regime of the REF-mod experiment with a very small probability of SSWs. In the lower stratosphere at 100 hPa, increased heating of tropical regions leads to an approximately linear strengthening and equatorward shift of the polar vortex consistent with thermal wind balance. In contrast to this, the circulation in the troposphere seems to experience almost no changes in the REF-mod-LS experiment as shown in Fig. 4.18. The latitude of the tropospheric jet at 300 hPa stays constant during the entire course of the experiment, and its strength decreases only slightly. At 850 hPa, a transition of the climatological-mean jet position to its poleward regime is observed at $q_0 = 1.6 \text{ K day}^{-1}$, but probabilities for the equatorward regime retain a finite magnitude.

When the tropical heating is located in the middle troposphere, stratospheric circulation changes gain some degree of sharpness. The polar vortex strength at 10 hPa decreases up to $q_0 = 1 \text{ K day}^{-1}$, after which a faster increase than in the REF-mod-LS experiment is

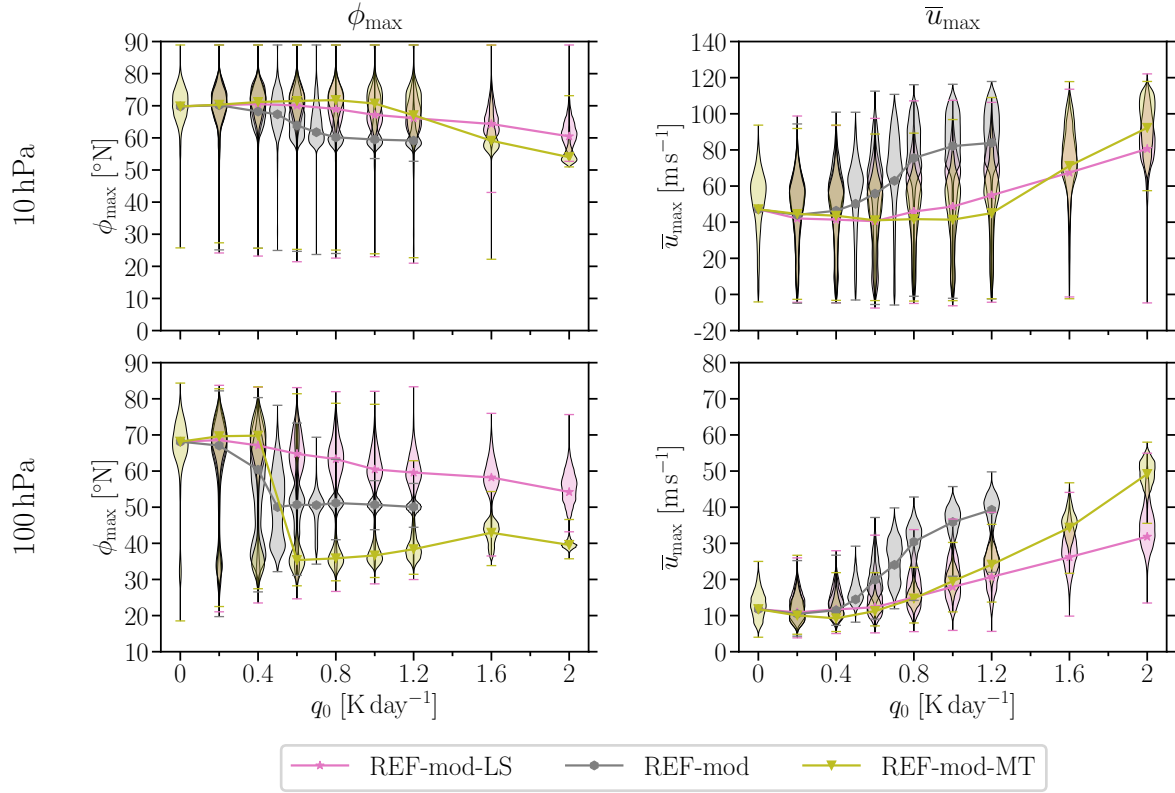


Figure 4.17: Same as Fig. 4.4, but for the REF-mod-LS, REF-mod, and REF-mod-MT experiments.

observed. The latitude of the polar vortex at 10 hPa moves even further equatorward than in the REF-mod experiment. At 100 hPa, latitude and strength of the zonal-mean zonal wind maximum are clearly influenced by the tropospheric jet for $q_0 \geq 0.6 \text{ K day}^{-1}$. Whereas the zonal-wind maximum at 100 hPa stays around 70°N up to $q_0 = 0.4 \text{ K day}^{-1}$, a jump to subtropical latitudes is observed at $q_0 = 0.6 \text{ K day}^{-1}$ in the climatological mean with a moderate poleward shift onward. The tropospheric jet at 300 hPa shifts only slightly poleward for increased heating amplitudes compared to the REF-mod experiment, but exhibits a linear strengthening consistent with thermal wind balance due to the maximum heating centered below at approximately 500 hPa. Constantly strengthening, the tropospheric jet eventually reaches a sufficient extent to dominate ϕ_{max} and \bar{u}_{max} at 100 hPa in the climatological mean for $q_0 \geq 0.6 \text{ K day}^{-1}$. Due to the expanding troposphere and the rising lower part of the polar vortex, the equatorward shift of the LS polar vortex in the REF-mod-MT experiment is not captured by ϕ_{max} at 100 hPa, but visible via ϕ_{max} at 10 hPa for $q_0 \geq 0.8 \text{ K day}^{-1}$. Similar to the other experiments, a transition of the jet at 850 hPa from its equatorward to its poleward regime can be observed which occurs at the same heating amplitude as in the REF-mod experiment, but the jet location at 850 hPa remains constantly equatorward of 40°N afterwards.

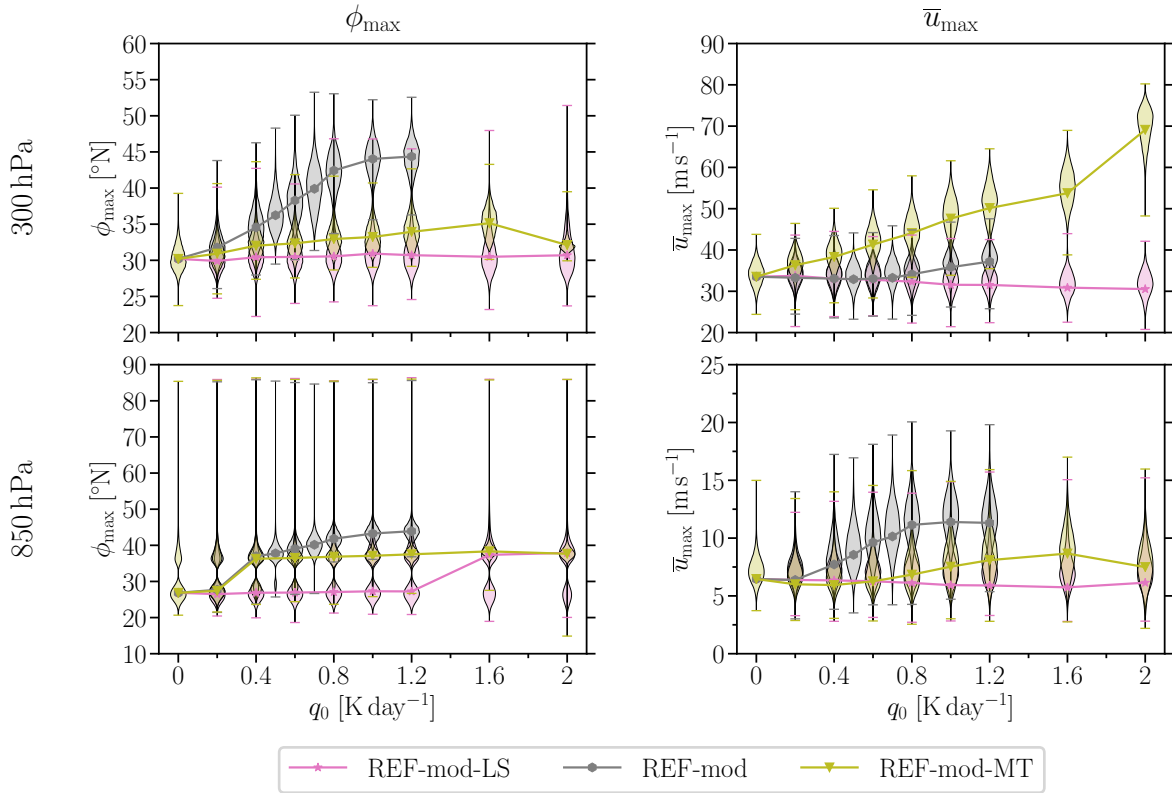


Figure 4.18: Same as Fig. 4.5, but for the REF-mod-LS, REF-mod, and REF-mod-MT experiments.

The different tropospheric-jet responses at 300 hPa of the REF-mod experiment with heating in the upper troposphere and the REF-mod-MT experiment with heating in the middle troposphere can be shown to be consistent with the different evolutions of the Hadley cell (HC). Ascending tropospheric air masses close to the equator are subject to move poleward below the tropopause. Due to the conservation of angular momentum, westerly winds are generated in subtropical regions. Hence, the strength of the HC is connected to the strength of the subtropical jet in good approximation (Schneider, 1977; Held and Hou, 1980; Kim and Lee, 2004). Here, the streamfunction of the climatological-mean Eulerian-mean meridional circulation

$$\Psi = \frac{2\pi a \cos(\phi)}{g} \int_0^P \bar{v} dp' \quad (4.5)$$

is used to quantify strength and meridional extent of the HC. Similar to the residual circulation strength, the HC strength is determined by the sum of the maximum streamfunction in the northern hemisphere and the magnitude of the minimum streamfunction in the southern hemisphere, i.e., by $\max(\Psi_{\phi>0}) + |\min(\Psi_{\phi<0})|$. The HC edge is given by the latitude where $\Psi = 0$ in subtropical regions. In the REF-mod experiment, the HC weakens and expands as shown in the top panels of Fig. 4.19, which is in line with a minor decrease of the tropospheric

jet strength at 300 hPa up to $q_0 = 0.6 \text{ K day}^{-1}$ and its poleward shift, respectively. Bottom left and bottom center panels of Fig. 4.19 reveal that the expansion of the HC proceeds uniformly at different heights. Weakening and expansion of the HC in response to global warming are robust results from idealized and complex GCMs (Butler et al., 2010; Wang et al., 2012; Frierson et al., 2007b; Lu et al., 2007) as well as from observations (Fu et al., 2006; Seidel and Randel, 2007; Seidel et al., 2008; Staten et al., 2020). In this regard, idealized GCMs with TUTW are able to mimic relevant tropospheric features of greenhouse-gas induced global warming. Apart from climatological time scales, HC edge and latitude of the subtropical jet, however, exhibit considerable differences (see Menzel et al., 2019, and references therein).

In the REF-mod-MT experiment, the correlation between the strength of the tropospheric jet and the HC at 300 hPa is very strong, whereas the latitude of the jet and the HC edge in the northern hemisphere do not agree very well during the course of the experiment. On closer inspection, the Eulerian-mean circulation reveals the development of two separated centers of the HC located around 300 and 900 hPa in the REF-mod-MT experiment as shown in the bottom right panel of Fig. 4.19. A reason for the development of two separated HC centers could be increased and decreased static stability below and above the mid-tropospheric heating, respectively. The circulation cell in the lower troposphere weakens and expands in response to increased heating similar to the REF-mod experiment. In contrast to this, the circulation cell in the upper troposphere strengthens with only minor changes in its latitudinal extent which is consistent with the accelerating, but latitudinally constrained tropospheric jet at 300 hPa. In the REF-mod-LS experiment, the Eulerian-mean circulation barely exhibits any deviations from the control-run circulation displayed in the bottom left panel of Fig. 4.19 (not shown) which is in accordance with the previously mentioned undisturbed tropospheric jet. Although both the REF-mod-LS and REF-mod-MT experiments with additional heating located in the lower stratosphere and in the middle troposphere, respectively, clearly lack realistic tropospheric circulation changes compared to the REF-mod experiment, their wave activity fluxes and waveguides will be analyzed in the following. In this way, both experiments with heating away from the tropical upper troposphere can serve as complementary tests for the dynamical mechanism underlying the PVRT.

In contrast to the critical-layer rise mechanism relevant in TUTW experiments where wave activity originating from the troposphere is able to propagate higher up into the stratosphere, the heating in the lower stratosphere of the REF-mod-LS experiment acts as an additional source of wave activity directly in the stratosphere as shown in the top panels of Fig. 4.20. Especially at the large heating amplitude of $q_0 = 1.6 \text{ K day}^{-1}$, an unrealistic region of positive EPFD above the tropospheric jet extending from the tropics to midlatitudes is visible. The result is, however, similar to the TUTW experiments and represents an elevated region of pronounced wave-flux dissipation in the subtropics compared to the control run presented in Fig. 4.8. Hence, the strength of the lower-stratospheric residual circulation increases, and due

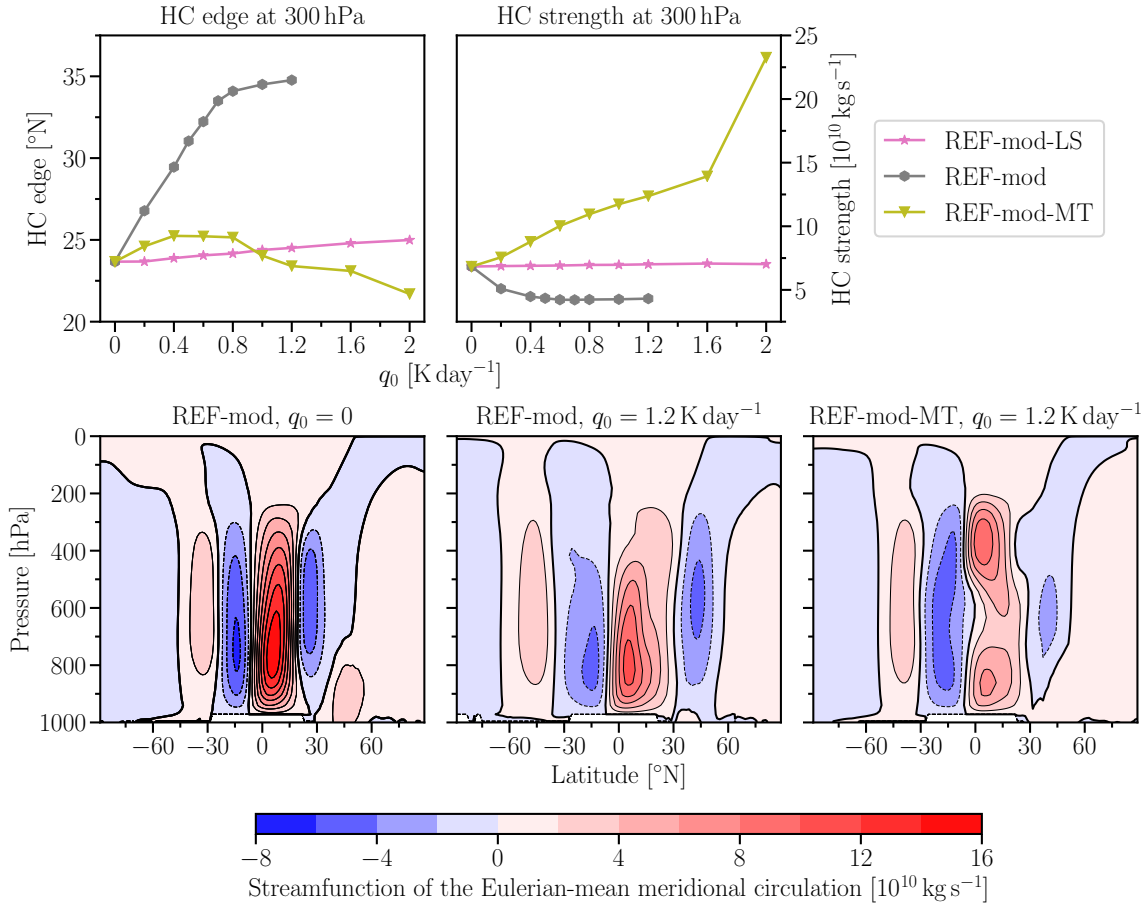


Figure 4.19: Hadley cell (HC) edge in the northern hemisphere (top left) and HC strength (top center) at 300 hPa as functions of the heating amplitude q_0 for the REF-mod-LS, REF-mod, and REF-mod-MT experiments in combination with the streamfunction of the Eulerian-mean meridional circulation as function of latitude and pressure for the REF-mod experiment without additional heating (bottom left), and with $q_0 = 1.2 \text{ K day}^{-1}$ (bottom center), as well as for the REF-mod-MT experiment with $q_0 = 1.2 \text{ K day}^{-1}$ (bottom right). In the entire REF-mod-LS experiment, the Eulerian-mean streamfunction remains very similar to the streamfunction of the REF-mod experiment at $q_0 = 0$.

to the additional heat source in the tropical lower stratosphere, it increases faster than in the REF-mod experiment (not shown). Such a strong residual circulation is able to considerably attenuate the meridional temperature gradient associated with the polar vortex, which is why extreme heating amplitudes are necessary to cause a significant increase in the polar vortex strength. Furthermore, the zonal-mean structure which is formed at intermediate and large heating amplitudes shown in the top panels of Fig. 4.21 exhibits a shallow region of high refractive index squared for stationary planetary-scale waves above 100 hPa. Thus, even in case of a strong polar vortex with large probability of a reflecting surface in the upper stratosphere, the zonal-mean structure lacks a meridionally confined waveguide such that reflected waves more likely reach critical lines in subtropical regions where they dissipate instead of influencing the troposphere (Perlwitz and Harnik, 2003; Shaw et al., 2010). Under these circumstances,

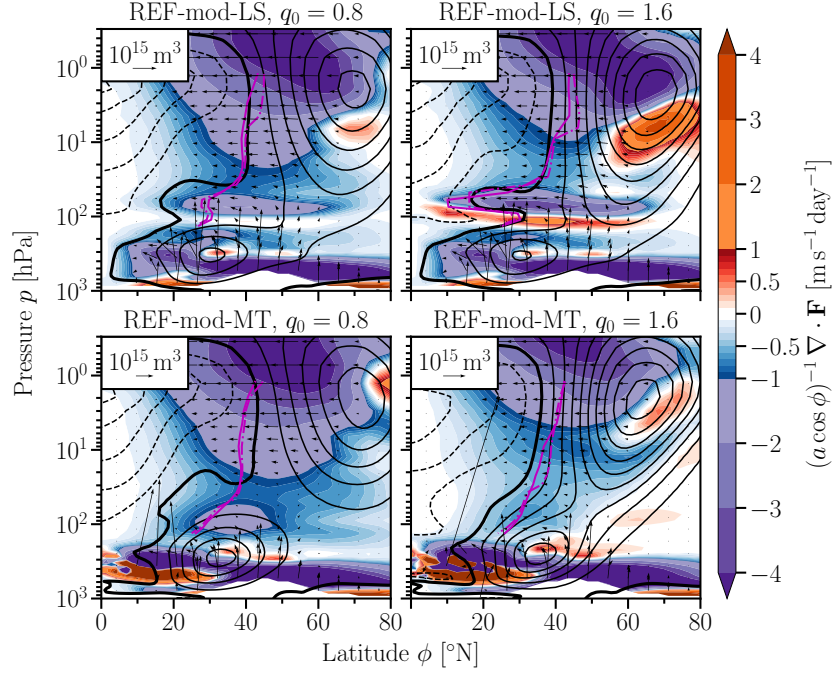


Figure 4.20: Tendencies of the zonal-mean zonal wind by the total Eliassen–Palm (EP) flux divergence $\bar{\mathcal{F}} = (a \cos \phi)^{-1} \nabla \cdot \mathbf{F}$ (color shading), total EP flux arrows $\hat{\mathbf{F}} = (\hat{F}^{(\phi)}, \hat{F}^{(p)})$ (arrows), and zonal-mean zonal winds (black contour lines with a contour interval of 10 m s^{-1} , negative contours dashed, thick zero-contour line) as functions of latitude and pressure for the REF-mod-LS (top) and REF-mod-MT (bottom) experiments with $q_0 = 0.8 \text{ K day}^{-1}$ (left) and $q_0 = 1.6 \text{ K day}^{-1}$ (right). EP flux arrows are defined as $(\hat{F}^{(\phi)}, \hat{F}^{(p)}) = 2\pi a g^{-1} \cos \phi (F^{(\phi)}, aF^{(p)}) / (-80.4 \text{ kPa})$ according to Edmon et al. (1980). The solid and dash-dotted magenta lines represent the turnaround latitudes of the residual-mean meridional circulation Ψ^* and the downward-control circulation Ψ_{dc}^* , respectively (McLandress and Shepherd, 2009; Haynes et al., 1991).

stratosphere-troposphere coupling in the sense of the strong polar vortex regime of previous TUTW experiments is absent, consistent with the fixed position of the mid-tropospheric jet in the REF-mod-LS experiment.

The accelerating and expanding tropospheric jet in the REF-mod-MT experiment again promotes a proper critical-layer rise mechanism similar to the weak polar vortex regime of previous TUTW experiments, elevating the region of pronounced wave-flux dissipation in the subtropics as shown in the bottom left panel of Fig. 4.20. From heating amplitudes larger than $q_0 = 1.2 \text{ K day}^{-1}$ onward, this region of pronounced wave-flux dissipation in the subtropics disappears and also the upper stratosphere experiences less deceleration (bottom right panel of Fig. 4.20) which is consistent with the sharp increase of \bar{u}_{max} at 10 hPa and reminiscent of the strong polar vortex regime established in the previous sections. Simultaneously, more wave activity is refracted equatorward within the troposphere. Taking the refractive index squared for stationary waves of wavenumber 2 into account as shown in the bottom panels of Fig. 4.21, the waveguides in the REF-mod-MT experiment at $q_0 = 0.8 \text{ K day}^{-1}$ and $q_0 = 1.6 \text{ K day}^{-1}$

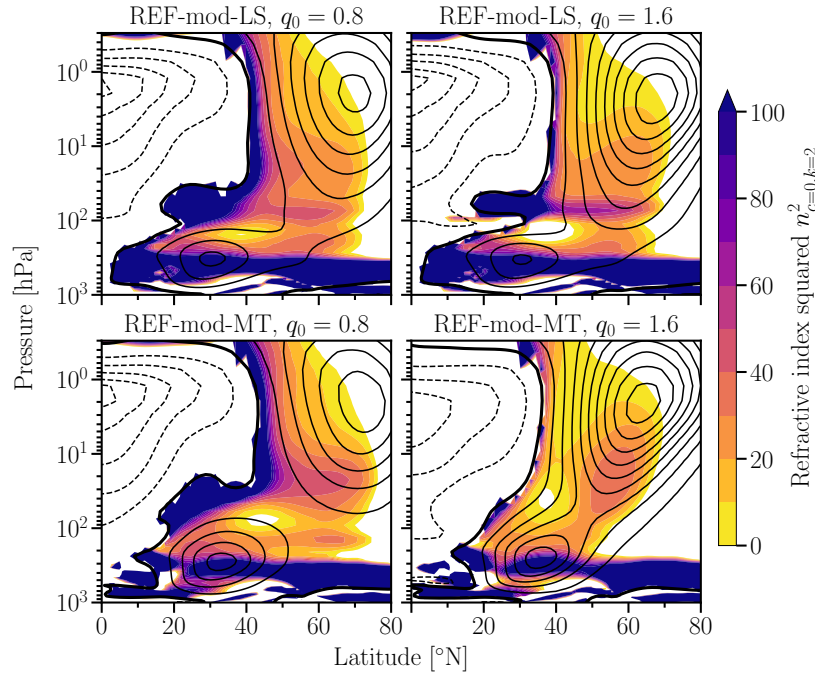


Figure 4.21: Refractive index squared $n_{c=0, k=2}^2$ for stationary waves of wavenumber 2 (color shading with a contour interval of 10) and zonal-mean zonal wind (black contour lines with a contour interval of 10 m s^{-1} , negative contours dashed, thick zero-contour line) as functions of latitude and pressure for the REF-mod-LS (top) and REF-mod-MT (bottom) experiments with $q_0 = 0.8 \text{ K day}^{-1}$ (left) and $q_0 = 1.6 \text{ K day}^{-1}$ (right).

indeed are very similar to the waveguides of the weak and strong polar vortex regimes of the REF experiments, respectively (see Fig. 4.13). At $q_0 = 1.6 \text{ K day}^{-1}$, supposedly representing the strong polar vortex regime, the waveguide of the REF-mod-MT experiment exhibits a similar region of minimum refractive index squared on the equatorward side of the polar vortex which has previously been identified to be crucial to guide reflected wave activity back to the troposphere. The main differences between the climate states with strong polar vortices in the REF-mod-MT and the REF experiments are the larger vertical extent of the troposphere in the REF-mod-MT experiment caused by the mid-tropospheric heating and the mitigated poleward shift of the tropospheric jet. A more enhanced poleward shift of the tropospheric jet might be suppressed by the strong and narrow upper-tropospheric HC center. Likewise, the accelerated and expanded tropospheric jet might already have reached a maximum poleward position. Nevertheless, the similarities of the zonal-mean flow in the REF-mod-MT experiment for $q_0 \geq 1.6 \text{ K day}^{-1}$ to the strong polar vortex regime suggest that the sharp increase of the polar vortex strength could also be accompanied by an increased number of downward wave coupling events which will be investigated in the future.

Both the REF-mod-LS and REF-mod-MT experiments further support the developed dynamical mechanism responsible for the PVRT in this chapter. In both experiments, a strengthened

RC in the lower stratosphere is observed in response to moderate heating amplitudes (not shown), and the LS polar vortex shifts equatorward. At a critical heating amplitude larger than $q_0 = 1.2 \text{ K day}^{-1}$, the polar vortex in the REF-mod-MT experiment transitions to a strong and stable regime and a meridionally confined waveguide for planetary-scale waves is formed. Although an enhanced poleward shift of the tropospheric jet accompanying the regime transition is suppressed, the reorganization of EP fluxes in the REF-mod-MT experiment proceeds similarly to the previous TUTW experiments. In the REF-mod-LS experiment, the LS RC keeps increasing even for large heating amplitudes (not shown). Due to extremely far equatorward located turnaround latitudes of the RC in the LS, the strong RC does not contradict a strong polar vortex. In any case, the strong polar vortex in the REF-mod-LS experiment is not able to influence the position of the mid-tropospheric jet or the tropospheric wave activity fluxes, consistent with the absence of low values of the refractive index squared on the equatorward side of the polar vortex. Reflected wave activity is therefore not able to influence the troposphere.

Furthermore, the REF-mod-LS experiment resembles the polar-stratospheric cooling experiment with identical topography (WN2T) and transition pressure of $p_T \equiv 100 \text{ hPa}$ (compare Figs. 4.17 and 4.18 with the top panels of Fig. 3.11). In both experiments, stratospheric circulation changes represent a strengthening of the polar vortex which are not able to influence the location of the mid-tropospheric jet. This suggests a more general condition for the strength of stratosphere-troposphere coupling which is searched for in the next chapter. In the following section, the guiding hypotheses of Sec. 4.1 are evaluated.

4.7 Discussion

The results of Secs. 4.2–4.6 confirm hypotheses 1, 3, and 4, and provide evidence for hypothesis 2.

1. In all TUTW experiments with (REF and CLS) and without polar vortex (NPV) the CLCM (Shepherd and McLandress, 2011) for stationary planetary-scale waves is able to explain the strengthened shallow branch of the RC. In the NPV experiment, the CLCM continues to be at work for increasing heating of all amplitudes investigated here. In the REF and CLS experiments, this mechanism terminates for heating rates at which the tropospheric jet and the LS polar vortex have sufficiently converged to shrink the critical line in subtropical regions to a minimum latitudinal extent.

A strengthened shallow branch of the RC is also observed in the REF-mod-LS and REF-mod-MT experiments where the tropical heating is located in the lower stratosphere and in the middle troposphere, respectively (not shown). In the REF-mod-MT experiment, not only the upper flanks of the tropospheric jets, but the entire jets are accelerated, consistent with a stronger upper-tropospheric HC compared to the TUTW experiments,

which are responsible for a similar CLCM. In the REF-mod-LS experiment, the strengthened shallow branch of the RC can, however, not be associated with the CLCM. The tropical heating located in the lower stratosphere directly increases tropical upwelling and constitutes an unrealistic source of wave activity located in the subtropical lower stratosphere dissipating directly above, both of which driving a stronger RC.

2. In presence of a polar vortex in the REF and CLS experiments, the strengthened shallow branch of the RC in the weak regime is consistent with structural changes in the LS that result in an equatorward shift of the LS polar vortex. The equatorward shift of the LS polar vortex is further consistent with enhanced equatorward refraction of planetary-scale wave flux due to the poleward and upward expansion of the tropospheric jet. Hence, further equatorward located deceleration of LS zonal-mean zonal winds is consistent with the LS polar vortex approaching the latitudes of strongest meridional gradient of the equilibrium temperature around 50°N in this idealized model setup.

The equatorward shift of the lower polar vortex in the REF experiments proceeds non-linearly in contrast to the linear strengthening of the LS RC in the weak polar vortex regime. This hints at a critical poleward and upward expansion of the tropospheric jet in the REF experiments for which sufficient amount of planetary-scale wave flux is refracted equatorward to induce the equatorward shift of the lower polar vortex. This is supported by the NPV experiments, where in absence of a polar vortex a sufficient pole- and upward expansion of the tropospheric jet is necessary for planetary-scale waves to reach the turnaround latitudes in the subtropical LS. Likewise, the REF-mod-MT experiment exhibits an equatorward shift of the LS polar vortex only after a similar vertical extent of the tropospheric jet is reached (not shown). The equatorward shift of the LS polar vortex in the REF-mod-LS experiment proceeds more linearly since the strengthening of the LS RC is directly caused by the tropical heat source in the LS which, nevertheless, is consistent with hypothesis 2.

The exact interplay between enhanced equatorward planetary-scale EP flux, the equatorward shift of the LS polar vortex, and the thermal structure of the LS can, however, not be disentangled with steady-state simulations. Furthermore, it remains to be clarified whether the somewhat unrealistic representation of the separation of the subtropical jet and the eddy-driven jet in the dynamical-core model influences the nature of the dynamical response in the LS to TUTW (Lu et al., 2010).

3. The regime transition to a strong and stable polar vortex at a critical TUTW level in the REF and CLS experiments is consistent with the reorganization of EP fluxes. Less EP flux propagates upward into the stratosphere and more EP flux is instead refracted equatorward in the troposphere as previously found by Wang et al. (2012). The fundamental change of the waveguide for planetary-scale waves is consistent with this

reorganization at the critical TUTW level. A reflecting surface in the upper stratosphere as well as a meridionally confined waveguide in the middle stratosphere are developed when number and duration of downward wave flux events sharply increase.

A critical warming level is also present in the REF-mod-MT experiment inducing a sharp strengthening of the polar vortex in combination with a reflecting surface in the upper stratosphere as well as a meridionally confined waveguide in the middle stratosphere. Similarly, less EP flux propagates upward into the stratosphere and more EP flux is refracted equatorward in the troposphere. Whether a sharp increase in number and duration of downward wave flux events can also be observed remains an open question. The polar vortex strength in the REF-mod-LS experiment increases more continuously after a minimum strength has been reached at $q_0 = 0.6 \text{ K day}^{-1}$, and the waveguide for planetary-scale waves does not develop a meridionally confined structure. Accordingly, no sharp reorganization of EP fluxes is present in the REF-mod-LS experiment.

4. Compared to the experiments without polar vortex (NPV), an enhanced poleward shift of the tropospheric jet is observed in the strong polar vortex regime of the REF and CLS experiments. Together with the reflecting configuration of a meridionally confined waveguide for planetary-scale waves, strong evidence for downward wave coupling in the strong polar vortex regime is provided.

The characteristics of a wave guide enabling downward wave coupling events (Perlwitz and Harnik, 2003; Shaw et al., 2010) have to be detected with separate refractive indices for meridional and vertical propagation of planetary-scale waves (Harnik and Lindzen, 2001). Nevertheless, similarities of the general refractive index squared $n_{c,k}^2$ for propagation in the meridional plane are found between the weak and strong polar vortex regimes of this chapter (Fig. 4.13) and two episodes of the 1996 southern hemisphere winter characterized by separate refractive indices to represent one nonreflective and one reflective episode which are shown in Fig. 4.22 (Harnik and Lindzen, 2001).

In the weak polar vortex regime as well as in the nonreflective episode of the southern polar vortex for 18 Jul–19 Aug 1996, contour lines of the refractive index squared are equatorward tilted with increasing height in the high-latitude upper stratosphere, and a meridionally wide region of refractive index squared above 10 is found in midlatitudes guiding wave activity to the top of the atmosphere. Under these circumstances, no reflecting surface is observed for vertical propagation (Harnik and Lindzen, 2001). In contrast to this, in the reflective episode of the southern polar vortex for 1–30 Sep 1996, contour lines of the refractive index squared are more horizontally aligned in the high-latitude stratosphere, whereas in the strong polar vortex regime, they are even poleward tilted with increasing height. In either case, values of the refractive index larger than 10 in the upper stratosphere are only found in a very narrow region in midlatitudes. As

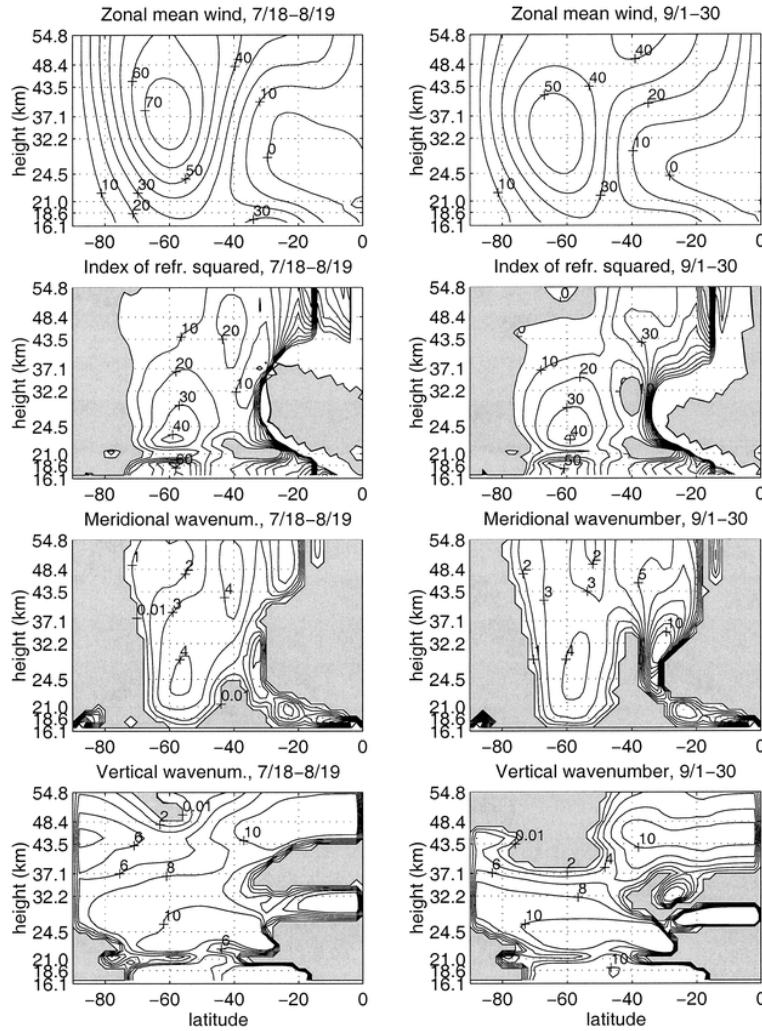


Figure 4.22: Zonal-mean zonal wind in m s^{-1} (first row), refractive index squared (second row), meridional wavenumber in rad^{-1} (third row), and vertical wavenumber in 10^{-5} m^{-1} (fourth row) for stationary waves of wavenumber 1 for 18 Jul–19 Aug (left) and 1–30 Sep (right) 1996. The figure is taken from Harnik and Lindzen (2001).

found by Harnik and Lindzen (2001), this configuration exhibits a reflecting surface in the high-latitude upper stratosphere as well as a meridionally confined waveguide. The fact that the southern polar vortex in the nonreflective episode for 18 Jul–19 Aug 1996 actually is stronger than in the reflective episode for 1–30 Sep 1996 is counterintuitive to the characterizations of weak and strong polar vortex regimes, but only the curvature of the zonal-mean zonal wind rather than its actual strength enters the calculation of the general refractive index squared $n_{c,k}^2$ (Harnik and Lindzen, 2001; Simpson et al., 2009; Gerber, 2012).

Due to the noticeable influence of the PVRT on the troposphere (in comparison to the experiments without polar vortex) and the increase in downward wave flux events,

downward wave coupling is considered to be the relevant process in the strong polar vortex regime (Perlwitz and Harnik, 2003; Shaw et al., 2010). Nevertheless, future investigations need to confirm downward wave coupling, e.g., by time lagged correlations of planetary-scale waves (Perlwitz and Graf, 2001; Perlwitz and Harnik, 2003, 2004; Shaw et al., 2010; Shaw and Perlwitz, 2013) in addition to separate refractive indices for meridional and vertical wave propagation (Harnik and Lindzen, 2001).

Lacking the meridionally confined waveguide for planetary-scale waves, even a strong polar vortex in the REF-mod-LS experiment is not able to influence the mid-tropospheric jet. This constitutes another confirmation of the dynamical mechanism developed in this chapter since only climate states with meridionally confined waveguides are associated with enhanced poleward shifts of the tropospheric jet. Although the REF-mod-MT experiment does not exhibit this enhanced tropospheric-jet shift when the polar vortex sharply strengthens, less wave activity enters the stratosphere from the troposphere, and more wave activity is refracted equatorward within the troposphere. The tropospheric jet in the REF-mod-MT experiment might already have reached a sufficient strength and meridional extent consistent with a strong and narrow upper-tropospheric HC center that prevent the jet from further poleward shifts. Additional analyses are necessary to characterize the regime transition in the REF-mod-MT experiment more precisely.

4.8 Conclusions

In order to investigate the transition of the stratospheric polar vortex from a weak and highly variable to a strong and stable regime in response to tropical upper-tropospheric warming (TUTW), and to answer the specific research question **S2**, simulations with an idealized general circulation model were performed. To this end, the TUTW experiment of Wang et al. (2012) was reproduced in presence of a polar vortex providing a reference experiment. It was confirmed that the polar vortex regime transition (PVRT) is accompanied by a reorganization of Eliassen–Palm (EP) fluxes with less wave activity entering the stratosphere, and more wave activity being refracted equatorward in the troposphere. Extending the work by Wang et al. (2012), the dynamical mechanism responsible for the PVRT and its corresponding influence on the troposphere (Fig. 4.1) could be revealed by repeating the simulated tropical warming levels of the reference experiment, but without polar vortex.

The response of the stratospheric circulation to TUTW is dominated by the critical-layer control mechanism (CLCM, Shepherd and McLandress, 2011) for all heating amplitudes in a state without polar vortex, and for heating amplitudes below a certain threshold in the state with polar vortex. Rising critical layers for planetary-scale Rossby waves enable more EP flux to enter the lower stratosphere (LS), which strengthens the residual circulation (RC). In the experiment without polar vortex, the poleward shift and the upward expansion of the

tropospheric jet lead to a crossover where the LS RC is driven less by synoptic-scale waves and more by planetary-scale waves.

In presence of a polar vortex, the RC exhibits a localized region of maximum downwelling at its equatorward edge. Strengthening the RC via the CLCM influences the thermal structure of the LS in a way that is consistent with an equatorward shift of the LS polar vortex. A first critical point is reached when the poleward shifting tropospheric jet and the equatorward shifting LS polar vortex have converged sufficiently to reduce the contribution of synoptic-scale wave flux to the residual-circulation strength. Planetary-scale wave flux is, however, able to partly compensate the loss of synoptic-scale wave contributions (similar to the experiment without polar vortex) since the waveguide for planetary-scale waves strengthens in the LS. Consistent with the dynamics around the first critical point, a first enhanced poleward shift of the tropospheric jet compared to the experiment without polar vortex and a first strengthening of the polar vortex are observed in this intermediate regime.

The transition to the strong polar vortex regime is completed when the poleward moving tropospheric jet and the equatorward moving LS polar vortex develop a confined waveguide which reflects planetary-scale waves back to the troposphere where they are refracted equatorward (Perlwitz and Graf, 2001; Shaw and Perlwitz, 2013), representing the second critical point. This is accompanied by an enhanced poleward shift of the tropospheric jet compared to the experiment without polar vortex. A large set of sensitivity experiments with modified thermal forcing provides strong evidence that the polar vortex regime transition is robustly linked to the development of a reflective and meridionally confined waveguide. Consequently, the stratospheric modulation of the troposphere in presence of the strong polar vortex regime is associated with the occurrence of downward wave coupling events of planetary-scale waves (Perlwitz and Harnik, 2003; Shaw et al., 2010). When, in turn, the waveguide does not establish a meridionally confined structure in the middle stratosphere, as is the case in a different experiment with the tropical heating located in the lower stratosphere instead of in the tropical upper troposphere, the position of the tropospheric jet remains unaffected even for a strong polar vortex. This hints at the importance of circulation changes in the extratropical lower stratosphere below ≈ 200 hPa for stratosphere-troposphere coupling corroborating the results of Chap. 3 where it was found that polar-stratospheric cooling has to extend similarly far down in order to exert significant influence on the troposphere. Therefore, the first part of the following chapter is dedicated to extract a unified criterion for circulation changes that determines the strength of stratosphere-troposphere coupling in both the performed polar-stratospheric cooling and tropical warming experiments.

The revealed dynamical mechanism in this idealized-model study might be relevant for explaining circulation changes detected in complex climate models. In particular, the strengthening of the SH polar vortex (Jucker et al., 2021) and the variable and nonlinear response of the NH polar vortex to global warming (Manzini et al., 2014, 2018; Simpson et al., 2018; Kretschmer

et al., 2020) are not fully understood. Some circulation changes that are crucial to the proposed mechanism are observed in complex climate models, e.g., the RC acceleration associated with the upper-flank strengthening of the subtropical jets (Hardiman et al., 2014; Shepherd and McLandress, 2011), the equatorward shift of the LS polar vortex (Butchart et al., 2010; Scaife et al., 2012), and the poleward migration of tropospheric jets (Lorenz and DeWeaver, 2007; Barnes and Polvani, 2013). The dependence of the critical warming level on the stratospheric basic state as shown here might help to explain the large spread in future climate projections (Manzini et al., 2014; Simpson et al., 2018). The TUTW experiment with colder polar LS showed that temperature increases of the tropical upper troposphere beyond 2 K are sufficient to trigger the PVRT, whereas temperature increases beyond 8 K are necessary in the reference experiment. In general, the regime transition found in the idealized model might be blurred in complex models both due to a broader spectrum of planetary-scale waves and transient effects of the annual cycle. The relevance of the introduced dynamical mechanism beyond idealized climate models will be investigated in the second part of the following chapter by analyzing complex models with a prescribed 1%-increase in carbon dioxide (CO_2) concentrations per year (1pct CO_2) as part of the Coupled Model Intercomparison Project Phase 6 (CMIP6, Eyring et al., 2016).

Chapter 5

Combined perspectives and implications beyond idealized models

The previous chapters 3 and 4 revealed a nonlinear circulation response to polar stratospheric cooling (PSC, Polvani and Kushner, 2002; Gerber and Polvani, 2009) and tropical upper-tropospheric warming (TUTW, Butler et al., 2010; Wang et al., 2012) in idealized-model setups. At moderate forcing levels, the residual circulation accelerates in both experiments and prevents the stratospheric polar vortex from substantially strengthening, exerting no significant influence on the tropospheric circulation. In the PSC experiment, the acceleration of the residual circulation is induced by an improving waveguide for planetary-scale waves in midlatitudes. In the TUTW experiment, rising critical-layers in the subtropics enable more wave flux to drive a stronger lower-stratospheric residual circulation. Beyond critical forcing levels, however, sharp increases in the strength of the stratospheric polar vortex, accompanied by a weakening of the residual circulation, are observed in both PSC and TUTW experiments, leading to significant downward influence reflected by a poleward shift of the tropospheric jet. The statistics of vertical wave activity fluxes in the midlatitude stratosphere in combination with the portrayed circulation changes suggest downward wave coupling events (Perlwitz and Harnik, 2003; Shaw et al., 2010) as the relevant process that characterizes the regime transition. The similarities in both experiments motivate to investigate whether a confined waveguide for planetary-scale waves that accompanies the transition to a strong and stable polar vortex with significant tropospheric impacts is universally developed. This is the aim of the first part of this chapter. Since nonlinear circulation changes have previously been found in the northern hemisphere in response to increased greenhouse-gas concentrations (Manzini et al., 2018; Kretschmer et al., 2020), the second part of this chapter is dedicated to discuss the relevance of previous findings with respect to complex climate models. Addressing the specific research question **S3**, the experiment with a prescribed CO₂-concentration increase of 1% per year (1pctCO2) is consulted from the Coupled Model Intercomparison Project

Phase 6 (CMIP6) multi-model ensemble (Eyring et al., 2016). Tropospheric and stratospheric circulation changes as well as the evolution of waveguides for planetary-scale waves are analyzed for eleven CMIP6 models participating in the 1pctCO2 experiment in order to discuss whether nonlinear polar vortex responses can be explained by the dynamical mechanism found in idealized experiments.

5.1 Universal behavior of the waveguide in idealized models

As a reminder, the transition from a weak and variable to a strong and stable polar vortex in response to TUTW was found in Chap. 4 to be accompanied by the development of a confined waveguide for stationary waves of wavenumber 2 in combination with an increased probability of downward wave flux events of these planetary-scale waves (see Figs. 4.13, 4.14, and 4.16). Indications of a similar behavior were also found in response to sufficient PSC in Chap. 3 (see Figs. 3.9 and 3.13). Here, the results of all PSC experiments with an integration length of at least 10 years listed in Tab. 2.1, including simulations without additional planetary-scale wave generation (WN0), with idealized WN2 topography (WN2T), with idealized WN2 heating (WN2H), and with both $\delta_z = 4.3\text{ K}$ and $\delta_z = 10\text{ K}$, as well as the results of all REF and CLS experiments listed in Tab. 2.2 in presence of a polar vortex with an integration length of 30 years and employing WN2T are combined. Before the behavior of the corresponding waveguides in all experiments is extensively analyzed, the nonlinear circulation response to PSC and tropical warming is recapitulated via the strength of the residual circulation (RC) in the middle and lower stratosphere as shown Fig. 5.1.

Starting from weak polar vortices in the PSC experiments with $p_{\text{Tw}} = 100\text{ hPa}$ and $\gamma = 1\text{ K km}^{-1}$ where a large region of wave evanescence occupies the midlatitude lower stratosphere as shown in Fig. 3.9, planetary-scale waves are not able to propagate upward and are subject to dissipate in the lower stratosphere. Accordingly, a strong, but shallow polar vortex is located in the upper stratosphere close to the latitudes of maximum meridional gradients of the equilibrium temperature. Increasing either p_{Tw} or γ improves the high-latitude waveguide and hence, the conditions for upward propagation of planetary-scale waves in the stratosphere, thereby weakening the LS and strengthening the mid-stratospheric RC. Whereas a strengthened polar vortex generally decreases the LS RC strength, the mid-stratospheric RC only accelerates up to a maximum strength. At the transition to the strong polar vortex regime accompanied by the development of a confined waveguide, the probability of downward planetary-scale wave flux events is increased which is consistent with the weakened mid-stratospheric RC. Therefore, an uninterrupted waveguide for planetary-scale waves has to be established first, before the transition to the strong polar vortex regime with confined waveguide can be observed.

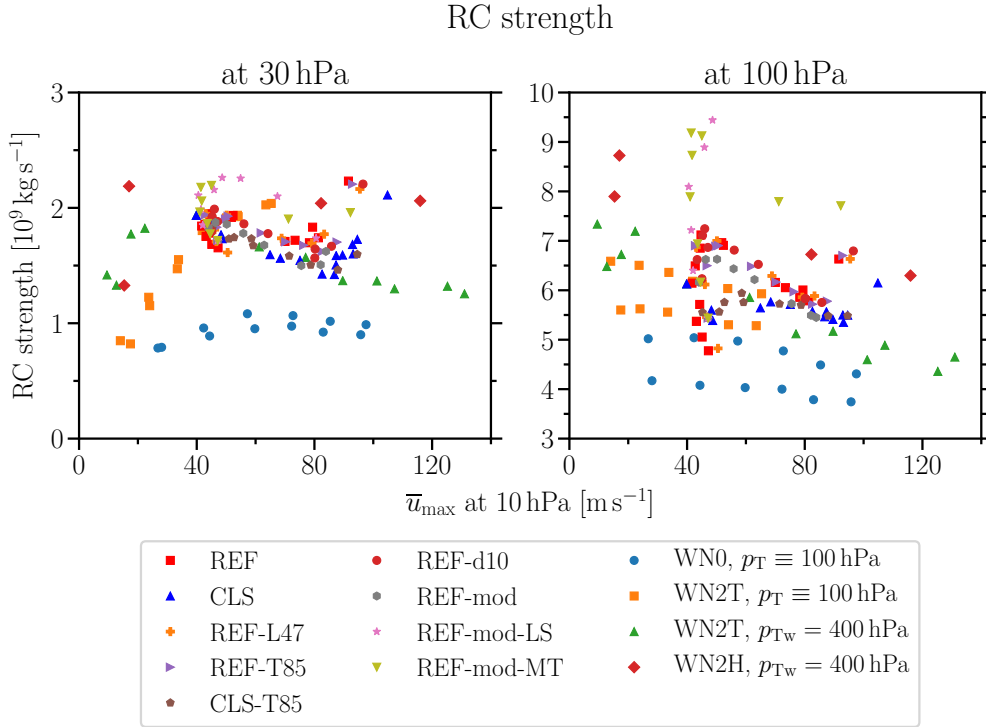


Figure 5.1: Residual circulation (RC) strength at 30 hPa (left) and 100 hPa (right) as functions of the maximum zonal-mean zonal wind \bar{u}_{\max} at 10 hPa for various PSC (WN0, WN2T, WN2H) and tropical warming (REF and CLS) experiments. The strength of the RC is based on the standard streamfunction Ψ^* of the residual-mean meridional circulation given in Eq. (2.19) and computed via $\max(\Psi^*) + |\min(\Psi^*)|$.

In case of the WN2T experiment with $p_{Tw} = 400$ hPa, this condition is already fulfilled for small γ .¹⁴ Therefore, a small increase of γ is sufficient to form the confined geometry of the waveguide. In case of the WN2T experiment with $p_{Tw} = 100$ hPa, even large polar vortex lapse rates as $\gamma = 6$ K km⁻¹ are not able to cause a sufficiently narrow waveguide that leads to the PVRT as will be shown in the following. The nonlinear mid-stratospheric RC response is less pronounced in the WN0 experiments due to generally smaller planetary-scale wave fluxes. Although sharp decreases of upward planetary-scale wave fluxes are present in the WN2H experiment (see Fig. 3.14), the mid-stratospheric RC strength stays constant hinting at the distorted stratosphere-troposphere coupling in presence of the idealized WN2 heating located in the midlatitude upper troposphere in this experiment.¹⁵ In the TUTW experiments, the LS RC weakening with increasing polar vortex strength in the strong polar vortex regime is preceded by the CLCM dominating the weak polar vortex regime which drives a stronger LS

¹⁴Note that in case of the WN2T simulation with $p_{Tw} = 400$ hPa, $\gamma = 1$ K km⁻¹, and $\delta_z = 4.3$ K, a small part of the midlatitude lower stratosphere is still occupied by negative $n_{c=0, k=2}^2$ for the 5-year simulation presented in Fig. 3.9. Employing the more robust 30-year simulation with $\delta_z = 10$ K, the midlatitude lower stratosphere is completely filled up with positive $n_{c=0, k=2}^2$ (not shown).

¹⁵Note that the RC strength of the WN2H experiment was even shown to continuously increase at 10 hPa in Fig. 3.12.

RC. As already mentioned in Sec. 4.6, a tropical heating located in the LS of the REF-mod-LS experiment is directly transferred to a stronger LS RC, but the mid-stratospheric RC exhibits a similar nonlinearity. In order to reconcile circulation changes in response to PSC and tropical warming, the waveguides of all experiments are analyzed in Fig. 5.2.

At the top of the polar vortex, the refractive index squared for stationary planetary-scale waves continuously decreases with increasing polar vortex strength (top left panel of Fig. 5.2). This process is very robust across various simulation setups with PSC and tropical warming, suggesting that the potential of a reflecting surface at the top of the polar vortex is inherent in Polvani and Kushner (2002)-type models with a sponge-layer damping of upper-atmospheric winds. Stronger zonal-mean zonal winds of the stratospheric polar vortex are subject to stronger damping at the top, causing increased vertical curvature that promotes a larger region of negative refractive index squared. Accordingly, the probability of downward wave flux events robustly increases with increasing polar vortex strength (top right panel of Fig. 5.2).

At the poleward edge of the polar vortex, the robust development of a growing region of wave evanescence is only present in the WN2T PSC experiment with $p_{T_w} = 400$ hPa and in the REF and CLS TUTW experiments (center right panel of Fig. 5.2). In the WN2T experiments with $p_T \equiv 100$ hPa and in the REF-mod-LS experiment, the development of a region of wave evanescence is damped. The waveguide narrowing also occurs in the REF-mod-MT experiment as shown in Fig. 4.21, but the expanding troposphere in this setup makes it difficult to portray this process together with other simulations for a fixed region for which the refractive index squared is averaged. The waveguide narrowing on the poleward side of the polar vortex can be related to its equatorward shift. In the (weak polar vortex regime of the) TUTW experiment, the equatorward shift of the lower-stratospheric polar vortex is induced by the CLCM (Shepherd and McLandress, 2011) that strengthens the lower-stratospheric residual circulation which forms a localized region of maximum downwelling at the equatorward edge of the polar vortex. Increased meridional temperature gradients at the polar vortex edge are consistent with its equatorward shift. In the PSC experiment, variations of the equilibrium temperature through p_{T_w} or γ directly prescribe enhanced meridional temperature gradients which are strongest at 50°N in the stratosphere. Largest equatorward shifts of the lower-stratospheric polar vortex and hence greatest increases in the poleward region of wave evanescence are, however, associated with the regime transition to a strong and stable polar vortex. The correspondingly sharply decreasing wave flux dissipation in the stratosphere is consistent with the strengthening polar vortex moving equatorward towards regions of strongest meridional gradient of the equilibrium temperature at 50°N in the stratosphere. When, in turn, the wave flux dissipation in the stratosphere and hence, the RC strength in the middle stratosphere never decrease as in the WN2T experiment with $p_T \equiv 100$ hPa, the waveguide consistently does not narrow significantly on the poleward side of the polar vortex.

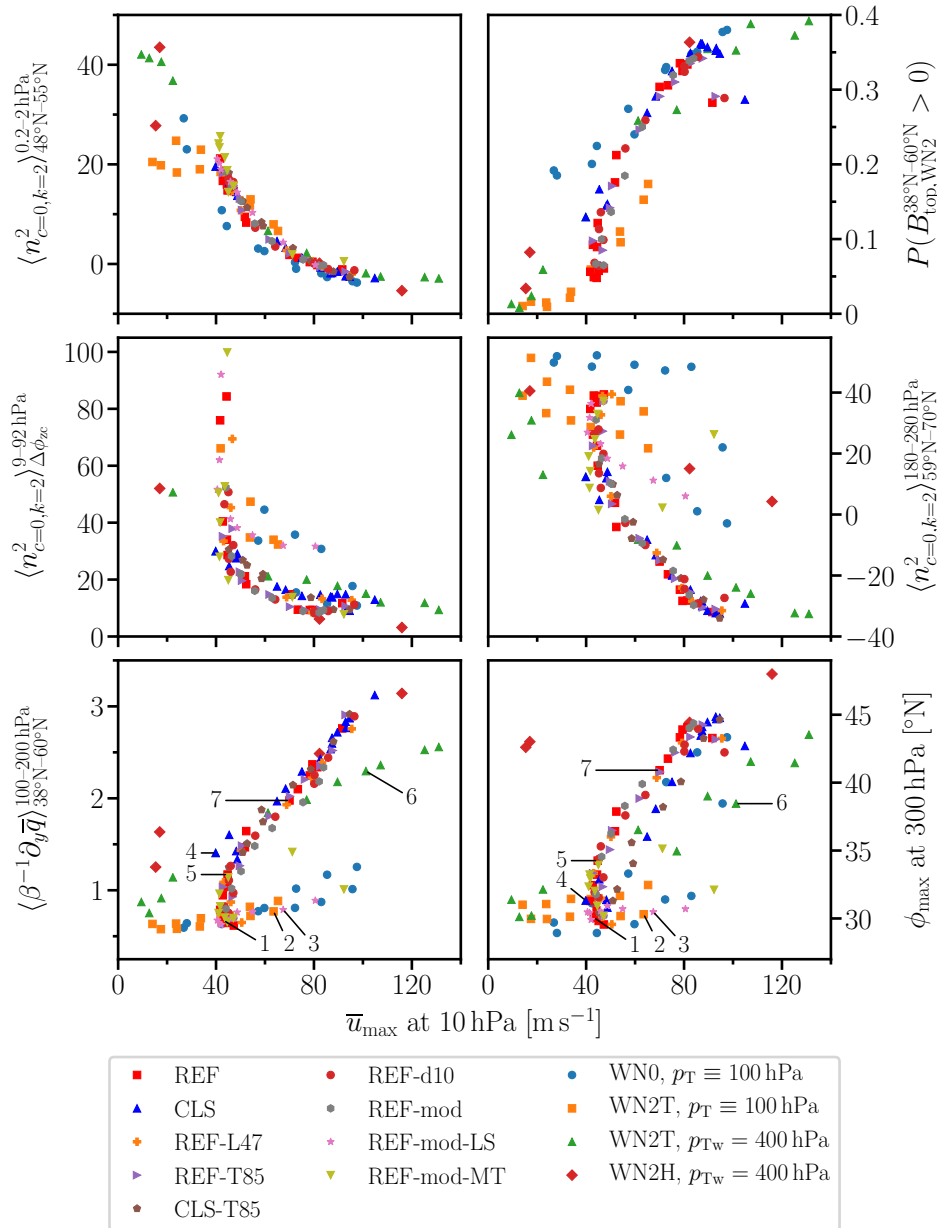


Figure 5.2: Refractive index squared $n_{c=0, k=2}^2$ for stationary waves of wavenumber 2 averaged over 0.2–2 hPa and 48°N–55°N (top left), over 9–92 hPa and $\Delta\phi_{zc}$ (center left), and over 180–280 hPa and 59°N–70°N (center right), as well as the normalized meridional potential vorticity gradient $\beta^{-1}\partial_y\bar{q}$ averaged over 100–200 hPa and 38°N–60°N (bottom left), the probability that the WN2 EP flux at 100 hPa integrated from 38°N to 60°N is downward (top right), and the latitude ϕ_{\max} of the maximum zonal-mean zonal wind at 300 hPa (bottom right) as functions of the maximum zonal-mean zonal wind \bar{u}_{\max} at 10 hPa for various PSC (WN0, WN2T, WN2H) and tropical warming (REF and CLS) experiments. The region $\Delta\phi_{zc}$ is located at least 4° northward of the latitude of the zonal-mean zonal-wind zero crossing at 1 hPa indicated by a black cross in Figs. 5.3 and 5.4 to avoid singular values of $n_{c=0, k=2}^2$ close to critical lines $\bar{u} = 0$, and it is 5.6° wide consisting of three and five latitude grid points for simulations with horizontal resolutions T42 and T85, respectively. The numbers in the bottom panels indicate simulations that are chosen for Figs. 5.3 and 5.4 to represent a reference state (1) as well as states forced by additional polar cooling (2,4,6) and tropical heating (3,5,7) which do (6,7) and do not (2,3) exhibit significant tropospheric circulation changes. Simulations 4 and 5 represent intermediate climate states.

The crucial region of the waveguide, however, that determines more precisely whether the polar vortex is able to enter the strong regime is located in the midlatitude lower stratosphere below or at the equatorward edge of the polar vortex. Once an uninterrupted waveguide is established in the midlatitude LS as discussed above, the equatorward boundary of the waveguide should exhibit a smooth and vertically aligned region of wave evanescence in order to prevent reflected wave activity from reaching critical lines and instead to conduct it back to the troposphere (Shaw et al., 2010). Such a region is supposed to be present in climate states with small refractive index squared on the equatorward side of the polar vortex as indicated by Fig. 4.22. In order to avoid critical lines $\bar{u} = 0$ on the equatorward side of the polar vortex which would disturb the calculation of refractive index squared averages, the waveguide is evaluated over a zonal-mean flow dependent latitudinal region $\Delta\phi_{zc}$ which is 5.6° wide and located at least 4° northward of the latitude of zero zonal-mean zonal wind at 1 hPa. As shown in the center left panel of Fig. 5.2, the entire set of experiments is divided into simulations that either reach values below 20, or those that level off above values of 30 of the averaged refractive index squared with increasing polar vortex strength. The latter of which are the WN2T PSC experiment with $p_T \equiv 100$ hPa and the REF-mod-LS experiment which both do not exhibit a significant stratospheric influence on the tropospheric circulation as shown in the bottom right panel of Fig. 5.2. In all other experiments where a smooth and vertically aligned region of wave evanescence is established on the equatorward side of the polar vortex, reflected wave activity is assumed to reach the troposphere, consistent with an enhanced poleward shift of the tropospheric jet (Shaw and Perlwitz, 2013, 2014; Dunn-Sigouin and Shaw, 2015). Special cases can, however, suppress tropospheric-jet shifts.

In case of the REF-mod-MT experiment, the tropospheric-jet shift is much weaker than in the TUTW experiments. The strengthened Hadley cell and the large meridional extent of the tropospheric jet in this setup could prevent a more enhanced poleward shift of the tropospheric jet. Similarly, the unrealistically pronounced wave flux generation in the midlatitude UTLS region of the WN2H setup (see Fig. 3.5) forces an already far poleward, but fixed position on the tropospheric jet even though less planetary-scale wave flux propagates into the stratosphere which is instead refracted equatorward within the troposphere (see Fig. 3.14). Also the strong and stable polar vortex generated by very high tropical-heating rates in the REF-mod-LS experiment is not able to exert any influence on the tropospheric jet. In case of the WN0 setup, the significant tropospheric jet shift cannot be identified with a sharp emergence of downward wave coupling events. A large number of downward wavenumber-2 wave flux events is present already at $\gamma = 1 \text{ K km}^{-1}$, and the amount of upward propagating wave activity stays approximately constant at levels half of the amount prevailing in the WN2T setup with $p_{Tw} = 100$ hPa. Due to the larger mobility of the tropospheric jet in the setup without topography (Polvani and Kushner, 2002; Gerber and Polvani, 2009), other processes of stratosphere-troposphere coupling might be responsible for the poleward jet shift accom-

panying the polar vortex strengthening (Kushner and Polvani, 2004; Domeisen and Plumb, 2012; Domeisen et al., 2013).

Whether or not the transition to a strong and stable polar vortex is accompanied by an enhanced poleward shift of the tropospheric jet seems to be connected to the meridional potential vorticity gradient in the midlatitude LS (bottom left panel of Fig. 5.2). Neglecting the WN0 setup without additional planetary-scale wave generation, a meridionally confined waveguide can only be established if the midlatitude LS between 100 and 200 hPa is significantly influenced. Additional thermal forcings—either polar stratospheric cooling or tropical heating—have to increase the meridional potential vorticity gradient by strengthening the zonal-mean flow in this region. In case of the WN2T PSC experiment with $p_T \equiv 100$ hPa and the REF-mod-LS experiment, an increased strength of the thermal forcing affects the meridional temperature gradient only above and around 100 hPa, respectively, which is not sufficient to develop a confined meridional waveguide. In contrast to this, the additional thermal forcings employed in the remaining set of experiments induce increased midlatitude zonal-mean zonal winds below 200 hPa.

In order to summarize the essential results regarding stratosphere-troposphere coupling gained from idealized GCMs in this thesis, Fig. 5.3 displays the refractive index squared for stationary planetary-scale waves for selected climate states in combination with sketched corresponding climatological-mean wave fluxes. Based on a reference state (1), WN2T simulations with additional PSC (2,4,6) as well as tropical heating (3,5,7) are on the one hand chosen to represent climate states whose increased polar vortex strength does not induce tropospheric circulation changes due to the lack of both a confined waveguide and increased meridional potential vorticity gradient in the midlatitude LS (2,3). On the other hand, climate states are chosen whose additional thermal forcings extend well below 200 hPa which moderately increases the midlatitude meridional potential vorticity gradient in the LS at moderate forcing levels (4,5), and which leads to enhanced stratosphere-troposphere coupling at high forcing levels (6,7). The climatological-mean wave fluxes in Fig. 5.3 have been sketched with the help of Fig. 5.4 where the total EP fluxes and the total EP flux divergence are shown for the reference state (1) as well as the differences of climate states 2–7 with respect to 1. All climate states are also marked in the bottom panels of Fig. 5.2, and both Figs. 5.3 and 5.4 contain the four regions for which the refractive index squared as well as the meridional potential vorticity gradient are averaged in Fig. 5.2. The parameters of the simulations representing climate states 1–7 are given in the caption of Fig. 5.3.

In the reference state with $p_T \equiv 100$ hPa and $\gamma = 4 \text{ K km}^{-1}$ (1), the zonal-mean flow guides wave flux generated at the surface equatorward to low latitudes, upward to the midlatitude LS, and to the upper stratosphere via the polar vortex. Strong additional polar cooling and tropical heating located above and around 100 hPa (2,3), respectively, weakly increase the zonal-mean zonal wind in the midlatitude LS, but strongly increase the wind above, imposing

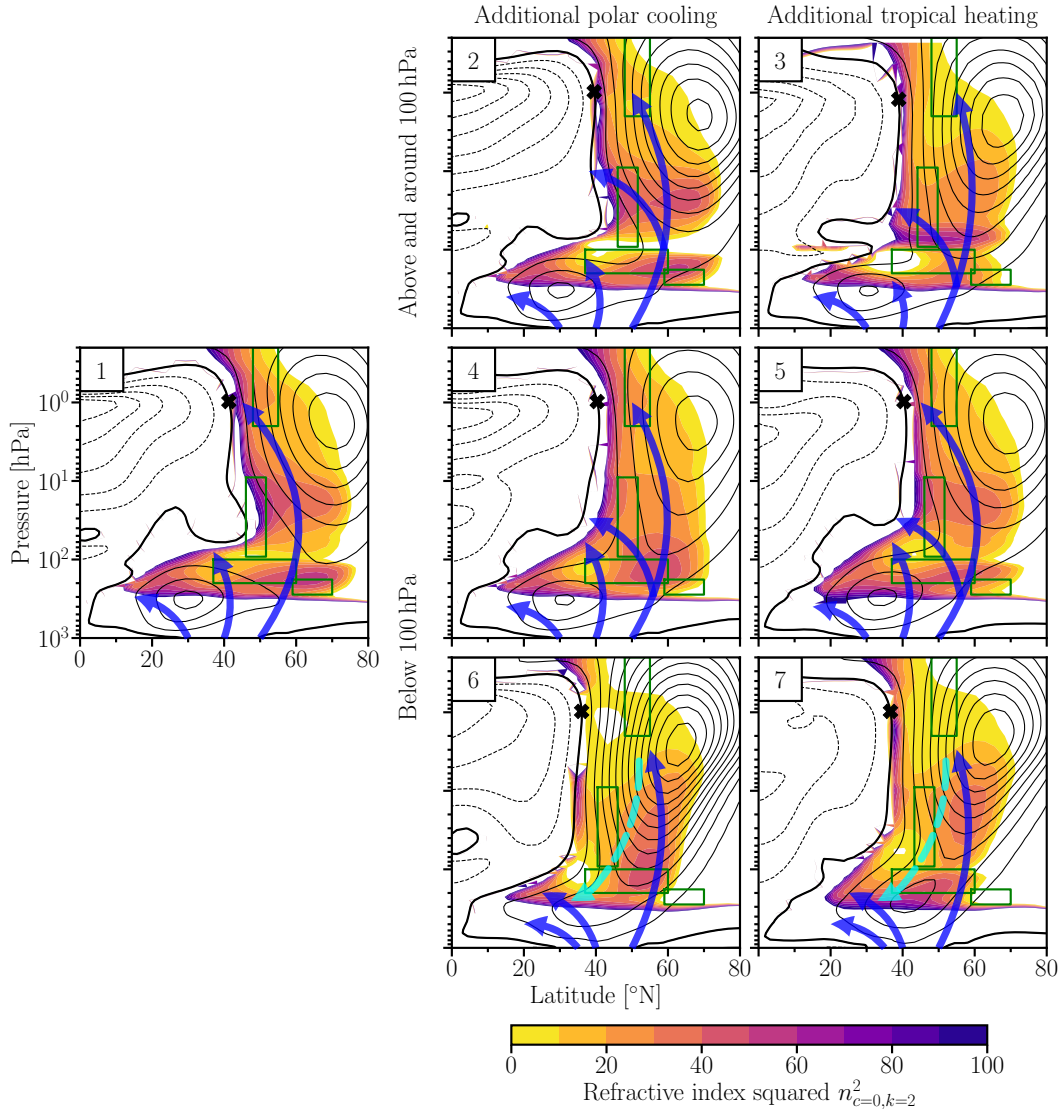


Figure 5.3: Refractive index squared $n_{c=0,k=2}^2$ for stationary waves of wavenumber 2 (color shading with a contour interval of 10) and zonal-mean zonal wind (black contour lines with a contour interval of 10 m s^{-1} , negative contours dashed, thick zero-contour line) as functions of latitude and pressure. Solid blue arrows represent climatological-mean upward propagating wave fluxes, whereas dashed turquoise arrows indicate an increased probability of downward wave flux events without changing the upward direction of climatological-mean wave fluxes. Green boxes represent regions for which quantities are averaged in Fig. 5.2, and black crosses denote the latitudes of the zonal-mean zonal-wind zero crossing at 1 hPa. All simulations employ an idealized WN2 topography and $\delta_z = 4.3 \text{ K}$. Starting from a reference state with $p_T \equiv 100 \text{ hPa}$ and $\gamma = 4 \text{ K km}^{-1}$ (1) neither additional polar cooling with $\gamma = 6 \text{ K km}^{-1}$ (2) nor tropical heating centered at 100 hPa with $q_0 = 1.6 \text{ K day}^{-1}$ (3) is able to significantly influence the troposphere. If the thermal forcings extend sufficiently downward below 100 hPa, additional moderate polar cooling with $p_{Tw} = 400 \text{ hPa}$ and $\gamma = 2 \text{ K km}^{-1}$ (4) or moderate tropical heating centered at 300 hPa with $q_0 = 0.25 \text{ K day}^{-1}$ (5) start to influence the location of the tropospheric jet and prepare the waveguide for the upcoming regime transition when thermal forcings further increase. Sufficiently strong thermal forcings below 100 hPa as additional polar cooling with $p_{Tw} = 400 \text{ hPa}$ and $\gamma = 3 \text{ K km}^{-1}$ (6) or tropical heating centered at 300 hPa with $q_0 = 0.4 \text{ K day}^{-1}$ (7) lead to a confined waveguide which directs reflected wave activity back to the troposphere, consistent with an enhanced poleward shift of the tropospheric jet.

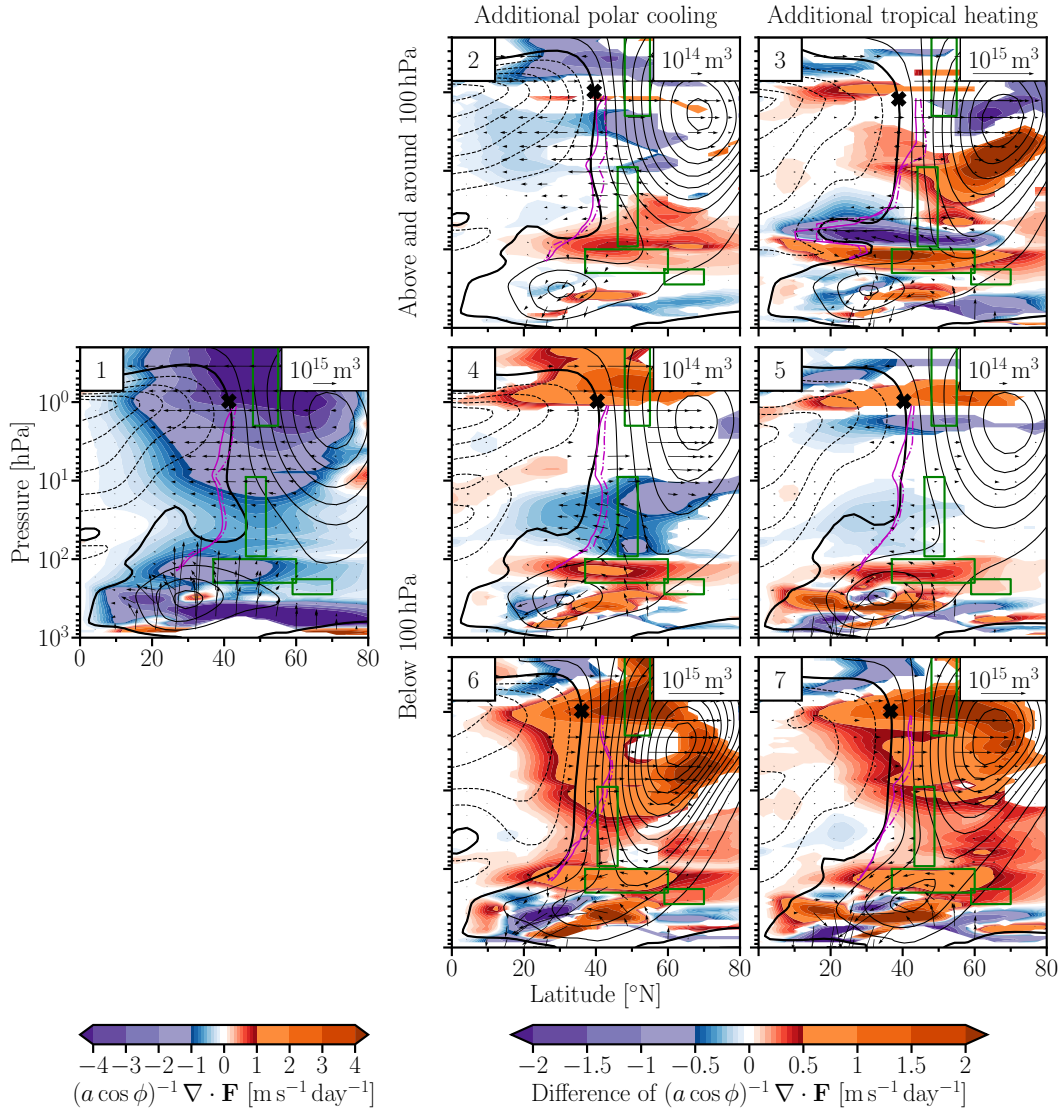


Figure 5.4: Tendency of the zonal-mean zonal wind by the total Eliassen–Palm (EP) flux divergence $\bar{\mathcal{F}} = (a \cos \phi)^{-1} \nabla \cdot \mathbf{F}$ (color shading) and total EP flux arrows $\hat{\mathbf{F}} = (\hat{F}^{(\phi)}, \hat{F}^{(p)})$ (arrows) as functions of latitude and pressure for a reference state (1) as well as the differences of $\bar{\mathcal{F}}$ and $\hat{\mathbf{F}}$ between climate states forced by additional polar cooling (2,4,6) as well as tropical heating (3,5,7) and the reference state. The additional thermal forcings are located above and around 100 hPa (2,3) and below 100 hPa (4,5,6,7). EP flux arrows are defined as $(\hat{F}^{(\phi)}, \hat{F}^{(p)}) = 2\pi a g^{-1} \cos \phi (F^{(\phi)}, a F^{(p)}) / (-80.4 \text{ kPa})$ according to Edmon et al. (1980). Only differences of $\bar{\mathcal{F}}$ and $\hat{\mathbf{F}}$ that are statistically significant on a 95%-confidence level are shown. Furthermore, climatological-mean zonal-mean zonal winds (black contour lines with a contour interval of 10 m s^{-1} , negative contours dashed, thick zero-contour line) are shown for every simulation. The solid and dash-dotted magenta lines represent the turnaround latitudes of the residual-mean meridional circulation Ψ^* and the downward-control circulation Ψ_{dc}^* , respectively (McLandress and Shepherd, 2009; Haynes et al., 1991). Green boxes indicate regions for which quantities are averaged in Fig. 5.2, and black crosses denote the latitudes of the zonal-mean zonal-wind zero crossing at 1 hPa. The specific parameters determining the simulations 1–7 are provided in the caption of Fig. 5.3 and in the body text.

very weak positive and even negative values of the meridional potential vorticity gradient above the tropospheric jet (not shown). As a result, negative values of the refractive index squared above the tropospheric jet spread out which is consistent with reduced upward propagating wave fluxes close to the tropospheric jet and a weakened LS RC, at least in the PSC experiment. The tropical heating located in the LS directly strengthens the LS RC in climate state 3, but upward propagating wave fluxes close to the tropospheric jet reduce nevertheless. Since the emerging region of wave evanescence above the tropospheric jet does not extend sufficiently upward into the stratosphere, the equatorward side of the polar vortex still exhibits high values of the refractive index squared which is consistent with enhanced equatorward refracted wave fluxes in the stratosphere, driving a stronger mid-stratospheric circulation.

Moderate additional polar cooling and tropical heating located below 100 hPa (4,5) strengthens the upper flank of the tropospheric jet causing a stronger LS RC via the CLCM. Furthermore, the meridional potential vorticity gradient starts to increase in the midlatitude LS. Due to the strengthened LS RC maintaining weak zonal-mean zonal winds in the LS, the refractive index squared in midlatitudes around 100 hPa increases compared to the reference state which is consistent with the strengthened RC also higher up in the stratosphere. The situation changes fundamentally in the strong polar vortex regime (6,7), where in contrast to climate states 2 and 3, the polar vortex strengthens far below 100 hPa reducing the refractive index squared everywhere but close to the latitudes of maximum zonal-mean zonal wind representing the region of maximum meridional potential vorticity gradient. What remains is a confined waveguide with a smooth and vertically aligned region of wave evanescence starting above the tropospheric jet and extending upward on the equatorward side of the polar vortex. Accordingly, the probability for reflected planetary-scale wave activity to be guided back to the troposphere is drastically increased which is consistent with the enhanced poleward shift of the tropospheric jet representing strong stratosphere-troposphere coupling.

This waveguide narrowing is to some extent also visible in climate state 3, but only present in the upper stratosphere. Assuming a high probability of planetary-scale wave reflection events consistent with the strong and stable polar vortex of climate state 3, reflected waves are likely subject to dissipate in the LS close to critical lines around 40°N before they can reach the troposphere. In order that a confined waveguide is also developed in the LS, the meridional potential vorticity gradient in the midlatitude LS between 100 and 200 hPa has to increase which is established by increased meridional temperature gradients in the LS induced by additional thermal forcings of either polar cooling or tropical heating. The accompanied strengthened LS circulation is consistent with an equatorward shift of the LS polar vortex and enhanced equatorward wave flux in the LS. Connecting the regions of high meridional potential vorticity gradients associated with the tropospheric jet and the polar vortex narrows the region of low meridional potential vorticity gradient above the tropospheric jet in latitudinal direction and elongates it upward on the equatorward side of the polar vortex (not shown). When the

polar vortex strengthens in that case, a confined waveguide with a smooth and vertically aligned region of wave evanescence remains as described above.

The strengthened meridional potential vorticity gradient in the midlatitude lower stratosphere is a necessary condition for the transition to the strong polar vortex regime with significant tropospheric impact as the accompanied enhanced poleward shift of the tropospheric jet. The specific process which triggers this transition, however, remains concealed since zonal-mean flow, wave fluxes, and RC are in equilibrium due to the steady-state simulations analyzed in this thesis. Therefore, the development of these physical quantities through the regime transition can only be described in a consistent manner rather than finding detailed causal connections. Analyzing the time dependent evolution of the atmosphere for prescribed equilibrium temperatures close to the regime transition could contribute to a better understanding. This is left for future studies. Since the idealized TUTW experiment performed in this thesis is designed to mimic the temperature response to increased greenhouse-gas concentrations (e.g., Shepherd and McLandress, 2011; Vallis et al., 2015; Shaw, 2019; Oudar et al., 2020b), indications of similar waveguide developments are searched for in complex climate models that are forced by increasing CO₂ concentrations in the following section.

5.2 Implications for the CMIP6 1pctCO₂ experiment

In the 1pctCO₂ experiment within the framework of CMIP6 (Eyring et al., 2016), climate models coupling various compartments of the Earth system are exposed to an exponential increase of CO₂ in the atmosphere by 1% every year starting from preindustrial levels (Meehl et al., 2000). A list of models which are analyzed from the 1pctCO₂ experiment in this section is given in Tab. 5.1. Eight spectral and three finite-volume models contribute monthly and zonally averaged data of zonal wind and temperature for the time being. To ensure a quadrupling of CO₂ concentrations by the year 140 of the experiment, all models are integrated for at least 150 years. After the year 140 of the experiment, CO₂ concentrations continue to increase by 1% every year (Eyring et al., 2016) such that the extremely long integration of AWI-ESM-1-1-LR reaches twelvefold carbon dioxide levels compared to the preindustrial era.

Apart from polar surface regions, the tropical upper troposphere receives pronounced warming compared to the remaining parts of the troposphere when greenhouse-gas concentrations increase (Shepherd and McLandress, 2011; Vallis et al., 2015; Shaw, 2019; Oudar et al., 2020b). In the CMIP6 1pctCO₂ experiment, the tropical upper-tropospheric temperature \bar{T}_{TUT} averaged over 25°S–25°N and 150–250 hPa exhibits a continuously accelerated rise consistent with the exponential increase of CO₂ as shown in the top panel of Fig. 5.5 for monthly data with a 30-year running mean applied. Most of the CMIP6 models exhibit a similar temperature sensitivity to increased CO₂ concentrations which is highlighted when the temperature change $\Delta\bar{T}_{\text{TUT}}$ with respect to the first 30-year mean is considered as shown in the bottom panel

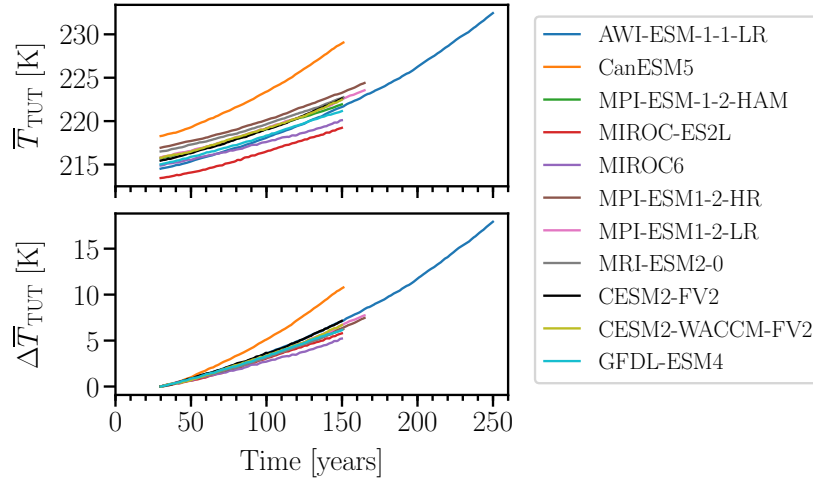


Figure 5.5: Monthly tropical upper-tropospheric temperature \bar{T}_{TUT} averaged over 25°S – 25°N and 150–250 hPa (top) and its change $\Delta\bar{T}_{\text{TUT}}$ with respect to the first 30-year mean (bottom) as functions of time for the CMIP6 models of the 1pctCO₂ experiment listed in Tab. 5.1 with a 30-year running mean applied.

of Fig. 5.5. The CanESM5 model warms much faster than the rest, of which the MIROC6 model warms slowest. Accordingly, the CMIP6 multi-model ensemble analyzed here exhibits temperature increases in the tropical upper troposphere between approximately 5 and 12 K averaged for the years 120 up to and excluding 150 since the start of the 1pctCO₂ experiment. The tropical upper-tropospheric temperature change $\Delta\bar{T}_{\text{TUT}}$ is used in the following to compare the winter-circulation response between the different models.

Institution	Model Name	Horizontal Grid	Resolution			Model top	Length [years]	References
			N_λ	N_ϕ	N_p			
AWI	AWI-ESM-1-1-LR	T63	192	96	47	80 km	250	Danek et al. (2020)
CCCma	CanESM5	$T_{L63} \equiv T42$	128	64	49	1 hPa	151	Swart et al. (2019b)
HAMMOZ-Consortium	MPI-ESM-1-2-HAM	T63	192	96	47	0.01 hPa	150	Neubauer et al. (2019)
MIROC	MIROC-ES2L	T42	128	64	40	0.03 hPa	150	Hajima et al. (2019)
MIROC	MIROC6	T85	256	128	81	0.004 hPa	150	Tatebe and Watanabe (2018)
MPI-M	MPI-ESM1-2-HR	T127	384	192	95	0.01 hPa	165	Jungclaus et al. (2019)
MPI-M	MPI-ESM1-2-LR	T63	192	96	47	0.01 hPa	165	Wieners et al. (2019)
MRI	MRI-ESM2-0	$T_{L159} \equiv T106$	320	160	80	0.01 hPa	151	Yukimoto et al. (2019)
NCAR	CESM2-FV2	FV $2.5^\circ \times 1.9^\circ$	144	96	70	0.00045 Pa	150	Danabasoglu (2020a)
NCAR	CESM2-WACCM-FV2	FV $2.5^\circ \times 1.9^\circ$	144	96	70	0.00045 Pa	150	Danabasoglu (2020b)
NOAA-GFDL	GFDL-ESM4	FV $1^\circ \times 1^\circ$	360	180	49	0.01 hPa	150	Krasting et al. (2018)

Table 5.1: List of CMIP6 models contributing to the 1pctCO2 experiment by providing monthly and zonally averaged (AERmonZ) data of zonal wind and temperature analyzed in Sec. 5.2. Only one member per model is used and selected by the first realization (r1) and first initialization (i1, consult Taylor et al., 2018, for definitions of CMIP6 global attributes). The first eight models employ spectral dynamical cores with triangular truncation (T) at wavenumbers given in the third column of the table. The CanESM5 and the MRI-ESM2-0 model use a spectral core with linear truncation (T_L). The last three models employ finite volume (FV) dynamical cores specifying the longitudinal and latitudinal distance between grid cell centers in $^\circ$. For better comparison, the numbers of longitudes N_λ , latitudes N_ϕ , and pressure levels N_p as well as the top level are given in the fourth, fifth, sixth, and seventh column of the table, respectively. All models were integrated for at least 150 years to ensure a quadrupling of CO₂ concentrations compared to the preindustrial level of the year 1850 (Eyring et al., 2016).

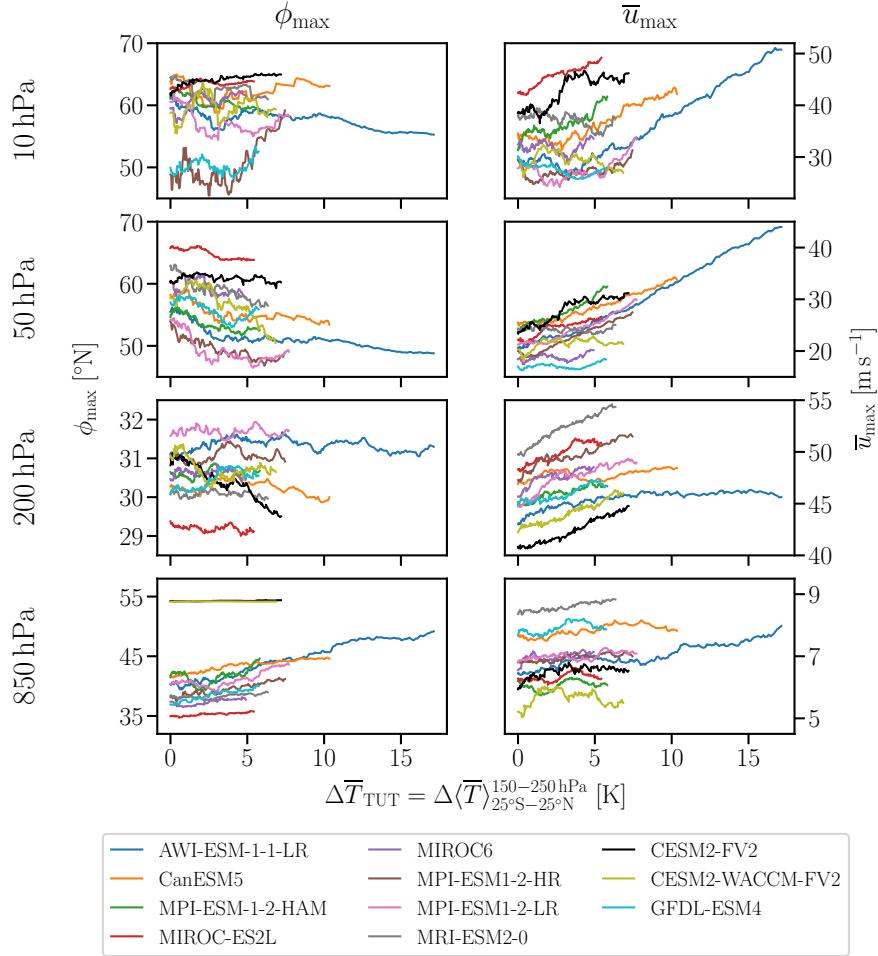


Figure 5.6: Latitude ϕ_{\max} (left) and strength \bar{u}_{\max} (right) of the December-January-February (DJF) seasonal-mean northern-hemispheric maximum zonal-mean zonal wind at 10 hPa (first row), 50 hPa (second row), 200 hPa (third row), and 850 hPa (fourth row) as functions of the temperature change $\Delta\bar{T}_{\text{TUT}} = \Delta\langle\bar{T}\rangle_{25^{\circ}\text{S}-25^{\circ}\text{N}}^{150-250\text{hPa}}$ [K] in the tropical upper troposphere for the CMIP6 models of the 1pctCO2 experiment listed in Tab. 5.1 with a 30-year running mean applied.

Figs. 5.6 and 5.7 show the 30-year running mean of latitude ϕ_{\max} and strength \bar{u}_{\max} of the maximum zonal-mean zonal wind at 10, 50, 200, and 850 hPa as functions of $\Delta\bar{T}_{\text{TUT}}$ for December-January-February (DJF) seasonal means in the northern hemisphere and for June-July-August (JJA) seasonal means in the southern hemisphere, respectively. The pressure levels are chosen to represent the central and lower part of the polar vortex, the tropospheric jet maximum, and the low-altitude eddy-driven jet, respectively. A robust poleward shift of the 850 hPa-jet is observed in both hemispheres for most of the models (Barnes and Polvani, 2013). In southern-hemispheric winter seasons, the CMIP6 multi-model ensemble confirms that more equatorward located eddy-driven jets experience more enhanced poleward shifts in response to increased CO_2 concentrations (Kidston and Gerber, 2010; Simpson and Polvani, 2016). Furthermore, the near-surface jets in the southern hemisphere exhibit a robust strengthening

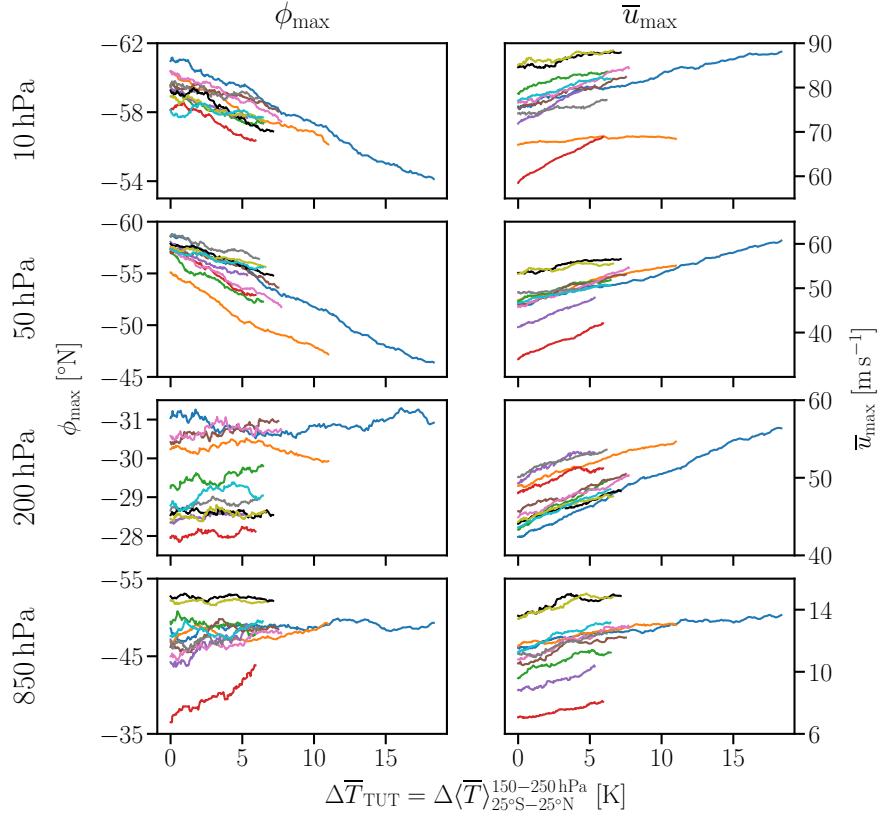


Figure 5.7: Same as Fig. 5.6, but for the June-July-August (JJA) seasonal-mean southern-hemispheric maximum zonal-mean zonal wind. The same legend as provided by Fig. 5.6 applies.

which is not obvious in the northern hemisphere. Only the 250-year long simulation of the AWI-ESM-1-1-LR model shows a moderate strengthening of the 850 hPa-jet. The CESM2-FV2 and CESM2-WACCM-FV2 models cannot show any change in ϕ_{\max} at 850 hPa since only very few data points are available at that pressure level. The tropospheric jet core at 200 hPa strengthens in both hemispheres, but barely any trend is visible in its latitudinal position with the exception of the CESM2-FV2 model, exhibiting a continuous equatorward shift in the northern hemisphere for increasing $\Delta\bar{T}_{\text{TUT}}$. Weaker increases of tropospheric jet strengths in the northern hemisphere are consistent with inverted temperature gradients in the lower troposphere caused by Arctic amplification. In contrast to this, the Antarctic lower troposphere does not exhibit such pronounced temperature increases. Hence, temperature differences between tropical and polar regions can uniformly increase throughout the troposphere in the southern hemisphere and therefore promote stronger winds (Held, 1993; Holland and Bitz, 2003; Butler et al., 2010; Barnes and Polvani, 2013; Harvey et al., 2014; Deser et al., 2015; McGraw and Barnes, 2016; Oudar et al., 2020b,a).

The stratosphere continues the differences between the hemispheres observed in the troposphere. The southern-hemispheric polar vortex experiences uniform changes across the CMIP6

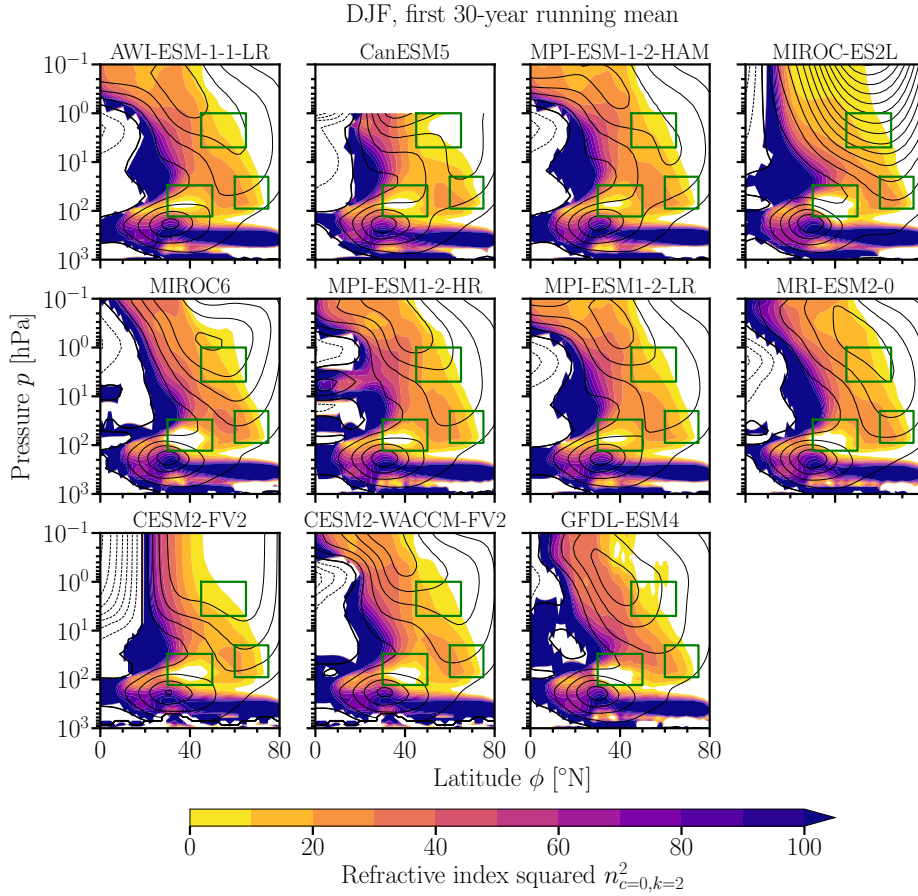


Figure 5.8: Refractive index squared $n_{c=0,k=2}^2$ for stationary waves of wavenumber 2 (color shading with a contour interval of 10) and zonal-mean zonal wind (black contour lines with a contour interval of 10 m s^{-1} , negative contours dashed, thick zero-contour line) of the first 30-year mean DJF-averaged northern-hemispheric zonal-mean circulation as functions of latitude and pressure for the CMIP6 models of the 1pctCO₂ experiment listed in Tab. 5.1. Green boxes represent the regions for which percentages of negative $n_{c=0,k=2}^2$ are computed in Fig. 5.12.

multi-model ensemble. A robust linear strengthening (Jucker et al., 2021) is accompanied by an equatorward shift in the middle and lower stratosphere in all models, except in the CanESM5 model where zonal-mean zonal wind speeds at 10 hPa remain constantly below 70 m s^{-1} throughout the 1pctCO₂ experiment. Stratospheric circulation changes in the northern hemisphere are more diverse and nonlinear (Manzini et al., 2014; Ayarzagüena et al., 2020). Two phases of the polar vortex strength at 10 hPa are present in most of the models: For small $\Delta\bar{T}_{\text{TUT}}$, the polar vortex strength stays roughly constant or decreases. For larger $\Delta\bar{T}_{\text{TUT}}$, the polar vortex strength increases linearly. In the CESM2-FV2 model, the polar vortex strength seems to saturate at some point in the second phase. The threshold separating the two phases depends on the model, and some model integrations might be too short to exhibit the polar vortex strengthening (MRI-ESM2-0, CESM2-WACCM-FV2, GFDL-ESM4). In the lower stratosphere, nearly all models show an equatorward shift of the polar vortex (Butchart et al.,

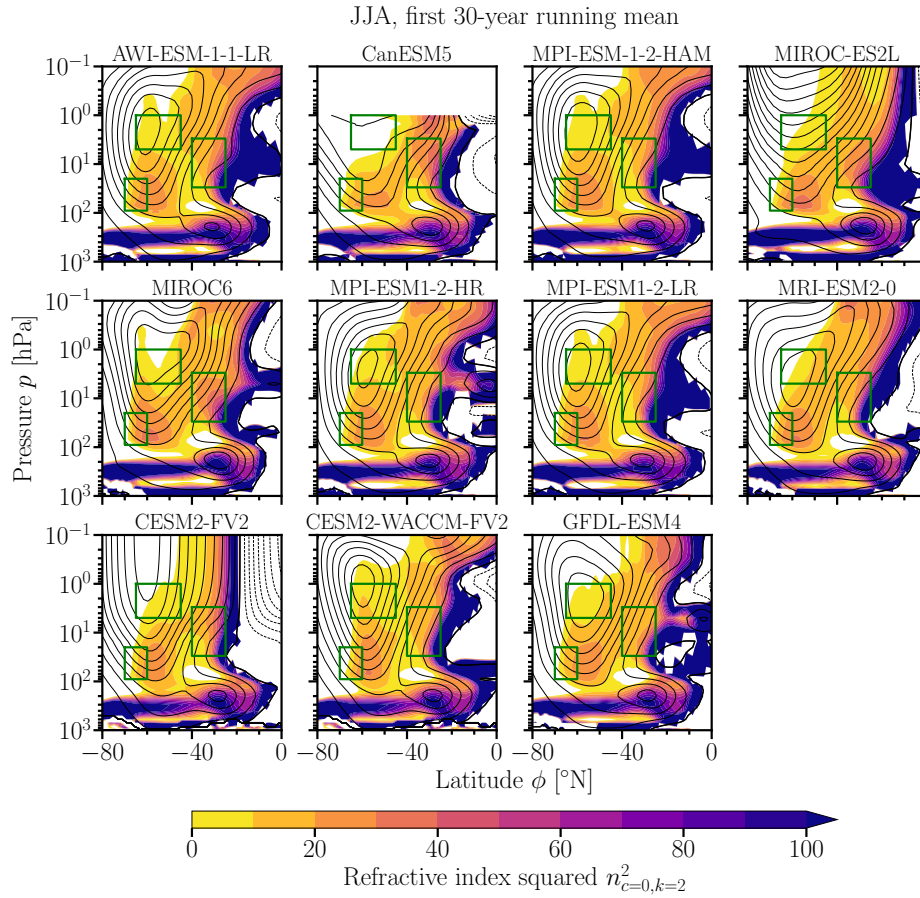


Figure 5.9: Same as Fig. 5.8, but for the first 30-year mean JJA-averaged southern-hemispheric zonal-mean circulation. Green boxes represent the regions for which percentages of negative $n_{c=0,k=2}^2$ are computed in Fig. 5.13.

2010; Scaife et al., 2012) which is also present in a similar CMIP6 experiment where CO₂ concentrations are abruptly quadrupled (abrupt-4xCO₂, Eyring et al., 2016; Oudar et al., 2020b). The abrupt-4xCO₂ experiment also confirms the model spread in the northern-hemispheric polar vortex strength in the middle stratosphere. Some models project increases in the polar vortex strength compared to preindustrial carbon dioxide concentrations, whereas others produce a polar vortex of constant strength (Ayarzagüena et al., 2020).

The large intermodel spread in the stratospheric polar vortex response to climate change in the northern hemisphere has already been noted in CMIP5 (Manzini et al., 2014). Recent studies suggest that this spread might be caused by different time scales at which certain regions of the Arctic ocean become ice-free (Manzini et al., 2018; Kretschmer et al., 2020, and references therein). As long as Arctic sea ice is present, but shrinking asymmetrically, an additional source of wave activity, caused by zonally asymmetric surface heating, might lead to the observed weakening of the polar vortex. As soon as this source of wave activity vanishes together with Arctic sea ice, potential increases in the polar vortex strength can occur. In

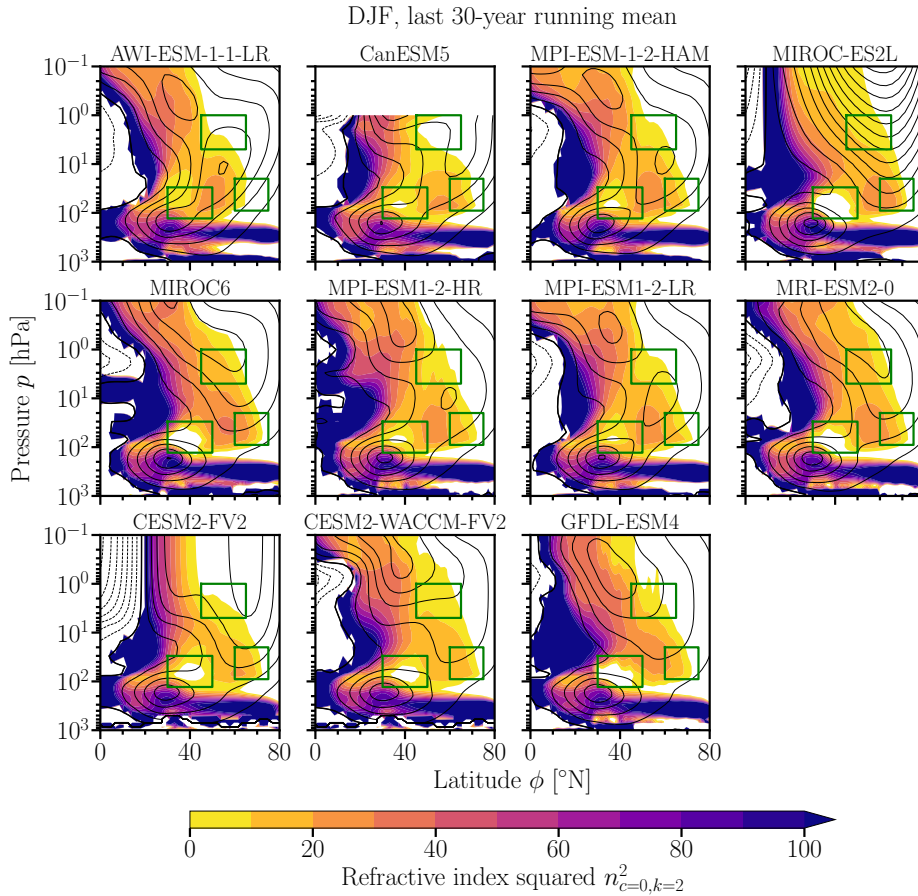


Figure 5.10: Same as Fig. 5.8, but for the last 30-year mean DJF-averaged northern-hemispheric zonal-mean circulation.

the southern hemisphere, sea ice is more zonally symmetrically distributed (Parkinson and Cavalieri, 2012), and Antarctic amplification is weaker (Collins et al., 2014; Salzmänn, 2017; Wang et al., 2021) which might be the reason for the generally smaller spread and the rather linear response of the polar vortex. In the previous section 5.1, an equatorward shifting and strengthening polar vortex has been shown to appear universally in various idealized-model setups during the development of a confined waveguide for planetary-scale waves. Therefore, also the development of waveguides in the CMIP6 models of the 1pctCO₂ experiment listed in Tab. 5.1 is investigated in the following. Although downward wave coupling is dominated by planetary-scale waves of wavenumber 1 (Perlwitz and Harnik, 2004; Shaw et al., 2010), waveguides for wavenumber 2 will be investigated to ensure consistency with previous analyses of idealized models. Future work needs to determine the spectrum and interplay of planetary-scale waves when more TEM quantities are available (Gerber and Manzini, 2016).

In the northern hemisphere, the DJF-averaged zonal-mean zonal winds of the first 30-year running mean of the 1pctCO₂ experiment and the corresponding waveguides exhibit large

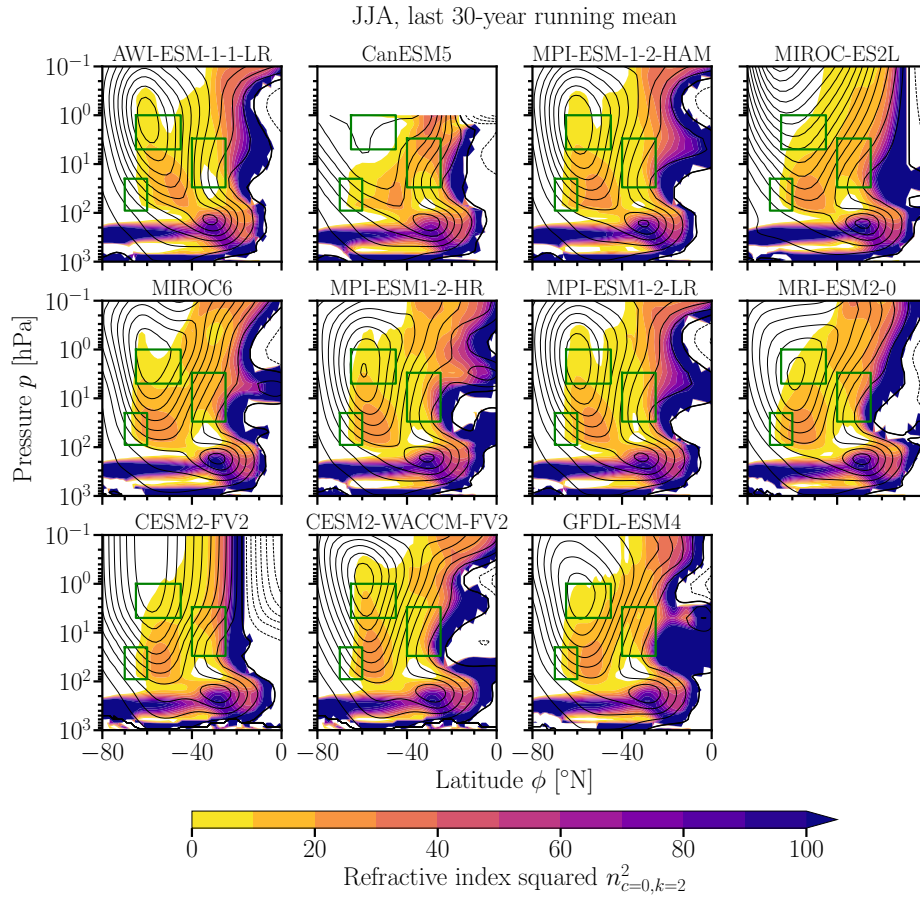


Figure 5.11: Same as Fig. 5.9, but for the last 30-year mean JJA-averaged southern-hemispheric zonal-mean circulation.

differences across the CMIP6 multi-model ensemble as shown in Fig. 5.8. Starting from such a diverse set of climate states, the large spread in different future projections is not surprising (Sigmond and Scinocca, 2010; Manzini et al., 2014; Simpson et al., 2018; Ayarzagüena et al., 2020). In the southern hemisphere, the JJA-averaged zonal-mean circulation of the first 30-year running mean is more conform within the CMIP6 multi-model ensemble as shown in Fig. 5.9. The rather low top at 1 hPa evident in the CanESM5 model as well as the coarse vertical resolution in the upper atmosphere suggested by the simple zonal-wind structure in the MIROC-ES2L and CESM2-FV2 models require to interpret circulation changes in these models with care (e.g., Shindell et al., 2001; Kushner and Polvani, 2004; Scaife et al., 2012; Wilcox and Charlton-Perez, 2013; England et al., 2016).

Taking the corresponding zonal-mean circulations of the last 30-year running means of the 1pctCO2 experiment in the DJF-averaged northern and in the JJA-averaged southern hemisphere into account as presented in Figs. 5.10 and 5.11, respectively, similar waveguide changes as in idealized models that were associated with the PVRT (Figs. 3.9 and 4.13) can be ob-

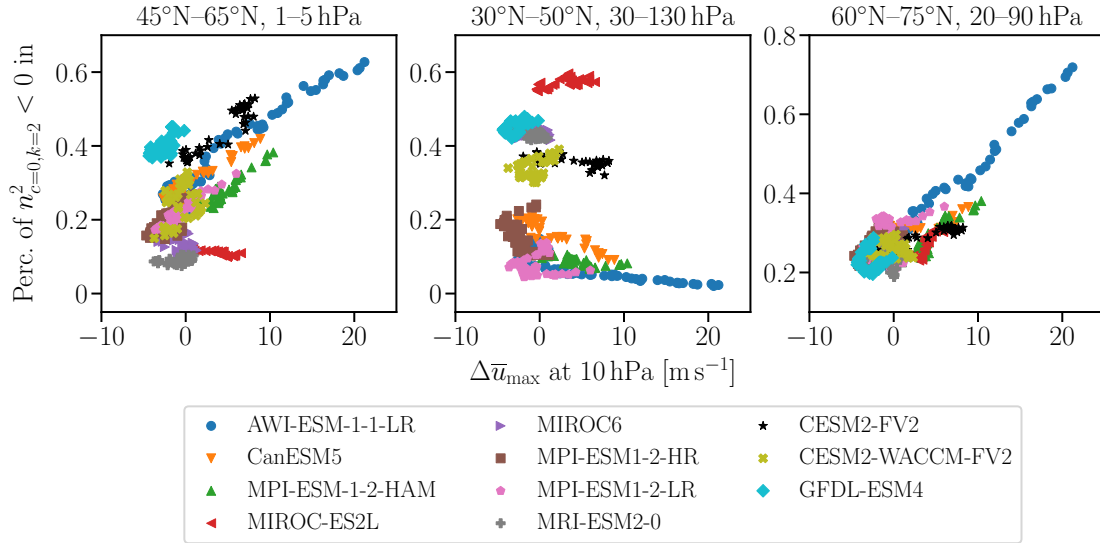


Figure 5.12: Percentages of negative $n_{c=0,k=2}^2$ of the DJF-averaged northern-hemispheric zonal-mean circulation in the regions of 45°N – 65°N and 1 – 5 hPa (left), 30°N – 50°N and 30 – 130 hPa (middle), and 60°N – 75°N and 20 – 90 hPa (right) as functions of the maximum zonal-mean zonal wind change $\Delta\bar{u}_{\max}$ at 10 hPa with respect to the first 30-year mean for the CMIP6 models of the 1pctCO2 experiment listed in Tab. 5.1 with a 30-year running-mean applied. The regions are drawn as green boxes in Figs. 5.8 and 5.10.

served. For example, the equatorward shift of the polar vortex in the AWI-ESM-1-1-LR and CanESM5 models reduces positive $n_{c=0,k=2}^2$ in high latitudes and manages to shrink the region of negative $n_{c=0,k=2}^2$ in midlatitudes above the tropospheric jet. In contrast to idealized models, the vanishing region of wave evanescence in the midlatitude lower stratosphere does not lead to a completely smooth vertically aligned waveguide. In the upper stratosphere, the strengthening of the polar vortex is accompanied by an expansion of the region of negative $n_{c=0,k=2}^2$. In the southern hemisphere, a pronounced shoulder-shaped geometry of the waveguide is already present in the first 30-year running mean in many models and is not subject to large changes towards the end of the 1pctCO2 experiment. Similar to the northern hemisphere, the equatorward shift of the lower-stratospheric polar vortex reduces positive $n_{c=0,k=2}^2$ on its poleward side. On the equatorward side of the polar vortex, the region of negative $n_{c=0,k=2}^2$ above the tropospheric jet is, however, filled in none of the models, but is shown to extent to higher altitudes indicating a more confined waveguide.

Figs. 5.8–5.11 provide a first impression on the evolution of waveguides in the 1pctCO2 experiment which is, however, rather coarse since the refractive index squared has been computed for 30-year averages of the circulation. Nevertheless, these figures expose crucial regions at the top of the polar vortex and on both its equatorward and poleward sides that are worth being investigated in greater detail. In order to closely relate the year-to-year variation of the polar vortex strength to the evolution of the waveguide, $n_{c=0,k=2}^2$ is computed for every

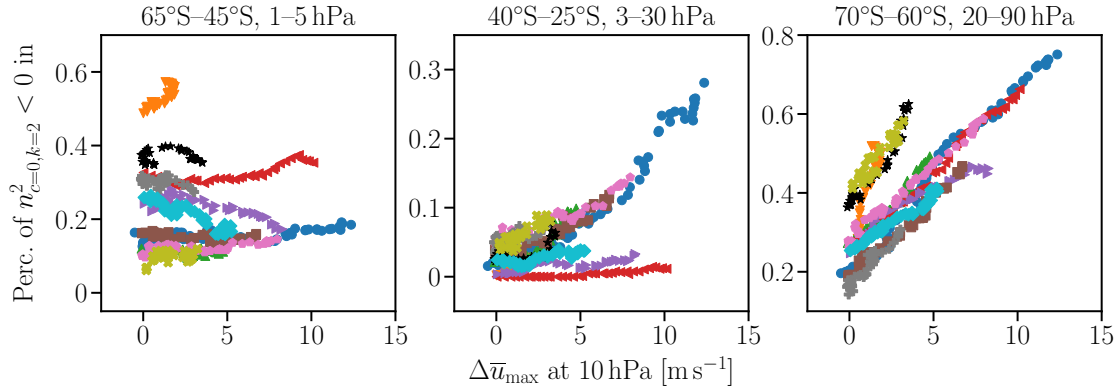


Figure 5.13: Same as Fig. 5.12, but for the JJA-averaged southern-hemispheric zonal-mean circulation for the regions of 65°S–45°S and 1–5 hPa (left), 40°S–25°S and 3–30 hPa (middle), and 70°S–60°S and 20–90 hPa (right). The regions are drawn as green boxes in Figs. 5.9 and 5.11. The same legend as provided by Fig. 5.12 applies.

DJF and JJA season in the northern and southern hemisphere first, respectively. Afterwards, percentages of negative $n_{c=0,k=2}^2$ are computed for suitable regions that are indicated by green boxes in Figs. 5.8–5.11. In contrast to Fig. 5.2 which presents averages of the refractive index squared for different regions, percentages of negative refractive index squared are preferred here due to simplicity. The large spread in climate states within the CMIP6 multi-model ensemble complicates the definition of regions that exclude singularities of $n_{c=0,k=2}^2$ close to critical lines $\bar{u} = 0$ which would lead to improper results when averages are computed. To this end, the evolution of waveguides in the CMIP6 multi-model ensemble is pursued by percentages of negative $n_{c=0,k=2}^2$ at the top and on both the equatorward and poleward sides of the polar vortex in the northern and southern hemisphere in Figs. 5.12 and 5.13, respectively, which are displayed as functions of the corresponding polar vortex strength change $\Delta\bar{u}_{\max}$ at 10 hPa with respect to the first 30-year mean and with a 30-year running mean applied in the end.

In the northern hemisphere, the CMIP6 multi-model ensemble exhibits the formation of a larger region of wave evanescence at the top of the polar vortex when it strengthens, similar to idealized models. Only the MIROC-ES2L model does not show any changes of the upper-stratospheric waveguide although the polar vortex strength increases. Confirming the earlier impression from Figs. 5.8 and 5.10, positive $n_{c=0,k=2}^2$ is reduced on the poleward side of the polar vortex accompanying its equatorward shift. Similar to idealized models with weak polar vortex (see Figs. 3.8 and 3.9), the equatorward side of the polar vortex can improve the waveguide by reducing the percentage of negative refractive index squared in four of the models (AWI-ESM-1-1-LR, CanESM5, MPI-ESM-1-2-HAM, and MPI-ESM1-2-LR) during the polar vortex strengthening. The development of a smooth and vertically aligned equatorward boundary of the waveguide is, however, difficult to detect with the rather low

located box on the equatorward side of the polar vortex. The use of percentages of negative $n_{c=0,k=2}^2$ instead of averages of $n_{c=0,k=2}^2$ implies to consider regions which are at least partly occupied with negative refractive index squared. Nevertheless, the refractive index squared does exhibit a decrease on the equatorward side of the polar vortex between 10 and 100 hPa in many models, and even falls below values of 10 in the climate states representing the last 30-year running mean of the 1pctCO2 experiment in the AWI-ESM-1-1-LR and CanESM5 models (see Figs. 5.8 and 5.10). Furthermore, the pronounced waveguide narrowing present in these models is consistent with largest increases in the polar vortex strength, hinting at a possible increase in downward wave coupling events in the future. Due to the large spread in northern-hemispheric circulation changes among the CMIP6 multi-model ensemble, more detailed investigations are necessary to establish robust conclusions.

In the southern hemisphere, the waveguide at the top of the polar vortex remains unchanged during the entire 1pctCO2 experiment in most of the models. In combination with the pronounced, shoulder-shaped geometry of the waveguide, it is assumed that a reflecting surface in the upper stratosphere is omnipresent in midwinter climate of the southern hemisphere polar vortex (see Fig. 4.22). Similar to the northern hemisphere, the uniform equatorward shift of the southern-hemispheric polar vortex is transferred to strongly enlarging the region of negative $n_{c=0,k=2}^2$ on its poleward side. In contrast to the northern hemisphere, however, a strengthening of the polar vortex is accompanied by the robust development of a region of wave evanescence on the equatorward side of the polar vortex in the middle stratosphere which is particularly pronounced in the AWI-ESM-1-1-LR (see also Figs. 5.9 and 5.11). Indications of a similar behavior on the equatorward side of the waveguide are also observed for the MIROC-ES2L, MIROC6, and GFDL-ESM4 models, but Fig. 5.13 is not able to capture it since the box defined for computing percentages of negative $n_{c=0,k=2}^2$ in this region is located too high. This clearly shows that the wavenumber-2 waveguide in the southern hemisphere robustly develops a meridionally confined geometry during polar vortex strengthening. In combination with the reflecting surface assumed to exist at the top of the polar vortex, the possibility of downward wave coupling events in southern hemisphere winters likely increases in future climates consistent with less frequent SSWs (Jucker et al., 2021).

5.3 Conclusions

The combined analysis of PSC and TUTW experiments performed with Polvani and Kushner (2002)-type models revealed that sponge-layer damping at the top of the atmosphere automatically reduces the refractive index squared in the upper stratosphere when the polar vortex strengthens which likely increases the probability of the formation of a reflecting surface. Whether or not a strengthened polar vortex is able to significantly influence the troposphere is solely determined by the latitudinal width of the waveguide for planetary-scale waves. If

additional thermal forcings that increase the polar vortex strength are located above or around 100 hPa, the lower-stratospheric waveguide is not sufficiently narrowed below 100 hPa. Hence, reflected wave activity is likely subject to dissipate close to critical lines on the equatorward side of the polar vortex. Only those additional thermal forcings which increase the meridional potential vorticity gradient in midlatitudes between 100 and 200 hPa manage to establish a confined waveguide also in the lower stratosphere, connecting the stratosphere with the troposphere. The convergence of the poleward moving tropospheric jet and the equatorward moving polar vortex displaces the region of low potential vorticity gradients originally located above the tropospheric jet to the equatorward side of the polar vortex. The resulting region of vertically aligned minimum refractive index squared of a strengthened polar vortex confines the waveguide on its equatorward side. Reflected wave activity is thus more likely guided back to the troposphere which is consistent with a weakened residual circulation and an enhanced poleward shift of the tropospheric jet. Future work needs to confirm an increased number of downward wave coupling events (Perlwitz and Harnik, 2003; Shaw et al., 2010) and the existence of confining regions of wave evanescence (Harnik and Lindzen, 2001) in the strong polar vortex regime of idealized PSC and TUTW experiments.

The southern-hemispheric circulation response of the CMIP6 multi-model ensemble in the 1pctCO₂ experiment proceeds linearly in good approximation which suggests that a regime transition similar to the idealized simulations might be absent. Nevertheless, observed circulation changes including the southern-hemispheric polar vortex strengthening could be explained by previous findings from idealized models. The southern-hemispheric polar vortex reflects characteristics of the strong polar vortex regime already in the preindustrial climate state, and up to now, only two sudden stratospheric warmings have been observed (Krüger et al., 2005; Rao et al., 2020). The development of a more confined waveguide in response to higher greenhouse-gas concentrations that shift the lower-stratospheric polar vortex equatorward implies an increased probability of wave reflection events (Fig. 5.2) which is consistent with even rarer breakdowns of the polar vortex in the future (Jucker et al., 2021) and later final warmings at the end of winter seasons (Wilcox and Charlton-Perez, 2013; Ceppi and Shepherd, 2019). Whereas later final warmings cause enhanced poleward shifts of the lower-tropospheric eddy-driven jet during late spring and summer (Ceppi and Shepherd, 2019), a possibly increased number of downward wave coupling events could lead to additional poleward jet shifts during the extended winter season which remains to be quantified. A concomitant feature of an increased number of downward wave flux events detected in idealized model experiments is a weakened residual circulation (see Figs. 5.1 and 5.2). Annual-mean trends of the residual circulation strength show, however, a robust increase in tropical upwelling for future climates (Hardiman et al., 2014; Abalos et al., 2021). Only the polar lower stratosphere of the southern hemisphere exhibits weakened downwelling during the 1pctCO₂ experiment (Abalos et al., 2021) which can be expected from pronounced equatorward shifts of the lower polar

vortex consistent with less wave activity reaching high latitudes of the lower stratosphere (see panels 6 and 7 of Fig. 5.4). Assuming weaker planetary-scale wave driving in future southern-hemispheric climates, the overall strengthening of the residual circulation could be caused by increasing contributions from smaller-scale gravity waves (Cohen et al., 2013; Sigmond and Shepherd, 2014; Abalos et al., 2021). In order to confirm this proposed mechanism for the southern-hemispheric polar vortex strengthening, the number of wave reflection and possible downward wave coupling events as well as several contributions to the residual circulation strength have to be determined for southern-hemispheric winter seasons only, rather than for the entire year.

In the northern hemisphere, circulation changes are found to be consistent for a small subset of CMIP6 models analyzed here and in Abalos et al. (2021). The models named MIROC6, MRI-ESM2-0, and GFDL-ESM4 correspond to the group of CMIP6 models that do not exhibit a significant increase in the polar vortex strength after 150 years of the 1pctCO₂ experiment which is in general consistent with a strengthened residual circulation. Circulation trends of other models provided by Abalos et al. (2021) are not analyzed in this thesis. At this point, it is difficult to assess whether the nonlinear response of the polar vortex strength observed in some CMIP6 models can be related to the dynamical mechanism revealed in idealized models. On the one hand, CMIP6 models with largest increases in the polar vortex strength (AWI-ESM-1-1-LR, CanESM5, and MPI-ESM-1-2-HAM) also exhibit a similar geometry change of the waveguide that was detected during the polar vortex regime transition in idealized models. Strengthened upper flanks of the subtropical jets induced by TUTW are consistent with a stronger lower-stratospheric residual circulation and the equatorward shift of the lower polar vortex (Shepherd and McLandress, 2011; Butchart et al., 2010; Scaife et al., 2012; Oudar et al., 2020b; Hardiman et al., 2014; Abalos et al., 2021). On the other hand, the poleward shift of the lower-tropospheric jet proceeds more or less linearly, and impacts of a possibly increased number of downward wave coupling events are difficult to detect in seasonal-mean climate states. Furthermore, the constant forcing of planetary-scale wave fluxes in idealized TUTW experiments simplified the observation of the regime transition. Increasing upward propagating wave fluxes due to shrinking Arctic sea ice could interfere with the development of a confined waveguide (Kretschmer et al., 2020). Even if asymmetrical shrinking of Arctic sea ice stops and the additional source of wave activity vanishes, Arctic amplification could still persist to prohibit enhanced poleward shifts of the tropospheric jet (McGraw and Barnes, 2016). Also smaller-scale wave activity associated with gravity waves which are not included in the idealized-model experiments of this thesis might influence the polar vortex response (Wu et al., 2019). Although the spread in residual circulation trends in the upper stratosphere is four times larger than in the lower stratosphere, the deep branch still accelerates in response to increased CO₂ concentrations (Abalos et al., 2021). Therefore, daily data including necessary TEM quantities to monitor the evolution of the residual circulation of longer climate-change

experiments as performed with the AWI-ESM-1-1-LR model in the 1pctCO2 experiment have to be investigated to provide a more confident perspective on northern-hemispheric climate change (Gerber and Manzini, 2016).

Chapter 6

Summary and outlook

This thesis investigated the mechanism of the dynamical coupling of the stratosphere and troposphere in a changing climate. The crucial region for this coupling during extended winter seasons has previously been identified to be the lower stratosphere which controls the amount of planetary-scale wave flux that enters the stratosphere (Chen and Robinson, 1992; Scott and Polvani, 2006; Martineau et al., 2018; Birner and Albers, 2017; White et al., 2019), raising the question:

- **S1:** How does the extratropical lower stratosphere control the dynamical coupling of the stratosphere and troposphere?

In Chap. 3, different realizations of the stratospheric polar vortex were simulated with a dry dynamical-core model forced by idealized wavenumber-2 (WN2) topography and polar stratospheric cooling (PSC, Polvani and Kushner, 2002; Gerber and Polvani, 2009; Garny et al., 2020) revealing that the lower stratospheric control of the dynamical coupling of the stratosphere and troposphere is characterized by the waveguide for planetary-scale waves. A discontinuous waveguide with existing regions of negative values of the refractive index squared in the extratropical lower stratosphere generally impedes upward propagating planetary-scale waves which are more likely subject to dissipate in the lower stratosphere, consistent with a strong lower-stratospheric residual circulation. In this dissipation-dominated regime, improvements of the waveguide associated with a stronger polar vortex generated by stronger meridional temperature gradients in the extratropical stratosphere are consistent with enhanced upward propagating wave activity and a weakened (strengthened) residual circulation in the lower (upper) stratosphere. As long as the upper-stratospheric residual circulation accelerates, a negative feedback is exerted on the meridional temperature gradient, preventing large increases of the polar vortex strength (Garny et al., 2020).

Further increases in the meridional temperature gradient can introduce a reflecting surface for planetary-scale waves in the upper stratosphere, potentially reducing the dissipation of upward

propagating wave activity which is consistent with a stronger polar vortex. Sec. 5.1 revealed that the occurrence of a reflecting surface for vertically propagating planetary-scale waves is strongly correlated with the strength of the polar vortex in idealized general circulation models (GCMs) which employ Rayleigh friction to damp horizontal winds at the top of the atmosphere (Polvani and Kushner, 2002). Promoting a stronger polar vortex by enhanced meridional temperature gradients in the extratropical stratosphere automatically causes stronger wind damping and hence, stronger vertical curvature of the zonal-mean zonal wind. This, in turn, contributes negatively to the refractive index squared and increases the probability of a region of wave evanescence for vertical propagation (Harnik and Lindzen, 2001). As an alternative to Rayleigh friction, Cohen et al. (2013) introduced an interactive parameterization of gravity-wave drag in the Polvani and Kushner (2002)-model. Future work could therefore examine whether the probability of a reflecting surface at the top of the stratosphere is still strongly correlated to the strength of the polar vortex when a more realistic wind-damping scheme is employed in idealized models.

In states with a reflecting surface above the polar vortex, reflected or upward propagating planetary-scale waves still have the possibility to reach critical lines in subtropical regions associated with the zero-wind contour of the polar vortex (Shaw et al., 2010). A stronger polar vortex forced by enhanced meridional equilibrium temperature gradients promoting an improved waveguide still exerts a negative feedback on the meridional temperature gradient via enhanced planetary-scale wave dissipation which drives a stronger residual circulation in the upper stratosphere. The disappearance of this negative feedback offers the possibility of a regime transition to a strong and stable polar vortex consistent with drastically reduced wave dissipation in the stratosphere and a weakened residual circulation. Sec. 5.1 showed that the decisive factor for this regime transition to occur is the meridional extent of the waveguide. Only if a meridionally confined waveguide with regions of wave evanescence on both the pole- and equatorward sides of the polar vortex is established in addition to a reflecting surface at its top, thus preventing reflected wave activity from dissipating close to critical lines in subtropical regions, the polar vortex is observed to transition to a strong and stable regime accompanied by a noticeable poleward shift of the tropospheric jet. The resulting circulation response in combination with an increased number and duration of downward wave flux events as well as the confined waveguide provide strong evidence for downward wave coupling events (Perlwitz and Harnik, 2003; Shaw et al., 2010) in the strong polar vortex regime although the refractive index squared used in this thesis is not able to differ between vertical and latitudinal wave propagation (Harnik and Lindzen, 2001). The region of wave evanescence on the equatorward side of the polar vortex is therefore only assumed to be present, indicated by a smooth, vertically aligned region of minimum refractive index squared on the equatorward side of the polar vortex (see Fig. 4.22). Supplemental studies have to confirm the existence of regions of wave evanescence for vertical and meridional planetary-scale wave propagation as

well as the presence of downward wave coupling events in the strong polar vortex regime of idealized Polvani and Kushner (2002)-type models.

Sec. 5.1 additionally revealed that the confined geometry of the waveguide can only be established if the polar stratospheric cooling employed to strengthen the polar vortex extends sufficiently below 100 hPa in the lower stratosphere. In this case, the meridional gradient of potential vorticity is observed to increase significantly between 100 and 200 hPa if larger gradients of the equilibrium temperature in the extratropical stratosphere are employed. The increasing strength of the zonal-mean zonal wind in the lower stratosphere can then act to shape a confined waveguide since the refractive index squared is stronger reduced everywhere except in the narrow region of increased potential vorticity gradients, creating a connection of relatively high refractive index squared between stratosphere and troposphere compared to the surrounding regions when the polar vortex strengthens. Increased cooling of the lower stratosphere below 200 hPa is also essential to induce poleward shifts of the tropospheric jet when the polar vortex regime transition is performed (see Figs. 3.8 and 3.11). Additional polar stratospheric cooling above 150 hPa can indeed strengthen the polar vortex, but is not able to induce significant poleward shifts of the tropospheric jet.

A similar nonlinear circulation response has previously been found to occur in response to tropical upper-tropospheric warming (TUTW, Wang et al., 2012) which is a robust feature of greenhouse gas-induced temperature signatures in the troposphere (e.g., Shepherd and McLandress, 2011; Vallis et al., 2015; Shaw, 2019). Up to a critical threshold of TUTW, the polar vortex strength stays roughly constant and the residual circulation strengthens. Beyond the critical threshold, a sharp increase of the polar vortex strength consistent with a weakened residual circulation is observed in combination with an enhanced poleward shift of the eddy-driven jet, prompting the question:

- **S2:** How does tropical upper-tropospheric warming (TUTW) trigger a nonlinear response of the coupled stratosphere-troposphere circulation?

To answer this question, the TUTW experiment with idealized WN2 topography performed by Wang et al. (2012) was repeated and extended in Chap. 4 by two additional stratospheric basic states, one with a colder polar lower stratosphere, and one without polar vortex to quantify the stratospheric influence on the troposphere during the polar vortex regime transition. The circulation response to TUTW is characterized by a poleward shift of the tropospheric jet in all three setups. The setups with polar vortex exhibit, however, an enhanced poleward shift of the tropospheric jet compared to the setup without polar vortex when the polar vortex transitions from a weak and variable to a strong and stable regime.

The weak regime of the TUTW experiment, i.e., the set of tropical upper-tropospheric heating amplitudes which does neither lead to an increase in the polar vortex strength, nor to a stronger poleward shift of the tropospheric jet compared to the experiment without polar vor-

tex, is characterized by the critical-layer control mechanism. TUTW induces stronger upper flanks of the subtropical jets which allow more wave activity to enter the lower stratosphere, strengthening the residual circulation in this regions (Shepherd and McLandress, 2011). In presence of a polar vortex which exhibits a local downwelling maximum at its poleward edge, the strengthened lower-stratospheric residual circulation is consistent with an equatorward shift of the lower polar vortex, narrowing the refractive index for planetary-scale waves on the poleward side of the polar vortex. Sec. 5.1 showed that the poleward moving tropospheric jet and the equatorward shifting lower polar vortex act to increase the meridional gradient of potential vorticity in the midlatitude lower stratosphere between 100 and 200 hPa. Additionally, the region of low potential vorticity gradients originally located above the tropospheric jet is elongated on the equatorward side of the polar vortex, preparing the confined waveguide for planetary-scale waves when the polar vortex strengthens.

At a critical level of TUTW, a sufficiently confined waveguide is established consistent with a sharp reduction of planetary-scale wave dissipation in the stratosphere, a strengthened polar vortex, a weakened residual circulation, and an increased number and duration of downward wave flux events. Similar to the polar stratospheric cooling experiments, strong evidence for downward wave coupling events as the dominating ingredient that emerges during the polar vortex regime transition in response to TUTW is provided. The critical warming level inducing the strong polar vortex regime depends on the stratospheric basic state. In case of the reference state provided by Wang et al. (2012), tropical upper-tropospheric temperature increases beyond 8 K are necessary, whereas only 2 K are sufficient in the stratospheric basic state with colder polar lower stratosphere. According to the results of the polar stratospheric cooling experiments, a colder polar lower stratosphere is consistent with larger meridional gradients of potential vorticity in the midlatitude lower stratosphere between 100 and 200 hPa. Therefore, lower levels of TUTW, which further increase the potential vorticity gradient, are sufficient to trigger the regime transition associated with the development of the confined geometry of the waveguide.

In a sensitivity experiment, the region of additional warming in the tropics was elevated from around 300 hPa in the upper troposphere to around 100 hPa in the lower stratosphere. Although this experiment lacks a realistic justification since stratospheric temperatures generally decrease in response to increased carbon dioxide concentrations (Vallis et al., 2015), it confirmed the dynamical mechanism responsible for the polar vortex regime transition in PSC and TUTW experiments accompanied by an enhanced poleward shift of the tropospheric jet. Additional warming in the lower stratosphere increases meridional temperature gradients in the extratropical stratosphere inducing a stronger polar vortex which exhibits indeed similarities to the stable polar vortex in the strong regime with very rare formations of sudden stratospheric warmings. A similar tropospheric influence with an enhanced poleward shift of the tropospheric jet is, however, not observed for any climate state of this sensitivity exper-

iment. Sec. 5.1 proved that the additional warming in the tropical lower stratosphere is not able to increase the meridional gradient of potential vorticity between 100 and 200 hPa which is necessary to trigger the regime transition. Consistently, the lower-stratospheric waveguide for planetary-scale waves does not exhibit the confined geometry and the tropospheric jet is unaffected.

The similarities in the PSC and TUTW experiments arise from the equatorward shift of the lower-stratospheric polar vortex. In the PSC experiments, a stronger meridional temperature gradient in the midlatitude stratosphere directly forces the polar vortex to move equatorward, consistent with enhanced equatorward propagating wave fluxes in the stratosphere. The direct circulation response in the TUTW experiments is characterized by a poleward moving tropospheric jet with strengthened upper flanks which, in turn, could cause the increased equatorward propagating wave flux in the lower stratosphere. Further equatorward located regions of wave dissipation in the stratosphere are then consistent with the equatorward shift of the lower polar vortex towards latitudes of maximum gradients of the equilibrium temperature. The retraction of the lower polar vortex from high latitudes thereby reduces the propagation of wave flux into the high-latitude stratosphere. As soon as a critical point is reached, the regime transition to a strong and stable polar vortex happens. The disentanglement of cause and effects of the equatorward moving polar vortex, further equatorward dissipating planetary-scale wave flux, and changes in the residual circulation is, however, not possible since time averages of climate states in equilibrium are analyzed. For the same reason, the polar vortex regime transition with all accompanying circulation changes as the sharp increase in downward wave flux events and the enhanced poleward shift of the tropospheric jet can also only be diagnosed, but not motivated to arise from one specific cause. Additional effort is necessary to investigate the cause-effect chain in preparation of and during the polar vortex regime transition in greater detail. Ensembles of transient model runs starting from the weak polar vortex regime which are forced towards the strong polar vortex regime could provide further insights.

A possible explanation for the overarching presence of the regime transition in different temperature-change experiments with Polvani and Kushner (2002)-type GCMs might be the vertically aligned region of strongest meridional temperature gradients in the stratosphere in combination with the dominance of wavenumber-2 wave fluxes. Sufficient equatorward shifts of the lower polar vortex are accompanied by stronger equatorward refracted wave activity which misses to decelerate the stratospheric polar vortex. Circulation changes that are necessary to lead to this polar vortex regime transition include the increased meridional potential vorticity gradient in the midlatitude lower stratosphere between 100 and 200 hPa as shown in Sec. 5.1. Due to the vertically aligned region of strongest meridional gradients of the stratospheric equilibrium temperature, planetary-scale wave fluxes which are equatorward refracted and thus missing in the upper stratosphere give the polar vortex no other opportunity but to

closely adjust to the equilibrium temperature. If a broader spectrum of planetary-scale waves was present, corresponding waveguides for different planetary-scale waves could form the confined geometry at different forcing levels such that the reorganization of wave fluxes loses sharpness. The experiments with idealized GCMs performed in this thesis could therefore be repeated with a more realistic equilibrium temperature (Jucker et al., 2013; Wu and Reichler, 2018) and idealized topographies that support a broader planetary-scale wave spectrum.

The reorganization of the coupled stratosphere-troposphere circulation during the regime transition in the Polvani and Kushner (2002)-type models has been proposed to arise from an increased number of downward wave coupling events. Strong polar vortices can, however, also influence the troposphere via anomalies of the zonal-mean circulation (Limpasuvan et al., 2005). If future studies confirm the presence of downward wave coupling events in the strong polar vortex regime, contributions from downward zonal mean coupling should also be taken into account (Perlwitz and Harnik, 2004). The possible effects of gravity waves regarding the dynamical mechanism of stratosphere-troposphere coupling introduced in this thesis have not been considered. Previous studies showed that a compensation mechanism between resolved Rossby waves and parameterized gravity waves in idealized and complex models is present (Cohen et al., 2013; Sigmond and Shepherd, 2014). A lack of wave flux missing to drive the residual circulation from one source of wave flux can be compensated by the other source. These studies have, however, not considered confined geometries of the waveguide for planetary-scale waves associated with wave reflections, which might suppress the compensating effect when Rossby waves are not able to dissipate within the stratosphere.

Finally, this thesis assessed whether the findings from idealized GCMs are relevant for explaining projected future circulation changes in more complex models. To this end, the CMIP6 multi-model ensemble forced by a 1% increase in carbon dioxide concentrations per year (1pctCO₂, Eyring et al., 2016) was consulted in Sec. 5.2 to answer the question:

- **S3:** Do indications of the dynamical mechanism revealed in idealized models exist in complex models?

Indications of the dynamical mechanism for the polar vortex regime transition in idealized models (Wang et al., 2012) which was revealed in Chap. 4 are indeed present in complex climate models. Accompanying greenhouse-gas induced tropical upper-tropospheric warming, midwinter polar vortices are shifted equatorward in the lower stratosphere in some models, narrowing the waveguide for planetary-scale waves on the poleward side of the polar vortex. This behavior is particularly pronounced in the southern hemisphere where all but one model show a linear increase in the June-July-August seasonal-mean polar vortex strength. Furthermore, the southern-hemispheric polar vortex strengthening is accompanied by a reduction of the refractive index squared for stationary waves of wavenumber 2 on the equatorward side of the polar vortex, indicating the development of a more confined waveguide. Reflecting

surfaces at the top of the polar vortex are assumed to be present already at preindustrial climate states, which is consistent with the linear circulation response. The strengthening of the southern-hemispheric polar vortex (Jucker et al., 2021) as well as later final warmings (Wilcox and Charlton-Perez, 2013; Ceppi and Shepherd, 2019) in future climates are therefore assumed to be accompanied by an increasing number of downward wave coupling events. Clear signals of the correlation between the confining waveguide and the polar vortex strengthening occur, however, only for strong temperature increases such that this mechanism might only be relevant for the late twenty-first century.

The linear strengthening of the southern-hemispheric polar vortex is reminiscent of the WN0 setup without additional planetary-scale wave generation and with low variability and almost half as strong planetary-scale wave fluxes than in the WN2 setup (Fig. 3.14). Although number and length of events of downward propagating wave flux increase in the WN0 setup forced by stronger meridional temperature gradients in the midlatitude stratosphere (Fig. 3.13), no sharp stratospheric circulation changes are observed, neither in the strength of the residual circulation (Fig. 3.12), nor in the strength of the polar vortex (Fig. 3.11). Therefore, even though more planetary-scale wave reflection events are likely to occur in the southern hemisphere in future climates, their influence on stratosphere-troposphere coupling might be small due to the overall small magnitude of wave activity in the southern hemisphere.

In the northern hemisphere, projected circulation changes exhibit larger uncertainties (Manzini et al., 2014; Ayarzagüena et al., 2020; Kretschmer et al., 2020) as well as nonlinear behaviors (Manzini et al., 2018). Some models predict no significant change or a weakening of the December-January-February seasonal-mean polar vortex strength after 150 years of exponentially increasing carbon dioxide concentrations which is in general consistent with a strengthened residual circulation (Hardiman et al., 2014; Abalos et al., 2021). Three of the models that include a strengthening of the polar vortex after the phase with constant or decreasing strength indeed show indications of more confined waveguides compared to their corresponding preindustrial climate states. Again, it can, however, not be distinguished whether the confined waveguide causes the strengthening of the northern-hemispheric polar vortex or vice versa.

Previously, this nonlinear polar vortex response in the northern hemisphere has been proposed to originate from missing zonally-asymmetric Arctic amplification as soon as marginal Arctic seas become ice-free (Manzini et al., 2018), and indeed, a small causal connection has been found by Kretschmer et al. (2020). Furthermore, a broader spectrum of planetary-scale waves in the CMIP6 multi-model ensemble is likely present compared to the idealized model experiments with predominant generation of wavenumber-2 waves. Therefore, sharp transitions of the polar vortex might be suppressed as the waveguides of different wavenumbers would reach their respective reflecting states at different levels of tropospheric warming. Since forcings of other wavenumbers would lead to additional contributions of wave-wave and wave-mean

flow interaction, the argument is not straightforward. Idealized TUTW experiments which additionally include wave-like heating in polar surface regions (Butler et al., 2010; Kim et al., 2014; McGraw and Barnes, 2016) as well as the analysis of daily instead of monthly data from complex models including wave fluxes (Gerber and Manzini, 2016) could help to clarify the role of Arctic sea-ice loss in northern-hemispheric climate change. So far, the nonlinear circulation response of the northern-hemispheric polar vortex in combination with the large uncertainty in its future response remains an open question (Manzini et al., 2014; Ayarzagüena et al., 2020).

Altogether, this thesis contributes to the general research questions:

- **G1:** How strongly do changes in the middle atmospheric circulation alter the circulation at the surface through dynamical downward coupling?
- **G2:** Is there a feedback of tropospheric warming via a strengthened stratospheric circulation on the troposphere?

The idealized model experiments performed with EMIL (Garny et al., 2020) suggest that stratospheric circulation changes need to exceed a certain threshold in order to exert a significant tropospheric influence, and that this influence is presumably mediated via downward wave coupling events (Perlwitz and Harnik, 2003; Shaw et al., 2010). In the setup with idealized WN2 topography and a standard transition pressure from tropospheric to stratospheric equilibrium temperatures in the polar winter hemisphere including a large isotherm layer (Polvani and Kushner, 2002; Gerber and Polvani, 2009), even a strong polar vortex is not able to lead to significant poleward shifts of the tropospheric jet. Only in presence of a colder polar lower stratosphere, the latitude of the tropospheric jet exhibits a larger sensitivity to the polar vortex strength. This thesis revealed that stratospheric circulation changes need to include a meridional potential vorticity gradient $\partial_y \bar{q}$ in the midlatitude lower stratosphere that is larger than the meridional gradient β of the Coriolis parameter to induce tropospheric jet shifts. On the other hand, poleward shifts of the tropospheric jet itself in combination with an equatorward moving lower polar vortex, induced by tropical upper-tropospheric heating, are able to increase $\partial_y \bar{q}$ for stratospheric basic states which would otherwise not be able to influence the troposphere. Exceeding the threshold $\partial_y \bar{q} > \beta$, sufficiently strong (depending on the stratospheric basic state) tropical upper-tropospheric warming triggers identical regime transitions to polar lower-stratospheric cooling.

The results of this thesis confirm the important role of the lower stratosphere for stratosphere-troposphere coupling and refine the understanding of its nature given by the shape and strength of the waveguide for planetary-scale waves in the lower stratosphere, contributing to the general research question **G1**. Furthermore, this thesis reveals that the role of the lower stratosphere extends to climatological or climate-change time scales which has, so far, been attributed to subseasonal time scales only. Finally, the feedback of tropospheric warm-

ing via a strengthened stratospheric circulation on the troposphere is observed, affirming the general research question **G2**.

In this idealized model setup, the dynamical coupling of the stratosphere and troposphere is characterized by the presence of a regime transition. The tropospheric jet as a whole shifts poleward, accompanied by drastic changes of the waveguide developing a confined geometry during the regime transition. The analysis of more complex models as part of the CMIP6 multi-model ensemble revealed that the core of the tropospheric jet located around 200 hPa, representing the subtropical jet, exhibits only weak latitudinal variations during the 1pctCO2 experiment, whereas the maximum zonal-mean zonal wind around 850 hPa, representing the eddy-driven jet, shifts poleward in response to increased carbon dioxide concentrations.¹⁶ Furthermore, diabatic heatings applied in idealized dry climate models can cause unintended circulation changes away from the region of diabatic heating (Shaw, 2019; Yuval and Kaspi, 2020). The next step towards higher complexity are idealized moist models including gray radiative transfer, but still excluding clouds and convection (Frierson et al., 2006, 2007a). These models provide a more realistic separation between subtropical and eddy-driven jets and could therefore serve as the next environment to test the dynamical mechanism introduced in this thesis. In this way, essential step-by-step improvements in the understanding of the climate system can be achieved (Held, 2005; Maher et al., 2019) to reduce the uncertainty in projections of future circulation changes (Hawkins and Sutton, 2009).

¹⁶Refer to Staten et al. (2020) for the definition of different tropical-width metrics.

Acronyms

1pctCO2	CMIP experiment with a CO ₂ concentration increase of 1% per year
abrupt-4xCO2	CMIP experiment with an abrupt quadrupling of CO ₂ concentrations
CLCM	critical-layer control mechanism
CLS	EMIL setup with polar vortex and colder polar lower stratosphere
CMIP	Coupled Model Intercomparison Project
CMIP5	Coupled Model Intercomparison Project Phase 5
CMIP6	Coupled Model Intercomparison Project Phase 6
CO ₂	carbon dioxide
CP1	first critical point
CP2	second critical point
DJF	December-January-February
ECHAM5	European Centre HAMburg general circulation model 5
ECMWF	European Centre for Medium-Range Weather Forecasts
EMIL	ECHAM/MESSy IdeaLized model
EP	Eliassen–Palm
EPFD	Eliassen–Palm flux divergence
ERA5	ECMWF’s next-generation reanalysis ERA5
GCM	general circulation model
HC	Hadley cell
JJA	June-July-August
LS	lower stratosphere
MERRA-2	Modern-Era Retrospective analysis for Research and Applications, Version 2
MESSy	Modular Earth Submodel System
NH	northern hemisphere
NPV	EMIL setup without polar vortex
PDF	probability density function
PSC	polar stratospheric cooling
PVRT	polar vortex regime transition
QG	quasi-geostrophic
RC	residual-mean meridional circulation
REF	reference EMIL setup with polar vortex
SH	southern hemisphere
SPARC	Stratosphere-troposphere Processes And their Role in Climate
SSW	sudden stratospheric warming

TEM	transformed Eulerian-mean
TUT	tropical upper troposphere
TUTW	tropical upper-tropospheric warming
UT	upper troposphere
UTLS	upper troposphere-lower stratosphere
WMO	World Meteorological Organization
WN	wavenumber
WN0	EMIL setup without additional planetary-scale wave generation
WN2	wavenumber-2
WN2H	EMIL setup with idealized wavenumber-2 heating
WN2T	EMIL setup with idealized wavenumber-2 topography

List of figures

1.1	Future changes in surface air temperature and precipitation.	3
1.2	Nontransport paradox for adiabatic flow in the stationary limit.	6
1.3	Constituents of the refractive index squared.	10
1.4	Wave-driven residual circulation in the middle atmosphere.	11
1.5	Annual statistics of the polar vortex strength in both hemispheres.	13
1.6	Circulation changes in response to increased greenhouse-gas concentrations. . .	16
1.7	Uncertainty of future tropospheric and stratospheric circulation changes.	17
2.1	Relevant parameters of the idealized general circulation model EMIL.	26
2.2	Tropospheric equilibrium temperatures for different δ_z in EMIL.	27
2.3	Robust computation of the latitude of maximum zonal-mean zonal wind.	35
2.4	Eliassen–Palm fluxes associated with a meridional subdomain.	37
2.5	Standard and downward-control streamfunction of the residual circulation. . . .	38
3.1	Temperature profiles for different polar vortex lapse rates.	42
3.2	Temperature and wind climatologies for different EMIL setups.	44
3.3	Temperature comparison of different EMIL setups with reanalysis data.	45
3.4	Polar vortex strength comparison of different EMIL setups with reanalysis data.	46
3.5	Eliassen–Palm fluxes for different EMIL setups.	47
3.6	Refractive index squared for different EMIL setups.	48
3.7	Refractive index squared for two reanalysis data sets during winter seasons. . .	49
3.8	Nonlinear circulation response to polar stratospheric cooling.	51
3.9	Refractive index squared for different polar vortex geometries.	52
3.10	Autocorrelation time scale for polar stratospheric cooling experiments.	53
3.11	Tropospheric-jet latitude and polar vortex strength for polar stratospheric cooling experiments.	54
3.12	Residual circulation strength for polar stratospheric cooling experiments.	55
3.13	Statistics of downward wavenumber-2 events for polar stratospheric cooling experiments.	56
3.14	Eliassen–Palm flux budgets in the extratropical upper troposphere for polar stratospheric cooling experiments.	57
4.1	Dynamical mechanism of the regime transition in tropical upper-tropospheric warming experiments.	63
4.2	Control-run climatologies for tropical warming experiments.	64

4.3	Resolution-dependent appearance of additional stratospheric jets in setups without polar vortex.	65
4.4	Latitude and strength of stratospheric zonal-wind maxima for tropical upper-tropospheric warming experiments.	66
4.5	Latitude and strength of tropospheric zonal-wind maxima for tropical upper-tropospheric warming experiments.	67
4.6	Autocorrelation time scale for tropical upper-tropospheric warming experiments.	68
4.7	Eliassen–Palm flux budgets in the extratropical upper troposphere for tropical upper-tropospheric warming experiments.	69
4.8	Eliassen–Palm fluxes for control runs.	71
4.9	Eliassen–Palm flux differences of tropical upper-tropospheric warming experiments with weak heating and control runs.	72
4.10	Eliassen–Palm flux differences of tropical upper-tropospheric warming experiments with strong heating and weak heating.	73
4.11	Residual circulation strength for tropical upper-tropospheric warming experiments.	74
4.12	Temperature differences and induced zonal-wind tendencies of weak tropical upper-tropospheric heating.	75
4.13	Refractive index squared for simulations with zero, weak, and strong tropical upper-tropospheric heating.	78
4.14	Statistics of downward wavenumber-2 events for tropical upper-tropospheric warming experiments.	79
4.15	Circulation changes for different tropical heating setups.	82
4.16	Waveguide changes for different tropical heating setups.	83
4.17	Latitude and strength of stratospheric zonal-wind maxima for tropical heating at different altitudes.	86
4.18	Latitude and strength of tropospheric zonal-wind maxima for tropical heating at different altitudes.	87
4.19	Hadley cell changes for tropical heating at different altitudes.	89
4.20	Eliassen–Palm fluxes for simulations with weak and strong tropical heating in the lower stratosphere and in the middle troposphere.	90
4.21	Refractive index squared for simulations with weak and strong tropical heating in the lower stratosphere and in the middle troposphere.	91
4.22	Waveguides during southern-hemispheric winter in 1996.	95
5.1	Residual circulation strength for various polar stratospheric cooling and tropical warming experiments.	101
5.2	Waveguide and tropospheric-jet changes for various polar stratospheric cooling and tropical warming experiments.	103
5.3	Waveguides and schematic wave fluxes for stratospheric cooling and tropical warming experiments with and without tropospheric influence.	106
5.4	Eliassen–Palm fluxes for stratospheric cooling and tropical warming experiments with and without tropospheric influence.	107
5.5	Tropical upper-tropospheric temperature for CMIP6 models of the 1pctCO2 experiment.	110
5.6	Latitude and strength of zonal-wind maxima in the DJF-averaged northern hemisphere for CMIP6 models of the 1pctCO2 experiment.	112

5.7	Latitude and strength of zonal-wind maxima in the JJA-averaged southern hemisphere for CMIP6 models of the 1pctCO2 experiment.	113
5.8	Waveguides in the first 30-year mean DJF-averaged northern hemisphere for CMIP6 models of the 1pctCO2 experiment.	114
5.9	Waveguides in the first 30-year mean JJA-averaged southern hemisphere for CMIP6 models of the 1pctCO2 experiment.	115
5.10	Waveguides in the last 30-year mean DJF-averaged northern hemisphere for CMIP6 models of the 1pctCO2 experiment.	116
5.11	Waveguides in the last 30-year mean JJA-averaged southern hemisphere for CMIP6 models of the 1pctCO2 experiment.	117
5.12	Waveguides in the DJF-averaged northern hemisphere as functions of polar vortex strength changes for CMIP6 models of the 1pctCO2 experiment.	118
5.13	Waveguides in the JJA-averaged southern hemisphere as functions of polar vortex strength changes for CMIP6 models of the 1pctCO2 experiment.	119

List of tables

2.1	Polar stratospheric cooling experiments analyzed in Chap. 3.	32
2.2	Tropical warming experiments analyzed in Chap. 4.	33
5.1	CMIP6 models contributing to the 1pctCO2 experiment analyzed in Sec. 5.2. .	111

Bibliography

- Abalos, M., Calvo, N., Benito-Barca, S., Garny, H., Hardiman, S. C., Lin, P., Andrews, M. B., Butchart, N., Garcia, R., Orbe, C., Saint-Martin, D., Watanabe, S., and Yoshida, K. The Brewer–Dobson circulation in CMIP6. *Atmospheric Chemistry and Physics*, 21(17): 13571–13591, 2021. <https://doi.org/10.5194/acp-21-13571-2021>.
- Adam, O., Grise, K. M., Staten, P., Simpson, I. R., Davis, S. M., Davis, N. A., Waugh, D. W., Birner, T., and Ming, A. The TropD software package (v1): standardized methods for calculating tropical-width diagnostics. *Geoscientific Model Development*, 11(10):4339–4357, 2018. <https://doi.org/10.5194/gmd-11-4339-2018>.
- Alexander, M. J., Geller, M., McLandress, C., Polavarapu, S., Preusse, P., Sassi, F., Sato, K., Eckermann, S., Ern, M., Hertzog, A., Kawatani, Y., Pulido, M., Shaw, T. A., Sigmond, M., Vincent, R., and Watanabe, S. Recent developments in gravity-wave effects in climate models and the global distribution of gravity-wave momentum flux from observations and models. *Quarterly Journal of the Royal Meteorological Society*, 136(650):1103–1124, 2010. <https://doi.org/10.1002/qj.637>.
- Andrews, D. G., Mahlman, J. D., and Sinclair, R. W. Eliassen-Palm Diagnostics of Wave-Mean Flow Interaction in the GFDL "SKYHI" General Circulation Model. *Journal of Atmospheric Sciences*, 40(12):2768–2784, 1983. [https://doi.org/10.1175/1520-0469\(1983\)040<2768:ETWATM>2.0.CO;2](https://doi.org/10.1175/1520-0469(1983)040<2768:ETWATM>2.0.CO;2).
- Andrews, D. G., Holton, J. R., and Leovy, C. B. *Middle Atmosphere Dynamics*. Academic Press, San Diego, 1987.
- Ayarzagüena, B., Charlton-Perez, A., Butler, A., Hitchcock, P., Simpson, I., Polvani, L., Butchart, N., Gerber, E., Gray, L., Hassler, B., Lin, P., Lott, F., Manzini, E., Mizuta, R., Orbe, C., Osprey, S., Saint-Martin, D., Sigmond, M., Taguchi, M., Volodin, E., and Watanabe, S. Uncertainty in the Response of Sudden Stratospheric Warmings and Stratosphere-Troposphere Coupling to Quadrupled CO₂ Concentrations in CMIP6 Models. *Journal of Geophysical Research: Atmospheres*, 125(6), 2020. <https://doi.org/10.1029/2019JD032345>.
- Baldwin, M. P., Gray, L. J., Dunkerton, T. J., Hamilton, K., Haynes, P. H., Randel, W. J., Holton, J. R., Alexander, M. J., Hirota, I., Horinouchi, T., Jones, D. B. A., Kinniersley, J. S., Marquardt, C., Sato, K., and Takahashi, M. The quasi-biennial oscillation. *Reviews of Geophysics*, 39(2):179–229, 2001. <https://doi.org/10.1029/1999RG000073>.

- Baldwin, M. P. and Dunkerton, T. J. Propagation of the arctic oscillation from the stratosphere to the troposphere. *Journal of Geophysical Research: Atmospheres*, 104(D24):30937–30946, 1999. <https://doi.org/10.1029/1999JD900445>.
- Baldwin, M. P. and Dunkerton, T. J. Stratospheric Harbingers of Anomalous Weather Regimes. *Science*, 294(5542):581–584, 2001. <https://doi.org/10.1126/science.1063315>.
- Baldwin, M. P., Stephenson, D. B., Thompson, D. W. J., Dunkerton, T. J., Charlton, A. J., and O’Neill, A. Stratospheric Memory and Skill of Extended-Range Weather Forecasts. *Science*, 301(5633):636–640, 2003. <https://doi.org/10.1126/science.1087143>.
- Barnes, E. A. and Polvani, L. Response of the Midlatitude Jets, and of Their Variability, to Increased Greenhouse Gases in the CMIP5 Models. *Journal of Climate*, 26(18):7117–7135, 2013. <https://doi.org/10.1175/JCLI-D-12-00536.1>.
- Baumgaertner, A. J. G., Jöckel, P., Kerkweg, A., Sander, R., and Tost, H. Implementation of the Community Earth System Model (CESM) version 1.2.1 as a new base model into version 2.50 of the MESSy framework. *Geoscientific Model Development*, 9(1):125–135, 2016. <https://doi.org/10.5194/gmd-9-125-2016>.
- Birner, T. and Albers, J. R. Sudden Stratospheric Warmings and Anomalous Upward Wave Activity Flux. *SOLA*, 13A(Special Edition):8–12, 2017. <https://doi.org/10.2151/sola.13A-002>.
- Brewer, A. W. Evidence for a world circulation provided by the measurements of helium and water vapour distribution in the stratosphere. *Quarterly Journal of the Royal Meteorological Society*, 75(326):351–363, 1949. <https://doi.org/10.1002/qj.49707532603>.
- Butchart, N., Cionni, I., Eyring, V., Shepherd, T. G., Waugh, D. W., Akiyoshi, H., Austin, J., Brühl, C., Chipperfield, M. P., Cordero, E., Dameris, M., Deckert, R., Dhomse, S., Frith, S. M., Garcia, R. R., Gettelman, A., Giorgetta, M. A., Kinnison, D. E., Li, F., Mancini, E., McLandress, C., Pawson, S., Pitari, G., Plummer, D. A., Rozanov, E., Sassi, F., Scinocca, J. F., Shibata, K., Steil, B., and Tian, W. Chemistry–Climate Model Simulations of Twenty-First Century Stratospheric Climate and Circulation Changes. *Journal of Climate*, 23(20): 5349–5374, 2010. <https://doi.org/10.1175/2010JCLI3404.1>.
- Butler, A. H., Sjoberg, J. P., Seidel, D. J., and Rosenlof, K. H. A sudden stratospheric warming compendium. *Earth System Science Data*, 9(1):63–76, 2017. <https://doi.org/10.5194/essd-9-63-2017>.
- Butler, A. H., Thompson, D. W. J., and Heikes, R. The Steady-State Atmospheric Circulation Response to Climate Change-like Thermal Forcings in a Simple General Circulation Model. *Journal of Climate*, 23(13):3474–3496, 2010. <https://doi.org/10.1175/2010JCLI3228.1>.
- Ceppi, P. and Shepherd, T. G. The Role of the Stratospheric Polar Vortex for the Austral Jet Response to Greenhouse Gas Forcing. *Geophysical Research Letters*, 46(12):6972–6979, 2019. <https://doi.org/10.1029/2019GL082883>.
- Chan, C. J. and Plumb, R. A. The Response to Stratospheric Forcing and Its Dependence on the State of the Troposphere. *Journal of the Atmospheric Sciences*, 66(7):2107–2115, 2009. <https://doi.org/10.1175/2009JAS2937.1>.

- Charlton, A. J. and Polvani, L. M. A New Look at Stratospheric Sudden Warmings. Part I: Climatology and Modeling Benchmarks. *Journal of Climate*, 20(3):449–469, 2007. <https://doi.org/10.1175/JCLI3996.1>.
- Charney, J. G. and Drazin, P. G. Propagation of planetary-scale disturbances from the lower into the upper atmosphere. *Journal of Geophysical Research (1896-1977)*, 66(1):83–109, 1961. <https://doi.org/10.1029/JZ066i001p00083>.
- Chen, P. and Robinson, W. A. Propagation of Planetary Waves between the Troposphere and Stratosphere. *Journal of Atmospheric Sciences*, 49(24):2533–2545, 1992. [https://doi.org/10.1175/1520-0469\(1992\)049<2533:POPWBT>2.0.CO;2](https://doi.org/10.1175/1520-0469(1992)049<2533:POPWBT>2.0.CO;2).
- Cohen, N. Y., Gerber, E. P., and Bühler, O. Compensation between Resolved and Unresolved Wave Driving in the Stratosphere: Implications for Downward Control. *Journal of the Atmospheric Sciences*, 70(12):3780–3798, 2013. <https://doi.org/10.1175/JAS-D-12-0346.1>.
- Cohen, N. Y., Gerber, E. P., and Bühler, O. What Drives the Brewer–Dobson Circulation? *Journal of the Atmospheric Sciences*, 71(10):3837–3855, 2014. <https://doi.org/10.1175/JAS-D-14-0021.1>.
- Collins, M., Knutti, R., Arblaster, J., Dufresne, J.-L., Fichefet, T., Friedlingstein, P., Gao, X., Gutowski, W., Johns, T., Krinner, G., Shongwe, M., Tebaldi, C., Weaver, A., Wehner, M., Allen, M., Andrews, T., Beyerle, U., Bitz, C., Bony, S., and Booth, B. *Long-term Climate Change: Projections, Commitments and Irreversibility*, pages 1029–1136. Climate Change 2013 – The Physical Science Basis: Working Group I Contribution to the Fifth Assessment Report of the Intergovernmental Panel on Climate Change. Cambridge University Press, Cambridge, United Kingdom and New York, NY, USA, 2014. <https://doi.org/10.1017/CB09781107415324.024>.
- Collins, W. J., Bellouin, N., Doutriaux-Boucher, M., Gedney, N., Halloran, P., Hinton, T., Hughes, J., Jones, C. D., Joshi, M., Liddicoat, S., Martin, G., O’Connor, F., Rae, J., Senior, C., Sitch, S., Totterdell, I., Wiltshire, A., and Woodward, S. Development and evaluation of an Earth-System model – HadGEM2. *Geoscientific Model Development*, 4(4):1051–1075, 2011. <https://doi.org/10.5194/gmd-4-1051-2011>.
- Danabasoglu, G. NCAR CESM2-FV2 model output prepared for CMIP6 CMIP 1pctCO2. Version 20200310. Earth System Grid Federation, 2020a. <https://doi.org/10.22033/ESGF/CMIP6.11283>.
- Danabasoglu, G. NCAR CESM2-WACCM-FV2 model output prepared for CMIP6 CMIP 1pctCO2. Version 20200226. Earth System Grid Federation, 2020b. <https://doi.org/10.22033/ESGF/CMIP6.11284>.
- Danek, C., Shi, X., Stepanek, C., Yang, H., Barbi, D., Hegewald, J., and Lohmann, G. AWI AWI-ESM1.1LR model output prepared for CMIP6 CMIP 1pctCO2. Version 20200212. Earth System Grid Federation, 2020. <https://doi.org/10.22033/ESGF/CMIP6.9321>.
- Dawson, A. eofs: A Library for EOF Analysis of Meteorological, Oceanographic, and Climate Data. *Journal of Open Research Software*, 4(1):e14, 2016. <https://doi.org/10.5334/jors.122>.

- Deser, C., Phillips, A., Bourdette, V., and Teng, H. Uncertainty in climate change projections: the role of internal variability. *Climate Dynamics*, 38:527–546, 2012. <https://doi.org/10.1007/s00382-010-0977-x>.
- Deser, C., Tomas, R. A., and Sun, L. The Role of Ocean–Atmosphere Coupling in the Zonal-Mean Atmospheric Response to Arctic Sea Ice Loss. *Journal of Climate*, 28(6):2168–2186, 2015. <https://doi.org/10.1175/JCLI-D-14-00325.1>.
- Dickinson, R. E. On the exact and approximate linear theory of vertically propagating planetary rossby waves forced at a spherical lower boundary. *Monthly Weather Review*, 96(7):405–415, 1968. [https://doi.org/10.1175/1520-0493\(1968\)096<0405:0TEAAL>2.0.CO;2](https://doi.org/10.1175/1520-0493(1968)096<0405:0TEAAL>2.0.CO;2).
- Dobson, G. M. B. and Massey, H. S. W. Origin and distribution of the polyatomic molecules in the atmosphere. *Proceedings of the Royal Society of London. Series A. Mathematical and Physical Sciences*, 236(1205):187–193, 1956. <https://doi.org/10.1098/rspa.1956.0127>.
- Dobson, G. M. B., Harrison, D. N., and Lindemann, F. A. Measurements of the Amount of Ozone in the Earth’s Atmosphere and its Relation to other Geophysical Conditions. *Proceedings of the Royal Society of London. Series A, Containing Papers of a Mathematical and Physical Character*, 110(756):660–693, 1926. <https://doi.org/10.1098/rspa.1926.0040>.
- Domeisen, D. I. V. and Plumb, R. A. Traveling planetary-scale Rossby waves in the winter stratosphere: The role of tropospheric baroclinic instability. *Geophysical Research Letters*, 39(20), 2012. <https://doi.org/10.1029/2012GL053684>.
- Domeisen, D. I. V., Sun, L., and Chen, G. The role of synoptic eddies in the tropospheric response to stratospheric variability. *Geophysical Research Letters*, 40(18):4933–4937, 2013. <https://doi.org/10.1002/grl.50943>.
- Dunn-Sigouin, E. and Shaw, T. A. Comparing and contrasting extreme stratospheric events, including their coupling to the tropospheric circulation. *Journal of Geophysical Research: Atmospheres*, 120(4):1374–1390, 2015. <https://doi.org/10.1002/2014JD022116>.
- Edmon, H. J., Hoskins, B. J., and McIntyre, M. E. Eliassen-Palm Cross Sections for the Troposphere. *Journal of the Atmospheric Sciences*, 37(12):2600–2616, 1980. [https://doi.org/10.1175/1520-0469\(1980\)037<2600:EPSFT>2.0.CO;2](https://doi.org/10.1175/1520-0469(1980)037<2600:EPSFT>2.0.CO;2).
- England, M. R., Shaw, T. A., and Polvani, L. M. Troposphere-stratosphere dynamical coupling in the southern high latitudes and its linkage to the Amundsen Sea. *Journal of Geophysical Research: Atmospheres*, 121(8):3776–3789, 2016. <https://doi.org/10.1002/2015JD024254>.
- Eyring, V., Waugh, D. W., Bodeker, G. E., Cordero, E., Akiyoshi, H., Austin, J., Beagley, S. R., Boville, B. A., Braesicke, P., Brühl, C., Butchart, N., Chipperfield, M. P., Dameris, M., Deckert, R., Deushi, M., Frith, S. M., Garcia, R. R., Gettelman, A., Giorgetta, M. A., Kinnison, D. E., Mancini, E., Manzini, E., Marsh, D. R., Matthes, S., Nagashima, T., Newman, P. A., Nielsen, J. E., Pawson, S., Pitari, G., Plummer, D. A., Rozanov, E., Schraner, M., Scinocca, J. F., Semeniuk, K., Shepherd, T. G., Shibata, K., Steil, B., Stolarski, R. S., Tian, W., and Yoshiki, M. Multimodel projections of stratospheric

- ozone in the 21st century. *Journal of Geophysical Research: Atmospheres*, 112(D16), 2007. <https://doi.org/10.1029/2006JD008332>.
- Eyring, V., Bony, S., Meehl, G. A., Senior, C. A., Stevens, B., Stouffer, R. J., and Taylor, K. E. Overview of the Coupled Model Intercomparison Project Phase 6 (CMIP6) experimental design and organization. *Geoscientific Model Development*, 9(5):1937–1958, 2016. <https://doi.org/10.5194/gmd-9-1937-2016>.
- Farrell, B. F. Optimal Excitation of Baroclinic Waves. *Journal of Atmospheric Sciences*, 46(9):1193–1206, 1989. [https://doi.org/10.1175/1520-0469\(1989\)046<1193:0E0BW>2.0.CO;2](https://doi.org/10.1175/1520-0469(1989)046<1193:0E0BW>2.0.CO;2).
- Frierson, D. M. W., Held, I. M., and Zurita-Gotor, P. A Gray-Radiation Aquaplanet Moist GCM. Part I: Static Stability and Eddy Scale. *Journal of the Atmospheric Sciences*, 63(10):2548–2566, 2006. <https://doi.org/10.1175/JAS3753.1>.
- Frierson, D. M. W., Held, I. M., and Zurita-Gotor, P. A Gray-Radiation Aquaplanet Moist GCM. Part II: Energy Transports in Altered Climates. *Journal of the Atmospheric Sciences*, 64(5):1680–1693, 2007a. <https://doi.org/10.1175/JAS3913.1>.
- Frierson, D. M. W., Lu, J., and Chen, G. Width of the Hadley cell in simple and comprehensive general circulation models. *Geophysical Research Letters*, 34(18), 2007b. <https://doi.org/10.1029/2007GL031115>.
- Fritts, D. C. and Alexander, M. J. Gravity wave dynamics and effects in the middle atmosphere. *Reviews of Geophysics*, 41(1), 2003. <https://doi.org/10.1029/2001RG000106>.
- Fu, Q., Johanson, C. M., Wallace, J. M., and Reichler, T. Enhanced Mid-Latitude Tropospheric Warming in Satellite Measurements. *Science*, 312(5777):1179–1179, 2006. <https://doi.org/10.1126/science.1125566>.
- Garny, H., Walz, R., Nützel, M., and Birner, T. Extending the Modular Earth Submodel System (MESSy v2.54) model hierarchy: the ECHAM/MESSy IdeaLized (EMIL) model setup. *Geoscientific Model Development*, 13(11):5229–5257, 2020. <https://doi.org/10.5194/gmd-13-5229-2020>.
- Gerber, E. P. and Manzini, E. The Dynamics and Variability Model Intercomparison Project (DynVarMIP) for CMIP6: assessing the stratosphere–troposphere system. *Geoscientific Model Development*, 9(9):3413–3425, 2016. <https://doi.org/10.5194/gmd-9-3413-2016>.
- Gerber, E. P. Stratospheric versus Tropospheric Control of the Strength and Structure of the Brewer–Dobson Circulation. *Journal of the Atmospheric Sciences*, 69(9):2857–2877, 2012. <https://doi.org/10.1175/JAS-D-11-0341.1>.
- Gerber, E. P. and Polvani, L. M. Stratosphere–Troposphere Coupling in a Relatively Simple AGCM: The Importance of Stratospheric Variability. *Journal of Climate*, 22(8):1920–1933, 2009. <https://doi.org/10.1175/2008JCLI2548.1>.
- Gerber, E. P., Voronin, S., and Polvani, L. M. Testing the Annular Mode Autocorrelation Time Scale in Simple Atmospheric General Circulation Models. *Monthly Weather Review*, 136(4):1523–1536, 04 2008. <https://doi.org/10.1175/2007MWR2211.1>.

- Gerber, E. P., Butler, A., Calvo, N., Charlton-Perez, A., Giorgetta, M., Manzini, E., Perlwitz, J., Polvani, L. M., Sassi, F., Scaife, A. A., Shaw, T. A., Son, S.-W., and Watanabe, S. Assessing and Understanding the Impact of Stratospheric Dynamics and Variability on the Earth System. *Bulletin of the American Meteorological Society*, 93(6):845–859, 2012. <https://doi.org/10.1175/BAMS-D-11-00145.1>.
- Hajima, T., Abe, M., Arakawa, O., Suzuki, T., Komuro, Y., Ogura, T., Ogochi, K., Watanabe, M., Yamamoto, A., Tatebe, H., Noguchi, M. A., Ohgaito, R., Ito, A., Yamazaki, D., Ito, A., Takata, K., Watanabe, S., Kawamiya, M., and Tachiiri, K. MIROC MIROC-ES2L model output prepared for CMIP6 CMIP 1pctCO2. Version 20190823. Earth System Grid Federation, 2019. <https://doi.org/10.22033/ESGF/CMIP6.5370>.
- Hardiman, S. C., Butchart, N., and Calvo, N. The morphology of the Brewer–Dobson circulation and its response to climate change in CMIP5 simulations. *Quarterly Journal of the Royal Meteorological Society*, 140(683):1958–1965, 2014. <https://doi.org/10.1002/qj.2258>.
- Harnik, N. Observed stratospheric downward reflection and its relation to upward pulses of wave activity. *Journal of Geophysical Research: Atmospheres*, 114(D8), 2009. <https://doi.org/10.1029/2008JD010493>.
- Harnik, N. and Lindzen, R. S. The Effect of Reflecting Surfaces on the Vertical Structure and Variability of Stratospheric Planetary Waves. *Journal of the Atmospheric Sciences*, 58(19):2872–2894, 2001. [https://doi.org/10.1175/1520-0469\(2001\)058<2872:TEORSO>2.0.CO;2](https://doi.org/10.1175/1520-0469(2001)058<2872:TEORSO>2.0.CO;2).
- Harnik, N., Perlwitz, J., and Shaw, T. A. Observed Decadal Changes in Downward Wave Coupling between the Stratosphere and Troposphere in the Southern Hemisphere. *Journal of Climate*, 24(17):4558–4569, 2011. <https://doi.org/10.1175/2011JCLI4118.1>.
- Harvey, B. J., Shaffrey, L. C., and Woollings, T. J. Equator-to-pole temperature differences and the extra-tropical storm track responses of the CMIP5 climate models. *Climate Dynamics*, 43(5):1171–1182, 2014. <https://doi.org/10.1007/s00382-013-1883-9>.
- Hawkins, E. and Sutton, R. The Potential to Narrow Uncertainty in Regional Climate Predictions. *Bulletin of the American Meteorological Society*, 90(8):1095–1108, 2009. <https://doi.org/10.1175/2009BAMS2607.1>.
- Haynes, P. H., McIntyre, M. E., Shepherd, T. G., Marks, C. J., and Shine, K. P. On the “Downward Control” of Extratropical Diabatic Circulations by Eddy-Induced Mean Zonal Forces. *Journal of the Atmospheric Sciences*, 48(4):651–678, 1991. [https://doi.org/10.1175/1520-0469\(1991\)048<0651:OTCOED>2.0.CO;2](https://doi.org/10.1175/1520-0469(1991)048<0651:OTCOED>2.0.CO;2).
- Held, I. M. The Gap between Simulation and Understanding in Climate Modeling. *Bulletin of the American Meteorological Society*, 86(11):1609–1614, 2005. <https://doi.org/10.1175/BAMS-86-11-1609>.
- Held, I. M. Large-Scale Dynamics and Global Warming. *Bulletin of the American Meteorological Society*, 74(2):228–242, 1993. [https://doi.org/10.1175/1520-0477\(1993\)074<0228:LSDAGW>2.0.CO;2](https://doi.org/10.1175/1520-0477(1993)074<0228:LSDAGW>2.0.CO;2).

- Held, I. M. and Hou, A. Y. Nonlinear Axially Symmetric Circulations in a Nearly Inviscid Atmosphere. *Journal of Atmospheric Sciences*, 37(3):515–533, 1980. [https://doi.org/10.1175/1520-0469\(1980\)037<0515:NASCIA>2.0.CO;2](https://doi.org/10.1175/1520-0469(1980)037<0515:NASCIA>2.0.CO;2).
- Held, I. M. and Suarez, M. J. A Proposal for the Intercomparison of the Dynamical Cores of Atmospheric General Circulation Models. *Bulletin of the American Meteorological Society*, 75(10):1825–1830, 1994. [https://doi.org/10.1175/1520-0477\(1994\)075<1825:APFTIO>2.0.CO;2](https://doi.org/10.1175/1520-0477(1994)075<1825:APFTIO>2.0.CO;2).
- Hersbach, H., Bell, B., Berrisford, P., Hirahara, S., Horányi, A., Muñoz-Sabater, J., Nicolas, J., Peubey, C., Radu, R., Schepers, D., Simmons, A., Soci, C., Abdalla, S., Abellan, X., Balsamo, G., Bechtold, P., Biavati, G., Bidlot, J., Bonavita, M., De Chiara, G., Dahlgren, P., Dee, D., Diamantakis, M., Dragani, R., Flemming, J., Forbes, R., Fuentes, M., Geer, A., Haimberger, L., Healy, S., Hogan, R. J., Hólm, E., Janisková, M., Keeley, S., Laloyaux, P., Lopez, P., Lupu, C., Radnoti, G., de Rosnay, P., Rozum, I., Vamborg, F., Villaume, S., and Thépaut, J.-N. The ERA5 global reanalysis. *Quarterly Journal of the Royal Meteorological Society*, 146(730):1999–2049, 2020. <https://doi.org/10.1002/qj.3803>.
- Hitchcock, P. and Simpson, I. R. The Downward Influence of Stratospheric Sudden Warmings. *Journal of the Atmospheric Sciences*, 71(10):3856–3876, 2014. <https://doi.org/10.1175/JAS-D-14-0012.1>.
- Holland, M. M. and Bitz, C. M. Polar amplification of climate change in coupled models. *Climate Dynamics*, 21:221–232, 2003. <https://doi.org/10.1007/s00382-003-0332-6>.
- Holton, J. R. *An Introduction to Dynamic Meteorology*. Academic Press, San Diego, 4th edition, 2004.
- Holton, J. R. and Mass, C. Stratospheric Vacillation Cycles. *Journal of Atmospheric Sciences*, 33(11):2218–2225, 1976. [https://doi.org/10.1175/1520-0469\(1976\)033<2218:SVC>2.0.CO;2](https://doi.org/10.1175/1520-0469(1976)033<2218:SVC>2.0.CO;2).
- Holton, J. R., Haynes, P. H., McIntyre, M. E., Douglass, A. R., Rood, R. B., and Pfister, L. Stratosphere-troposphere exchange. *Reviews of Geophysics*, 33(4):403–439, 1995. <https://doi.org/10.1029/95RG02097>.
- Hurrell, J. W. Decadal Trends in the North Atlantic Oscillation: Regional Temperatures and Precipitation. *Science*, 269(5224):676–679, 1995. <https://doi.org/10.1126/science.269.5224.676>.
- Hurrell, J. W., Holland, M. M., Gent, P. R., Ghan, S., Kay, J. E., Kushner, P. J., Lamarque, J.-F., Large, W. G., Lawrence, D., Lindsay, K., Lipscomb, W. H., Long, M. C., Mahowald, N., Marsh, D. R., Neale, R. B., Rasch, P., Vavrus, S., Vertenstein, M., Bader, D., Collins, W. D., Hack, J. J., Kiehl, J., and Marshall, S. The Community Earth System Model: A Framework for Collaborative Research. *Bulletin of the American Meteorological Society*, 94(9):1339–1360, 2013. <https://doi.org/10.1175/BAMS-D-12-00121.1>.
- IPCC. *Climate Change 2013 – The Physical Science Basis: Working Group I Contribution to the Fifth Assessment Report of the Intergovernmental Panel on Climate Change*. [Stocker, T. F., Qin, D., Plattner, G.-K., Tignor, M., Allen, S. K., Boschung, J., Nauels, A., Xia,

- Y., Bex, V., and Midgley, P. M. (eds.)). Cambridge University Press, Cambridge, United Kingdom and New York, NY, USA, 2014. <https://doi.org/10.1017/CB09781107415324>.
- IPCC. *Climate Change 2021: The Physical Science Basis. Contribution of Working Group I to the Sixth Assessment Report of the Intergovernmental Panel on Climate Change*. [Masson-Delmotte, V., Zhai, P., Pirani, A., Connors, S. L., Péan, C., Berger, S., Caud, N., Chen, Y., Goldfarb, L., Gomis, M. I., Huang, M., Leitzell, K., Lonnoy, E., Matthews, J. B. R., Maycock, T. K., Waterfield, T., Yelekçi, O., Yu, R., and Zhou, B. (eds.)]. Cambridge University Press, Cambridge, United Kingdom and New York, NY, USA, 2022. <https://doi.org/10.1017/9781009157896>.
- Jöckel, P., Sander, R., Kerkweg, A., Tost, H., and Lelieveld, J. Technical Note: The Modular Earth Submodel System (MESSy) - a new approach towards Earth System Modeling. *Atmospheric Chemistry and Physics*, 5(2):433–444, 2005. <https://doi.org/10.5194/acp-5-433-2005>.
- Jöckel, P., Tost, H., Pozzer, A., Brühl, C., Buchholz, J., Ganzeveld, L., Hoor, P., Kerkweg, A., Lawrence, M. G., Sander, R., Steil, B., Stiller, G., Tanarhte, M., Taraborrelli, D., van Aardenne, J., and Lelieveld, J. The atmospheric chemistry general circulation model ECHAM5/MESSy1: consistent simulation of ozone from the surface to the mesosphere. *Atmospheric Chemistry and Physics*, 6(12):5067–5104, 2006. <https://doi.org/10.5194/acp-6-5067-2006>.
- Jöckel, P., Kerkweg, A., Pozzer, A., Sander, R., Tost, H., Riede, H., Baumgaertner, A., Gromov, S., and Kern, B. Development cycle 2 of the Modular Earth Submodel System (MESSy2). *Geoscientific Model Development*, 3(2):717–752, 2010. <https://doi.org/10.5194/gmd-3-717-2010>.
- Jöckel, P., Tost, H., Pozzer, A., Kunze, M., Kirner, O., Brenninkmeijer, C. A. M., Brinkop, S., Cai, D. S., Dyroff, C., Eckstein, J., Frank, F., Garny, H., Gottschaldt, K.-D., Graf, P., Grewe, V., Kerkweg, A., Kern, B., Matthes, S., Mertens, M., Meul, S., Neumaier, M., Nützel, M., Oberländer-Hayn, S., Ruhnke, R., Runde, T., Sander, R., Scharffe, D., and Zahn, A. Earth system chemistry integrated modelling (escimo) with the modular earth submodel system (messy) version 2.51. *Geoscientific Model Development*, 9(3):1153–1200, 2016. <https://doi.org/10.5194/gmd-9-1153-2016>.
- Jucker, M. and Gerber, E. P. Untangling the Annual Cycle of the Tropical Tropopause Layer with an Idealized Moist Model. *Journal of Climate*, 30(18):7339–7358, 2017. <https://doi.org/10.1175/JCLI-D-17-0127.1>.
- Jucker, M., Fueglistaler, S., and Vallis, G. K. Maintenance of the Stratospheric Structure in an Idealized General Circulation Model. *Journal of the Atmospheric Sciences*, 70(11):3341–3358, 2013. <https://doi.org/10.1175/JAS-D-12-0305.1>.
- Jucker, M., Reichler, T., and Waugh, D. W. How Frequent Are Antarctic Sudden Stratospheric Warmings in Present and Future Climate? *Geophysical Research Letters*, 48(11):e2021GL093215, 2021. <https://doi.org/10.1029/2021GL093215>.
- Jungclaus, J., Bittner, M., Wieners, K.-H., Wachsmann, F., Schupfner, M., Legutke, S., Giorgetta, M., Reick, C., Gayler, V., Haak, H., de Vrese, P., Raddatz, T., Esch, M.,

- Mauritsen, T., von Storch, J.-S., Behrens, J., Brovkin, V., Claussen, M., Crueger, T., Fast, I., Fiedler, S., Hagemann, S., Hohenegger, C., Jahns, T., Kloster, S., Kinne, S., Lasslop, G., Kornbluh, L., Marotzke, J., Matei, D., Meraner, K., Mikolajewicz, U., Modali, K., Müller, W., Nabel, J., Notz, D., Peters-von Gehlen, K., Pincus, R., Pohlmann, H., Pongratz, J., Rast, S., Schmidt, H., Schnur, R., Schulzweida, U., Six, K., Stevens, B., Voigt, A., and Roeckner, E. MPI-M MPI-ESM1.2-HR model output prepared for CMIP6 CMIP 1petCO2. Version 20190710. Earth System Grid Federation, 2019. <https://doi.org/10.22033/ESGF/CMIP6.6434>.
- Karoly, D. J. and Hoskins, B. J. Three-dimensional propagation of planetary waves. *Journal of the Meteorological Society of Japan. Ser. II*, 60(1):109–123, 1982. https://doi.org/10.2151/jmsj1965.60.1_109.
- Karpechko, A. Y. and Manzini, E. Arctic Stratosphere Dynamical Response to Global Warming. *Journal of Climate*, 30(17):7071–7086, 2017. <https://doi.org/10.1175/JCLI-D-16-0781.1>.
- Karpechko, A. Y., Hitchcock, P., Peters, D. H. W., and Schneidereit, A. Predictability of downward propagation of major sudden stratospheric warmings. *Quarterly Journal of the Royal Meteorological Society*, 143(704):1459–1470, 2017. <https://doi.org/10.1002/qj.3017>.
- Kidston, J. and Gerber, E. P. Intermodel variability of the poleward shift of the austral jet stream in the CMIP3 integrations linked to biases in 20th century climatology. *Geophysical Research Letters*, 37(9), 2010. <https://doi.org/10.1029/2010GL042873>.
- Kidston, J., Scaife, A. A., Hardiman, S. C., Mitchell, D. M., Butchart, N., Baldwin, M. P., and Gray, L. J. Stratospheric influence on tropospheric jet streams, storm tracks and surface weather. *Nature Geoscience*, 8:433–440, 05 2015. <https://doi.org/10.1038/ngeo2424>.
- Kim, B.-M., Son, S.-W., Min, S.-K., Jeong, J.-H., Kim, S.-J., Zhang, X., Shim, T., and Yoon, J.-H. Weakening of the stratospheric polar vortex by Arctic sea-ice loss. *Nature Communications*, 5:4646, 2014. <https://doi.org/10.1038/ncomms5646>.
- Kim, H.-K. and Lee, S. The Wave–Zonal Mean Flow Interaction in the Southern Hemisphere. *Journal of the Atmospheric Sciences*, 61(9):1055–1067, 2004. [https://doi.org/10.1175/1520-0469\(2004\)061<1055:TWMFII>2.0.CO;2](https://doi.org/10.1175/1520-0469(2004)061<1055:TWMFII>2.0.CO;2).
- Kim, J. and Kim, K.-Y. Characteristics of stratospheric polar vortex fluctuations associated with sea ice variability in the Arctic winter. *Climate Dynamics*, 54:3599–3611, 2020. <https://doi.org/10.1007/s00382-020-05191-9>.
- Kolstad, E. W., Breiteig, T., and Scaife, A. A. The association between stratospheric weak polar vortex events and cold air outbreaks in the Northern Hemisphere. *Quarterly Journal of the Royal Meteorological Society*, 136(649):886–893, 2010. <https://doi.org/10.1002/qj.620>.
- Krasting, J. P., John, J. G., Blanton, C., McHugh, C., Nikonov, S., Radhakrishnan, A., Rand, K., Zadeh, N. T., Balaji, V., Durachta, J., Dupuis, C., Menzel, R., Robinson, T., Underwood, S., Vahlenkamp, H., Dunne, K. A., Gauthier, P. P., Ginoux, P., Griffies, S. M.,

- Hallberg, R., Harrison, M., Hopturlin, W., Malyshev, S., Naik, V., Paulot, F., Paynter, D. J., Ploshay, J., Reichl, B. G., Schwarzkopf, D. M., Seman, C. J., Silvers, L., Wyman, B., Zeng, Y., Adcroft, A., Dunne, J. P., Dussin, R., Guo, H., He, J., Held, I. M., Horowitz, L. W., Lin, P., Milly, P., Shevliakova, E., Stock, C., Winton, M., Wittenberg, A. T., Xie, Y., and Zhao, M. NOAA-GFDL GFDL-ESM4 model output prepared for CMIP6 CMIP 1pctCO2. Version 20180701. Earth System Grid Federation, 2018. <https://doi.org/10.22033/ESGF/CMIP6.8473>.
- Kretschmer, M., Zappa, G., and Shepherd, T. G. The role of Barents–Kara sea ice loss in projected polar vortex changes. *Weather and Climate Dynamics*, 1(2):715–730, 2020. <https://doi.org/10.5194/wcd-1-715-2020>.
- Krüger, K., Naujokat, B., and Labitzke, K. The Unusual Midwinter Warming in the Southern Hemisphere Stratosphere 2002: A Comparison to Northern Hemisphere Phenomena. *Journal of the Atmospheric Sciences*, 62(3):603–613, 2005. <https://doi.org/10.1175/JAS-3316.1>.
- Kushner, P. J. and Polvani, L. M. Stratosphere–Troposphere Coupling in a Relatively Simple AGCM: The Role of Eddies. *Journal of Climate*, 17(3):629–639, 2004. [https://doi.org/10.1175/1520-0442\(2004\)017<0629:SCIARS>2.0.CO;2](https://doi.org/10.1175/1520-0442(2004)017<0629:SCIARS>2.0.CO;2).
- Kushner, P. J. and Polvani, L. M. Stratosphere–Troposphere Coupling in a Relatively Simple AGCM: Impact of the Seasonal Cycle. *Journal of Climate*, 19(21):5721–5727, 2006. <https://doi.org/10.1175/JCLI4007.1>.
- Larsen, M. F., Swartz, W. E., and Woodman, R. F. Gravity-wave generation by thunderstorms observed with a vertically-pointing 430 MHz radar. *Geophysical Research Letters*, 9(5):571–574, 1982. <https://doi.org/10.1029/GL009i005p00571>.
- Lim, E.-P., Hendon, H. H., Boschath, G., Hudson, D., Thompson, D. W. J., Dowdy, A. J., and Arblaster, J. M. Australian hot and dry extremes induced by weakenings of the stratospheric polar vortex. *Nature Geoscience*, 12:896–901, 2019. <https://doi.org/10.1038/s41561-019-0456-x>.
- Limpasuvan, V., Thompson, D. W. J., and Hartmann, D. L. The Life Cycle of the Northern Hemisphere Sudden Stratospheric Warmings. *Journal of Climate*, 17(13):2584–2596, 2004. [https://doi.org/10.1175/1520-0442\(2004\)017<2584:TLCOTN>2.0.CO;2](https://doi.org/10.1175/1520-0442(2004)017<2584:TLCOTN>2.0.CO;2).
- Limpasuvan, V., Hartmann, D. L., Thompson, D. W. J., Jeev, K., and Yung, Y. L. Stratosphere-troposphere evolution during polar vortex intensification. *Journal of Geophysical Research: Atmospheres*, 110(D24), 2005. <https://doi.org/10.1029/2005JD006302>.
- Lindgren, E. A., Sheshadri, A., and Plumb, R. A. Sudden Stratospheric Warming Formation in an Idealized General Circulation Model Using Three Types of Tropospheric Forcing. *Journal of Geophysical Research: Atmospheres*, 123(18):10,125–10,139, 2018. <https://doi.org/10.1029/2018JD028537>.
- Lorenz, D. J. and DeWeaver, E. T. Tropopause height and zonal wind response to global warming in the IPCC scenario integrations. *Journal of Geophysical Research: Atmospheres*, 112(D10), 2007. <https://doi.org/10.1029/2006JD008087>.

- Lu, J., Vecchi, G. A., and Reichler, T. Expansion of the Hadley cell under global warming. *Geophysical Research Letters*, 34(6), 2007. <https://doi.org/10.1029/2006GL028443>.
- Lu, J., Chen, G., and Frierson, D. M. W. The Position of the Midlatitude Storm Track and Eddy-Driven Westerlies in Aquaplanet AGCMs. *Journal of the Atmospheric Sciences*, 67(12):3984–4000, 2010. <https://doi.org/10.1175/2010JAS3477.1>.
- Maher, P., Gerber, E. P., Medeiros, B., Merlis, T. M., Sherwood, S., Sheshadri, A., Sobel, A. H., Vallis, G. K., Voigt, A., and Zurita-Gotor, P. Model Hierarchies for Understanding Atmospheric Circulation. *Reviews of Geophysics*, 57(2):250–280, 2019. <https://doi.org/10.1029/2018RG000607>.
- Manzini, E., Karpechko, A. Y., Anstey, J., Baldwin, M. P., Black, R. X., Cagnazzo, C., Calvo, N., Charlton-Perez, A., Christiansen, B., Davini, P., Gerber, E., Giorgetta, M., Gray, L., Hardiman, S. C., Lee, Y.-Y., Marsh, D. R., McDaniel, B. A., Purich, A., Scaife, A. A., Shindell, D., Son, S.-W., Watanabe, S., and Zappa, G. Northern winter climate change: Assessment of uncertainty in CMIP5 projections related to stratosphere-troposphere coupling. *Journal of Geophysical Research: Atmospheres*, 119(13):7979–7998, 2014. <https://doi.org/10.1002/2013JD021403>.
- Manzini, E., Karpechko, A. Y., and Kornbluh, L. Nonlinear response of the stratosphere and the north atlantic-european climate to global warming. *Geophysical Research Letters*, 45(9):4255–4263, 2018. <https://doi.org/10.1029/2018GL077826>.
- Martineau, P., Chen, G., Son, S.-W., and Kim, J. Lower-Stratospheric Control of the Frequency of Sudden Stratospheric Warming Events. *Journal of Geophysical Research: Atmospheres*, 123(6):3051–3070, 2018. <https://doi.org/10.1002/2017JD027648>.
- Matsuno, T. Vertical Propagation of Stationary Planetary Waves in the Winter Northern Hemisphere. *Journal of the Atmospheric Sciences*, 27(6):871–883, 1970. [https://doi.org/10.1175/1520-0469\(1970\)027<0871:VPOSPW>2.0.CO;2](https://doi.org/10.1175/1520-0469(1970)027<0871:VPOSPW>2.0.CO;2).
- McGraw, M. C. and Barnes, E. A. Seasonal Sensitivity of the Eddy-Driven Jet to Tropospheric Heating in an Idealized AGCM. *Journal of Climate*, 29(14):5223–5240, 2016. <https://doi.org/10.1175/JCLI-D-15-0723.1>.
- McLandress, C. and Shepherd, T. G. Simulated Anthropogenic Changes in the Brewer–Dobson Circulation, Including Its Extension to High Latitudes. *Journal of Climate*, 22(6):1516–1540, 2009. <https://doi.org/10.1175/2008JCLI2679.1>.
- Meehl, G. A., Boer, G. J., Covey, C., Latif, M., and Stouffer, R. J. The Coupled Model Intercomparison Project (CMIP). *Bulletin of the American Meteorological Society*, 81(2):313–318, 2000. <http://www.jstor.org/stable/26215108>.
- Menzel, M. E., Waugh, D., and Grise, K. Disconnect Between Hadley Cell and Subtropical Jet Variability and Response to Increased CO₂. *Geophysical Research Letters*, 46(12):7045–7053, 2019. <https://doi.org/10.1029/2019GL083345>.
- Nakicenovic, N., Alcamo, J., Davis, G., Vries, B. d., Fenhann, J., Gaffin, S., Gregory, K., Grubler, A., Jung, T. Y., Kram, T., Rovere, E. L., Michaelis, L., Mori, S., Morita, T., Pepper, W., Pitcher, H., Price, L., Riahi, K., Roehrl, A., Rogner, H.-H., Sankovski, A.,

- Schlesinger, M., Shukla, P., Smith, S., Swart, R., Rooijen, S. v., Victor, N., and Zhou, D. Special report on emissions scenarios. *Lawrence Berkeley National Laboratory*, LBNL Report Number: LBNL-59940, 2000. Retrieved from <https://escholarship.org/uc/item/9sz5p22f>. Accessed: 2021-11-21.
- Neubauer, D., Ferrachat, S., Siegenthaler-Le Drian, C., Stoll, J., Folini, D. S., Tegen, I., Wieners, K.-H., Mauritsen, T., Stemmler, I., Barthel, S., Bey, I., Daskalakis, N., Heinold, B., Kokkola, H., Partridge, D., Rast, S., Schmidt, H., Schutgens, N., Stanelle, T., Stier, P., Watson-Parris, D., and Lohmann, U. HAMMOZ-Consortium MPI-ESM1.2-HAM model output prepared for CMIP6 CMIP 1pctCO2. Version 20190628. Earth System Grid Federation, 2019. <https://doi.org/10.22033/ESGF/CMIP6.4999>.
- Newman, P., Nash, E., and Pawson, S. Annual Meteorological Statistics from the Modern-Era Retrospective analysis for Research and Applications, Version 2 (MERRA-2) provided by the Atmospheric Chemistry and Dynamics Laboratory of the NASA Goddard Space Flight Center, 2021. Retrieved from https://acd-ext.gsfc.nasa.gov/Data_services/met/ann_data.html. Accessed: 2021-09-13.
- Oberländer-Hayn, S., Gerber, E. P., Abalichin, J., Akiyoshi, H., Kerschbaumer, A., Kubin, A., Kunze, M., Langematz, U., Meul, S., Michou, M., Morgenstern, O., and Oman, L. D. Is the Brewer-Dobson circulation increasing or moving upward? *Geophysical Research Letters*, 43(4):1772–1779, 2016. <https://doi.org/10.1002/2015GL067545>.
- Oudar, T., Sanchez-Gomez, E., Chauvin, F., Cattiaux, J., Terray, L., and Cassou, C. Respective roles of direct GHG radiative forcing and induced Arctic sea ice loss on the Northern Hemisphere atmospheric circulation. *Climate Dynamics*, 49:3693–3713, 2017. <https://doi.org/10.1007/s00382-017-3541-0>.
- Oudar, T., Cattiaux, J., and Douville, H. Drivers of the Northern Extratropical Eddy-Driven Jet Change in CMIP5 and CMIP6 Models. *Geophysical Research Letters*, 47(8):e2019GL086695, 2020a. <https://doi.org/10.1029/2019GL086695>.
- Oudar, T., Cattiaux, J., Douville, H., Geoffroy, O., Saint-Martin, D., and Roehrig, R. Robustness and drivers of the Northern Hemisphere extratropical atmospheric circulation response to a CO₂-induced warming in CNRM-CM6-1. *Climate Dynamics*, 54:2267–2285, 2020b. <https://doi.org/10.1007/s00382-019-05113-4>.
- Parkinson, C. L. and Cavalieri, D. J. Antarctic sea ice variability and trends, 1979–2010. *The Cryosphere*, 6(4):871–880, 2012. <https://doi.org/10.5194/tc-6-871-2012>.
- Peings, Y., Cattiaux, J., and Magnusdottir, G. The Polar Stratosphere as an Arbiter of the Projected Tropical Versus Polar Tug of War. *Geophysical Research Letters*, 46(15):9261–9270, 2019. <https://doi.org/10.1029/2019GL082463>.
- Perlwitz, J. and Graf, H.-F. Troposphere-stratosphere dynamic coupling under strong and weak polar vortex conditions. *Geophysical Research Letters*, 28(2):271–274, 2001. <https://doi.org/10.1029/2000GL012405>.
- Perlwitz, J. and Harnik, N. Observational Evidence of a Stratospheric Influence on the Troposphere by Planetary Wave Reflection. *Journal of Climate*, 16(18):3011–3026, 2003. [https://doi.org/10.1175/1520-0442\(2003\)016<3011:OE0ASI>2.0.CO;2](https://doi.org/10.1175/1520-0442(2003)016<3011:OE0ASI>2.0.CO;2).

- Perlwitz, J. and Harnik, N. Downward Coupling between the Stratosphere and Troposphere: The Relative Roles of Wave and Zonal Mean Processes. *Journal of Climate*, 17(24):4902–4909, 2004. <https://doi.org/10.1175/JCLI-3247.1>.
- Plumb, R. A. On the Three-Dimensional Propagation of Stationary Waves. *Journal of Atmospheric Sciences*, 42(3):217–229, 1985. [https://doi.org/10.1175/1520-0469\(1985\)042<0217:OTDPO>2.0.CO;2](https://doi.org/10.1175/1520-0469(1985)042<0217:OTDPO>2.0.CO;2).
- Plumb, R. A. Stratospheric transport. *J. Meteorol. Soc. Jpn.*, 80(4B):793–809, 2002. <https://doi.org/10.2151/jmsj.80.793>.
- Polvani, L. M. and Kushner, P. J. Tropospheric response to stratospheric perturbations in a relatively simple general circulation model. *Geophysical Research Letters*, 29(7):18–1–18–4, 2002. <https://doi.org/10.1029/2001GL014284>.
- Randel, W., Udelhofen, P., Fleming, E., Geller, M., Gelman, M., Hamilton, K., Karoly, D., Ortland, D., Pawson, S., Swinbank, R., Wu, F., Baldwin, M., Chanin, M.-L., Keckhut, P., Labitzke, K., Remsberg, E., Simmons, A., and Wu, D. The SPARC Intercomparison of Middle-Atmosphere Climatologies. *Journal of Climate*, 17(5):986–1003, 2004. [https://doi.org/10.1175/1520-0442\(2004\)017<0986:TSIOMC>2.0.CO;2](https://doi.org/10.1175/1520-0442(2004)017<0986:TSIOMC>2.0.CO;2).
- Randel, W. J. and Held, I. M. Phase Speed Spectra of Transient Eddy Fluxes and Critical Layer Absorption. *Journal of Atmospheric Sciences*, 48(5):688–697, 1991. [https://doi.org/10.1175/1520-0469\(1991\)048<0688:PSSOTE>2.0.CO;2](https://doi.org/10.1175/1520-0469(1991)048<0688:PSSOTE>2.0.CO;2).
- Rao, J., Garfinkel, C. I., White, I. P., and Schwartz, C. The Southern Hemisphere Minor Sudden Stratospheric Warming in September 2019 and its Predictions in S2S Models. *Journal of Geophysical Research: Atmospheres*, 125(14):e2020JD032723, 2020. <https://doi.org/10.1029/2020JD032723>.
- Ray, E. A., Moore, F. L., Rosenlof, K. H., Davis, S. M., Sweeney, C., Tans, P., Wang, T., Elkins, J. W., Bönisch, H., Engel, A., Sugawara, S., Nakazawa, T., and Aoki, S. Improving stratospheric transport trend analysis based on SF6 and CO2 measurements. *Journal of Geophysical Research: Atmospheres*, 119(24):14,110–14,128, 2014. <https://doi.org/10.1002/2014JD021802>.
- Roeckner, E., Brokopf, R., Esch, M., Giorgetta, M., Hagemann, S., Kornbluh, L., Manzini, E., Schlese, U., and Schulzweida, U. Sensitivity of Simulated Climate to Horizontal and Vertical Resolution in the ECHAM5 Atmosphere Model. *Journal of Climate*, 19(16):3771–3791, 2006. <https://doi.org/10.1175/JCLI3824.1>.
- Roeckner, E., Bäuml, G., Bonaventura, L., Brokopf, R., Esch, M., Giorgetta, M., Hagemann, S., Kirchner, I., Kornbluh, L., Manzini, E., Rhodin, A., Schlese, U., Schulzweida, U., and Tompkins, A. The atmospheric general circulation model ECHAM 5. PART I: Model description. *Report / Max-Planck-Institut für Meteorologie*, 349, 2003. https://mpimet.mpg.de/fileadmin/models/echam/mpi_report_349.pdf. Accessed: 2021-10-12.
- Rosenlof, K. H. Seasonal cycle of the residual mean meridional circulation in the stratosphere. *Journal of Geophysical Research: Atmospheres*, 100(D3):5173–5191, 1995. <https://doi.org/10.1029/94JD03122>.

- Salzmann, M. The polar amplification asymmetry: role of Antarctic surface height. *Earth System Dynamics*, 8(2):323–336, 2017. <https://doi.org/10.5194/esd-8-323-2017>.
- Santer, B. D., Painter, J. F., Bonfils, C., Mears, C. A., Solomon, S., Wigley, T. M. L., Gleckler, P. J., Schmidt, G. A., Doutriaux, C., Gillett, N. P., Taylor, K. E., Thorne, P. W., and Wentz, F. J. Human and natural influences on the changing thermal structure of the atmosphere. *Proceedings of the National Academy of Sciences*, 110(43):17235–17240, 2013. <https://doi.org/10.1073/pnas.1305332110>.
- Scaife, A. A., Butchart, N., Warner, C. D., and Swinbank, R. Impact of a Spectral Gravity Wave Parameterization on the Stratosphere in the Met Office Unified Model. *Journal of the Atmospheric Sciences*, 59(9):1473–1489, 2002. [https://doi.org/10.1175/1520-0469\(2002\)059<1473:IOASGW>2.0.CO;2](https://doi.org/10.1175/1520-0469(2002)059<1473:IOASGW>2.0.CO;2).
- Scaife, A. A., Spanghel, T., Fereday, D. R., Cubasch, U., Langematz, U., Akiyoshi, H., Bekki, S., Braesicke, P., Butchart, N., Chipperfield, M. P., Gettelman, A., Hardiman, S. C., Michou, M., Rozanov, E., and Shepherd, T. G. Climate change projections and stratosphere–troposphere interaction. *Climate Dynamics*, 38:2089–2097, 2012. <https://doi.org/10.1007/s00382-011-1080-7>.
- Scheffer, M., Bascompte, J., Brock, W. A., Brovkin, V., Carpenter, S. R., Dakos, V., Held, H., van Nes, E. H., Rietkerk, M., and Sugihara, G. Early-warning signals for critical transitions. *Nature*, 461:53–59, 2009. <https://doi.org/10.1038/nature08227>.
- Schneider, E. K. Axially Symmetric Steady-State Models of the Basic State for Instability and Climate Studies. Part II. Nonlinear Calculations. *Journal of Atmospheric Sciences*, 34(2):280–296, 1977. [https://doi.org/10.1175/1520-0469\(1977\)034<0280:ASSSM0>2.0.CO;2](https://doi.org/10.1175/1520-0469(1977)034<0280:ASSSM0>2.0.CO;2).
- Scinocca, J. F. and Haynes, P. H. Dynamical Forcing of Stratospheric Planetary Waves by Tropospheric Baroclinic Eddies. *Journal of the Atmospheric Sciences*, 55(14):2361–2392, 1998. [https://doi.org/10.1175/1520-0469\(1998\)055<2361:DFOSPW>2.0.CO;2](https://doi.org/10.1175/1520-0469(1998)055<2361:DFOSPW>2.0.CO;2).
- Scott, R. K. and Polvani, L. M. Internal Variability of the Winter Stratosphere. Part I: Time-Independent Forcing. *Journal of the Atmospheric Sciences*, 63(11):2758–2776, 2006. <https://doi.org/10.1175/JAS3797.1>.
- Seidel, D. J. and Randel, W. J. Recent widening of the tropical belt: Evidence from tropopause observations. *Journal of Geophysical Research: Atmospheres*, 112(D20), 2007. <https://doi.org/10.1029/2007JD008861>.
- Seidel, D. J., Fu, Q., Randel, W. J., and Reichler, T. J. Widening of the tropical belt in a changing climate. *Nature Geoscience*, 1:21–24, 2008. <https://doi.org/10.1038/ngeo.2007.38>.
- Shaw, T. A. Mechanisms of Future Predicted Changes in the Zonal Mean Mid-Latitude Circulation. *Current Climate Change Reports*, 5:345–357, 2019. <https://doi.org/10.1007/s40641-019-00145-8>.
- Shaw, T. A. and Perlwitz, J. The Life Cycle of Northern Hemisphere Downward Wave Coupling between the Stratosphere and Troposphere. *Journal of Climate*, 26(5):1745–1763, 2013. <https://doi.org/10.1175/JCLI-D-12-00251.1>.

- Shaw, T. A. and Perlwitz, J. On the Control of the Residual Circulation and Stratospheric Temperatures in the Arctic by Planetary Wave Coupling. *Journal of the Atmospheric Sciences*, 71(1):195–206, 2014. <https://doi.org/10.1175/JAS-D-13-0138.1>.
- Shaw, T. A., Perlwitz, J., and Harnik, N. Downward Wave Coupling between the Stratosphere and Troposphere: The Importance of Meridional Wave Guiding and Comparison with Zonal-Mean Coupling. *Journal of Climate*, 23(23):6365–6381, 2010. <https://doi.org/10.1175/2010JCLI3804.1>.
- Shaw, T. A., Perlwitz, J., Harnik, N., Newman, P. A., and Pawson, S. The Impact of Stratospheric Ozone Changes on Downward Wave Coupling in the Southern Hemisphere. *Journal of Climate*, 24(16):4210–4229, 2011. <https://doi.org/10.1175/2011JCLI4170.1>.
- Shaw, T. A., Perlwitz, J., and Weiner, O. Troposphere-stratosphere coupling: Links to North Atlantic weather and climate, including their representation in CMIP5 models. *Journal of Geophysical Research: Atmospheres*, 119(10):5864–5880, 2014. <https://doi.org/10.1002/2013JD021191>.
- Shepherd, T. G. Atmospheric circulation as a source of uncertainty in climate change projections. *Nature Geoscience*, 7:703–708, 2014. <https://doi.org/10.1038/ngeo2253>.
- Shepherd, T. G. and McLandress, C. A Robust Mechanism for Strengthening of the Brewer–Dobson Circulation in Response to Climate Change: Critical-Layer Control of Subtropical Wave Breaking. *Journal of the Atmospheric Sciences*, 68(4):784–797, 2011. <https://doi.org/10.1175/2010JAS3608.1>.
- Sheshadri, A., Plumb, R. A., and Gerber, E. P. Seasonal Variability of the Polar Stratospheric Vortex in an Idealized AGCM with Varying Tropospheric Wave Forcing. *Journal of the Atmospheric Sciences*, 72(6):2248–2266, 2015. <https://doi.org/10.1175/JAS-D-14-0191.1>.
- Shindell, D. T., Schmidt, G. A., Miller, R. L., and Rind, D. Northern hemisphere winter climate response to greenhouse gas, ozone, solar, and volcanic forcing. *Journal of Geophysical Research: Atmospheres*, 106(D7):7193–7210, 2001. <https://doi.org/10.1029/2000JD900547>.
- Sigmond, M. and Scinocca, J. F. The Influence of the Basic State on the Northern Hemisphere Circulation Response to Climate Change. *Journal of Climate*, 23(6):1434–1446, 2010. <https://doi.org/10.1175/2009JCLI3167.1>.
- Sigmond, M. and Shepherd, T. G. Compensation between Resolved Wave Driving and Parameterized Orographic Gravity Wave Driving of the Brewer–Dobson Circulation and Its Response to Climate Change. *Journal of Climate*, 27(14):5601–5610, 2014. <https://doi.org/10.1175/JCLI-D-13-00644.1>.
- Simpson, I. R. and Polvani, L. M. Revisiting the relationship between jet position, forced response, and annular mode variability in the southern midlatitudes. *Geophysical Research Letters*, 43(6):2896–2903, 2016. <https://doi.org/10.1002/2016GL067989>.
- Simpson, I. R., Blackburn, M., and Haigh, J. D. The Role of Eddies in Driving the Tropospheric Response to Stratospheric Heating Perturbations. *Journal of the Atmospheric Sciences*, 66(5):1347–1365, 2009. <https://doi.org/10.1175/2008JAS2758.1>.

- Simpson, I. R., Hitchcock, P., Seager, R., Wu, Y., and Callaghan, P. The Downward Influence of Uncertainty in the Northern Hemisphere Stratospheric Polar Vortex Response to Climate Change. *Journal of Climate*, 31(16):6371–6391, 2018. <https://doi.org/10.1175/JCLI-D-18-0041.1>.
- Smith, S., Baumgardner, J., and Mendillo, M. Evidence of mesospheric gravity-waves generated by orographic forcing in the troposphere. *Geophysical Research Letters*, 36(8), 2009. <https://doi.org/10.1029/2008GL036936>.
- SPARC. SPARC Intercomparison of Middle Atmosphere Climatologies. *SPARC Report No. 3*, 2002. Edited by Randel, W., Chanin, M.-L., and Michaut, C. Retrieved from <https://www.sparc-climate.org/publications/sparc-reports/sparc-report-no-3/>. Accessed: 2021-09-20.
- Staten, P. W., Grise, K. M., Davis, S. M., Karnauskas, K. B., Waugh, D. W., Maycock, A. C., Fu, Q., Cook, K., Adam, O., Simpson, I. R., Allen, R. J., Rosenlof, K., Chen, G., Ummenhofer, C. C., Quan, X.-W., Kossin, J. P., Davis, N. A., and Son, S.-W. Tropical Widening: From Global Variations to Regional Impacts. *Bulletin of the American Meteorological Society*, 101(6):E897–E904, 2020. <https://doi.org/10.1175/BAMS-D-19-0047.1>.
- Swart, N. C., Cole, J. N. S., Kharin, V. V., Lazare, M., Scinocca, J. F., Gillett, N. P., Anstey, J., Arora, V., Christian, J. R., Hanna, S., Jiao, Y., Lee, W. G., Majaess, F., Saenko, O. A., Seiler, C., Seinen, C., Shao, A., Sigmond, M., Solheim, L., von Salzen, K., Yang, D., and Winter, B. The Canadian Earth System Model version 5 (CanESM5.0.3). *Geoscientific Model Development*, 12(11):4823–4873, 2019a. <https://doi.org/10.5194/gmd-12-4823-2019>.
- Swart, N. C., Cole, J. N., Kharin, V. V., Lazare, M., Scinocca, J. F., Gillett, N. P., Anstey, J., Arora, V., Christian, J. R., Jiao, Y., Lee, W. G., Majaess, F., Saenko, O. A., Seiler, C., Seinen, C., Shao, A., Solheim, L., von Salzen, K., Yang, D., Winter, B., and Sigmond, M. CCCma CanESM5 model output prepared for CMIP6 CMIP 1pctCO2. Version 20190429. Earth System Grid Federation, 2019b. <https://doi.org/10.22033/ESGF/CMIP6.3151>.
- Swinbank, R. and Ortland, D. A. Compilation of wind data for the Upper Atmosphere Research Satellite (UARS) Reference Atmosphere Project. *Journal of Geophysical Research: Atmospheres*, 108(D19), 2003. <https://doi.org/10.1029/2002JD003135>.
- Tatebe, H. and Watanabe, M. MIROC MIROC6 model output prepared for CMIP6 CMIP 1pctCO2. Version 20190912. Earth System Grid Federation, 2018. <https://doi.org/10.22033/ESGF/CMIP6.5371>.
- Taylor, K. E., Stouffer, R. J., and Meehl, G. A. An Overview of CMIP5 and the Experiment Design. *Bulletin of the American Meteorological Society*, 93(4):485–498, 2012. <https://doi.org/10.1175/BAMS-D-11-00094.1>.
- Taylor, K. E., Juckes, M., Balaji, V., Cinquini, L., Denvil, S., Durack, P. J., Elkington, M., Guilyardi, E., Kharin, S., Lautenschlager, M., Lawrence, B., Nadeau, D., and Stockhause, M. CMIP6 Global Attributes, DRS, Filenames, Directory Structure, and CV's, 2018. Retrieved from <https://goo.gl/v1drZ1>. Accessed: 2021-11-08.

- Tebaldi, C., Debeire, K., Eyring, V., Fischer, E., Fyfe, J., Friedlingstein, P., Knutti, R., Lowe, J., O'Neill, B., Sanderson, B., van Vuuren, D., Riahi, K., Meinshausen, M., Nicholls, Z., Tokarska, K. B., Hurtt, G., Kriegler, E., Lamarque, J.-F., Meehl, G., Moss, R., Bauer, S. E., Boucher, O., Brovkin, V., Byun, Y.-H., Dix, M., Gualdi, S., Guo, H., John, J. G., Kharin, S., Kim, Y., Koshiro, T., Ma, L., Olivié, D., Panickal, S., Qiao, F., Rong, X., Rosenbloom, N., Schupfner, M., Séférian, R., Sellar, A., Semmler, T., Shi, X., Song, Z., Steger, C., Stouffer, R., Swart, N., Tachiiri, K., Tang, Q., Tatebe, H., Voldoire, A., Volodin, E., Wyser, K., Xin, X., Yang, S., Yu, Y., and Ziehn, T. Climate model projections from the Scenario Model Intercomparison Project (ScenarioMIP) of CMIP6. *Earth System Dynamics*, 12(1): 253–293, 2021. <https://doi.org/10.5194/esd-12-253-2021>.
- Tebaldi, C. and Knutti, R. The use of the multi-model ensemble in probabilistic climate projections. *Philosophical Transactions of the Royal Society A: Mathematical, Physical and Engineering Sciences*, 365(1857):2053–2075, 2007. <https://doi.org/10.1098/rsta.2007.2076>.
- Thompson, D. W. J. and Wallace, J. M. Annular Modes in the Extratropical Circulation. Part I: Month-to-Month Variability. *Journal of Climate*, 13(5):1000–1016, 2000. [https://doi.org/10.1175/1520-0442\(2000\)013<1000:AMITEC>2.0.CO;2](https://doi.org/10.1175/1520-0442(2000)013<1000:AMITEC>2.0.CO;2).
- Thompson, D. W. J., Baldwin, M. P., and Solomon, S. Stratosphere–Troposphere Coupling in the Southern Hemisphere. *Journal of the Atmospheric Sciences*, 62(3):708–715, 2005. <https://doi.org/10.1175/JAS-3321.1>.
- Thompson, D. W. J., Seidel, D. J., Randel, W. J., Zou, C.-Z., Butler, A. H., Mears, C., Osso, A., Long, C., and Lin, R. The mystery of recent stratospheric temperature trends. *Nature*, 491:692–697, 2012. <https://doi.org/10.1038/nature11579>.
- U.S. Government Printing Office. *U.S. Standard Atmosphere*. Washington, D.C., 1976.
- Vallis, G. K. *Atmospheric and Oceanic Fluid Dynamics: Fundamentals and Large-Scale Circulation*. Cambridge University Press, Cambridge, U.K., 2nd edition, 2017.
- Vallis, G. K., Zurita-Gotor, P., Cairns, C., and Kidston, J. Response of the large-scale structure of the atmosphere to global warming. *Quarterly Journal of the Royal Meteorological Society*, 141(690):1479–1501, 2015. <https://doi.org/10.1002/qj.2456>.
- Walz, R., Garny, H., and Birner, T. Stratospheric Modulation of Tropical Upper-Tropospheric Warming-Induced Circulation Changes in an Idealized General Circulation Model. *Journal of the Atmospheric Sciences*, in review.
- Wan, H., Giorgetta, M. A., and Bonaventura, L. Ensemble Held–Suarez Test with a Spectral Transform Model: Variability, Sensitivity, and Convergence. *Monthly Weather Review*, 136(3):1075–1092, 2008. <https://doi.org/10.1175/2007MWR2044.1>.
- Wang, S.-M., Xie, A.-H., and Zhu, J.-P. Does polar amplification exist in Antarctic surface during the recent four decades? *Journal of Mountain Science*, 18:2626–2634, 2021. <https://doi.org/10.1007/s11629-021-6912-2>.
- Wang, S., Gerber, E. P., and Polvani, L. M. Abrupt Circulation Responses to Tropical Upper-Tropospheric Warming in a Relatively Simple Stratosphere-Resolving AGCM. *Journal of Climate*, 25(12):4097–4115, 2012. <https://doi.org/10.1175/JCLI-D-11-00166.1>.

- White, I., Garfinkel, C. I., Gerber, E. P., Jucker, M., Aquila, V., and Oman, L. D. The Downward Influence of Sudden Stratospheric Warmings: Association with Tropospheric Precursors. *Journal of Climate*, 32(1):85–108, 2019. <https://doi.org/10.1175/JCLI-D-18-0053.1>.
- Wieners, K.-H., Giorgetta, M., Jungclaus, J., Reick, C., Esch, M., Bittner, M., Legutke, S., Schupfner, M., Wachsmann, F., Gayler, V., Haak, H., de Vrese, P., Raddatz, T., Mauritsen, T., von Storch, J.-S., Behrens, J., Brovkin, V., Claussen, M., Crueger, T., Fast, I., Fiedler, S., Hagemann, S., Hohenegger, C., Jahns, T., Kloster, S., Kinne, S., Lasslop, G., Kornbluh, L., Marotzke, J., Matei, D., Meraner, K., Mikolajewicz, U., Modali, K., Müller, W., Nabel, J., Notz, D., Peters-von Gehlen, K., Pincus, R., Pohlmann, H., Pongratz, J., Rast, S., Schmidt, H., Schnur, R., Schulzweida, U., Six, K., Stevens, B., Voigt, A., and Roeckner, E. MPI-M MPI-ESM1.2-LR model output prepared for CMIP6 CMIP 1pctCO2. Version 20190710. Earth System Grid Federation, 2019. <https://doi.org/10.22033/ESGF/CMIP6.6435>.
- Wilcox, L. J. and Charlton-Perez, A. J. Final warming of the Southern Hemisphere polar vortex in high- and low-top CMIP5 models. *Journal of Geophysical Research: Atmospheres*, 118(6):2535–2546, 2013. <https://doi.org/10.1002/jgrd.50254>.
- Wilcox, L. J., Charlton-Perez, A. J., and Gray, L. J. Trends in Austral jet position in ensembles of high- and low-top CMIP5 models. *Journal of Geophysical Research: Atmospheres*, 117(D13), 2012. <https://doi.org/10.1029/2012JD017597>.
- Williamson, D. L. The Evolution of Dynamical Cores for Global Atmospheric Models. *Journal of the Meteorological Society of Japan. Ser. II*, 85B:241–269, 2007. <https://doi.org/10.2151/jmsj.85B.241>.
- WMO. Definition of the tropopause. *WMO Bull.*, 6:136, 1957.
- Wu, Y., Simpson, I. R., and Seager, R. Intermodel Spread in the Northern Hemisphere Stratospheric Polar Vortex Response to Climate Change in the CMIP5 Models. *Geophysical Research Letters*, 46(22):13290–13298, 2019. <https://doi.org/10.1029/2019GL085545>.
- Wu, Z. and Reichler, T. Towards a More Earth-Like Circulation in Idealized Models. *Journal of Advances in Modeling Earth Systems*, 10(7):1458–1469, 2018. <https://doi.org/10.1029/2018MS001356>.
- Yoden, S. Bifurcation Properties of a Stratospheric Vacillation Model. *Journal of Atmospheric Sciences*, 44(13):1723–1733, 1987. [https://doi.org/10.1175/1520-0469\(1987\)044<1723:BPOASV>2.0.CO;2](https://doi.org/10.1175/1520-0469(1987)044<1723:BPOASV>2.0.CO;2).
- Yukimoto, S., Koshiro, T., Kawai, H., Oshima, N., Yoshida, K., Urakawa, S., Tsujino, H., Deushi, M., Tanaka, T., Hosaka, M., Yoshimura, H., Shindo, E., Mizuta, R., Ishii, M., Obata, A., and Adachi, Y. MRI MRI-ESM2.0 model output prepared for CMIP6 CMIP 1pctCO2. Version 20200303. Earth System Grid Federation, 2019. <https://doi.org/10.22033/ESGF/CMIP6.5356>.
- Yuval, J. and Kaspi, Y. Eddy Activity Response to Global Warming-Like Temperature Changes. *Journal of Climate*, 33(4):1381–1404, 2020. <https://doi.org/10.1175/JCLI-D-19-0190.1>.

- Zängl, G., Reinert, D., Rípodas, P., and Baldauf, M. The ICON (ICOsahedral Non-hydrostatic) modelling framework of DWD and MPI-M: Description of the non-hydrostatic dynamical core. *Quarterly Journal of the Royal Meteorological Society*, 141(687):563–579, 2015. <https://doi.org/10.1002/qj.2378>.
- Zappa, G., Pithan, F., and Shepherd, T. G. Multimodel Evidence for an Atmospheric Circulation Response to Arctic Sea Ice Loss in the CMIP5 Future Projections. *Geophysical Research Letters*, 45(2):1011–1019, 2018. <https://doi.org/10.1002/2017GL076096>.
- Zappa, G. and Shepherd, T. G. Storylines of Atmospheric Circulation Change for European Regional Climate Impact Assessment. *Journal of Climate*, 30(16):6561–6577, 2017. <https://doi.org/10.1175/JCLI-D-16-0807.1>.

Used software, data, and computational resources

This thesis was carried out at the Institute of Atmospheric Physics (IPA) of the German Aerospace Center (Deutsches Zentrum für Luft- und Raumfahrt, DLR) and also used resources of the German Climate Computing Center (Deutsches Klimarechenzentrum, DKRZ) granted by its Scientific Steering Committee (WLA) to develop the idealized climate model EMIL further (Garny et al., 2020), to perform simulations with it, and to process and visualize data with the help of the following software:

- The Fortran program I developed for the computation of important TEM quantities as EP fluxes, their divergence, and the residual circulation is available within the MESSy community (https://www.messy-interface.org/current/auto/messy_tools.html).
- The NCL program for the zonal-wavenumber decomposition of temperature and wind fields was provided by Hella Garny (<https://www.ncl.ucar.edu/>).
- CDO was used for data processing (<https://code.mpimet.mpg.de/projects/cdo>).
- Ferret was used for data visualization (<https://ferret.pmel.noaa.gov/Ferret/>).
- Python 3 (<https://www.python.org/>) including the packages eofs, jupyter, matplotlib, netcdf4, notebook, numpy, pandas, and scipy (<https://pypi.org/>) was used for data processing and visualization.

Furthermore, the following data sets were used:

- The SPARC reference climatologies for temperature and zonal wind were provided by Markus Kunze. They are available at ftp://sparc-ftp1.ceda.ac.uk/sparc/ref_clim/randel/temp_wind/, and a description can be found at <https://www.sparc-climate.org/data-centre/data-access/reference-climatology/randals-climatologies/temperature-wind-climatology/> (SPARC, 2002; Randel et al., 2004; Swinbank and Ortland, 2003).
- The ERA5 data sets for temperature and zonal wind were provided by Hella Garny. They are available at <https://www.ecmwf.int/en/forecasts/datasets/reanalysis-datasets/era5/> (Hersbach et al., 2020).
- Monthly-mean zonal-mean multi-model output from the CMIP6 1pctCO2 experiment was used. I acknowledge the World Climate Research Programme, which, through its Working Group on Coupled Modelling, coordinated and promoted CMIP6. I thank the

climate modeling groups for producing and making available their model output, the Earth System Grid Federation (ESGF) for archiving the data and providing access, and the multiple funding agencies who support CMIP6 and ESGF. I thank the DKRZ for providing access to the CMIP6 multi-model output via <https://esgf-data.dkrz.de/projects/cmip6-dkrz/>.

Acknowledgments

First of all, I would like to thank Hella Garny for her priceless supervision during the entire time of this work. Thank you for your support, your encouragement, your expertise, your boundless optimism, and for always making time for discussions. Discovering science with you is a valuable experience and a pleasure.

Furthermore, I thank Thomas Birner not only for taking a part as the second reviewer of this thesis, but also for sharing profound insights, helpful comments, and exciting facts beyond usual topics.

I thank Markus Rapp, Robert Sausen, and Martin Dameris for enabling my work at DLR.

Apart from that, many others contributed to this thesis and the enjoyable atmosphere at work. In particular, I thank:

- Simone Dietmüller, Roland Eichinger, Frauke Fritsch, Sheena Löffel, Matthias Nützel, Mariano Mertens, Björn Brötz, Manuel Schlund, Johannes Pletzer, Franziska Winterstein, Pooja Verma, and Daniel Senftleben for useful discussions and their help on data processing.
- Patrick Jöckel for sharing his expertise in climate model developing and for providing assistance with programming.
- Winfried Beer and Karl-Ernst Müller for their IT support.
- Daniela Domeisen, Edwin Gerber, and Hauke Schmidt for valuable discussions.
- Markus Kunze for his help on accessing SPARC data.
- Sonja Gisinger for substantial comments on earlier versions, and Simon Grosche for proofreading all parts of this thesis.
- Robert Sausen, Luisa Cristini, Nadine Wieters, and in particular Mariano Mertens for organizing a fantastic ESM Summer School 2019.
- Natalia Calvo, among many others, for hosting an inspiring DynVarMIP workshop in 2019 where I had the chance to meet scientists from all over the world.
- My colleagues in the ESM department as well as in IPA for nice breaks and refreshing social activities.

Last but not least, I would like to thank my family and friends who had to put up with my sparse presence lately. Thank you for everything!

